

DISS. ETH NO. 27131

**Enzyme-Enabled DNA Biosensors for  
Field-deployable Diagnostics**

A thesis submitted to attain the degree of

DOCTOR OF SCIENCES of ETH ZÜRICH

(Dr. sc. ETH Zürich)

presented by

**AKKAPOL SUEA-NGAM**

M.Sc. in Chemistry, Chulalongkorn University

born on 8<sup>th</sup> October 1991

citizen of THAILAND

accepted on the recommendation of

Prof. Dr. Andrew J. deMello

Prof. Dr. Paolo Arosio

Dr. Philip D. Howes

2020

‘Understanding each other is intelligence.  
Understanding oneself is wisdom’

*Helga Nowotny*

# Acknowledgements

First of all, I would like to express my sincere gratitude to the *Swiss Government Excellence Scholarship* (2016–2019) that allowed me to come to ETH Zürich, and my supervisor, *Prof. Dr. Andrew J. deMello*, who accepted me to join his research group and supervised me since I was first applying for the scholarship. Professor deMello has not only given me excellent supervision through his scientific expertise and publication knowledge, gained from his extraordinary experience, but has also given me many opportunities to discover new knowledge beyond that already established in his lab. He has never said ‘no’ to any proposed projects, and he encourages his students to learn from the failures, to let them truly achieve a *Philosophy* of science degree. Beyond the science, Prof. deMello puts his student mental health as a priority. He takes it seriously when his students have personal challenges, and tries his best to help and protect them. Having a magnanimous supervisor was such a gift for my PhD studies; being one of his students has been an excellent opportunity in my career.

*Dr. Philip D. Howes* joined the deMello group in more or less the same period that I joined, and he became my mentor in January 2018. Dr. Howes has done a fantastic job supervising and encouraging my research. I admire his excellent scientific knowledge and experience, and in particular his selflessness. Although it is not easy to supervise a student who is researching a different field from his background, he has never given up. He gave opportunities to himself to discover new knowledge, has obviously enjoyed learning new things, and is always willing to ask his supervisee if he does not understand, without ego. He is one of the people I trust and am able to tell everything about myself, from research to personal life, so practically apart from science, he is also my counsellor. I appreciate his endeavor and camaraderie, and do not know how to thank him enough. Without him along with my PhD studies, I could not make it.

Further, I would like to thank *Prof. Dr. Paolo Arosio* for being so kind to be on the committee for my thesis. Further, I thank *Ms. Zahra* and *Dr. Ilada*, my collaborators, who helped me carry out excellent research smoothly. They not only showed their professional research skills, but also offered great friendship, and kept listening and supporting me when I was down. Also, I have to thank my office mate, *Dr. Yun Ding*, who helped me through many challenges with technology, suggesting how to behave in the group, and being my travel companion. I wish also to thank *Ms. Tamara* and *Mr. Leif*, whom I supervised during their Masters studies, and *Mr. Léonard*, my junior PhD fellow who has taken up my interests in electrochemical analysis for the point-of-care. I also appreciate friendships with many deMello members, including *Dr. Hess*, *Dr. Yang*, *Dr. Berger*, *Dr. Cao*, *Dr. Abrishamkar*, *Dr. Richards*, *Dr. Du*, *Dr. Li*, *Ms. Probst*, *Mr. Sevim*, *Ms. Villois*, and so on, and in particular *Ms. Nette* for translating my thesis abstract into German. Importantly, all the documentation could not have been possible without *Frau. Gassmann*, who helped me from the beginning of my PhD application, and was always feeding us with her delicious carrot and lemon cakes, and *Frau. Gröbli*, who has given great help preparing all documentation after Jenny left.

I have also made many friends outside of the group. I would like to thank the Swiss Government Excellent Scholarship fellows, including *Mr. Kumar*, *Ms. Vuković*, and in particular *Ms. Ninomiya*, who was my first friend when I arrived Zürich. I also thank my Thai friends, including *Mr. Jindakun*, *Mr. Pienroj*, *Ms. Ratananakorn*, *Ms. Keerati*, and so on, in particular *Ms. Kaewsawan*, *Mr. Jantz*, and *Ms. Meister*. These people have kept me during my years in Switzerland.

Thanks to the technology that allows me to communicate with my family and friends in my home country, Thailand, I have had a lot of support from my friends, including *Ms. Puangdech*, *Ms. Techawongsuwan*, *Ms. Pornphongsa*, *Mr. Tawiporn*, *Mr. Jivarungsinee*, *Ms. Jirakit*, *Mr. Chanyam*, *Dr. Angsujinda*, and so on. I appreciate my previous supervisors in Thailand, *Prof. Dr. Srisa-Art*, *Prof. Dr. Wongravee*, and *Prof. Dr. Chailapakul* and their research group members, who were my inspiration to study for a PhD abroad, and have always supported me. Also, *Prof. Dr. Aeungmaitrepirom*, *Dr. Puthongkham*, and *Dr. Wirojsangthong* are people that keep supporting me; I genuinely appreciate your friendship and kindness.

Last, but the most important, I would like to express my deepest gratitude to my father, *Mr. Pradid*, who brought me up as a single dad since my mother passed away when I was seven years old. He is a strong, brave, kind, generous, honest, loyal, funny, helpful, smart, and humble man, and is my beloved one, whom I can call home. He offers me not only the purest true love, but also a way of thinking critically with good plans for everything in my life, so that I grew up to be a man who can handle anything. Another important man in my life is my brother, who is my second parent, who brought me up and has kept supporting me no matter what. We are siblings, friends, family, and foe who always argue about who is dad's favorite. Indeed, I would like to thank my grandmother, *Ms. Orasa*, and aunts, in particular, *Ms. Amphawan* and *Ms. Arunwan* who fulfilled my childhood with love and joy, and other family members, including *Mr. Sornwisit*, *Mr. Jirawat*, and so on. Without these people, I am sure that I cannot reach this point in life.

# Abstract

A vast number of people in resource-limited areas suffer disease and environmental toxicity due to insufficient diagnostic tools. Accordingly, the development of diagnostic devices that can be readily deployed in such locations is vital. DNA has been proven as an excellent biorecognition element in the production of cost-effective biosensors due to a combination of its highly specific binding capacity with its cheap and scalable synthesis routes. Further, DNA can be modified, amplified or digested by many different enzymes, including polymerases, nucleases and redox enzymes, which offers significant functionalities in the development of sensitive biosensors. In recent decades, microfluidic platforms have been leveraged to make cost-effective and high-performance diagnostic devices. This approach allows reactions to proceed in a confined volume through the manipulation of reagents and samples at the micro to picoliter scale, and can achieve excellent analytical performance. However, although many microfluidic-based analytical methods have been developed, it remains a significant challenge to achieve excellent analytical performance with truly field-deployable diagnostic devices.

Herein, field-deployable diagnostic devices are developed for various applications. Specifically, DNA-enzyme interactions were leveraged within microfluidic platforms to realise ultrasensitive detection of toxins and disease biomarkers. Ochratoxin A (OTA), a common cancer-causing mycotoxin, and methicillin-resistant *S. aureus* (MRSA), a common drug-resistant bacterium that kills a million people yearly, were chosen as representative toxins and pathogens. MRSA was detected via loop-mediated isothermal amplification (LAMP), and also using a clustered regularly interspaced short palindromic repeats (CRISPR) biosensor. The *mecA* gene, which is shared throughout all MRSA strains, was chosen as the target. A colorimetric assay using silver nanoplates that bind with the LAMP amplicons, enabled detection of the *mecA* gene down to the single-molecule level. Subsequently, a colorimetric paper-based analytical device (PAD) incorporating immobilized LAMP primers was used to enable single-molecule detection via smartphone-based analysis. Hydrogel droplets were then used to realise a digital LAMP platform, which for the first time provides for a sensitive and straightforward route to pathogen detection and quantification. Finally, an electrochemical CRISPR biosensor was developed to target the *mecA* gene, where activation of trans-cleavage and removal of ssDNA probes on an electrode, allows sensitive and specific detection down to the single nucleotide mismatch level and without the need for additional DNA amplification. OTA was detected and quantified by both electrochemical and colorimetric methods. Specifically, ssDNA was metallized on electrode surfaces to allow for detection of OTA down to sub-pg/mL levels using square wave voltammetry. Using a colorimetric approach, the well-known starch-iodide complex was used to provide a colour in the presence of OTA, through formation of a sandwich complex with an antibody and ssDNA-glucose oxidase. In the presence of glucose, iodine and starch, a blue-purple solution is generated, allowing detection of OTA down to pg/mL levels via smartphone analysis.

All developed diagnostic devices have significant potential utility for use in resource-limited environments and represent a significant advance in field-deployable diagnostic tool development.

# Zusammenfassung

Eine große Zahl von Menschen in Gebieten mit begrenzten Ressourcen leidet aufgrund unzureichender diagnostischer Hilfsmittel an Krankheiten und Umwelttoxizität. Dementsprechend ist die Entwicklung von Diagnosegeräten, die an solchen Orten leicht eingesetzt werden können, von entscheidender Bedeutung. DNA hat sich aufgrund der Kombination ihrer hochspezifischen Bindungskapazität mit ihren kostengünstigen und skalierbaren Synthesewegen als hervorragendes Biorekennungselement für die Herstellung kostengünstiger Biosensoren erwiesen. Darüber hinaus kann DNA durch viele verschiedene Enzyme, einschließlich Polymerasen, Nukleasen und Redox-Enzyme, modifiziert, amplifiziert oder verdaut werden, was bedeutende Funktionalitäten bei der Entwicklung empfindlicher Biosensoren bietet. In den letzten Jahrzehnten wurden mikrofluidische Plattformen genutzt, um kostengünstige und leistungsstarke Diagnosegeräte herzustellen. Dieser Ansatz ermöglicht Reaktionen in einem begrenzten Volumen durch die Manipulation von Reagenzien und Proben im Mikro- bis Pikolitermaßstab und kann eine ausgezeichnete analytische Leistung erzielen. Obwohl viele auf Mikrofluidik basierende Analysemethoden entwickelt wurden, bleibt es jedoch eine große Herausforderung, mit wirklich vor Ort einsetzbaren Diagnosegeräten eine ausgezeichnete analytische Leistung zu erzielen.

Hier werden vor Ort einsetzbare Diagnosegeräte für verschiedene Anwendungen entwickelt. Insbesondere wurden DNA-Enzym-Interaktionen innerhalb von Mikrofluidik-Plattformen genutzt, um einen ultrasensitiven Nachweis von Toxinen und Krankheitsbiomarkern zu realisieren. Ochratoxin A (OTA), ein häufiges krebserzeugendes Mykotoxin, und Methicillin-resistenter *S. aureus* (MRSA), ein häufiges arzneimittelresistentes Bakterium, das jährlich eine Million Menschen tötet, wurden als repräsentative Toxine und Krankheitserreger ausgewählt. MRSA wurde über eine schleifenvermittelte isotherme Amplifikation (LAMP) und auch über einen geclusterten Biosensor mit regelmäßig interspaced short palindromic repeats (CRISPR) nachgewiesen. Das *mecA*-Gen, das allen MRSA-Stämmen gemeinsam ist, wurde als Ziel gewählt. Ein kolorimetrischer Assay unter Verwendung von Silber-Nanoplaten, die an die LAMP-Amplikons binden, ermöglichte den Nachweis des *mecA*-Gens bis auf Einzelmolekülebene. Anschließend wurde ein kolorimetrisches papierbasiertes Analysegerät (PAD) mit immobilisierten LAMP-Primern verwendet, um den Einzelmolekül-Nachweis mittels Smartphone-basierter Analyse zu ermöglichen. Hydrogeltröpfchen wurden dann verwendet, um eine digitale LAMP-Plattform zu realisieren, die zum ersten Mal einen empfindlichen und unkomplizierten Weg zum Nachweis und zur Quantifizierung von Krankheitserregern bietet. Schliesslich wurde ein elektrochemischer CRISPR-Biosensor entwickelt, der auf das *mecA*-Gen abzielt, wobei die Aktivierung der Trans-Spaltung und die Entfernung der ssDNA-Sonden auf einer Elektrode einen empfindlichen und spezifischen Nachweis bis hinunter zur Einzelnukleotid-Ebene ermöglicht, ohne dass eine zusätzliche DNA-Amplifikation erforderlich ist. OTA wurde sowohl mit elektrochemischen als auch mit kolorimetrischen Methoden nachgewiesen und quantifiziert. Insbesondere wurde ssDNA auf Elektrodenoberflächen metallisiert, um den Nachweis von OTA bis hinunter zu sub-pg/mL mittels Rechteckwellenvoltammetrie zu ermöglichen. Unter Verwendung eines kolorimetrischen Ansatzes wurde der bekannte Stärke-Iodid-Komplex verwendet, um in Gegenwart von OTA durch Bildung eines Sandwich-Komplexes mit einem Antikörper und ssDNA-Glucoseoxidase eine Farbe zu liefern. In Gegenwart von Glukose, Jod und Stärke wird eine blau-violette Lösung erzeugt, die den Nachweis von OTA bis hinunter zu pg/mL mittels Smartphone-Analyse ermöglicht.

Alle entwickelten Diagnosegeräte haben einen bedeutenden potentiellen Nutzen für den Einsatz in ressourcenbeschränkten Umgebungen und stellen einen bedeutenden Fortschritt in der Entwicklung von vor Ort einsetzbaren Diagnosewerkzeugen dar.

# Table of Contents

Acknowledgements .....	3
Abstract .....	5
Table of Contents .....	7
List of Figures .....	11
List of Schemes .....	17
List of Tables.....	18
Chapter 1	
Introduction.....	19
1.1 Introduction.....	20
1.1.1 Point-of-care infectious disease diagnostics .....	20
1.1.2 Nucleic acid biomarkers in infectious disease.....	21
1.1.3 The role of enzymes in nucleic acid biosensing .....	22
1.1.4 Application of nucleic acids in toxin analysis.....	22
1.2 Enzyme-assisted nucleic acid amplification.....	23
1.2.1 Polymerase chain reaction.....	23
1.2.2 Isothermal PCR .....	24
1.3 Enzyme-assisted signal generation .....	29
1.3.1 CRISPR/Cas enzymes .....	29
1.3.2 Redox enzymes .....	33
1.4 Enzyme-enabled aptasensors for toxin detection .....	34
1.4.1 Enzyme treatments to reduce background signal.....	34
1.4.2 Enzyme-enhanced signal generation.....	34
1.5 Point-of-care systems .....	35
1.5.1 System requirements .....	35
1.5.2 Benchtop systems .....	36
1.5.3 Chip-based microfluidic systems .....	37
1.5.4 Paper-based systems.....	39
1.6 Thesis overview .....	42
Chapter 2	
<i>In situ</i> nucleic acid amplification and ultrasensitive colorimetric readout in a paper-based analytical device using silver nanoplates .....	44
2.1 Introduction.....	45

2.2 Materials and methods.....	47
2.2.1 Instrumentation .....	47
2.2.2 LAMP reaction conditions .....	47
2.2.3 Device design.....	49
2.2.4 Image analysis.....	49
2.2.5 Immobilized primer study .....	49
2.2.6 Lysate testing and selectivity study .....	50
2.3 Results and discussion .....	50
2.3.1 Colorimetric detection using silver nanoplates .....	50
2.3.2 Assay development .....	53
2.3.3 Comparison between LAMP and PCR.....	57
2.3.4 Sample testing and specificity study.....	57
2.3.5 Paper-based device integration .....	58
2.4 Conclusions.....	62
<b>Chapter 3</b>	
Hydrogel Digital LAMP Development for Highly Sensitive Drug-Resistance Bacteria Detection	64
3.1 Introduction .....	65
3.2 Materials and methods .....	67
3.2.1 Chemicals.....	67
3.2.2 Biological samples and reagents .....	67
3.2.3 Microfluidic device design and fabrication.....	67
3.2.4 Polyacrylamide microgel preparation .....	68
3.2.5 MRSA assay procedure.....	68
3.2.6 Selectivity study .....	69
3.3 Results and Discussion.....	69
3.3.1 PAA hydrogel characterization .....	69
3.3.2 HD-LAMP characterization.....	71
3.3.3 DNA quantitation with digital droplet LAMP.....	73
3.3.4 Selectivity.....	75
3.3.5 Accuracy and precision .....	76
3.3.6 Stability of hydrogel beads .....	76
3.4 Conclusions.....	77
<b>Chapter 4</b>	
An Amplification-Free Ultra-Sensitive Electrochemical CRISPR/Cas Biosensor for Drug-Resistant Bacteria Detection Using Silver Metallization.....	78



4.1 Introduction.....	79
4.2 Methodology.....	81
4.2.1 Materials and reagents .....	81
4.2.2 <i>mecA</i> gene preparation .....	82
4.2.3 Electrochemical detection.....	82
4.2.4 Fluorescence detection.....	82
4.2.5 Mismatch analysis .....	82
4.2.6 Human sample and bacterial sample analyses.....	83
4.3 Results and discussion .....	84
4.3.1 Electrode characterisation.....	84
4.3.2 Optimization .....	87
4.3.3 Analytical performance .....	91
4.4 Conclusions.....	96
Chapter 5	
An Exonuclease I-Assisted Silver-Metallized Electrochemical Aptasensor for Ochratoxin A	
Detection.....	97
5.1 Introduction.....	98
5.2 Material and methods.....	99
5.2.1 Materials and reagents .....	99
5.2.2 Electrochemical detection.....	99
5.2.3 System optimization .....	100
5.2.4 Real sample analysis.....	104
5.3 Results and discussion .....	105
5.3.1 Characterization of modified electrodes.....	105
5.3.2 Optimization .....	108
5.3.3 Analytical performance .....	114
5.4 Conclusions.....	118
Chapter 6	
An Ultrasensitive Non-Noble Metal Colorimetric Assay Using Starch–Iodide Complexation for	
Ochratoxin A Detection .....	119
6.1 Introduction.....	120
6.2 Materials and methods .....	122
6.2.1 Reagents and materials .....	122
6.2.2. Device fabrication.....	122
6.2.3 Aptasensor-GOx conjugation .....	123
6.2.4 Assay procedures.....	123

6.2.5 GOx optimization .....	123
6.2.6 System optimization.....	123
6.2.7 Operation of PAD and real sample analysis.....	129
6.2.8 Characterization.....	129
6.3 Results and discussion .....	129
6.3.1 Colorimetric method validation.....	129
6.3.2 Assay optimization.....	131
6.3.3 Enzymatic activity .....	132
6.3.4 Analytical performance .....	134
6.3.5 Complex sample analysis.....	138
6.3.6 Assay stability .....	138
6.4 Conclusions.....	139
Chapter 7	
Outlook for Field-Deployable Diagnostics .....	140
7.1 Current state and future prospects.....	140
7.2 Future areas of focus.....	141
Chapter 8	
Conclusions .....	143
References .....	145
Curriculum Vitae.....	163

# List of Figures

- Figure 1. 1** The path towards the point-of-care, illustrating standalone, benchtop, and handheld systems that are providing from centralized laboratory to end user/community depending on the affordability, accessibility, and ease of use. .... 21
- Figure 1.2** Schematic representations of different isothermal amplification techniques. LAMP: Binding of the inner primers (FIP, BIP) is followed by strand displacement and polymerization by Bst polymerase. Subsequent binding of an outer primer (F3, B3), and polymerization, displaces the newly synthesized strand which forms a self-hybridizing loop structure. This process repeats on the opposite end of the target sequence with the reverse primer, forming short 'dumbbell' loop structures that can be amplified into dsDNA concatemers. RCA: Target DNA binds to a padlock probe template, circularized by DNA ligase, followed by  $\Phi$ 29 polymerase which rolls around the circular template to produce an ssDNA amplicon. RPA. A recombinase enzyme inserts forward and reverse primers into a dsDNA target template, resulting in strand displacement. Single-strand binding proteins (SSBs) bind to prevent strand recombination, and Bsu polymerase amplifies the template. SDA. After an initial round of amplification, an endonuclease nicks the newly synthesized strands between the primer and the target, allowing a new polymerase enzyme to bind and amplify the target whilst simultaneously displacing the old strand. HDA. Initial DNA denaturation is performed by helicase, which is followed by an SSB to prevent recombination. Subsequent binding of the primers is followed by polymerization. NASBA. A P1 forward primer, containing complementary regions for both the target and a T7 promoter region, binds to a target RNA(-) strand. In the initial stage, reverse transcriptase extends the primer to produce a DNA:RNA duplex, and the RNA strand is subsequently degraded by RNase H to produce an ssDNA template. Binding of the P2 reverse primer and extension by reverse transcriptase produces a dsDNA, which can then enter the amplification stage. T7 polymerase binds the dsDNA to create an RNA strand that is anti-sense to the original target, the P2 reverse primer can bind, and the whole process begins again, resulting in RNA amplicons. .... 28
- Figure 1. 3** Schematic representations of different Cas enzyme activities. Cas9: Binding of target dsDNA to the gRNA-Cas9 complex is followed by cis-cleavage of the DNA. Cas12/14: Binding of the target ds/ssDNA to the gRNA-Cas12 complex and subsequent cis-cleavage of the DNA is followed by collateral trans-cleavage of ssDNA molecular beacon probes to generate fluorescence. Cas13: Binding of the ssRNA to the gRNA-Cas13 complex and subsequent cis-cleavage of the RNA is followed by collateral trans-cleavage of ssRNA molecular beacon probes to generate fluorescence. .... 32
- Figure 2. 1** a)-d) TEM images of the stock AgNPIs, AgNPIs with LAMP amplicons, AgNPIs with LAMP amplicons and NaBr (positive control), and etched AgNPIs with NaBr in the absence of target molecule (negative control), respectively. .... 52
- Figure 2. 2** a) AgNPI absorption spectra when incubated with different halide salts. b) The degree of AgNPI etching, and solution colour, changes in the presence of the different reaction components, revealing the protective effect that the LAMP product has against etching, and the promise of this mechanism for nucleic acid detection. .... 53
- Figure 2. 3** Image of agarose gel electropherogram containing the DNA ladder (100–1000 kb, Promega, Switzerland), negative LAMP, 1, 10,  $10^2$ ,  $10^3$ , and  $10^4$  copies of *mecA*

	template using optimised condition in <b>Table 2.2</b> and incubate in electrophoresis bath (Bio-Rad, Switzerland) for 20 minutes. The gel electrophoresis was carried out using 2% agarose gel in 1X TBE buffer, operating under 100 V for 60 minutes, and visualised by Novel juice (Sigma Aldrich) under the 300 nm UV lamp. .... 54
<b>Figure 2. 4</b>	TEM image of a) LAMP product with AgNPIs embedded (1 hour incubation, no NaBr) and b) AgNPIs with PCR product DNA, after addition of NaBr. .... 55
<b>Figure 2. 5</b>	a) Absorption spectra at various LAMP product concentrations, revealing that degree of etching is concentration dependent. b) Calibration curves from absorbance at 520 nm and colorimetric analysis (greyscale intensity). Inset: the corresponding reaction solutions. c) The full assay dose-response curves, comparing PCR and LAMP product performance for the AgNPI assay. d) Specificity for MRSA versus other bacteria, for the PCR and LAMP assays..... 56
<b>Figure 2. 6</b>	Accuracy test comparing the LAMP and PCR assays using known concentration ( $10^3$ , $10^4$ , and $10^5$ ag/ $\mu$ L) of <i>mecA</i> gene..... 57
<b>Figure 2. 7</b>	a) Comparing the effect of immobilization versus non-immobilization of the LAMP primer on the cellulose surface, revealing an enhanced signal in the immobilized case. b) Direct comparison of the dose–response for the paper-based and tube-based formats, revealing no significant difference in performance. .... 58
<b>Figure 2. 8</b>	a) Fluorescence response of DNA amplification of LAMP system by missing inner (FIP and BIP), outer (F3 and B3) and additional (LF and LB) primers b) CT value corresponding to the missing results in a). .... 59
<b>Figure 2. 9</b>	The PAD device components and test process. After adding the sample and LAMP buffer to the device it is sealed and heated to 58°C for 30 minutes. A 30 second incubation with added AgNPIs, then NaBr, reveals the test result which can then be read by the naked eye (qualitative), or captured by a camera for image analysis (quantitative)..... 60
<b>Figure 2. 10</b>	a) Specificity test for MRSA versus other bacteria for the paper-based test, revealing excellent specificity. Inset: Raw (upper) and processed images (lower) of the devices. b) Accuracy test for the tube (left axis) and paper-based (right axis) assay formats, revealing excellent correlation with the PCR (bottom axis). .... 61
<b>Figure 2. 11</b>	Stability test of the paper-based device over one month using three concentrations of <i>mecA</i> (N=3)..... 62
<b>Figure 3. 1</b>	a) The microfluidic step-emulsification device used for high-throughput generation of PAA microgel particles. b) overview of the static micromixer design and COMSOL simulation of mixing performance. c) The obtained PAA beads, imaged after 120 days at 4 °C. d) A histogram of the droplet size distribution. .... 70
<b>Figure 3. 2</b>	Agarose gel electrophoresis of methicillin-resistance <i>mecA</i> gene with different concentration (1, 10,100,1000 fg/ $\mu$ L) and negative control, ladder, negative control, 1, 10, 100, 1000 fg/ $\mu$ L of <i>mecA</i> gene. .... 71
<b>Figure 3. 3</b>	Images of a) positive (100 pg/ $\mu$ L) and b) negative (0 pg/ $\mu$ L) LAMP reaction using hydrogel beads, incubated at 60 °C for 60 min. c) Variation of fluorescence as a function of time for both the positive and negative LAMP reactions in a) and b). .... 72
<b>Figure 3. 4</b>	a) Time-dependence fluorometric signal. b) Linear range of <i>mecA</i> gene using droplet hydrogel counting ratio..... 74
<b>Figure 3. 5</b>	Fluorescence images of the droplet monolayers in an observation channel for the tested concentrations (0.001, 0.01, 0.1, 1, 10, 100, 1000 pg/ $\mu$ L <i>mecA</i> gene) and the

	non-template control (NTC) for the HD-LAMP (representative image sections cropped). Bright green beads images represent positive droplets. negative control, 0.001, 0.01, 0.1, 1, 10, 100, and 1000 pg/ $\mu$ L, respectively. .... 75
<b>Figure 3. 6</b>	a) Dynamic range of <i>mecA</i> gene using hydrogel counting ratio. b) Selectivity study of <i>E. coli</i> , <i>E. faecalis</i> , <i>S. epidermis</i> , MSSA, MRSA target DNA in HD-LAMP method. c) Accuracy test by comparing DNA amplification results (N=3) PCR tube and HD-LAMP system detecting <i>mecA</i> concentration (1 to 10 <sup>2</sup> pg/ $\mu$ L) ( <i>mecA</i> HDLAMP versus <i>mecA</i> PCR curve). d) Size stability test of hydrogel beads over 120 days..... 76
<b>Figure 4. 1</b>	Fluorometric signal of 1 nM and 50 pM <i>mecA</i> compared to the negative control (i.e. without the <i>mecA</i> gene target). .... 85
<b>Figure 4. 2</b>	MCH-modified, ssDNA-modified, and Cas-treated electrodes were compared using (a) square wave voltammetry (SWV), (b) cyclic voltammetry (CV), (c) electrochemical impedance spectroscopy (EIS), and (d) controlled potential coulometry. Square wave voltammograms of silver metallized electrodes were carried out using a potential step of 0.01 V, an amplitude of 0.06 V, and a frequency of 200 Hz. For cyclic voltammograms and Nyquist plots, 10 mM [Fe(CN) <sub>6</sub> ] <sup>3-/4-</sup> in 0.1 M PBS was used as the working solution and 0.1 M PBS was used as the background electrolyte. The reversible cyclic voltammograms were carried out using a scan rate of 100 mV/s, while Nyquist plots were obtained by applying a 5 mV sine wave potential within a frequency range of 10 <sup>-2</sup> to 10 <sup>5</sup> Hz. For coulometry, silver was deposited using a similar protocol as SWV, then applying 0.5 V potential for 30 seconds to collect silver metallized amount on electrode..... 86
<b>Figure 4. 3</b>	Heat maps of square wave voltammetry optimization for (a) full width half maximum (FWHM), (b) peak current, and (c) peak position, where meshed areas show the desired value ranges. SWV optimization was carried out by varying frequency from 100 to 500 Hz and amplitude from 0.01 to 0.1 V. The CRISPR system was optimized for percentage difference between treated and untreated electrode current as a function of (d) MgSO <sub>4</sub> concentration, (e) trans-cleavage period, and (f) Cas-gRNA complex concentration. .... 88
<b>Figure 4. 4</b>	Electrochemical reduction optimization for E-Si-CRISPR as function of a) applied voltage (-100 to -800 mV), and b) electrodeposition time (0 to 5 minutes). .... 89
<b>Figure 4. 5</b>	a) Thiolated ssDNA length optimization on the electrode surface for E-Si-CRISPR, studied from 10 to 40 nt. b) Thiolated ssDNA concentration optimization on electrode surface for E-Si-CRISPR, studied from 0.01 to 50 $\mu$ M. The ssDNA was modified and the surface passivated by MCH later..... 90
<b>Figure 4. 6</b>	(a) Square wave voltammograms of a series of <i>mecA</i> concentrations (10 <sup>-6</sup> to 10 <sup>2</sup> nM) using the previously optimized conditions: ssDNA concentration = 1 $\mu$ M, ssDNA length = 30 nt, applied potential = -0.5 V, electrochemical deposition time = 3 minutes, Cas-gRNA complex concentration = 50 nM, a trans-cleavage period = 45 min, MgSO <sub>4</sub> concentration = 20 mM, step potential = 0.01 V, amplitude = 0.06 V, and frequency = 200 Hz. (b) Calibration curve of anodic current (N = 3) obtained from (a), versus <i>mecA</i> concentration (linear range 10 fM to 100 pM shown in inset). Comparison of a) calibration curves between buffer- and human serum-based tests, using the concentration series of <i>mecA</i> as in figure b, and d) detection of the <i>mecA</i> gene in both media, at 1, 10, and 100 pM. .... 92

<b>Figure 4. 7</b>	(a) Target strands with mismatches at different positions, including in the PAM region and crRNA complement at different positions (1, 5, and 10). (b) Evaluation of the influence of mismatches at different positions on the E-CRISPR signal. A target concentration of 1 pM was applied for all the targets (wild type (WT) and mismatched targets). ..... 93
<b>Figure 4. 8</b>	Trans-cleavage period optimization of the lysed MRSA for E-Si-CRISPR, studied from 10 to 80 minutes. .... 94
<b>Figure 4. 9</b>	(a) Comparison of <i>mecA</i> concentrations between the E-Si-CRISPR and PCR at 1, 10 and 100 pM. (b) Specificity test for MRSA versus other bacteria for the E-Si-CRISPR technique, revealing excellent specificity. (c, d) Stability of the ssDNA-immobilized electrode for detecting <i>mecA</i> (1, 10, and 100 pM) over 30 days (N = 3). ..... 95
<b>Figure 5. 1</b>	Conversion of actual and coded values of (a) aptamer concentration, (b) enzyme concentration, and (c) incubation time for the central composite design. .... 101
<b>Figure 5. 2</b>	MCH modified (MCH), aptamer modified (Apt), ochratoxin A-aptamer modified (OTA-Apt) and screen-printed gold electrodes (SPGE) were compared using (a) square wave voltammetry, (b) cyclic voltammetry, and (c,d) electrochemical impedance spectroscopy. Square wave voltammograms of silver-metallized electrodes were carried out using a potential step of 0.01 V, an amplitude of 0.06 V, and a frequency of 200 Hz. For cyclic voltammograms and Nyquist plots, 10 mM $[\text{Fe}(\text{CN})_6]^{-3/-4}$ in 0.1 M PBS were used as the working solution and 0.1 M PBS was used as the background electrolyte. The reversible cyclic voltammograms were carried out using a scan rate of 100 mV/s, while Nyquist plots were obtained by applying a 5 mV sine wave potential within a frequency range of $10^{-2}$ to $10^5$ Hz..... 106
<b>Figure 5. 3</b>	Coulometric response of silver-metallized DNA, DNA modified, and bare SPGE electrodes, respectively, using applied potential at 0.2 V with the duration time of 60 s. .... 107
<b>Figure 5. 4</b>	(a) Square wave voltammograms of silver metallization comparing chemical, electrochemical and combined reductions. (b) Deposition time of Ag on the aptamer-modified SPGE. An applied potential of -0.5 V, a potential step of 0.01 V, an amplitude of 0.06 V, and a frequency of 200 Hz, were used. .... 108
<b>Figure 5. 5</b>	Surface contour plots of the percentage difference between peak current and background as a function of (a) concentration of aptamer and enzyme, (b) concentration of aptamer and incubation time, and (c) enzyme concentration and incubation time. The red points indicate the theoretical optimum values, and the blue points indicate the practical optimum values. (d) A plot of the predicted values as obtained from regression ( <b>Equation 5.3</b> ) against experimental values. .... 109
<b>Figure 5. 6</b>	Conversion of actual and coded values of (a) voltage step, (b) amplitude, and (c) frequency for central composite design. .... 111
<b>Figure 5. 7</b>	Surface response and contour plots of the percentage difference between peak current and background as a function of (a) voltage step and amplitude, (b) voltage step and frequency, and (c) amplitude and frequency. (d) A plot of predicted values as obtained from the regression <b>Equation 5.7</b> against experimental values. .... 112
<b>Figure 5. 8</b>	Surface responses of the studied square wave voltammetry amplitude and frequency, obtaining current (a), peak position (b), and peak full-width half maximum (c). The preferred regions for the peak height peak position are indicated with a dotted line

	and an arrow in (a) and (b). The peak FWHM range lies between the two dotted lines in (c).....	113
<b>Figure 5. 9</b>	(a) Square wave voltammograms of a series of OTA concentrations from $10^{-5}$ to $10^2$ using the CCD-optimized conditions: an aptamer concentration of $1.25 \mu\text{M}$ , an enzyme concentration of $375 \text{ U/mL}$ , an incubation time of 75 minutes, a step potential of $0.01 \text{ V}$ , an amplitude of $0.06 \text{ V}$ and a frequency of $200 \text{ Hz}$ . (b) A calibration curve of anodic current ( $N=5$ ) obtained from (a), versus OTA concentration showing a linear range from $10^{-3}$ to $10^2 \text{ ng/mL}$ , as shown in the inset. ....	114
<b>Figure 5. 10</b>	(a) Electrochemical signal from the silver-metallized aptasensor in the presence of potential interferents, with OTB and AFB2 concentrations of $1.0 \text{ ng/mL}$ , an OTA concentration of $0.1 \text{ ng/mL}$ , and their mixture ( $N=3$ ). (b) Stability of the electrochemical aptasensor for detecting OTA ( $0.01, 0.1, \text{ and } 1 \text{ ng/mL}$ ) over 30 days ( $N=3$ ). Comparison of OTA concentrations between the electrochemical aptasensor and UPLC carried out from the (c) standard solutions and (d) spiked beer samples. ....	116
<b>Figure 6. 1</b>	Conversion of actual and coded values of (a) aptamer concentration, (b) enzyme concentration and (c) incubation time for the central composite design. ....	124
<b>Figure 6. 2</b>	Different permutations of the assay components were studied in solution by UV-vis absorption spectroscopy to characterise the starch–iodide complexation process. The plots present absorption spectra of (a) $\text{H}_2\text{O}_2$ , starch and KI combinations, and (b) starch, KI tested with and without glucose (Glc), aptamer-conjugated GOx (AGOx) and unconjugated GOx. All solutions were prepared in $0.1 \text{ M}$ PBS buffer at $\text{pH } 7.4$ .....	130
<b>Figure 6. 3</b>	Central composite design was used to ascertain the concentrations of three assay variables, starch concentration (%), glucose concentration ( $\mu\text{M}$ ) and KI concentration ( $\mu\text{M}$ ), that yielded optimal assay response. (a, b, c) Surface contour plots report how normalised signal intensities (assay response) vary across parameter space; plotted against two variables at a time. (d) The variation of predicted values (obtained from regression of <b>Equation 6.5</b> ) as a function of experimental values reveals close correspondence between the model and experimental data (dashed line indicates $y=x$ ). ....	132
<b>Figure 6. 4</b>	A study of the colorimetric response due starch–iodide complexation in the presence of GOx and glucose under optimised conditions ( $N=3$ ). (a) Variation of intensity as a function of GOx concentration for experiments performed in microwell plate format. The photo (left) shows the assay solutions in the microwells, with GOx concentration increasing down the columns. (b) Variation of intensity as a function of GOx concentration for experiments performed in the PAD device. The photo (left) shows the paper device, with GOx concentration increasing down the columns. Insets show the linear response regions for both microwell- and paper-based assays, and the black dashed lines indicate the position of the linear range in the context of the whole data set. ....	133
<b>Figure 6. 5</b>	Time course study of assay response using the optimized values from the CCD study. Based on this, a time of 30 minutes was chosen for GOx incubation.....	134
<b>Figure 6. 6</b>	Characterisation of the paper-based assay. (a) A calibration curve presenting normalised signal intensity obtained from the corresponding PAD image as a function of OTA concentration, with the inset showing the linear range from $10^0$ to $10^4 \text{ ng/mL}$ ( $N=5$ ). (b) Normalised signal intensity from PADs in the presence of potential	

interferents (OTB, AFB1, and AFB2 at 10 ng/mL) and OTA at 1 ng/mL, and their mixture (N=3)..... 135

Further characterization of the paper-based assay. (a) A comparison of OTA concentrations obtained when using the PAD, UPLC and an electrochemical aptasensor, to analyse standard solutions. (b) Normalized signal intensity obtained from the different sample matrices: PBS, beer, artificial urine and human serum, both blank and spiked with OTA to 1 ng/mL. (c) Comparison of OTA concentrations between the PADs and UPLC in beer samples spiked with OTA to 1, 5 and 10 ng/mL. (d) Variation of efficiency as a function of storage time for PADs detecting OTA (1, 10, and 100 ng/mL) over a period of 30 days (N=3). ..... 137

**Figure 6. 7**



# List of Schemes

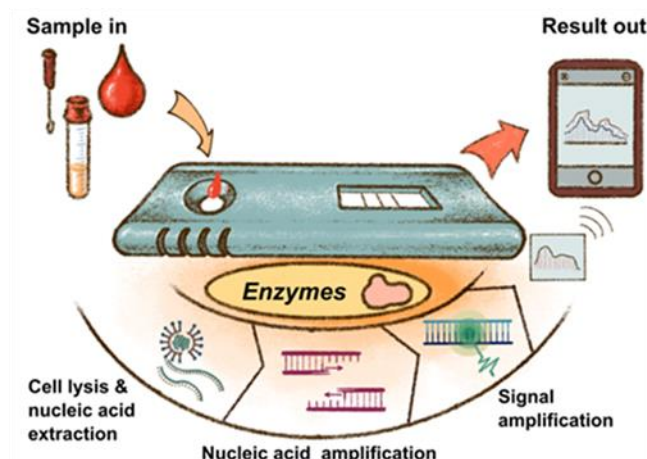
<b>Scheme 2. 1</b>	Schematic illustration of <i>in situ</i> loop-mediated isothermal amplification (LAMP) on paper using AgNPIs in the presence and absence of target DNA. ....	46
<b>Scheme 2. 2</b>	Schematic illustrates colorimetric detection of MRSA using LAMP and AgNPIs. In the presence of the target <i>mecA</i> gene (top), the LAMP reaction yields a large amount of long DNA concatamer product. Upon addition of a solution of AgNPIs, the particles coordinate with the DNA, which then protects them against etching by the subsequently added bromide, and the solution turns red. In contrast, in the absence of the target (bottom), LAMP does not proceed and there is no reaction product to protect the AgNPIs from etching, and the reaction solution turns pale yellow. ....	51
<b>Scheme 2. 3</b>	a) Schematic of a silver nanoplate (AgNPI) structure with facets orientation on the nanoplate structure.....	51
<b>Scheme 3. 1</b>	Schematic illustrates HD-LAMP protocol using droplet hydrogel platform that absorbs LAMP master mix and target gene for MRSA analysis. ....	66
<b>Scheme 4. 1</b>	Schematic of the E-Si-CRISPR technique. ssDNA immobilized on the electrode are removed by the triplex Cas, only in the presence of a target gene. Subsequent addition of the Ag <sup>+</sup> and NaBH <sub>4</sub> seeds the silver metallization, and an applied potential of -0.5 V allows the 'double metallization', providing a minimized SWV signal (target positive result). In the absence of target gene, the ssDNA cannot be removed, yielding a high electrochemical signal (target negative result).....	80
<b>Scheme 4. 2</b>	Schematic of the fluorometric assay for the CRISPR/Cas biosensor.....	84
<b>Scheme 5. 1</b>	Schematic Illustration of the Silver Metallization Assay for OTA Detection Using Enzyme-Assisted Background Current Suppression.....	105
<b>Scheme 6. 1</b>	A schematic illustration of the colorimetric paper-based assay. Surface-immobilised antiOTA antibodies bind OTA from solution, with aptamer-GOx conjugates then binding to OTA and forming a sandwich complex. Subsequent addition of glucose, starch and potassium iodide sees the GOx produce H <sub>2</sub> O <sub>2</sub> , leading to the formation of triiodide that complexes with starch and produces the blue color. In the absence of OTA, the sandwich complex cannot form and the blue coloration does not occur. ....	121
<b>Scheme 6. 2</b>	Schematic illustration of the covalent immobilization process of antibodies on the cellulose paper surface of the paper-based analytical device. ....	122

# List of Tables

<b>Table 2. 1</b>	LAMP and PCR primers sets for <i>mecA</i> amplification. ....	47
<b>Table 2. 2</b>	The concentration of each component of the LAMP reaction. ....	48
<b>Table 4. 1</b>	PCR primers for <i>mecA</i> amplification, and the oligonucleotides for E-Si-CRISPR .....	81
<b>Table 5. 1</b>	Experimental Range and Level of the Respective Independent Variables for Electrode Optimization.....	100
<b>Table 5. 2</b>	The central composite design model of the total 20 experimental runs and the polynomial factor for the equation calculation. ....	102
<b>Table 5. 3</b>	The square wave voltammetric signal obtained from conditions designed in the CCD. ....	102
<b>Table 5. 4</b>	Central Composite Design for Electrode Optimization Using Aptamer Concentration, Enzyme Concentration, Incubation Time, and Normalized Peak Current Response Data .....	104
<b>Table 5. 5</b>	The experimental range and level of the respective independent variables of square wave voltammetry.....	110
<b>Table 5. 6</b>	A comparison of reported electrochemical techniques for OTA determination. ....	115
<b>Table 5. 7</b>	Determination of OTA concentration in spiked beer samples comparing the electrochemical aptasensor with UPLC. ....	117
<b>Table 6. 1</b>	Experimental ranges and levels of the three independent variables used in the central composite design for signal optimisation .....	123
<b>Table 6. 2</b>	Experiments conducted for the central composite design for signal optimisation using KI concentration, starch concentration, glucose concentration. The normalised intensity response data for the experiments and the back-calculated response from the resultant model are shown.....	125
<b>Table 6. 3</b>	Central composite design model for a total of 20 experimental runs and the polynomial factor for equation calculation. ....	126
<b>Table 6. 4</b>	The colorimetric signal obtained from conditions designed in the CCD. ....	127
<b>Table 6. 5</b>	A comparison of reported colorimetric detection techniques for OTA determination .....	136
<b>Table 6. 6</b>	Determination of OTA concentration in spiked beer samples comparing the PADs with UPLC, and comparing OTA concentration in blank and spiked artificial urine and human serum. ....	139

# Chapter 1

## Introduction



Driven by complex and interconnected factors, including population growth, climate change, and geopolitics, infectious diseases and toxin contaminations represent one of the greatest healthcare challenges of the 21<sup>st</sup> century. Diagnostic technologies are the first line of defense in the fight against infectious disease, providing critical information to inform epidemiological models, track diseases, decide treatment choices, and ultimately prevent epidemics. The diagnosis of infectious disease at the genomic level using nucleic acid disease biomarkers has proven to be the most effective approach to date. Likewise, toxin detection is crucial as it can prevent many problematic non-infectious diseases that exhibit high morbidity and mortality in the human population. The development of nucleic acid-based biosensors has demonstrated much promise in the realization of cost-effective diagnostics. Such methods rely heavily on enzymes to specifically amplify or detect nucleic acids in complex samples, and significant effort has been exerted to harness the power of enzymes for *in vitro* nucleic acid diagnostics. Unfortunately, significant challenges limit the potential of enzyme-assisted nucleic acid diagnostics, particularly when translating diagnostic technologies from the lab toward point-of-use or point-of-care environments. Herein, we discuss the current state of the field in the context of work presented in this thesis.

This chapter is adapted from a paper entitled "*Enzyme-Assisted Nucleic Acid Detection for Infectious Disease Diagnostics: Moving toward the Point-of-Care*", authored by Akkapol Suea-Ngam, Leonard Bezing, Bogdan Mateescu, Philip D. Howes, Andrew J. deMello and Daniel A. Richards. Published in *ACS Sensors* **2020**, 5, 2701–2723.

## 1.1 Introduction

The ability to detect disease with a high degree of sensitivity and specificity is an essential part of any healthcare pipeline, and an important tool in biomedical research. In vitro diagnostics (IVDs) inform clinical decisions, and play a primary role in determining therapeutic pathways at both the individual and the population level. This is particularly important for infectious diseases, where IVDs provide key data for epidemiological models and aid in disease tracing, helping to slow or prevent the spread of disease. The global impact of infectious diseases is exemplified by the current SARS-CoV-2 outbreak (COVID-19), which, at the time of writing, has caused over 37 million infections and over a million deaths globally.<sup>1</sup> Unfortunately, the ultimate cost of the COVID-19 pandemic is yet to be felt, as the resultant economic damage is likely to have a lasting impact on multiple sectors including healthcare and agriculture, which will almost certainly exacerbate morbidity and mortality, particularly in resource limited settings. Although the current outbreak is receiving unprecedented global attention, the more general problems associated with infectious disease are underestimated. In 2016, the World Health Organization (WHO) found that infectious diseases were implicated in three of the top ten causes of death globally.<sup>2</sup> This picture worsens still when looking at populations in low income regions such as Africa, where infectious diseases such as human immunodeficiency virus (HIV), malaria, tuberculosis (TB), and lower-respiratory tract infections (LRTs) accounted for over 35% of total deaths in 2016.<sup>3</sup> Fortunately, some progress is being made in this area. For example, it is widely accepted that increased access to diagnostics played a key role in controlling the HIV epidemic in Uganda in the 1990s, helping to drive a 67% reduction in prevalence between 1991 and 2001.<sup>4</sup> This trend has continued across Africa; between 2000 and 2016 deaths from HIV in the region decreased by 61%.<sup>3</sup> While tackling epidemics is a multifaceted problem, it is clear that the correct use of diagnostic data can have a significant impact by enabling early intervention, and reducing the overall burden on healthcare systems and the infrastructure that supports them. Additionally, sensing, tracking and analyzing markers of infectious disease within a research setting can help scientists to develop fundamental disease models, find new druggable targets, and test the efficacy of medicines both in vitro and in vivo. Accordingly, developing new technologies for sensing disease is of paramount importance.

### 1.1.1 Point-of-care infectious disease diagnostics

Whilst multiple technologies have proven effective for in vitro infectious disease diagnostics, currently employed systems are largely dependent on complex equipment, centralized laboratories and highly trained personnel. These requirements introduce several limitations that severely diminish their overall utility. Diagnostics laboratories require substantial infrastructure to operate effectively, and training personnel to use complex equipment is labor intensive. In addition, samples must be effectively stored at the point of collection and transported to the testing location. These factors ultimately serve to increase the cost per test, and also introduce a lag period between sample collection and result, limiting the utility of these tests for disease tracing and containment. Unfortunately, these problems are intensified within resource-limited communities where infectious disease diagnostics are likely to have the greatest impact.

In the context of IVDs, the term point-of-care (PoC) refers to systems that have been developed to address the aforementioned limitations, commonly through miniaturization and simplification. PoC systems are designed as self-contained devices that ideally contain a complete diagnostic platform within a single unit. Such systems should be portable (or at least transportable), provide results quickly, and be easy to operate either by the end user or a field-deployed care worker. Diagnostic assays that meet these requirements are typically termed rapid

diagnostics tests (RDTs). It is important to consider the transition from centralized laboratories towards the point-of-care as a continuum, rather than a discrete series of steps, and understand that there is significant overlap between the different systems and the situations in which they are effectively deployed. Thus, whilst highly portable PoC systems are designed for the end user, many systems can also be highly beneficial in more developed settings (Figure 1.1).

The efficacy of PoC testing for infectious disease is well documented, and the development of RDTs has been highlighted as a priority by organizations such as the WHO. In 2003, the WHO Special Programme for Research and Training in Tropical Diseases (WHO/TDR) published a list of criteria for in vitro infectious disease PoC diagnostics. These criteria were labeled ASSURED; Affordable, Sensitive, Specific, User friendly, Rapid and robust, Equipment-free, and Deliverable to end users. In 2019, Peeling and colleagues evaluated the effectiveness of ASSURED and proposed two new criteria, namely Real-time connectivity and Ease of specimen collection, to create the new REASSURED standards for infectious disease diagnostics.<sup>5</sup> The addition of connectivity and specimen collection bridges apparent gaps in the original criteria, and also reflects the advent of mobile health (mHealth) and improved communications infrastructure.

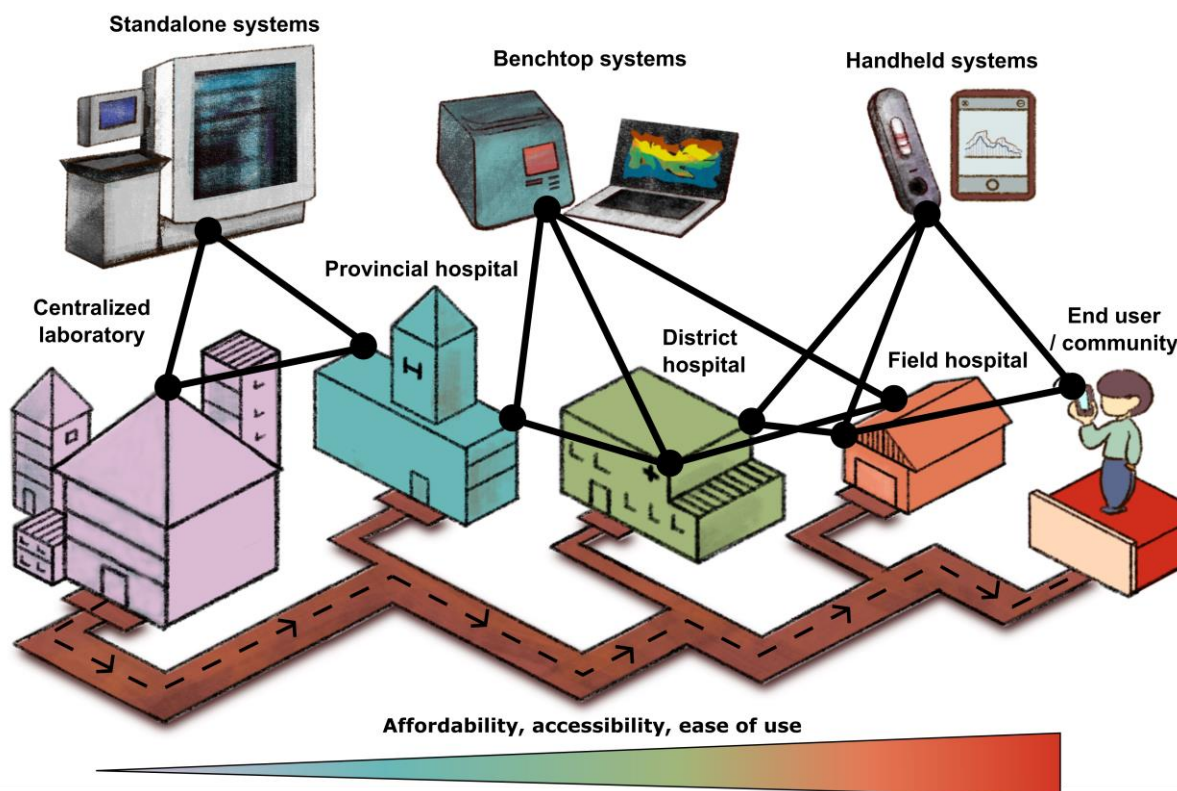


**Figure 1.1** The path towards the point-of-care, illustrating standalone, benchtop, and handheld systems that are providing from centralized laboratory to end user/community depending on the affordability, accessibility, and ease of use.

### 1.1.2 Nucleic acid biomarkers in infectious disease

IVDs can be broadly categorized by the type of biomarker that they detect e.g. antigen, antibody, metabolite, or nucleic acid. Though each of these markers has unique advantages, and it is important to consider this when designing a diagnostic assay, nucleic acids are particularly promising in the context of infectious diseases. Viral and bacterial pathogens contain genomes which encode them. Parts of this genetic information, which are highly specific to the disease, can be exploited as a direct marker of the disease. This genotypic specificity is not always replicated

at the phenotypic level, a factor which can lead to crossreactivity and false diagnoses when sensing phenotypic biomarkers such as proteins. A good example of this is the spike protein of SARS-CoV, which is maintained across both SARS-CoV-1 and SARS-CoV-2.<sup>6</sup> Tests based on this antigen are not readily able to differentiate between the two strains, though genotypic differences can be easily distinguished.<sup>7</sup> The ability to differentiate between closely related diseases at a genetic level is particularly important for bacterial or viral pathogens, which are able to rapidly mutate and form new strains. A further advantage of the extraneous nature of infectious disease nucleic acid biomarkers is that they can be detected in the body immediately after infection. This, in theory, enables earlier diagnosis and can be invaluable in slowing or preventing the spread of the disease. Perhaps the biggest advantage of nucleic acid testing in the context of infectious disease diagnostics is the speed at which the tests can be developed after the emergence of a new disease. Such agility is a result of the relative simplicity of both nucleic acid biomarker identification and disease-specific targeting-ligand generation. Thanks to advances in automated gene sequencing, it is now possible to sequence entire viral or bacterial genomes quickly, often within a matter of days.<sup>8-9</sup> Similarly, generating target-specific ligands (in the form of primers), is simpler for nucleic acid targets due to the well understood process of complementary base pairing. Computational techniques, coupled with high-throughput screening, can generate optimized nucleic acid-specific ligands within hours, whereas antibody ligands for protein-based biomarkers may take months to develop.<sup>10</sup> These factors culminate in a rapid turnaround time between disease identification and the deployment of a working assay; reports of assays being developed in under one week exist in the literature.<sup>11</sup> Unfortunately, life is never simple and nucleic acid biomarkers present several diagnostic challenges. They are frequently present in vanishingly small quantities amongst a large background of indigenous nucleic acids, can be sensitive to extraction techniques and storage methods and are readily degraded by common contaminants. Researchers from across the scientific spectrum have dedicated significant time to developing, adapting, and exploiting technologies to overcome these barriers and develop effective diagnostics for nucleic acid targets.

### **1.1.3 The role of enzymes in nucleic acid biosensing**

The vast majority of nucleic acid biosensors employ enzymes to amplify, bind, degrade or otherwise manipulate nucleic acids. This is unsurprising, given that enzymes have been evolved by nature to perform a wide array of complex operations on nucleic acids during the process of transcription and translation. Discovering novel enzymes and elucidating their interactions with nucleic acids has played an important role in the development of nucleic acid biosensors, and has formed the basis for a new generation of diagnostic platforms. While the most common role of enzymes remains the specific amplification of target nucleic acids, they also play important roles throughout the entire diagnostic work-flow, from sample preparation and extraction, through to signal generation and analysis. Though it is clear at this time that enzymes are essential for effective nucleic acid sensing, our reliance on them presents several practical problems. Enzymes generally require quite specific physical and chemical conditions (e.g. temperature, pH) in order to operate effectively, and can rapidly degrade if not handled correctly. This creates both technological and logistical challenges that must be overcome to ensure practical impact.

### **1.1.4 Application of nucleic acids in toxin analysis**

Although the majority of nucleic acid biosensors are made for targeting complementary nucleic acid biomarkers, in particular for infectious diseases, nucleic acid possesses the ability to bind to a variety of other molecules with high specificity. A process called 'systematic evolution of ligands by exponential enrichment (SELEX)' is employed to find nucleic acid sequences (termed aptamers) that exhibit strong and specific binding to target molecules, for example toxins, from a nucleic acid library. Deploying aptamers in sensors (termed 'aptasensors') can yield function and

performance comparable to antibodies, and has drawn significant attention in the biosensing field, resulting in popularity in a broad range applications.<sup>12</sup> The step from using expensive and organism-based synthesis of antibodies to the inexpensive and automated synthesis of nucleic acids has positively impacted biosensor development, and has given a new direction for toxin analysis. Of particular note for biosensor development is that aptasensors can be combined with many existing analytical techniques. However, though it is clear that using aptasensors alone can provide sensitive and specific detection, their use does present several practical problems, in particular high background signals and false-positive results. Aptasensors generally require quite specific physical and chemical conditions (e.g. temperature, pH, and ionic strength) in order to operate effectively, and typically do not bind to the analyte if not handled correctly. There is definite scope for improvement in this field, and one very promising avenue is to combine aptamers with nucleic acid-related enzymes, for example to reduce background signal, enhance the sensitivity of detection or remove false-positive results.

## 1.2 Enzyme-assisted nucleic acid amplification

Arguably, the most important role of enzymes in nucleic acid biosensors, and particularly disease diagnostics, is the amplification of nucleic acids. Amplification of a target biomarker from the background greatly simplifies the process of detection and enables the use of multiple downstream signal and detection technologies. Fortunately, many enzymes have been discovered or developed to achieve efficient nucleic acid amplification.

### 1.2.1 Polymerase chain reaction

Polymerase chain reaction (PCR), first reported in 1985,<sup>13-14</sup> is still the most popular method for amplifying DNA. PCR employs thermostable polymerase enzymes, most commonly Taq polymerase from the thermophilic bacterium *Thermus aquaticus*. Since its inception, PCR has become one of the most important tools in molecular biology and the primary driver for IVDs that target nucleic acids. PCR mixtures comprise several reagents, including forward and backward DNA primers specific to a target sequence, a polymerase, and a dNTP-rich buffer. Optimal amplification requires cycling through three temperatures, each with a specific function: 95°C for double-stranded DNA (dsDNA) dissociation, 55–72°C for primer annealing, and 70–80°C for polymerization. PCR can also be used to detect RNA by first employing the enzyme reverse transcriptase to transcribe RNA into DNA prior to amplification. Early PCR technologies were hindered by the relatively high error rates in DNA replication caused by Taq polymerase. These issues were remedied by the characterization of alternative thermostable enzymes, such as Pfu polymerase, that possess exonuclease proofreading abilities. These features allow the enzymes to correct errors in nucleotide incorporation during PCR, though the polymerization rate is generally lower than Taq.

#### 1.2.1.1 Quantitative polymerase chain reaction

Over the last 30 years there have been multiple advances in PCR technology, particularly through the development of detection reagents and novel systems which allow for real time monitoring of amplicon generation. These approaches have engendered the widespread implementation of quantitative PCR (qPCR) for DNA, and quantitative reverse transcriptase PCR (qRT-PCR) for RNA. As the names suggest, qPCR and qRT-PCR are capable of delivering a quantitative readout of the degree of amplification in real-time, which in turn can be used to determine the concentration of the target biomarker from a calibration curve. First developed in the 1990s,<sup>15</sup> qPCR has rapidly grown to become the gold standard for laboratory-based nucleic acid diagnostics. Semiautomated commercial qPCR systems, such as the GeneXpert® from Cepheid or Cobas® from Roche are the mainstay of diagnostics laboratories throughout the developed world, and are capable of processing up to 4000 tests per day.<sup>16</sup>

### ***1.2.1.2 Signal generation in PCR***

Obtaining a signal in PCR is achieved by detecting the amplicon during amplification (qPCR) or post-amplification by addition of a detection probe, most commonly a dye that exhibits an enhanced fluorescence yield upon intercalation into DNA. These methods can be cost effective and easy to implement into a biosensing system, and thus offer significant utility in the context of diagnostics. Multiple intercalating dyes have been developed for visualization of DNA, including cyanine-based dyes such as DNAzure®, Novel Juice®, SYBR® and TOTO®. These dyes emit at distinct wavelengths, from the blue through to the red, providing a degree of flexibility in regards to signal generation. However, one key drawback of these compounds is that they bind indiscriminately to dsDNA, and thus emit even in the presence of background DNA or off-target amplicons. Sequence-specific probes based on FRET-molecular beacons provide an elegant solution to these issues. Here, a fluorophore is attached to the 5' end of an oligonucleotide probe specific to the target sequence, and a FRET quencher is attached to the 3' end to quench the fluorescence of the fluorophore when nearby. After the denaturation and annealing of the probe to its target, the exonuclease activity of the polymerase can degrade the beacon, cleaving the quencher and releasing the fluorophore. The complementarity between the nucleotide linker on the probe and the target sequence provides a high degree of specificity (down to the single nucleotide level) and decreases background signal. The most famous and commonly employed of such probes are the TaqMan series of probes, first reported in 1991,<sup>17</sup> which work with Taq polymerase. Multiple different fluorophores and quencher pairs are commercially available, providing flexibility and facilitating target multiplexing.

## **1.2.2 Isothermal PCR**

Although qPCR is recognized as the gold standard for nucleic acid amplification, multiple fundamental limitations hinder the application of the technology for RDTs. The largest barrier is the reliance on thermal cycling for amplification. Thermal cycling is a slow, energy intensive process that requires relatively complex heating elements to provide the necessary temperature control. In addition, the majority of PCR systems are relatively large and require a steady power supply; this limits the portability of the technology and excludes many PoC applications. Significant effort has been put into the development of isothermal techniques to overcome this issue (Table 1). Isothermal amplification techniques can operate optimally at a single temperature, greatly simplifying the heating requirements of the system.

### ***1.2.2.1 Loop-mediated isothermal amplification***

Loop-mediated isothermal amplification (LAMP), first reported in 2000,<sup>18</sup> is one of the most popular isothermal techniques for nucleic acid amplification. LAMP requires four primers; inner primers, termed the forward inner primer and backward inner primer (FIP and BIP), and forward and backward outer primers (F3 and B3). These primers bind to six unique sequences on the target sense and anti-sense strands. Additional loop forward and loop backwards (LF and LB) primers can be introduced to accelerate the reaction. Amplification in LAMP relies on Bst polymerase, which exhibits strand displacement activity, i.e. the ability to unwind double stranded DNA (**Figure 1.2**). This eliminates the need for high temperature DNA denaturation, but since Bst polymerase optimally operates between 55 and 65°C, heating is still required for optimal results. Since LAMP yields dsDNA products, signal can be generated using methods commonly employed for PCR and qPCR. Interestingly, the high amplification capacity of LAMP facilitates unique methods for generating signal. For example, during elongation of dsDNA, a significant amount of pyrophosphate is generated, which sequesters magnesium from the buffer to create magnesium pyrophosphate. This process can be exploited through the use of metal indicators that fluoresce or change color upon chelation of Mg<sup>2+</sup>. For example, Goto et al. used hydroxy naphthol blue to detect bacterial DNA from *Pseudomonas aeruginosa*, a common cause of



secondary infections in hospitalized patients, in fecal samples, achieving a limit of detection down to 130 CFU per 0.1g of sample.<sup>19-20</sup> Similar colorimetric methods have been successfully employed for the detection of Shigella, Salmonella, and Vibrio cholerae, though these tests were performed on spiked samples rather than clinical specimens.<sup>21</sup> The colorimetric nature of this approach is clearly advantageous for PoC settings as it precludes the need for additional equipment, and facilitates naked eye qualitative analysis.

The most compelling feature of LAMP is its high amplification capacity. Indeed, a  $10^9$ -fold amplification can be achieved within an hour. Additionally, the use of multiple primers enhances specificity, a feature that is particularly valuable in the context of infectious disease IVDs. Due to these advantages, LAMP has become a common component of many PoC infectious disease IVDs, particularly for paper-based systems.<sup>22-23</sup>

### ***1.2.2.2 Recombinase polymerase amplification***

Recombinase polymerase amplification (RPA) relies on the coordinated actions of multiple enzymes to achieve isothermal amplification. First reported in 2006,<sup>24</sup> RCA has since been developed and patented as a proprietary technology of TwistDX. RPA requires only two primers, in addition to three enzymes: A recombinase enzyme, an ssDNA binding protein (SSB) named gp32, and Bsu DNA polymerase. The recombinase and SSB act in a complementary fashion to initiate strand dissociation and insert the primers, negating the need for high temperature dissociation (**Figure 1.2**). Bsu polymerase has been shown to work optimally between 37–42°C. RPA is compatible with all signal generation techniques applicable to dsDNA, such as fluorescence staining or FRET-beacons.<sup>25</sup>

Amplification using RPA is exponential in nature, and has demonstrated a  $10^9$ – $10^{11}$ -fold amplification of target DNA, making it an excellent option for the detection of low abundance nucleic acids. Unfortunately, the rapid amplification can be a significant source of error and background if the primers bind off-target, an issue made worse by the relatively long primer lengths required in RPA (32–35 nt).<sup>25</sup> This is problematic when sensitivity and specificity is paramount e.g. in infectious disease PoC diagnostics. Additionally, the proprietary nature of RPA poses a problem for PoC diagnostics. Here a reliance on a single supplier can complicate supply chains and increase costs, particularly when compared to conventional ‘open source’ alternatives. Nevertheless, RPA is a popular choice for PoC infectious disease diagnostics, and has been successfully employed for multiple diseases including Influenza,<sup>26</sup> Dengue,<sup>27</sup> and Ebola.<sup>28</sup>

### ***1.2.2.3 Rolling circle amplification***

Rolling-circle amplification (RCA) takes inspiration from the natural rolling circle transcription of circular plasmids and viral genomes to generate an amplicon around a circular DNA template. The first examples of RCA appeared in the 1990s,<sup>29-30</sup> and many iterations have since been reported.<sup>31</sup> In RCA, an ssDNA ‘padlock-probe’ sequence containing a target binding sequence is ligated end-to-end using DNA ligase to generate circular template. Binding of the target DNA to the complementary sequence on the circular template is followed by binding of  $\Phi 29$ , a polymerase isolated from bacteriophage  $\Phi 29$ , which then proceeds to ‘roll’ around the circular template to create a linear ssDNA amplicon (**Figure 1.2**). The  $\Phi 29$  polymerase is capable of debranching double stranded DNA, precluding the need for thermal DNA denaturation. Furthermore,  $\Phi 29$  can operate efficiently at temperatures between 35 and 40°C, and has an innate exonuclease proofreading capacity that minimizes copy errors. As with conventional PCR, fluorescent probes can be used for quantification and assessing disease load. Another approach specific to RCA has been the incorporation of G-quadruplex sequences, i.e. guanidine rich sequences, into the RCA template to facilitate the generation of DNAzymes during RCA.<sup>32</sup> These structures are capable of sequestering metal complexes such as the Hemin porphyrin, which can

subsequently catalyze the oxidation of chromogenic substrates to produce a colorimetric signal. This strategy provides for a more rapid signal by exploiting the catalytic nature of both the RCA reaction and the oxidation of 3,3',5,5'-Tetramethylbenzidine (TMB) by the G-quadruplex-Hemin complex.

Due to the linear nature of the amplification, RCA is relatively slow (approximately a  $10^3$ -fold amplification per hour); this can limit sensitivity in diagnostic tests, particularly when minimizing the total assay time is paramount. This drawback has somewhat decreased the popularity of RCA in PoC applications, although many successful examples exist.<sup>33</sup> Moreover, adaptations to RCA designed to improve the amplification rate have been moderately successful. One notable approach has been to utilize multiple target binding sequences on the linear padlock probe, and thus provide multiple points for primer attachment on a single circular template. This method, termed hyper-branching RCA (HRCA), enables concurrent amplification of multiple ssDNA targets from a single template and thus increases the overall rate of amplification.<sup>34</sup>

#### ***1.2.2.4 Strand displacement amplification***

Strand displacement amplification (SDA) was first reported in the early 1990s,<sup>35-36</sup> and as such is one of the earliest described isothermal amplification techniques. SDA exploits specific restriction endonucleases to initiate strand dissociation, and so negates the need for thermal dissociation. The technique requires two target-specific primers, a suitable polymerase enzyme and the presence of a nicking exonuclease capable of cleaving the newly synthesized strand between the primer and target sequence. This nicking process allows partial dissociation and unwinding of the newly synthesized strand and the template strand, allowing a new polymerase to bind. As the polymerase moves along the template the new amplicon displaces the old amplicon, eliminating the need for heat induced dissociation (**Figure 1.2**). Early reports of SDA required an initial denaturation step at 95°C, so could not be considered truly isothermal, though modern developments have incorporated additional “bumper” primers to accomplish initial denaturation and achieve true isothermal amplification.<sup>37</sup> SDA has proven to be a flexible technique, and works well with multiple polymerases including Bst,  $\Phi$ 29, and Exo- Klenow; this flexibility allows SDA to operate at temperatures ranging between 21 and 65°C. Depending on the polymerase used, target amplification between  $10^7$  and  $10^9$ -fold in 20–120 –minutes can be achieved using SDA. However, the dependence of SDA on restriction enzymes, which can only cut at specific restriction sites, is a limitation. Indeed, successful SDA requires that the primers are designed to bind upstream of an endogenous nicking site, thus allowing the restriction enzyme to cleave the primer and facilitate strand dissociation. The optimal temperature of operation for the nicking enzyme must also be considered. However, multiple nicking endonucleases for distinct restriction sites have been successfully employed in SDA, including Nb.BbvCI, Nt.BstNBI, HincII-EcoRI(GI11), BsoBI, Nt.AlwI, Nt.BsmAI and HincII. Unsurprisingly, several examples of SDA being employed in with PoC diagnostics for infectious disease have been reported.<sup>37-38</sup>

#### ***1.2.2.5 Helicase-dependent amplification***

Helicase-dependent amplification (HDA), first reported in 2004 by scientists at BioHelix,<sup>39</sup> takes inspiration from in vivo cellular DNA replication, and achieves isothermal amplification by employing a helicase enzyme to perform dsDNA denaturation (**Figure 1.2**). Initial embodiments employed UvrD helicase isolated from *E. Coli.*, though the process was rapidly adapted to work with Tte-UvrD, a thermostable helicase capable of operating at significantly higher temperatures.<sup>40</sup> HDA is flexible with regards to polymerase, and has notably been implemented using, Bst, Gsp, and Gst polymerases, amongst others.<sup>41-42</sup> As with SDA, this theoretically enables efficient operation across a broad range of temperatures. However, helicase-mediated strand separation is most efficient at 60°C; thus, for isothermal amplification a polymerase that operates in the range of 60–65°C is usually chosen.

Despite being an exponential technique, the amplification efficiency of HDA is relatively low, achieving a  $10^6$ -fold amplification after one hour. This is likely due to the unwinding of DNA by helicase, which is the rate determining step, and significantly constrains the sensitivity of systems based on HDA.<sup>43</sup> Additionally, early iterations of HDA suffered from low specificity due to the reliance on long primers, which can lead to false positives in diagnostic applications.<sup>43</sup> Despite these limitations, HDA has been successfully incorporated into PoC IVDs for HIV,<sup>44</sup> *Staphylococcus aureus*,<sup>45</sup> and Herpes simplex virus,<sup>46</sup> amongst others.<sup>43</sup>

#### ***1.2.2.6 Nucleic acid sequence-based amplification***

Nucleic acid sequence-based amplification (NASBA) is a partially isothermal technique that mimics retroviral RNA replication, generating ssRNA as the product. NASBA was first introduced in 1991,<sup>47</sup> and has remained popular due to the fact it works innately with RNA, rather than DNA, making it ideal for detecting single stranded viral RNA or endogenous RNA (e.g. mRNA or miRNA). NASBA requires two primers (forward P1 and reverse P2), as well as three enzymes: T7 DNA dependent RNA polymerase, RNase H, and reverse transcriptase. The process works optimally at 41°C, though an initial primer annealing that requires higher temperatures (55–65°C) step is necessary. The coordinated action of reverse transcriptase and RNase H produces single stranded DNA, precluding the need for high temperature strand dissociation. Target specificity is imparted by the P1 forward primer, which contains a region that is complementary to the target RNA and another distinct region that is complementary to a T7 promoter region (**Figure 1.2**).

NASBA is an efficient amplification process, and is able to amplify RNA  $10^9$ -fold 90 minutes. Though NASBA is regarded as a robust isothermal method, it is not without disadvantages. As RNA stability can be greatly impacted by pH, temperature and the presence of RNase, additional precautions must be taken during sample preparation and reaction assembly. Moreover, the enzymes required for NASBA are also thermolabile and can suffer significant performance degradation if the temperature goes above 42°C.<sup>48</sup> Despite this, examples of NASBA being effectively utilized within PoC systems for infectious diseases do exist. Gulliksen et al. employed NASBA in a proof-of-concept PoC device for detecting human papillomavirus (HPV),<sup>49</sup> and the technique is also integral to the emerging synthetic gene network / CRISPR diagnostics reported by Collins and co-workers for the detection of Zika virus.<sup>50</sup>

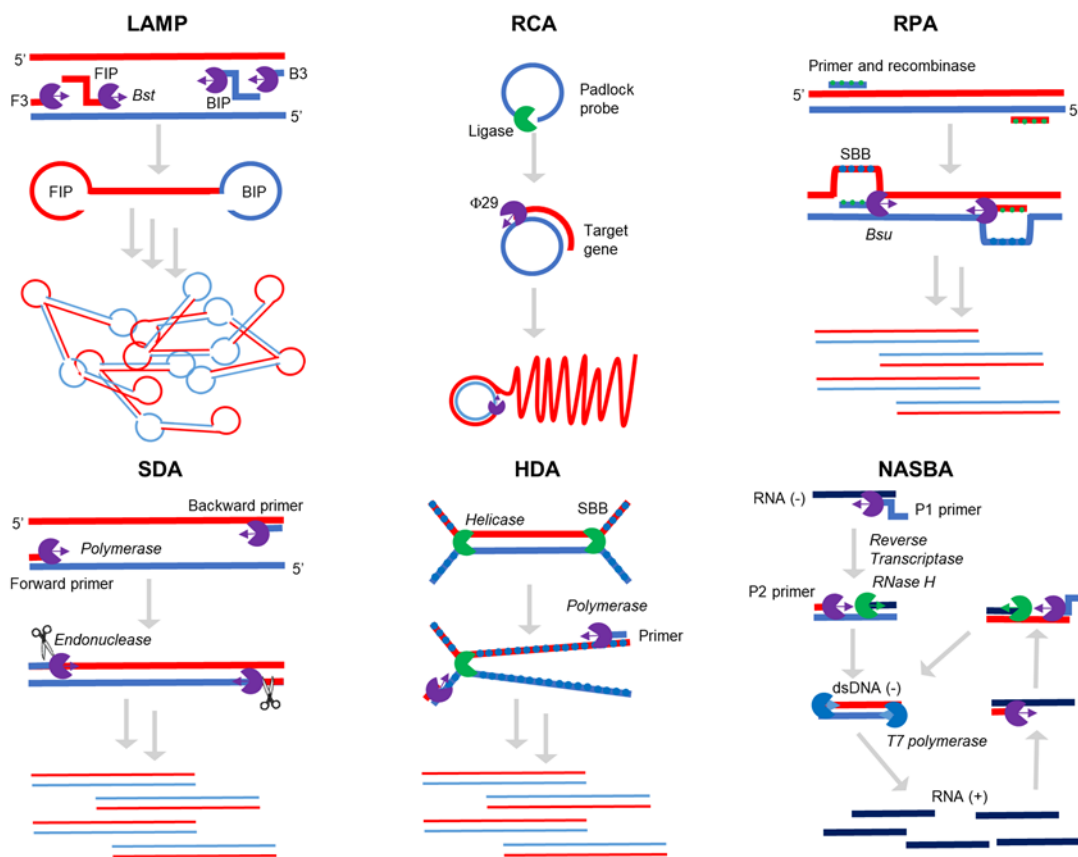


**Figure 1.2** Schematic representations of different isothermal amplification techniques. LAMP: Binding of the inner primers (FIP, BIP) is followed by strand displacement and polymerization by Bst polymerase. Subsequent binding of an outer primer (F3, B3), and polymerization, displaces the newly synthesized strand which forms a self-hybridizing loop structure. This process repeats on the opposite end of the target sequence with the reverse primer, forming short 'dumbbell' loop structures that can be amplified into dsDNA concatemers. RCA: Target DNA binds to a padlock probe template, circularized by DNA ligase, followed by  $\Phi 29$  polymerase which rolls around the circular template to produce an ssDNA amplicon. RPA. A recombinase enzyme inserts forward and reverse primers into a dsDNA target template, resulting in strand displacement. Single-strand binding proteins (SSBs) bind to prevent strand recombination, and Bsu polymerase amplifies the template. SDA. After an initial round of amplification, an endonuclease nicks the newly synthesized strands between the primer and the target, allowing a new polymerase enzyme to bind and amplify the target whilst simultaneously displacing the old strand. HDA. Initial DNA denaturation is performed by helicase, which is followed by an SSB to prevent recombination. Subsequent binding of the primers is followed by polymerization. NASBA. A P1 forward primer, containing complementary regions for both the target and a T7 promoter region, binds to a target RNA(-) strand. In the initial stage, reverse transcriptase extends the primer to produce a DNA:RNA duplex, and the RNA strand is subsequently degraded by RNase H to produce an ssDNA template. Binding of the P2 reverse primer and extension by reverse transcriptase produces a dsDNA, which can then enter the amplification stage. T7 polymerase binds the dsDNA to create an RNA strand that is anti-sense to the original target, the P2 reverse primer can bind, and the whole process begins again, resulting in RNA amplicons.

## 1.3 Enzyme-assisted signal generation

Enzymes have evolved an incredible variety of mechanisms, and the range of chemical and biochemical process that they can catalyze is exceptionally broad. These processes can be readily exploited to generate signals in the presence of disease biomarkers. In this section we will highlight some of the more commonly employed approaches.

### 1.3.1 CRISPR/Cas enzymes

Enzymes that catalyze the degradation of nucleic acids (nucleases) are common, and have been employed in nucleic acid amplification for the last several decades (see **section 1.1**). More recently, various nucleases have found use as tools for gene editing, though many groups are now beginning to harness their potential for diagnostic applications. Of the various gene editing tools available, the CRISPR-Cas systems have established themselves as the most useful in terms of diagnostics. Clustered regularly interspaced short palindromic repeats (CRISPR) is a system that provides adaptive immunity against invasive genetic elements in bacteria and archaea. CRISPR notably allows for the processing and storage of exogenous invasive genetic sequences in the form of short DNA sequences (protospacers). Once integrated, these disease-specific sequences are transcribed and processed into small non-coding RNAs, which can subsequently bind to Cas nucleases and guide them to selectively degrade the corresponding target disease nucleic acids. CRISPR systems are currently categorized into two classes, class 1 and class 2, with further subcategorization into types and subtypes.<sup>51</sup> Determination of the CRISPR class is guided primarily by the makeup of the Cas effector protein complexes; Class 1 Cas systems typically comprise multiple proteins that complex to form an active nuclease, whereas Class 2 systems are characterized by a single large Cas nuclease. The types and subtypes are typically categorized by the presence of a signature Cas protein, or complement of multiple Cas proteins. The capacity to reprogram these nucleases in vitro to target specific nucleic acid sequences, e.g. disease-specific targets, has established Cas enzymes as promising candidates for diagnostics applications. Below we will highlight the properties of four distinct Cas proteins (Cas9, Cas12, Cas13, and Cas14), and highlight their promise in the context of infectious disease diagnostics.

#### 1.3.1.1 Cas9

Cas9 (class 2, type II) is an RNA-guided endonuclease that primarily cleaves dsDNA,<sup>52</sup> but specific orthologs of the protein have also been shown to promote the cleavage of ssDNA or ssRNA under certain conditions.<sup>53-54</sup> The specific targeting and function of Cas9 is guided by two RNAs, CRISPR RNA (crRNA), and trans-activating CRISPR RNA (tracrRNA). The crRNA is formed by cleavage of a crRNA precursor (pre-crRNA) directly transcribed from the CRISPR loci, and can base pair with complementary protospacer sequences of invading viral or plasmid target. Importantly, the crDNA contains a spacer sequence which can be modified to target a specific nucleic acid target. The tracrRNA participates in the maturation of pre-crRNA, and associates with crRNA to form an essential base paired structure within Cas9. Importantly, Jinek et al demonstrated the possibility to fuse crRNA and tracrRNA to form a single guide RNA (gRNA) without compromising the capacity of the protein to cleave dsDNA.<sup>52</sup> After binding between the crRNA (or gRNA) and the target sequence, the Cas9 enzyme is activated and the target DNA can be cleaved (**Figure 1.3**). It should be noted that the presence of a specific sequence on the target DNA, termed the protospacer adjacent motif (PAM), is required for Cas activation. In the case of Cas9 the PAM is a 5'-NGG-3' sequence which is present downstream of the target sequence.

Though not as widely employed for diagnostics as Cas12 and Cas13 (see below), there are examples of Cas9 being used within infectious disease RDTs.<sup>55</sup> For example, Pardee et al. successfully combined Cas9 with toehold switches to enable differentiation of the American and African strains of Zika virus.<sup>50</sup> The team designed a gRNA specific to a nucleic acid sequence

upstream of a PAM region on American ZIKV, enabling Cas9 to cleave the dsDNA produced during NASBA. The cleaved dsDNA was unable to undergo transcription and translation, and thus expression of the reporter protein ( $\beta$ -gal) was repressed. The African ZIKV did not contain the necessary gRNA / PAM combination and thus expression was able to continue unimpeded, producing a colorimetric signal to indicate disease load and differentiate the two strains. Huang et al. also employed Cas9 to develop a primer-free DNA biosensor capable of detecting DNA down to low aM concentrations.<sup>56</sup> In this elegant strategy, the DNA released after Cas-mediated cleavage serves to initiate an isothermal Exponential Amplification Reaction (EXPAR), producing a fluorescent readout. By employing reverse transcriptase alongside this technique, the group were able to detect RNA from *L. monocytogenes*, the bacteria responsible for listeriosis, in spiked samples. Taking a slightly different approach, Müller et al. designed Cas9-gRNA complexes able to selectively target and cleave genes associated with antibiotic resistance in plasmids isolated from *E. coli* and *K. pneumoniae*.<sup>57</sup> By coupling the Cas9 enzymes ability to cleave plasmids in particular locations with optical DNA mapping, the group were able to quantify the prevalence of different resistance genes in patient samples. In a similar approach, Crawford and co-workers combined Cas9 with next-generation sequencing to detect antibiotic resistance genes in their Finding Low Abundance Sequences by Hybridization (FLASH) system.<sup>58</sup> Though these systems are not yet being employed at the point-of-care, it is possible that the technology could be moved in that direction in the future.

### 1.3.1.2 Cas12/14

The success of Cas9 for both genome editing and biosensing led to researchers devoting significant effort towards finding and exploiting alternative CRISPR/Cas systems. This line of research proved fruitful, and multiple new Cas enzymes were successfully characterized. Cas12a (class 2, type V) is capable of targeting and cleaving dsDNA and ssDNA, and, like Cas9, contains a PAM region (5'-TTTV-3') which directs the cleavage of the nucleotide after complexation with the gRNA. However, Cas12 enzymes have an additional catalytic activity which facilitates a novel modality for generating signal. After initial cleavage of the dsDNA, termed cis-cleavage, Cas12a goes on to randomly cleave nearby ssDNA via a process known as trans-cleavage, or 'collateral' cleavage. This trans-cleavage occurs indiscriminately and requires minimal sequence specificity. Thus, quenched ssDNA probes can be combined with the molecular specificity of the Cas12a-gRNA complex to develop all-in-one systems that generate fluorescence in the presence of target DNA. Chen et al. demonstrated this in their DNA Endonuclease-Targeted CRISPR Trans Reporter (DETECTR) assay. In this assay, the target DNA, amplified using RPA, and Cas12a-gRNA complex are first mixed together, followed by addition of ssDNA probes carrying a fluorescent dye and a quencher. After cis-cleavage of the target DNA, the collateral trans-cleavage was able to release the fluorophore from the quencher to provide a concentration-dependent signal.<sup>59</sup> The team used this technique to positively identify DNA associated with human papillomavirus in clinical samples, and obtained results that were in agreement with PCR. More recently, Broughton et al. combined the DETECTR platform with RT-LAMP to detect RNA associated with SARS-CoV-2.<sup>11</sup> The team combined this with reporter probes that could be captured on a lateral flow test line to develop a paper-based PoC test with a limit-of-detection of 10 copies per  $\mu$ L in 40 minutes. Similar assays based around the trans-cleavage mechanism of Cas12 have been reported. One example is the HOuR Low-cost Multipurpose highly Efficient System (HOLMES),<sup>60</sup> which utilizes PCR for the initial amplification, and its second-generation analogue HOLMESv2 which employs a Cas12 orthologue (Cas12b) and LAMP.<sup>61</sup> These techniques have been shown to detect target DNA down to 10 aM in biofluid samples.

The collateral cleavage activity of Cas12a is shared amongst other reported type V CRISPR/Cas nucleases.<sup>62</sup> Of particular note are the Cas14 (class 2, type V) enzymes, which are typically much smaller than Cas12 enzymes (~400–700 amino acids vs ~1000 amino acids) and demonstrate

exquisite selectivity for ssDNA targets. Doudna and co-workers showed that Cas14a1 was able to identify ssDNA with single-nucleotide specificity independent of a PAM sequence, and also displays efficient collateral cleavage.<sup>63</sup> The team were able to incorporate this enzyme into a redesigned DETECTR assay to detect specific single-nucleotide polymorphisms conferring blue and brown eye phenotypes.

### ***1.3.1.3 Cas13***

While Cas9 and Cas12/14 enzymes evolved to recognize DNA, Cas 13 (class 2, type VI) enzymes recognize RNA with a high degree of specificity. Similar to their type V counterparts, Cas13 enzymes possess collateral cleavage activity, though Cas13 requires a protospacer flanking site (PFS) rather than PAM to initiate cleavage. The combination of these two traits makes them attractive for use in diagnostics. In 2017 the Collins and Zhang groups reported the Cas13a-driven Specific High Sensitivity Enzymatic Reporter Un-LOCKing (SHERLOCK) platform.<sup>64-65</sup> The SHERLOCK system employs either RPA or RT-RPA to produce a DNA template, which is subsequently amplified into RNA amplicons that feed into Cas13a. This triggers collateral cleavage of RNA quencher-fluorophore pairs to produce a concentration dependent fluorescent signal. The system was able to detect specific strains of Zika and Dengue virus at aM concentrations, and also differentiate single-nucleotide polymorphisms.

Interestingly, reported Cas13 orthologues have displayed different di-nucleotide specificity (e.g. AA for PsmCas13b, UA for CcaCas13) with regards to their collateral cleavage activity. This has enabled multiplexed assays in which different RNA targets can be coupled with different Cas13 orthologues (or even Cas12/14) and orthogonal fluorescent molecular probes.<sup>66</sup> Akerman et al. leveraged this strategy in their Combinatorial Arrayed Reactions for Multiplexed Evaluation of Nucleic acids (CARMEN) assay.<sup>67</sup> This assay relies on nanoliter droplets containing the CRISPR reagents, and was notably able to detect up to 4500 targets on a single microarray chip. Though the relatively complexity of this approach reduces its appeal for PoC applications, the low volumes significantly minimize reagent usage, and thus substantially reduce the overall cost-per-test.

As previously demonstrated for genome engineering, the flexibility offered by CRISPR/Cas nucleases, i.e. their ability to be rapidly reprogrammed to target novel sequences using simple synthetic gRNA, has enabled them to revolutionize the field of nucleic acid biosensors. This flexibility facilitates the rapid development (within weeks) of tests in response to novel infectious disease outbreaks. CRISPR-based systems, coupled with isothermal amplification, frequently achieve sensitivities that parallel PCR, and can easily be adapted to work with PoC friendly systems (e.g. paper-based lateral flow). On the 6th May 2020, the FDA granted Emergency Use Authorization (EUA) to the SHERLOCK CRISPR SARS-CoV-2 kit, making it the first CRISPR-based diagnostic to be authorized by the FDA for clinical use.<sup>68</sup>

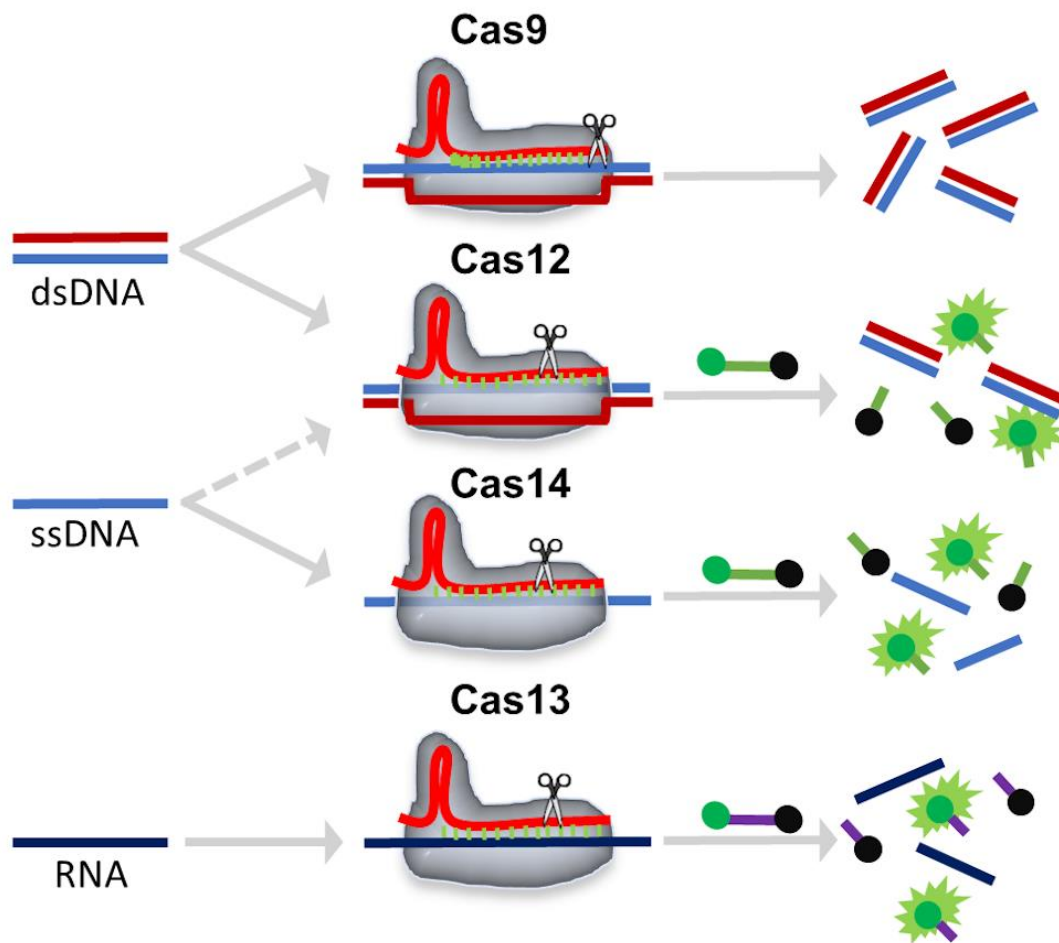


**Figure 1.3** Schematic representations of different Cas enzyme activities. Cas9: Binding of target dsDNA to the gRNA-Cas9 complex is followed by cis-cleavage of the DNA. Cas12/14: Binding of the target ds/ssDNA to the gRNA-Cas12 complex and subsequent cis-cleavage of the DNA is followed by collateral trans-cleavage of ssDNA molecular beacon probes to generate fluorescence. Cas13: Binding of the ssRNA to the gRNA-Cas13 complex and subsequent cis-cleavage of the RNA is followed by collateral trans-cleavage of ssRNA molecular beacon probes to generate fluorescence.



### 1.3.2 Redox enzymes

Redox enzymes generate signal through their ability to oxidize or reduce substrates, such as chromogenic small molecules or nanoparticles,<sup>69</sup> to produce a detectable change e.g. in the optical or electrochemical properties of the substrate. Redox enzymes are a popular choice for immunoassays, particular ELISA, due to their ability to rapidly produce a colored signal that can be easily analyzed using a variety of techniques. Unsurprisingly, these enzymes have also been adapted to aid in signal generation in nucleic acid diagnostics; some of the more commonly used approaches are highlighted below.

#### 1.3.2.1 Oxidases

Oxidase enzymes catalyze oxidation-reduction reactions, commonly utilizing molecular oxygen as the electron acceptor and hydrogen as the electron donor to reduce oxygen to water or hydrogen peroxide. The reduced species, such as hydrogen peroxide, can subsequently go on to induce a signal through downstream redox processes. The most common oxidase enzyme is glucose oxidase (GOx), which oxidizes glucose into glucono-1,5-lactone, producing hydrogen peroxide in the process. The redox process can be detected directly, commonly via electrochemical methods. For example, Zhang et al. reported a system based on electrochemiluminescence that was able to detect single nucleotide mismatches down to 1 pM. The group developed a sandwich assay using thiolated oligonucleotide capture probes, biotinylated oligonucleotide detection probes and an avidin-GOx conjugate. The hydrogen peroxide produced by the GOx in the sandwich complex was used oxidize luminol to 3-aminophtalate, producing incident photons as a measurable signal.<sup>70</sup> Whilst the team used this method to determine mutations in genes associated with breast cancer, this technique could be generalized and used for infectious disease monitoring.

#### 1.3.2.2 Peroxidases

Peroxidase enzymes catalyze the splitting of peroxidases into either water or alcohol in the presence of an electron donor. The most popular and commonly employed peroxidase is horseradish peroxidase (HRP), a metalloenzyme that derives its redox capacity from an iron-containing heme group. A variety of chromogenic organic compounds that produce a color change upon oxidation, such as 3,3',5,5'-Tetramethylbenzidine (TMB) or 4-chloro-1-naphthol/3,3'-diaminobenzidine tetra-hydrochloride (CN/DAB), have been developed to exploit the redox activity of peroxidases. Though most commonly employed in protein-based sandwich immunoassays, there have been several reports of HRP being used to generate signal for the detection of nucleic acids in a similar fashion. Bodulev et al. utilized HRP-labelled oligonucleotide detection probes to specifically hybridize to hepatitis B viral DNA that was captured onto microtiter plates.<sup>71</sup> By exploiting the HRP-mediated oxidation of 3-(10'-phenothiazinyl)propionic acid/N-morpholinopyridine the group were able to detect the target DNA down to 3 pM using a chemiluminescent signal. A more recent, and promising application of peroxidases is in electrochemical signal generation. Many electroactive species can be utilized for electrochemical detection, often with excellent sensitivity. For example, Zhang et al. utilized HRP-modified DNA probes to oxidize TMB, and measured the resulting electrochemical signal using a gold electrodes. The group were able to measure genomic DNA from *E. coli* down to 1 pM when coupled with PCR amplification.<sup>72</sup> Hydroquinone and o-phenylamine-based substrates have also been employed in a similar fashion for electrochemical detection.<sup>73-74</sup> A similar approach was taken by Mao and co-workers, who attached biotin-conjugated DNA capture probes to a gold electrode. Upon binding of the target DNA, a conformational change enables binding of streptavidin-HRP to the electrode. Subsequent oxidation of hydroquinone by HRP could be detected electrochemically.<sup>75</sup> The group were able to achieve a limited of detection of 0.1 nM, and could specifically detect a single base mismatch in their target ssDNA.

## 1.4 Enzyme-enabled aptasensors for toxin detection

Aptasensors for toxin detection have emerged in the biosensor field due to their cost-effectiveness and remarkable selectivity, combined with a versatility that sees them deployed a wide range of analytical methods, providing excellent detection performance. Unsurprisingly, aptasensors have been leveraged to detect food toxins and biomarkers in complex matrices, e.g. beverages, meats, and human samples.<sup>76</sup> With the assistance of enzymes, the typical flaws of aptasensors (e.g. high background signal and false positive rates) can be alleviated, yielding improvements in analytical performance. High detection sensitivities with broad dynamic ranges are obtained using co-working elements, which has facilitated field-deployable diagnostic tool development.

### 1.4.1 Enzyme treatments to reduce background signal

A vast number of enzymes are used to amplify nucleic acids, as discussed in **Section 1.2**, which particularly highlighted the crucial role of polymerases in the detection of infectious diseases. In some amplification methods (i.e. SDA and NASBA), nuclease enzymes are required to either remove or cleave nucleic acid specifically and marked as is imperative. Exploiting nuclease enzymes can improve sensor performance by removing background current and excess nucleic acid in the system. Both endo- and exonucleases are commonly used in such scenarios.<sup>77</sup>

Endonucleases are enzymes that specifically cleave or digest nucleic acid at the specific nucleotide within a nucleic acid sequence. In contrast, exonucleases digest nucleic acid strands from either the 3' or 5' ends. For example, Zhao et al. reported a system based on a fluorometric assay that was able to detect Pb<sup>2+</sup> ions down to 0.1 nM using a combination of a DNAzyme and Nt.BbvCI, an endonuclease.<sup>78</sup> The group utilized the 8-17E DNAzyme to cleave its substrate, facilitating DNA recycling for signal generation by allowing products to form dsDNA with a molecular beacon that was recognized by the Nt.BbvCI. Moreover, Liu et al. demonstrated the exploitation of exonuclease III (exo III) coupled with an aptamer to detect ochratoxin A (OTA) in red wine with limit of detection of 4.7 ng/mL.<sup>80</sup> The group utilized an aptamer hybridized with complementary DNA, yielding a G-quadruplex complex of the aptamer and ssDNA of the complementary DNA which cannot be digested by the exo III, in the presence of OTA. However, in the absence of OTA, the dsDNA was digested by exonuclease III, and did not yield a fluorometric signal after addition of a fluorescent dye (SYBR gold).

### 1.4.2 Enzyme-enhanced signal generation

Like disease detection, redox enzymes play a crucial role in improving the sensitivity of detection by either oxidizing or reducing electroactive substrates, resulting in signal enhancement. Using the well-known ELISA approach, Huang et al reported a colorimetric assay on a paper-based microfluidic platform using AuNPs conjugated with HRP/streptavidin/biotinylated-DNA and anti-kallikrein-3 (aKLK3) antibodies to target KLK3 (a prostate cancer biomarker) in human serum.<sup>81</sup> By applying patient serum on the sampling zone, the decorated nanoparticles were immobilized when KLK3 was presented. After a washing step, the HRP on the DNA structure then oxidized TMB, and yielded a dark blue solution, enabling detection of the KLK3 down to 10 pg/mL.

Further, Hu et al. reported a system based on electrochemistry to detect epithelial tumour marker MUC1 using AuNP-aptamer conjugates and HRP.<sup>83</sup> The aptamer was modified with a thiol group on one end and a biotin at the other, allowing immobilization on a streptavidin-modified electrode after MUC1 opens the aptamer hairpin structure. The HRP on AuNP surface then oxidizes o-phenylenediamine by H<sub>2</sub>O<sub>2</sub>, allowing ultrasensitive detection of the biomarker down to 2.2 nM. Whilst the group used this method to detect a tumour biomarker, these techniques could be generalized and utilized for healthcare monitoring.

## 1.5 Point-of-care systems

### 1.5.1 System requirements

Above the vast array of different enzymes that can be employed for nucleic acid amplification, and the different signals that enzymes can generate to detect nucleic acids, have been discussed. It is imperative that any RDT designed to take advantage of enzymes is capable of exploiting these functions (**Figure 1.4A**). Whilst these features are essential for any nucleic acid IVD, there are additional contextual requirements for field-deployable or PoC devices, particularly in the context of infectious disease and healthcare monitoring. These requirements broadly parallel the REASSURED criteria, with a few notable additions specific to enzyme-assisted nucleic acid detection.

#### *1.5.1.1 Biocompatibility*

To fully exploit the benefits of enzymes it is imperative that a system is capable of maintaining an environment that supports their function. This includes important chemical and physical factors such as pH, salinity, co-factor content, temperature, and pressure. Materials, electronics, physical dimensions and mode of operation can all be tweaked to influence these parameters. The approach taken is often specific to the type of system employed, and the context in which the diagnosis is going to take place. For example, large benchtop systems are typically able to take advantage of simple heating elements and pre-manufactured reaction cartridges to maintain temperature and pressure. Conversely, microfluidic devices require a more carefully considered approach, with factors such as material, device footprint and flow rate playing an important role in regulating pressure and temperature.

#### *1.5.1.2 Signal transduction capacity*

As previously highlighted, enzymatic mechanisms can be transduced into a variety of signals, including colorimetric, fluorescence and electrochemical, and diverse schemes for each of these signals have been developed. These detectors vary in complexity and can provide different degrees of sensitivity and dynamic range, depending on the need. The simplest colorimetric systems can even take advantage of the human eye; this is particularly useful for PoC IVDs as it greatly minimizes reliance on external technology. Whilst this approach is purely qualitative, it is still useful for infectious diseases where a positive confirmation of disease holds value. Fortunately, the simple addition of a CMOS sensor, even within a smartphone camera, can be enough to enable quantitative interpretation of systems designed around colorimetric signals. Systems built around fluorescence generally require further engineering, though commonly offer greater signal-to-noise compared to colorimetric signals. Fluorescence detection has successfully been incorporated into a variety of commercial tests, and is particularly amenable to microfluidic systems where the small volumes enable high localized concentrations of fluorescent substances.<sup>84</sup> Historically, electrochemical signals have not been widely reported for PoC applications, with a few notable exceptions (e.g. glucose monitoring). Nevertheless, recent advances in miniaturization have facilitated the development of micron scale electrical components and renewed interest in electrochemical signals for PoC nucleic acid diagnostics.

#### *1.5.1.3 Usability*

One of the primary REASSURED criteria is “user friendliness”, and highlights the importance of designing a system that is both practical for its application and easy to operate. Multiple factors determine how ‘easy’ a device is to operate in a PoC setting, including portability, user interface, robustness and degree of automation. An ideal system will be able to meet the disease-specific requirements for sensitivity and specificity, whilst maintaining a portable and robust form factor, simple user interface, and be able to automate the entire analytical process from sample preparation through to signal output. Automation is of particular importance for diagnostics,

where manual human input can increase operator risk, in addition to introducing errors into the process.

#### ***1.5.1.4 Manufacturability***

The ultimate utility of a diagnostic system is dependent on the ability to deliver it to the desired location, at an affordable price and in sufficient quantity to meet demand. System simplicity is clearly favorable, though multiple factors can affect the manufacturability of a device. The ability to source the necessary materials globally, rather than relying on a single material source, is advantageous, particularly in the context of infectious disease epidemics where transport chains can be easily disrupted. Minimizing reliance on cold-chain transport is also beneficial as it can dramatically reduce transport costs. In the context of enzyme-dependent systems, methods for lyophilizing enzymes and their substrates onto paper or other easily transportable materials (to enable transportation at ambient temperatures) are being explored.<sup>85</sup> Due to their low manufacturing costs, and the simplicity of the resources required to manufacture them, paper-based devices are particularly promising candidates when large scale, global manufacturing is paramount. A major challenge here is the robustness of such devices, particularly with respect to their ability to withstand the varied environmental conditions experienced during the supply chain. Although industrial partners are ideally suited to tackling these issues, the reality of these requirements must be considered from the outset.

#### ***1.5.1.5 Adaptability***

An ideal diagnostic platform can be quickly and easily retargeted to many different diseases with minimal changes in operation. This is particularly important for diagnostics due to the possibility that rapid mutations will lead to novel strains, invalidating existing diagnostics tests within short time periods. If a system can be easily adapted to a new strain then it can be more rapidly deployed. For more complex systems there is also the additional burden of building the prerequisite infrastructure and training personnel. Utilizing a single system for multiple diseases can minimize this impact, since a single user can run multiple tests simultaneously.

#### ***1.5.1.6 Connectivity***

Once nucleic acid IVDs are moved from centralized laboratories and into the field, it is essential to have mechanisms in place to interpret test data and remotely transmit results to the appropriate authorities. Fortunately, the smartphone boom of the last ten years has provided technologists with powerful and portable solutions for connecting diagnostic systems. Indeed, many modern devices exploit smartphones themselves to connect their data when necessary.<sup>86</sup> The smartphone revolution has also helped to drive investment into global communication infrastructure, even in the developing world, and many countries have significantly improved their communications networks over the last decade.<sup>87</sup> These technological innovations are simplifying the process of developing connected diagnostic devices, and it is anticipated that going forwards, most major diagnostic systems will include connectivity options. This concept of mobile health, or mHealth, is particularly key for the decentralization of diagnostics and the transition towards the end user.

### **1.5.2 Benchtop systems**

Whilst benchtop systems are typically associated with centralized laboratories, many manufacturers have realized the need for smaller, more portable systems. Though these systems still require significant infrastructure, they can be effectively operated from regional or even field hospitals. These types of devices are termed 'near point-of-care', and provide an important function in the fight against infectious disease.

### ***1.5.2.1 Benchtop PCR***

Recent outbreaks have highlighted the reliance of nucleic acid IVDs on PCR, and the historical prevalence of PCR-based benchtop IVDs reflects this.<sup>88</sup> The first thermal cycler for PCR was launched in 1987 by PerkinElmer, with the aim of limiting the interaction of the user with the system, thus streamlining the analytical process. Since then, devices have evolved to include higher levels of automation and real-time quantification capabilities (qPCR), though still require significant input from trained personnel. Unfortunately, these benchtop instruments require power and can be highly sensitive to temperature variations, limiting their utility in resource-limited settings. Furthermore, the large number of temperature cycles fundamentally limits the assay time due to thermal inertia, and multiplexing capabilities remain limited.<sup>89</sup> Recent developments have focused on making PCR instruments more compact, battery powered and smartphone connected, such as the two3™ thermocycler from Biomeme. Similarly, a number of compact qPCR systems have been developed commercially, including Open qPCR from CHAIbio, Franklin™ from Biomeme, and Mic Real-Time PCR from Labgene Scientific. These systems provide multiple accessibility options including remote operation and data analysis using cloud-based frameworks. More recently, there has been a focus on incorporating additional workflows into existing PCR technologies to enhance diagnostic utility. For example, sample extraction is a common bottleneck in high-throughput diagnostics. To address this issue, the private sector is moving towards modular systems that integrate nucleic acid extraction and pre-concentration, aiming to create fully automated sample-to-result platforms. Many of these platforms are highly versatile and can be rapidly adapted to specific diseases and enzymatic amplification reactions, such as the QIAstat-Dx® Respiratory 2019-CoV Panel by Qiagen.<sup>90</sup>

### ***1.5.2.2 Isothermal approaches***

In recent years, isothermal amplification approaches have gained traction. By doing away with complicated temperature programs, the instrumentation associated with isothermal amplification can be greatly simplified, making isothermal methods highly promising as field-deployable IVDs. For example, Crannell and co-workers reported the use of body heat to regulate RPA reactions, an approach with obvious advantages at the point-of-care.<sup>91</sup> Similar PoC-friendly approaches have been combined with various detection methods including fluorescence and electrochemical detection,<sup>92-93</sup> and can be performed using lyophilized reagents (in test tubes) for in-the-field use.<sup>92, 94</sup> Benchtop instruments for isothermal amplification, such as the ID Now™ by Abbott, are now commercially available and commonly employ disposable cartridges containing dried-down reagents.<sup>95</sup> That said, these test tube-based, semi-open systems require a skilled operator to perform complex reagent manipulations, potentially exposing the assays to contamination. Greater automation could help to minimize human interaction during the diagnostic pipeline and unlock the true potential of isothermal technologies.

## **1.5.3 Chip-based microfluidic systems**

Over the past three decades, microfluidic systems have transformed the way in which chemical and biological experiments are performed.<sup>96</sup> By shrinking the length scales associated with an analytical process down to the micronscale, both mass and heat transport can be significantly enhanced. This in turn means that fluidic mixing occurs in a rapid and controllable fashion, thermal homogeneity can be maintained across the system and rapid heat transfer will occur between the device and the contained fluid. In practical terms, microfluidic technologies are ideally suited to perform complex operations on small volumes and have paved the way for portable diagnostic systems (**Figure 1.4B**).<sup>97</sup> Their ability to perform a range of functional operations (such as sample pre-concentration, filtration, extraction, reaction, separation and product detection) in an automated and integrated fashion, enables the creation of fully

integrated platforms able to perform sample-to-answer assays without the need for an expert operator.

### ***1.5.3.1 On-chip PCR***

Microfluidic-based PCR was perhaps the first application of microfluidics in diagnostics.<sup>98-100</sup> In such systems, thermal cycling may proceed in a batch, continuous- or segmented-flow fashion, with the extent of the reaction being monitored in real time or via end-point analysis. Flow-based systems are especially advantageous in this regard, since thermal masses are significantly reduced, and thus the time constraints associated with heating and cooling can be as short as a few milli-seconds. Multiplexing can be achieved by parallelizing batch microsystems or by sequential addition of sample in flow-based systems.<sup>101</sup> It is important to note that monolithic systems comprising, for example, sample lysis, nucleic acid extraction, sample preconcentration, target amplification and signal detection, can be realized through standard micromachining methods.<sup>100</sup>

Several commercial platforms leverage proprietary microfluidic cartridges to achieve fully automated molecular diagnostic work flows (e.g. GeneXpert® from Cepheid or Filmarray® from bioMérieux). While such systems provide for fully automated workflows, with no user-controlled operation, their high cost, large size and reliance on single-use cartridges somewhat limits their utility at the point-of-care. Nevertheless, there are a number of reports of these systems being used successfully in RDTs for infectious disease. For example, Opollo and co-workers employed the GeneXpert® HIV-1 Qual for in-field testing of infant HIV in Kenya and found that it performed well in comparison to the gold standard laboratory test.<sup>102</sup> Moreover, Andrews et al. compared the Filmarray® system to traditional laboratory testing for monitoring of upper respiratory tract infections in the UK, and found that the microfluidic system facilitated faster treatment decisions.<sup>103</sup>

### ***1.5.3.2 On-chip isothermal amplification***

The last ten years have seen a renewed effort in harnessing the power of nucleic acid amplification in increasingly miniaturized, handheld devices.<sup>104-105</sup> Unfortunately, the majority of these are still at a very early stage of development and require significant off-chip manipulations during sample preparation and loading. The integration of nucleic acid extraction and amplification within microfluidic devices remains a significant challenge. Fortunately, isothermal amplification greatly simplifies the hardware required to perform nuclei acid amplification in chip-based systems, leaving more resources dedicated to on-chip sample pretreatment without compromising with respect to footprint or cost. For example, Yeh et al. recently presented the low-cost and self-powered “SIMPLE” platform for digital nucleic acid amplification.<sup>106</sup> Based on RPA, the chip-based system uses a pre-evacuated chamber to slowly draw fluid through a channel network. DNA extraction is achieved in one step using a branched design with a deep main channel. The extracted DNA, mixed with the RPA reagents, is then directed into an array of microwells where the reaction is triggered by the rehydration of pre-patterned reagents and the fluorescence signal can be read. Using this approach, the authors were able to successfully detect methicillin-resistant *Staphylococcus aureus* bacteria, achieving a limit of detection of 10 DNA copies per  $\mu\text{L}$ . Delamarche and colleagues showcased the use of a silicon chip capable of dispensing enzymes and other RPA reagents in a timed and passive manner, through control of coalescence in capillary-driven flows.<sup>107</sup> Their approach, while still being preliminary from a diagnostic point of view, is simple, modular, and uses standard microfabrication technologies. The simplicity and portability of these approaches demonstrate the potential of microfluidic systems to perform complex biological workflows in a fully integrated manner.

When designing a microfluidic device, it is important to consider the range of signals that can be generated by the assay under investigation. As discussed previously, enzyme-assisted nucleic acid sensors can output a broad range of signals, each with their own advantages and disadvantages. A problematic aspect of fluorescence-based approaches remains the need for bulky and often expensive optical components (such as lenses, filters, cameras and photodiodes), though progress is being made in developing miniaturized optical components for the quantification of fluorescence in small-volume environments, even using mobile phone cameras.<sup>84, 108-110</sup> On the other hand, electrochemical detectors are intrinsically more compact than optical systems, with electrical signals readily processable using mobile phones. For example, Hsieh and co-workers reported a compact electrochemical microfluidic platform capable of detecting as little as 16 copies of *S. typhimurium* genomic DNA in a single microfluidic chamber.<sup>111</sup> In this system, LAMP reactions were monitored quantitatively in real-time using an intercalating electroactive dye. However, it should be noted that spiked DNA samples in buffer were used in all experiments, with no consideration of sample pre-treatment in real-world application. That said, cell lysis and DNA pre-concentration have been achieved within microfluidic platforms,<sup>112</sup> and we expect that fully integrated microfluidic systems with electrochemical detection will play a crucial role in bringing nucleic acid detection to the field. Finally, we would like to highlight that label-free detection methods have also been used to good effect in nucleic acid analysis. For example, Toumazou and colleagues fabricated microfluidic devices with integrated ion-sensitive field effect transistors using conventional CMOS fabrication methods.<sup>113</sup> Such a device is able to monitor ssDNA amplification in real time by taking advantage of the small change in pH that results from the release of hydrogen ions during amplification (the greater the initial concentration of the target, the more rapid the pH change). Although the technique has yet to be used for the detection of disease biomarkers, the method shows significant promise.

### 1.5.4 Paper-based systems

Microfluidic paper-based analytical devices (or  $\mu$ PADs) have emerged as a promising point-of-care diagnostic platform owing to their ultra-low cost, biocompatibility and relative independence from external power sources.<sup>114-115</sup> In recent years, several paper-based immunoassays have been approved by the WHO for malaria and HIV antigen/antibody detection.<sup>116</sup>  $\mu$ PADs for nucleic acid detection are currently less developed due to the increased complexity of the assays, but are the subject of intense research.<sup>117-118</sup> Several challenges remain with paper-based nucleic acid tests, including reduced specificity due to non-specific adsorption, reproducibility and storage lifetimes.

#### 1.5.4.1 Paper-based PCR

Lateral flow assays are the most recognizable  $\mu$ PAD format. Here, sample flows unidirectionally along a paper strip and the targets and/or labs are captured on a line for detection. In the case of a colorimetric label, the result can be read qualitatively by the naked eye, or quantitatively analyzed using digital cameras and image analysis software. The detection of PCR amplicons was among the first use of  $\mu$ PADs for nucleic acid detection.<sup>119</sup> In such applications, primers are typically modified with a hapten or a unique overhang so that they can be captured and labelled with plasmonic gold nanoparticles on the test line. Similarly, line probe assays have also been developed using the same approach and are now commercially available for the rapid detection of genes associated with resistance to first- and second-line antibiotics.<sup>120-121</sup> For example, the GenoType MTBDRplus assay system from Hain Lifescience can detect up to 27 different PCR amplicons on a single strip, using alkaline phosphatase enzymes to amplify the colorimetric signal. Multiplexing is achieved by printing the capture oligonucleotides sequentially along the flow path, with results analyzed as a barcode.

Motivated by the need for equipment free methods for field testing,  $\mu$ PADs are becoming established tools for the quantification of isothermal amplification reactions. TwistDx is now offering TwistAmp® kits for RPA with a lateral flow colorimetric readout.<sup>122</sup> Amplification is typically performed in a test tube, and the lateral flow strip is subsequently dipped into the reaction mixture to generate a readout without the need for additional equipment. Similar approaches have also been developed using LAMP.<sup>23, 123</sup> Due to the nature and large size of the amplification product, other strategies based on size discrimination have also been explored in LAMP-based techniques. For example, Du et al. reported a ‘signal-off’ approach, using the fact that the LAMP product is too large to migrate through cellulose paper, effectively detecting the excess of unbound labels on the test line.<sup>124</sup> The team reported a limit of detection of 20 copies of the Ebola virus in spiked serum within 150 minutes.

#### ***1.5.4.2 Paper-based CRISPR/Cas diagnostics***

After their initial discovery, Cas-based nucleic acid detection platforms were swiftly incorporated into  $\mu$ PAD systems. This is unsurprising, as the collateral cleavage activity of CRISPR/Cas13 combines ideally with probes commonly used for lateral flow assays. An early system, termed specific high-sensitivity enzymatic reporter unlocking (SHERLOCK), developed in the Collins and Zheng labs at MIT, exploits oligomers with FAM- and biotin-modified ends to enable lateral flow readout.<sup>64</sup> After RPA, anti-FAM gold nanoparticles are added to the sample and flowed through a lateral flow strip modified with a streptavidin test line. The assay can then be read visually using the plasmonic properties of the gold nanoparticles. The power of this approach was showcased by detecting RNA targets for both Zika and Dengue viruses, and clinically relevant limits of detection were achieved in patient samples. Following on from this, the team reported SHERLOCKV2, in which they achieved multiplexing by employing orthogonal CRISPR/Cas systems and fluorophores.<sup>66</sup> Myhrvold et al. subsequently refined the SHERLOCK work-flow to incorporate sample pre-treatment, comprising reducing agents and two subsequent heating steps to lyse viral particles and inactivate ribonucleases found in bodily fluids.<sup>125</sup> This protocol enables testing for nucleic acids in unprocessed whole blood, saliva or urine, thereby providing an instrument free sample-to-answer assay. A major advantage of Cas-based diagnostic platforms is that they can be rapidly adapted to new sequences, and thus new diseases. This adaptability was perfectly illustrated in the COVID-19 pandemic, with protocols based on RT-LAMP and the SHERLOCK or DETECTR platforms being rapidly developed once the virus had been sequenced.<sup>11,</sup>

126

#### ***1.5.4.3 Paper-based translational diagnostics***

Perhaps one of the most promising technologies to be combined with  $\mu$ PADs is in vitro transcription/translation, demonstrating great potential in point-of-care nucleic acid IVDs.<sup>50, 85</sup> Remarkably, all of the transcription/translation components required for this complex reaction network showed long-term stability when freeze-dried on paper, with activity remaining even after a year of storage at room temperature.<sup>85</sup> When rehydrated with the diluted sample solution, the mixture is incubated on small paper discs for two hours at 37°C to yield a fluorescent or colorimetric signal. As proof-of-concept, Collins and colleagues developed a test capable of differentiating the Sudan and Zaire strains of the Ebola virus with good sensitivity.<sup>85</sup> The colorimetric test, based on a LacZ-expressing toehold switch, requires 25–60 minutes to complete and is quantifiable using a smartphone camera or an in-house developed optical reader (< 100 USD). Each test is cheap (< 65 cents per sensor), quick to manufacture and can be rapidly adapted to a new disease by high-throughput screening (240 reactions in parallel on a single sheet of paper). Still, as a standalone method, the detection limit of approximately 30 nM is insufficient for clinical application. In a follow-up study, the authors showed that synthetic gene networks can be combined with NASBA for increased sensitivity, and when integrated with an additional CRISPR/Cas9-mediated selection downstream of the amplification yielded single-nucleotide



discrimination.<sup>50</sup> This approach resulted in a sample-to-answer test in under three hours with low femtomolar sensitivity for both Zika and Dengue viruses. Nevertheless, the method still required a nucleic acid extraction step performed by a skilled user.

#### ***1.5.4.4 Fully integrated paper-based systems***

A major limitation of the paper-based methods discussed thus far is that the sample preparation and amplification steps are performed 'off-paper'. This increases the number of liquid-transfer steps, increasing the chances of error. The reliance on such pre-processing is not surprising; the complete integration of a nucleic acid test on paper is a considerable challenge. Controlling all the necessary parameters (flow rate, temperature, concentration) for both extraction and amplification on paper is complicated by factors such as evaporation and the absorptivity of the paper itself. Additionally, cellulose paper has been shown to inhibit enzymatic isothermal amplification reactions,<sup>127</sup> though the exact cause of inhibition remains unclear. Nonetheless, many groups have found creative ways to exploit the peculiar properties of paper to perform complex operations, ranging from nucleic acid extraction to elaborate detection methods.<sup>118</sup> For example, Byrnes et al. showed that paper strips are able to extract DNA from cell lysate by flow separation, effectively removing possible amplification inhibitors for subsequent nucleic acid analysis.<sup>128</sup> The same group also demonstrated an in-flow DNA concentration method using chitosan-coated paper as a solid-phase material for anion exchange chromatography.<sup>129</sup> DNA capture and purification can also be performed with reasonable efficiency on cellulose paper.<sup>130-131</sup>

An interesting example of a highly-integrated  $\mu$ PAD was reported by Cooper and co-workers for malaria detection in low resource settings.<sup>132-133</sup> This origami-based  $\mu$ PAD comprises different panels containing the necessary reagents for cell lysis and DNA amplification (via LAMP), which are folded to sequentially perform each step. Multiplexing is achieved by having a 2D-patterned layer to dispense the lysed sample to different reaction zones; up to five, including a positive control for LAMP.<sup>134</sup> The required temperatures can be realized by simply laying the device on a hotplate, or even a cooking stove, with the top and bottom layer being covered with a plastic film to limit evaporation. Signal can be generated either directly via fluorescence or by contacting the bottom layer to multiple lateral flow strips containing dried nanoparticle labels. Their method is able to process crude clinical samples, such as whole blood, and if the sample is too viscous lysis can be performed off-device before dilution. This platform was recently deployed in rural Uganda for the diagnosis of malaria. Enzymes and reagents were stored and transported in lyophilized form and, once rehydrated, retained their activity for more than three days without refrigeration. Buffers for the LAMP reaction and the lateral flow assay were stored in sealed plastic chambers that opened when pressed with the finger, thus limiting the contact of users with the sample. During field tests the device worked well, demonstrating 93% specificity and sensitivity when compared to qPCR. A similar origami-based approach was developed by Magro et al. for diagnosing Ebola using reverse-transcriptase RPA.<sup>135</sup> Here, the necessary reagents were freeze-dried onto the paper, and no significant reduction in the signal-to-noise ratio was observed after one month of storage; after three months of storage a 20% loss in performance was reported. However, it should be noted that these stability tests were performed using high viral loads, and it is unclear how the limit-of-detection will be affected at lower concentrations. Yager and colleagues also presented a prototype of a fully integrated  $\mu$ PAD with no moving/foldable parts for methicillin-resistant *Staphylococcus aureus* detection from nasal swabs.<sup>38</sup> The 3D-printed device comprised several resistive heating blocks with associated electronics and a  $\mu$ PAD. Heat-actuated wax valves were printed on the channel to achieve automated timing of the various steps. Achromo-peptidase, an enzyme with bacteriolytic properties, was dried in the fluid introduction tubing, and iSDA and detection reagents (nanoparticle labels and capture probes) were freeze-dried onto the lateral flow strips. The device provided robust results even when

stored for more than six weeks at room temperature, and confirms the feasibility of fully automated, low-cost nucleic diagnostic tools for in-field testing. That said, the prototypes did exhibit some reliability issues, in particular overheating during valve actuation and non-ideal flow conditions due to evaporation, thus highlighting the ongoing challenges associated with fully automated paper-based nucleic acid detection.

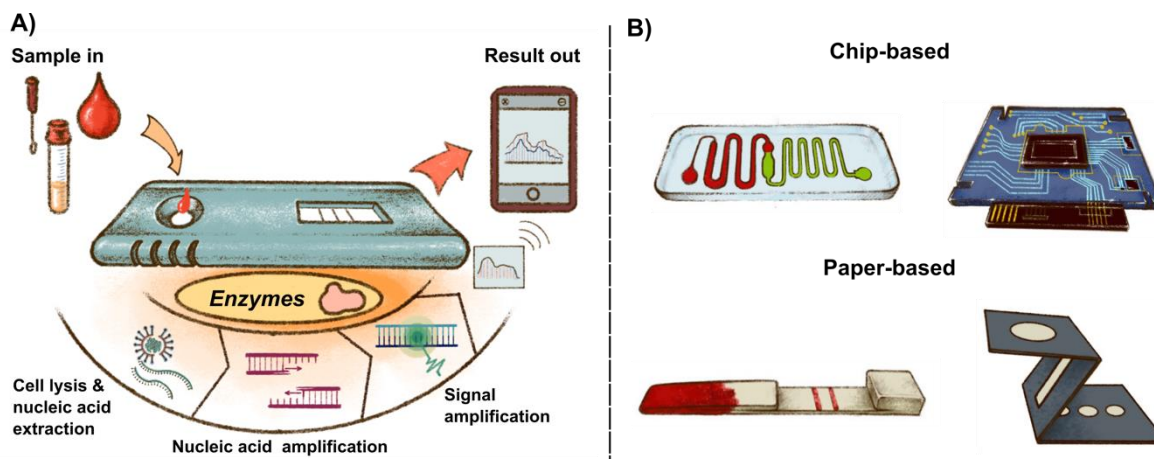


**Figure 1.4** A) An idealized point-of-care diagnostic utilizing enzyme-assisted nucleic acid biosensing. B) Different microfluidic devices used in point-of-care diagnostics.

## 1.6 Thesis overview

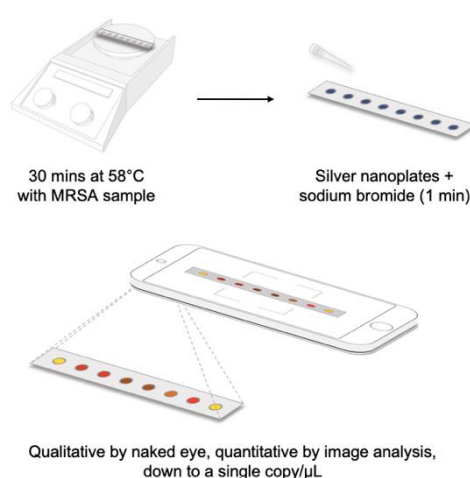
Throughout the work presented in this thesis, enzymes have been used in the development of DNA biosensors for pathogen and toxin analysis within various types of PoC platforms, yielding novel contributions to the development of field-deployable diagnostic devices. For **Chapter 2** and **3**, *Bst* polymerase was utilized in a LAMP system to amplify an MRSA genome nucleotide sequence, the *mecA* gene, allowing robust and highly-sensitive detection on PADs and in a droplet-hydrogel platform. The role, mechanism, and application of a silver nanoplate-mediated colorimetric assay for LAMP amplicon detection are described in **Chapter 2**. Using LAMP amplicons to protect silver nanoplates from  $\text{Br}^-$ , single-molecule detection was achieved, with readout by the naked eye, in both solution and paper-based devices. A similar LAMP protocol was applied in the droplet-hydrogel platform, as discussed in **Chapter 3**. Here, having robust polyacrylamide hydrogel droplets in the LAMP solution, with simple shaking in oil, allowed sample compartmentalisation and subsequent digital droplet detection of the *mecA* gene, yielding a facile, sensitive and specific assay.

A CRISPR/Cas biosensor was employed in **Chapter 4** to detect MRSA using ssDNA-modified disposable electrodes. By taking advantage of the trans-cleavage activity of Cas12a, the ssDNA on the electrode was cleaved only in the presence of the *mecA* gene. Combining this with the DNA silver metallization technique allowed ultrasensitive detection down to the fM level without target amplification, using simple electrochemical measurement. In **Chapter 5**, silver metallization of DNA was applied to detect an OTA-ssDNA complex on disposable electrodes. In the absence of the target OTA, the unbound ssDNA was digested by the Exo I enzyme, whereas the presence of the OTA protected the DNA from digestion. This mechanism yielded a sub-pg/mL limit of detection, with excellent analytical performance. **Chapter 6** presents a simple, cost-effective, and environmentally friendly colorimetric assay to detect OTA on PADs using GOx-

modified ssDNA to form a sandwich complex with an immobilised antibody. In the presence of OTA, the complex produced  $H_2O_2$  that induced a colour change in a glucose, starch and  $I^-$  solution, allowing OTA detection down to the pg/mL level using smartphone-based analysis. Finally, an outlook for PoC platform development is presented in **Chapter 7**, and the thesis conclusions are presented in **Chapter 8**, summing up the works presented herein, and providing the author's final perspective.

## Chapter 2

# *In situ* nucleic acid amplification and ultrasensitive colorimetric readout in a paper-based analytical device using silver nanoplates



We present a rapid, highly sensitive and quantitative colorimetric paper-based analytical device (PAD) based on silver nanoplates (AgNPLs) and loop-mediated isothermal amplification (LAMP) for drug-resistant bacteria detection. We show that cauliflower-like concatemer LAMP products can mediate crystal etching of AgNPLs, with a three-fold signal enhancement versus linear dsDNA. We target methicillin-resistant *Staphylococcus aureus* (MRSA), an antimicrobial resistant bacterium that poses a formidable risk with persistently high mortality, as a model pathogen. Due to the excellent color contrast provided by AgNPLs, the PAD allows qualitative analysis by the naked eye and quantitative analysis using a smartphone camera, with detection limits down to the single copy level in just 30 minutes and a linear response from 1 to  $10^4$  copies ( $R^2=0.994$ ). The entire assay runs *in situ* on the paper surface, which drastically simplifies operation. This is the first demonstration of single copy detection using colorimetric readout, with the developed PAD showing great promise for translation into an ultrasensitive point-of-care tests for diverse disease target, via modification of the LAMP primer set.

This chapter is adapted from a manuscript entitled "*In situ nucleic acid amplification and ultrasensitive colorimetric readout in a paper-based analytical device using silver nanoplates*", authored by Akkapol Suea-Ngam, Ilada Choopara, Shangkun Li, Mathias Schmelcher, Naraporn Somboonna, Philip D. Howes and Andrew J. deMello. Published in *Advanced Healthcare Materials*, *In press*.

## 2.1 Introduction

Effective diagnostic tools are key in limiting the spread of infectious diseases.<sup>5</sup> Targeting the genetic material of pathogens in clinical samples using nucleic acid amplification tests (NAATs) allows for versatile and rapid diagnostic tests that can be readily adapted to new targets, for example during epidemic and pandemic scenarios.<sup>136</sup> Although the transferral of NAATs from specialized labs to point-of-care environments is an ongoing challenge,<sup>137</sup> diagnostic devices that can be easily read using a mobile device (such as a smartphone or tablet) show great promise.<sup>86</sup> Colorimetric test readouts are highly desirable here as they can be analysed using a camera and standard software.<sup>138</sup> That said, simple colorimetric sensing mechanisms that are highly sensitive in themselves are often lacking. NAATs are recognized as desirable alternatives to traditional culture-based assays,<sup>139</sup> but as yet are insufficiently developed as robust PoC diagnostics. Amongst isothermal amplification approaches,<sup>140</sup> loop-mediated isothermal amplification (LAMP) has attracted most attention due to its ability to robustly and sensitively amplify specific DNA targets.<sup>141</sup> Although colorimetric LAMP detection has been demonstrated (e.g. using DNA-staining dyes<sup>142</sup>), sensitive and quantitative analysis remains challenging.

Paper-based analytical devices (PADs) are cost-effective, allow attachment and/or storage of reaction components in the fibre network, and are amenable to production scale-up.<sup>143-144</sup> Recently, Henry and co-workers reported a PAD for AMR detection in bacteria-contaminated water, employing a  $\beta$ -lactamase and nitrocefin assay.<sup>145</sup> Although this method is excellent for assessing bacterial activity, it lacks species specificity, which can be critical in treating infections.<sup>146</sup> Targeting genetic material would allow for a much deeper analysis.

LAMP has recently been combined with PADs for rapid and cost-effective diagnostics. For example, Cooper and co-workers have developed origami-based PADs allowing the analysis of complex samples such as whole blood and bovine semen.<sup>132, 134</sup> The same group also developed a multiplex lateral flow system using a similar protocol, which shows promise for PoC testing.<sup>16</sup> However, *in situ* analysis of LAMP has to date relied on fluorescence detection,<sup>132-134, 147</sup> providing a minimum limit of detection of  $10^2$  DNA copies.<sup>148</sup> Although readout is relatively simple under a UV lamp, fluorescence detection adds an extra layer of complexity that would be preferable to remove. Accordingly, colorimetric approaches are desirable. Although a number of colorimetric LAMP assays have been reported in the literature, limitations in sensitivity and a lack of *in situ* amplification have prevented field-deployable applications.<sup>149-150</sup>

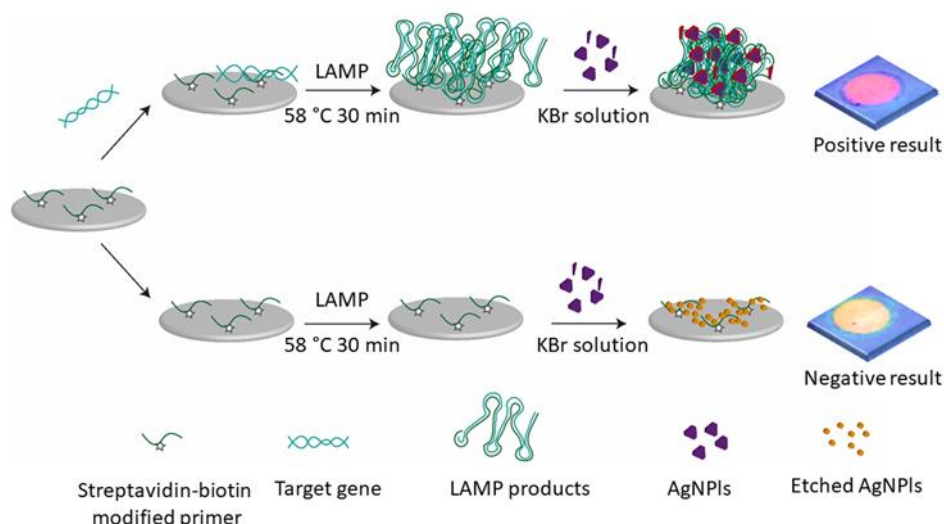
Noble metal nanoparticles exhibit dramatic shifts in plasmonic character, and therefore their color in solution, as a function of particle aggregation or etching. Linking these processes to biologically-related stimuli (e.g. biomolecular binding, pH changes and enzyme-mediated redox reactions)<sup>151</sup> makes them potentially excellent colorimetric biosensors.<sup>152</sup> Further, they are relatively easy to synthesize, can be dressed with a large variety of capping agents and functional groups for bioconjugation, can be stabilized in a wide range of physiological conditions, and can resist non-specific binding.<sup>153</sup> Accordingly, nanoplasmonics has played a key role in the development of PADs for the sensitive colorimetric detection of many different analytes.<sup>154-155</sup> A particular advantage in this regard is the ability to tune the colorimetric response to the physiology of the human eye, thus favoring sensitive detection even with a simple visual readout.<sup>156</sup>

Silver nanoparticles exhibit similar chemistry to gold nanoparticles, including strong thiol binding for capping and conjugation control,<sup>157</sup> but possess some key advantages, including facile size and morphology control using mild and simple chemistry, and silver's lower cost.<sup>158-159</sup> The interaction of silver with DNA has seen various applications, such as silver metallization of DNA for biosensing,<sup>79</sup> silver-induced DNA damage in bacteria,<sup>160</sup> DNA-templated silver nanocluster

synthesis<sup>161</sup> and dsDNA-based silver nanowires.<sup>162</sup> These studies suggest promise in developing nanosystems that co-employ both nucleic acids and AgNPs.

Antimicrobial resistance (AMR) in bacterial infections kills more than seven hundred thousand people per year; a number predicted to rise to ten million by 2050.<sup>163</sup> Unsurprisingly, The World Health Organization has stressed the importance of controlling infections on the front line through the provision of appropriate *in vitro* diagnostics for rapid AMR detection.<sup>164</sup> Motivated by this importance, we use methicillin-resistant *Staphylococcus aureus* (MRSA), the most prevalent AMR pathogen,<sup>165</sup> as a model target in the development of our colorimetric PAD.

Specifically, we report a new and highly sensitive assay concept and paper-based analytical device, allowing detection of a target gene down to the single copy level. These studies represent the first use of silver nanoplates (AgNPIs) for sensitive colorimetric detection of DNA amplicons based on nanocrystal etching. In addition, LAMP-mediated AgNPI etching allows extremely sensitive detection, down to a single copy, with excellent selectivity against other bacteria. Finally, successful integration of the scheme into a PAD presented, including the first demonstration of conjugation of LAMP primers to the cellulose surface. Qualitative results can be read by the naked eye, whilst quantitative results can be obtained by smartphone image capture and analysis, as shown in **Scheme 2.1**. Overall, the developed paper-based test shows excellent promise as a versatile field-deployable PoC test for infectious diseases.



**Scheme 2.1** Schematic illustration of *in situ* loop-mediated isothermal amplification (LAMP) on paper using AgNPIs in the presence and absence of target DNA.

## 2.2 Materials and methods

NaCl, NaI, NaBr, KCl, KI, KBr, 2,2,6,6-tetramethylpiperidine 1-oxyl (TEMPO), agarose, mixed deoxynucleotide (dNTPs), biotin, streptavidin (*Streptomyces avidinii*), betaine, and N-hydroxysuccinimide purum (NHS) were obtained from Sigma-Aldrich (Buchs, Switzerland). MgSO<sub>4</sub>, polymerase buffer and DNA polymerase (*Bst* 2.0) were obtained from New England Biolabs (Frankfurt am Main, Germany). All primers and modified primers were purchased from Microsynth (Balgach, Switzerland). TBE buffer pH 8.3 (Acros Organics, Geel, Belgium), N-(3-dimethylaminopropyl)-N'-ethylcarbodiimide hydrochloride (EDC) (Roth AG Gerlafingen, Switzerland) were analytical grade. All aqueous solutions were prepared with DNase and RNase free water (Thermo Fisher Scientific, Reinach, Switzerland). Silver nanoplates were a gift from Prime Nanotechnology (Bangkok, Thailand).

### 2.2.1 Instrumentation

DNA reactions were analyzed using a Quanstudio Real-time PCR machine (Thermo Fisher Scientific, Reinach, Switzerland) and gel electrophoresis (85 V applied potential for 75 minutes in TBE buffer). Transmission electron microscopy (TEM), was performed on a HT7700 Hitachi TEM at an accelerating voltage of 100 kV.

### 2.2.2 LAMP reaction conditions

For the LAMP process, the *mecA* gene—located in the *SCCmec* region found in every MRSA strain—was chosen as the target.<sup>1</sup> LAMP and PCR primers were manually designed using online resources (<http://primerexplorer.jp/elamp5.0.0/index.html> and [http://www.premierbiosoft.com/tech\\_notes/PCR\\_Primer\\_Design.html](http://www.premierbiosoft.com/tech_notes/PCR_Primer_Design.html), respectively). Reported sequences for the *mecA* gene were obtained from the NCBI database, and analysed using the program MEGA 5.2. The *mecA* sequence used for assay development herein was amplified from the MRSA strain (*Staphylococcus aureus* USA300 JE2; source: Annelies Zinkernagel, Division of Infectious Diseases and Hospital Epidemiology, University Hospital Zurich, University of Zurich, Zurich, Switzerland; properties: methicillin-resistant *S. aureus*) using PCR (primers shown in **Table 2.1**). The PCR products were quantified using a Nanodrop 2000 (Thermo Fisher Scientific, Reinach, Switzerland).

**Table 2.1** LAMP and PCR primers sets for *mecA* amplification.

Reaction	Name	Oligonucleotide sequence
LAMP	FIB	5' ACCTAATAGATGTGAAGTCGCTTTTTTTCATCTTACAATAATGAAACAGAA 3'
	BIP	5' TATGTTGGTCCCATTAAGTCTGAAGTCCCTTTTTACCAATAACTGCA 3'
	LF	5' TTCTAGAGGATAGTTACGACT 3'
	LB	5' CAAAAAGAATATAAAGGCTATAA 3'
	F3	5' GATGAATATTTAAGWGATTTTCGC 3'
	B3	5' TGGAGCTT TTTATCGTAAAGTT 3'
PCR	Forward	5' AGATTGGGATCATAGCGTCAT 3'
	Backward	5' TTGAGGGTGGATAGCAGTACC 3'

The LAMP reaction was performed following the standard methodology (Table 2.2), which requires 0.8  $\mu\text{M}$  of two outer primers (F3 and B3) for strand displacement activity during the non-cyclic step only, and 1.6  $\mu\text{M}$  of the inner primers (FIB, BIP) for both the sense and antisense sequence, which helps in loop formation.<sup>136</sup> Further, two additional loop primers (LF and LB) were added to 1.6  $\mu\text{M}$  to accelerate the reaction, thus reducing the required incubation time.<sup>137</sup> Optimal concentrations of *Bst* polymerase,  $\text{MgSO}_4$ , betaine, and dNTPs were found to be 480U/mL (8 units per reaction), 4 mM, 1 M, and 1.4 mM, respectively. To obtain quantitative results from the tube-based LAMP reaction (at 58 °C),  $C_T$  values (time at which the amplification curve reaches one third of its maximum value), were plotted against the obtained signal to acquire the calibration curve.

**Table 2.2** The concentration of each component of the LAMP reaction.

Components	Final amount for 3 reactions
FIP and BIP (20 $\mu\text{M}$ )	4 $\mu\text{L}$ each
F3 and B3 (10 $\mu\text{M}$ )	1 $\mu\text{L}$ each
LF and LB (20 $\mu\text{M}$ )	3.5 $\mu\text{L}$ each
Betaine	10 $\mu\text{L}$
dNTPs (10 mM)	7 $\mu\text{L}$
Polymerase buffer (10X)	5 $\mu\text{L}$
SYBR green (1/5000X)	2 $\mu\text{L}$
$\text{MgSO}_4$ (10 mM)	2 $\mu\text{L}$
DNase/RNase free water	1 $\mu\text{L}$
Target DNA	3 $\mu\text{L}$
<i>Bst</i> Polymerase (8,000 unit/mL)	3 $\mu\text{L}$
Total	50 $\mu\text{L}$

The PCR reaction was carried out as follows: 12.5  $\mu\text{L}$  Go Taq ® Hot Start Green Master Mix, 2.5  $\mu\text{L}$  of both 10  $\mu\text{M}$  forward primer and backward primer (designed for *mecA* gene), 1  $\mu\text{L}$  of MRSA lysate, and 6.5  $\mu\text{L}$  RNase/DNase free water were mixed. The amplification process was initiated by heating at 95 °C for 2 minutes, following by 30 cycles of denaturation at 95 °C for 30 seconds, annealing at 55 °C for 30 seconds, and extension at 72 °C for 1 minute. The final extension was applied at 72 °C for 5 minutes before storing at 4 °C.

To validate the LAMP reaction for single *mecA* gene detection, 2% agarose gel (Sigma-Aldrich, Buch, Germany) was prepared in 1X TBE buffer, followed by 2  $\mu\text{L}$  of 1x diamond dye (Promega, Switzerland) for fluorescence visualisation. To visualise the running electrophoresis processes, DNA ladder (100-100 kb, Promega, Switzerland), negative, and a concentration series (1-10<sup>4</sup> copies/ $\mu\text{L}$ ) of positive LAMP samples were mixed well with Novel Juice DNA stain (Sigma-Aldrich, Buch, Germany) before loading to the electrophoresis chamber. The gel was run in an electrophoresis bath for 60 minutes using a 100 V applied potential. The electropherogram was visualised under 300 nm UV lamp, and taken picture via smartphone.



### 2.2.3 Device design

The paper-based analytical devices (PADs) were assembled with 5 layers: adhesive tape (Scotch tape™), double layer adhesive tape (3M), and wax-patterned cellulose paper (Whatmann No.1). A Colorcube wax printer (Xerox AG, Opfikon, Switzerland) was used to pattern reaction wells directly onto the cellulose paper. The primer immobilization on the cellulose paper was achieved by introducing TEMPO to generate carboxyl groups on the cellulose fibers, which then reacted with an EDC/NHS solution, followed by addition of the streptavidin. The biotinylated FIB primers were then modified on the paper surface via streptavidin-biotin binding.

### 2.2.4 Image analysis

Images were taken by the smartphone and have operated using Photoshop to convert RGB-based images to grey-scale images. The converted images were then measured its intensity. It should be noted that the PADs comprised of positive control, negative control, and detecting reservoirs, facilitating illuminating background removal and remaining testing precision. The grey scale intensity of the sampling reservoirs were detected using the following equation:

$$\text{Sample intensity} = \text{Negative control} - \text{Sample} + \text{Positive control} \quad (2.1)$$

The highest intensity for the grey scale is the brightest reservoir, which is the negative control in this case, and the positive control provided the lowest intensity. Therefore, using the same amount of reagents with same AgNPLs batch should be applicable for this method.

### 2.2.5 Immobilized primer study

Due to the high cost of biotinylated primer, the chosen LAMP primer to fabricate on paper was studied. The LAMP conditions as shown in **Table 2.2** was used, yet removed one of each primer in different tube in **Table 2.2**. Resulting as illustrated in **Figure 2.8 a and b** shows the comparing of missing of inner, outer, and accelerating primers.  $C_T$  value was used as the indicating factor, where the less obtaining  $C_T$  value, the faster amplification is performed. It should be noted that the slower amplification might increase the risk of obtaining the false positive, resulting nonspecific amplifications (i.e. mis-priming events<sup>4</sup> and primer-primer interactions<sup>5</sup>). By missing outer (F3 and B3) and accelerating (LF and LB) primers,  $C_T$  values were found to be ~15 to 25 minutes. The significantly greatest  $C_T$  value (40-45 minutes) showed when missing loop primers (BIP and FIP), indicating its importance in LAMP process. In addition, this result was supported by the LAMP mechanism where loop forming of those BIP and FIP primers can hold the amplicons on the cellulose paper surfaces, while others primers would release amplicons into the reaction solution. Therefore, the chosen primer to fabricate on cellulose paper was loop-forming primer. According to the  $C_T$  value in **Figure 2.8**, FIP primer was then chosen due to the slowest amplification time when it was disappeared.

Thus, to perform *in situ* LAMP on the PADs, the same reaction solution as used in the tube-based reaction (excluding the FIP primer) was applied to the FIP modified PADs. For quantitative results from the LAMP-PAD system, the reaction was incubated for 40 minutes at 58 °C in an oven, then after removal AgNPLs (5 µL of 500 ppm) were applied allowing incubation for 30 s, followed halide salts (5 µL of 10 mM). All pictures for colorimetric detection were taken by Samsung Note 9 smartphone, photos were processed using Photoshop™ (isolating the red channel before conversion into grey scale), and then analysed using ImageJ.

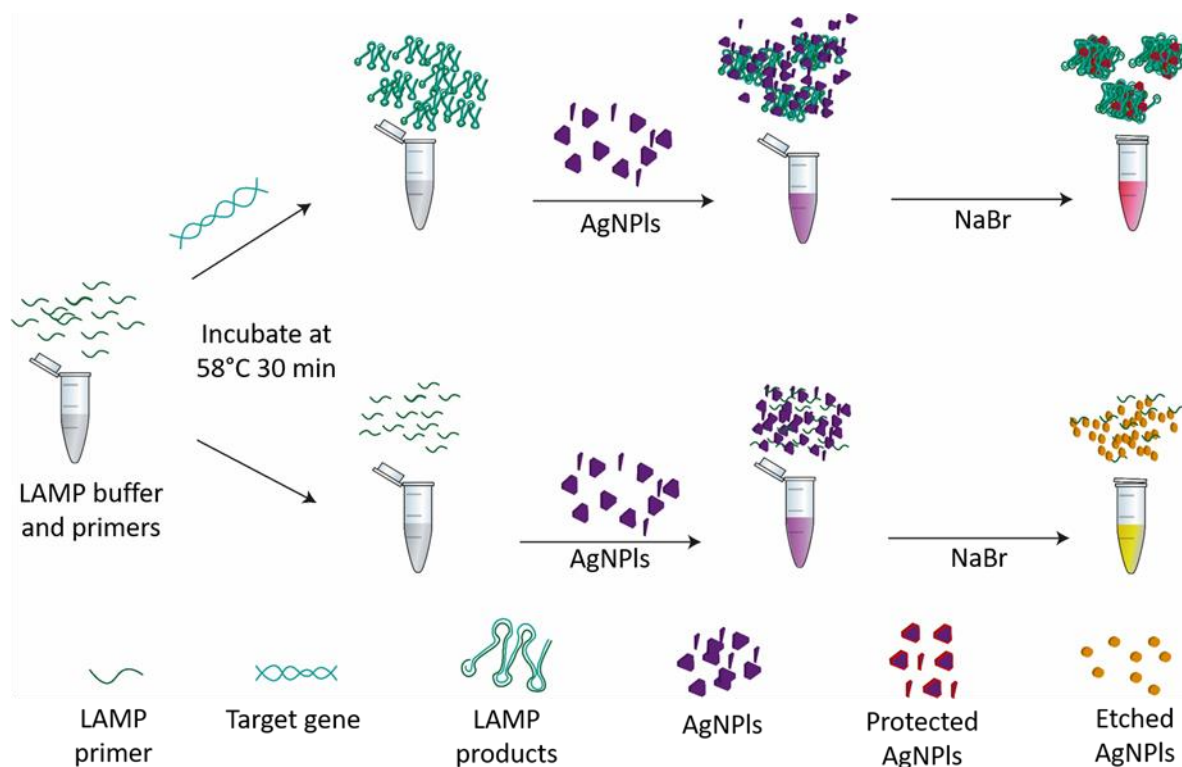
### 2.2.6 Lysate testing and selectivity study

MRSA (*Staphylococcus aureus* USA300 JE2; source: Annelies Zinkernagel, Division of Infectious Diseases and Hospital Epidemiology, University Hospital Zurich, University of Zurich, Zurich, Switzerland; properties: methicillin-resistant *S. aureus*) colonies were collected and lysed in TE buffer (Fischer Scientific, Reinach, Switzerland) at 95 °C for 5 minutes. Then 1 µL of the lysate was added to the LAMP, PCR or LAMP-PAD working solutions before proceeding with the amplification reaction and readout. For the specificity tests, the same procedure was followed for the following bacteria: *E. coli* (*Escherichia coli* JM109; source: Stratagene, San Diego, CA, USA; properties: *E. coli* lab strain, non-pathogenic), *E. faecalis* (*Enterococcus faecalis* ATCC 19433; source: ATCC 19433; properties: type strain), *L. monocytogenes* (*Listeria monocytogenes* Scott A; source: Weihenstephan Listeria Collection; properties: clinical isolate, serovar 4b), *S. epidermidis* (*Staphylococcus epidermidis* MP04; source: Max Paape, ARS, USDA, Beltsville, MD, USA; properties: bovine mastitis isolate) and methicillin-sensitive *S. aureus* (MSSA) (*Staphylococcus aureus* Newman; source: NCTC 8178, Annelies Zinkernagel, Division of Infectious Diseases and Hospital Epidemiology, University Hospital Zurich, University of Zurich, Zurich, Switzerland) were obtained from Institute of Food, Nutrition and Health, ETH Zurich, Switzerland.

## 2.3 Results and discussion

### 2.3.1 Colorimetric detection using silver nanoplates

We combined AgNPLs with LAMP to realize the sensitive, specific and colorimetric detection of MRSA via the *mecA* gene (**Scheme 2.2**). Although the numerous MRSA strains contain many different genes that confer drug resistance, the *mecA* gene is found in all MRSA strains,<sup>166</sup> and as such was chosen as a marker for MRSA in the current study. AgNPLs are highly anisotropic flat nanostructures (**Figure 2.1a**),<sup>167</sup> whose solutions exhibit varied colors due to the dependence of the plasmonic peaks (between 350 and 1000 nm)<sup>168</sup> on both particle size and shape. They readily undergo oxidative etching and crystal reformation as a function environmental redox character.<sup>169</sup> These processes result in significant shifts in solution colors. Halides are known to bind to and etch AgNPLs, inducing morphological changes,<sup>169</sup> and DNA is known to interact strongly with silver ions and metal surfaces. It has recently been shown that DNA (particularly short poly sequences) can exert morphological control over AgNPLs growing from Ag nanoparticle seeds.<sup>170</sup> Given the etching abilities of halides and the potential of DNA to bind and protect Ag facets, we hypothesized that by exposing the AgNPLs to halide salts in various concentrations of LAMP DNA product, a ratiometric shift in AgNPL solution color as a function of *mecA* would occur.



**Scheme 2.2** Schematic illustrates colorimetric detection of MRSA using LAMP and AgNPs. In the presence of the target *mecA* gene (top), the LAMP reaction yields a large amount of long DNA concatamer product. Upon addition of a solution of AgNPs, the particles coordinate with the DNA, which then protects them against etching by the subsequently added bromide, and the solution turns red. In contrast, in the absence of the target (bottom), LAMP does not proceed and there is no reaction product to protect the AgNPs from etching, and the reaction solution turns pale yellow.



**Scheme 2.3** a) Schematic of a silver nanoplate (AgNPI) structure with facets orientation on the nanoplate structure

The AgNPs used herein are starch-stabilized, appearing blue-purple in aqueous solution (**Figure 2.1a inset**).<sup>171</sup> TEM analysis (**Figure 2.1a**) revealed a mixture of truncated triangular and circular plates ( $42 \pm 8.9$  nm diameter) and small discs ( $7.7 \pm 3.9$  nm diameter). Absorption spectra (**Figure 2.2**) display a sharp low-intensity peak at 339 nm indicating the presence of plates, and a broad peak at 400 nm corresponding to the presence of smaller nanoplates and/or nanoparticles. A broad peak occurring between 500 and 550 nm corresponds to the in-plane dipole resonance of larger nanoplates, and shifts as a function of vertex sharpness and lateral size.

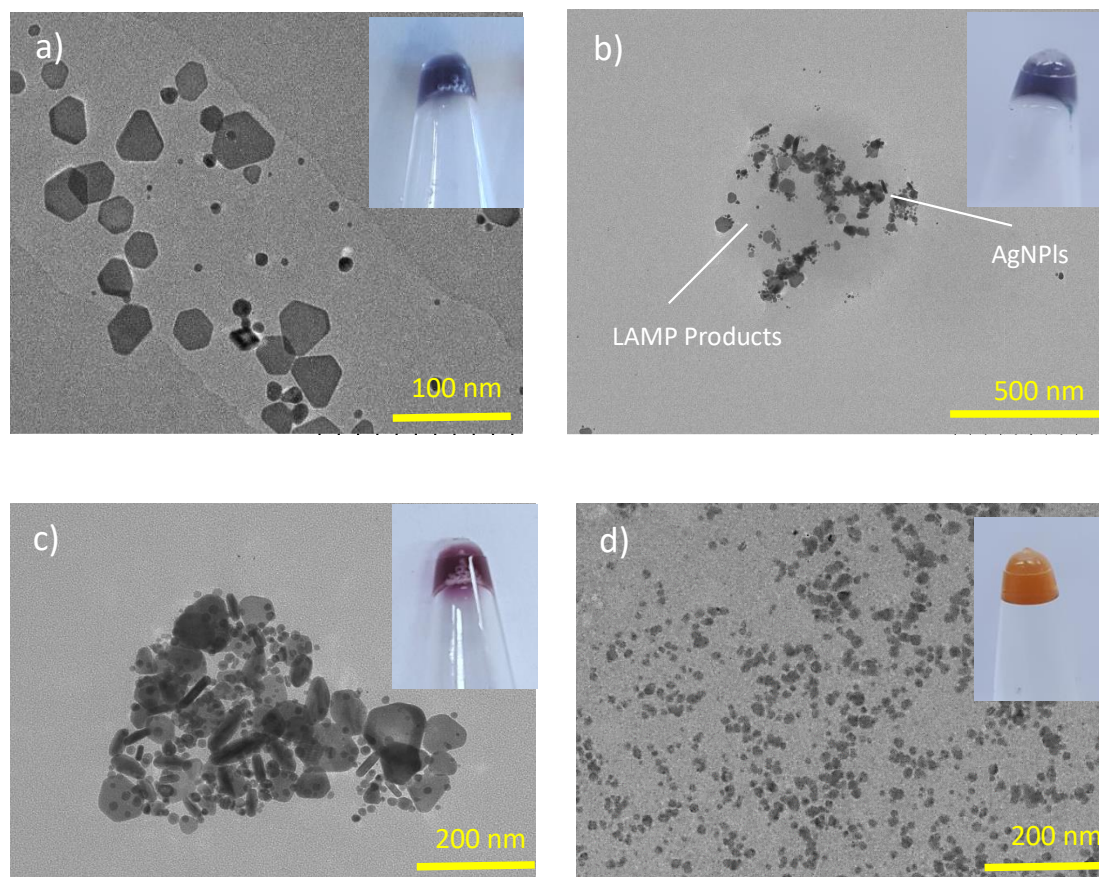


**Figure 2.1** a)-d) TEM images of the stock AgNPLs, AgNPLs with LAMP amplicons, AgNPLs with LAMP amplicons and NaBr (positive control), and etched AgNPLs with NaBr in the absence of target molecule (negative control), respectively.

First, we identified which halide salts yield the greatest plasmonic shift (**Figure 2.2a**), finding that NaBr provides the greatest, with solutions changing from blue-purple to yellow. Accordingly, the in-plane dipole resonance peak blue shifts from 550 to 419 nm, indicating a rounding of nanoplate corners and the formation of smaller nanodiscs.<sup>172-173</sup>

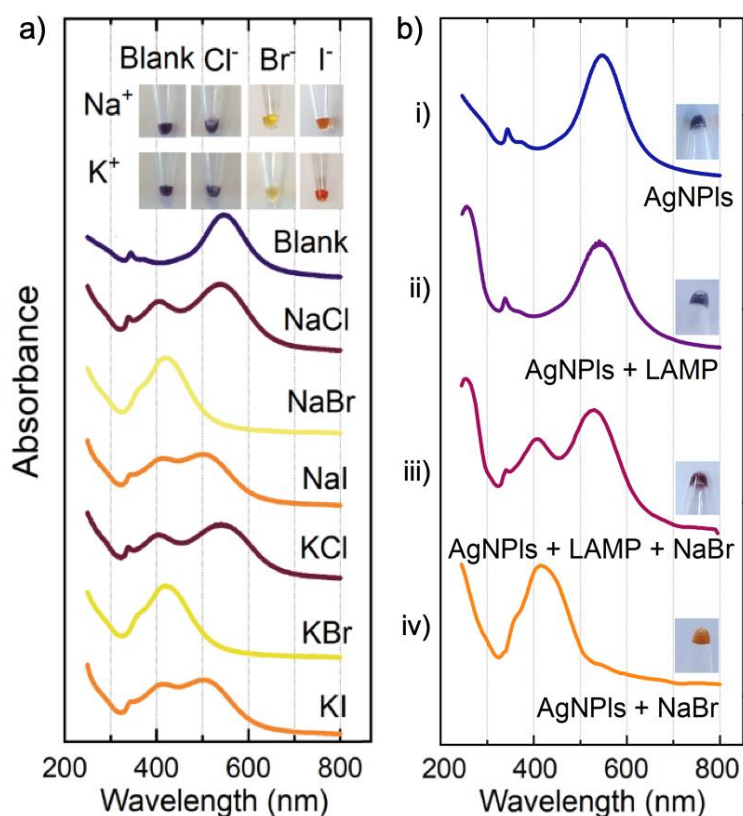


**Figure 2.2** a) AgNPI absorption spectra when incubated with different halide salts. b) The degree of AgNPI etching, and solution colour, changes in the presence of the different reaction components, revealing the protective effect that the LAMP product has against etching, and the promise of this mechanism for nucleic acid detection.

### 2.3.2 Assay development

To validate the LAMP reaction for detection of the *mecA* gene, we designed (Table 2.1) and optimized (Table 2.2) a LAMP primer set. Gel electrophoresis (Figure 2.3) confirmed the synthesis of the LAMP product, with a small amount of product visible even for the single copy/ $\mu\text{L}$  sample. Next, we assessed the effect of pre-incubating AgNPIs with LAMP products. These amplicons are ‘cauliflower-like’ DNA structures with a range of lengths (up to thousands of bases), comprising a mixture of stem-loops with varied stem lengths.<sup>18</sup> TEM analysis confirmed that the AgNPIs were successfully captured by LAMP products (Figure 2.1b), resulting in a greying of the blue solution, which is expected given the closer nanoparticle proximity. Capture of AgNPIs is explained by the affinity of DNA for Ag surfaces, and the fact that a proportion of the LAMP product is single-stranded (the loop segments), exposing free bases to the Ag. Further, as starch-capped AgNPIs are neutral, they do not experience a repulsive force with DNA, in contrast to commonly used citrate-capped Ag nanostructures which are negatively charged at neutral pH.

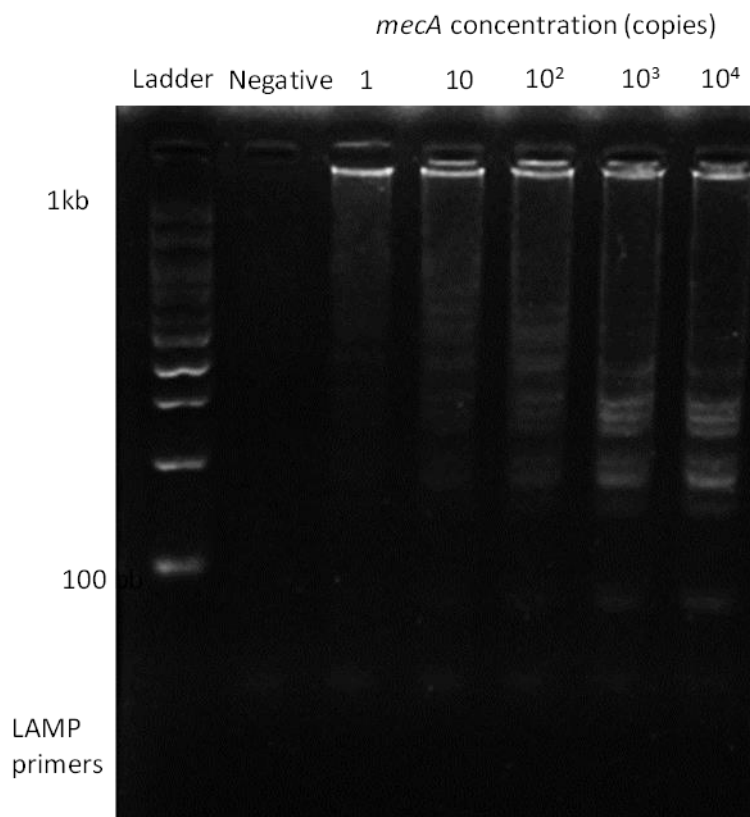


**Figure 2.3** Image of agarose gel electropherogram containing the DNA ladder (100–1000 kb, Promega, Switzerland), negative LAMP, 1, 10, 10<sup>2</sup>, 10<sup>3</sup>, and 10<sup>4</sup> copies of *mecA* template using optimised condition in **Table 2.2** and incubate in electrophoresis bath (Bio-Rad, Switzerland) for 20 minutes. The gel electrophoresis was carried out using 2% agarose gel in 1X TBE buffer, operating under 100 V for 60 minutes, and visualised by Novel juice (Sigma Aldrich) under the 300 nm UV lamp.

We next compared solutions of AgNPs with and without pre-incubation with LAMP product (**Figure 2.2b**). Incubation with LAMP product (30 seconds, followed by addition of NaBr) saw the solution rapidly turn red-purple (**Figure 2.2biii**), with TEM indicating dense nanoparticle aggregates (**Figure 2.1b**). Absorption spectra exhibited a slight blue shift of the in-plane dipole resonance (550 to 520 nm), with the appearance of a 400 nm peak (**Figure 2.2biii**), indicating that some etching occurs, rounding nanoplate vertices and reducing lateral size.<sup>168</sup> In contrast, in the absence of the target *mecA* (i.e. where no LAMP product forms), the solution rapidly turned yellow-orange, indicating significant etching. TEM analysis (**Figure 2.12c**) demonstrated a reduction in nanoplate size ( $36.4 \pm 10.7$  nm diameter) and number, with a significant background population of very small particles. Etching was accompanied by a significant shift of the in-plane dipole resonance peak to 420 nm (**Figure 2.2biv**). We therefore conclude that LAMP product inhibits the etching of the AgNPs by bromide. Interestingly, the AgNPs appear to undergo some morphological changes in the presence of only LAMP product under extended incubation (one hour), without the addition of NaBr (**Figure 2.4a**). Hu et al. suggested that DNA can etch silver nanoparticles in the presence of C/G content.<sup>174</sup> The chosen *mecA* consisting of ~30% of C/G, thus, having potential to etch AgNPs as observed.



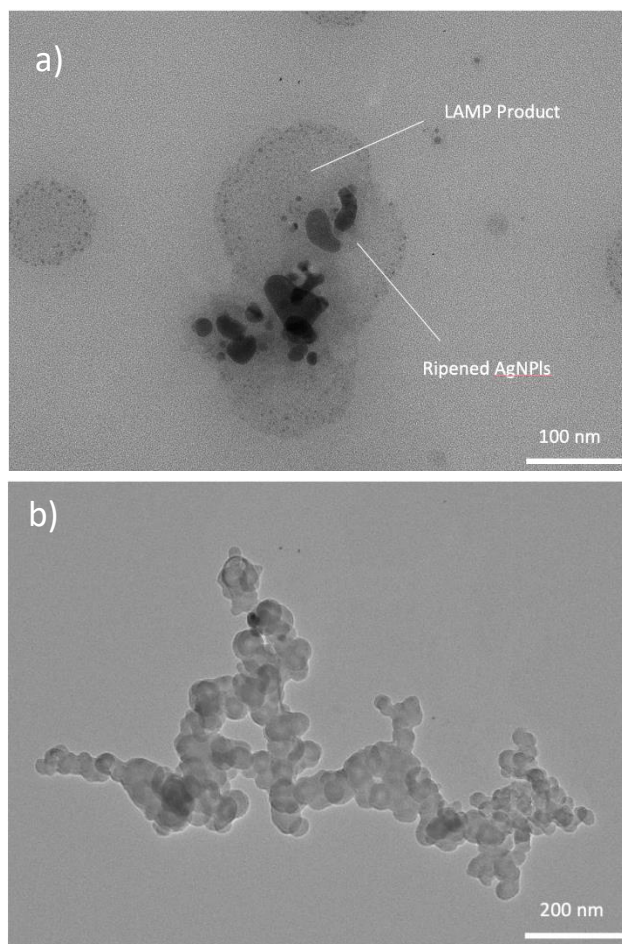


**Figure 2.4** TEM image of a) LAMP product with AgNPLs embedded (1 hour incubation, no NaBr) and b) AgNPLs with PCR product DNA, after addition of NaBr.

Here, we observe well-rounded, asymmetric nanoplates, with a morphology distinctly different from the parent stock. This concurs with previous studies by Hu *et al.*, who observed poly-C DNA-mediated AgNPL etching and Ostwald ripening.<sup>174</sup> Other studies report that low concentrations of bromide may actually stabilize AgNP [100] facets, but with excess bromide still leading to etching.<sup>175</sup> Accordingly, we note that the mechanism of DNA and bromide stabilization versus etching remains an open question worthy of further attention.

We then assessed LAMP product-mediated etching as a quantitative colorimetric readout for *mecA* by studying AgNPL response across a range of LAMP product concentrations (100 to 1200 ng). Absorption spectra (**Figure 2.5a**) indicate nanoplate etching through a gradual blue shift of the in-plane dipole resonance peak and a concurrent increase in the 400 nm plasmon peak, as a function of decreasing LAMP product, which is consistent with our observation that it protects the AgNPLs. The signal at 260 nm originates from the LAMP DNA. The LAMP product concentration series data were quantified by two methods (**Figure 2.5b**). First, by absorbance at 520 nm ( $A_{520}$ ). Second, by photographing samples using a smartphone camera, applying a filter to isolate the red channel, converting the images to greyscale and then extracting the greyscale intensity. **Figure 2.5b** reveals a linear relationship for both approaches ( $R^2=0.984$  for  $A_{520}$  and  $R^2=0.992$  for greyscale).

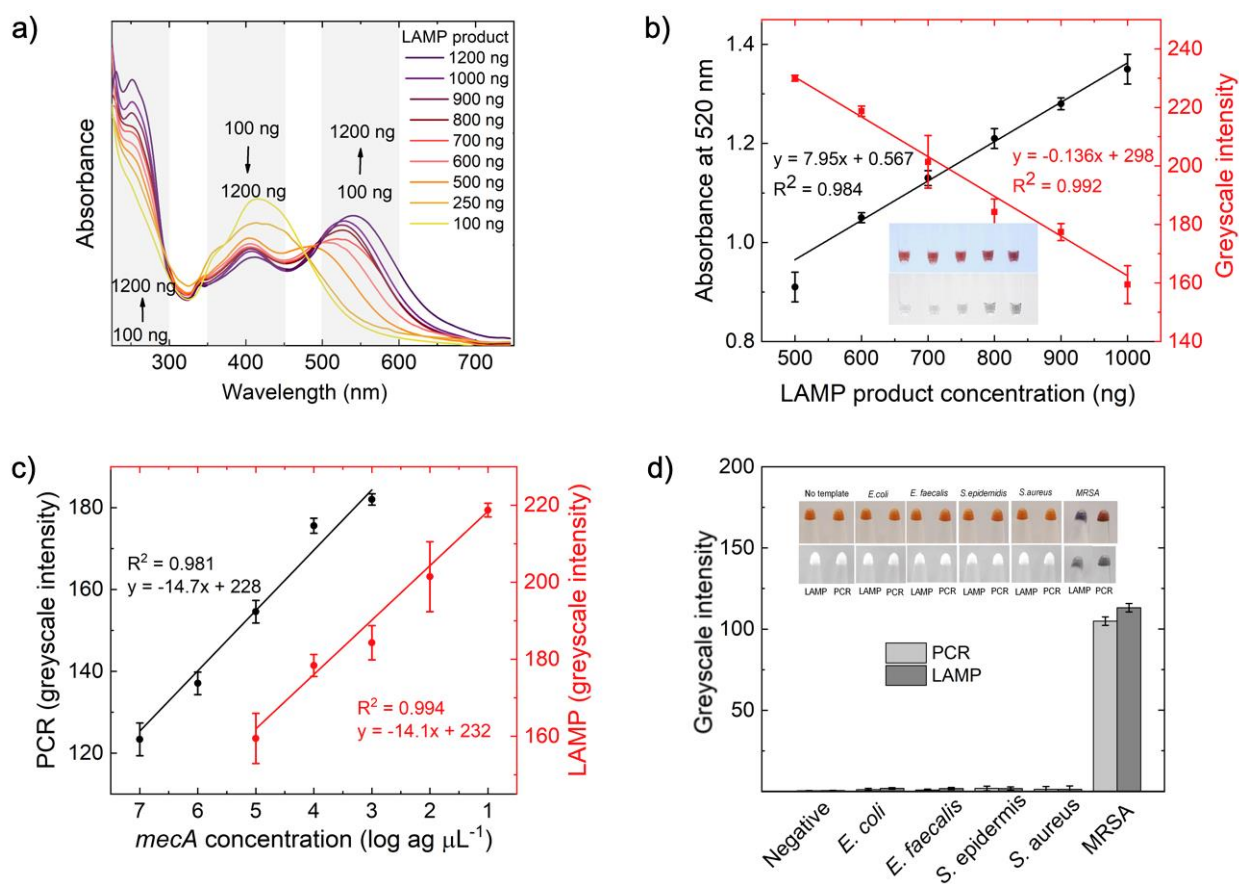


**Figure 2.5** a) Absorption spectra at various LAMP product concentrations, revealing that degree of etching is concentration dependent. b) Calibration curves from absorbance at 520 nm and colorimetric analysis (greyscale intensity). Inset: the corresponding reaction solutions. c) The full assay dose-response curves, comparing PCR and LAMP product performance for the AgNPI assay. d) Specificity for MRSA versus other bacteria, for the PCR and LAMP assays.

Next, to test the full assay concept, a concentration series of *mecA* (10 to  $10^{10}$  ag/ $\mu$ L, or 1 to  $10^9$  copies/ $\mu$ L) and a negative control were amplified by LAMP and assayed using AgNPIs. The process is summarized in **Scheme 2.1**. The data in **Figure 2.5c (red line)** highlight the linear relationship between the greyscale intensity and the log target concentration ( $R^2=0.994$ ) across the entire range. Importantly, the excellent sensitivity of LAMP and the sensitive concentration-dependent AgNPI etching allowed for detection even down to a single copy of the *mecA* target, with an easily readable colorimetric output. We note that, in the initial optimization of the LAMP primers and reaction conditions (**Tables 2.1 and 2.2**), the small amount of reaction product from the single copy sample was not detectable within the real-time PCR machine, but only after multiple stainings of the agarose gel (**Figure 2.3**). This highlights the excellent sensitivity of the AgNPI mechanism described herein, and is a significant result, as it moves ultrasensitive nucleic acid assays away from a reliance on fluorescence for signal transduction, and opens the door for a far simpler readout at the point-of-care, for example using smartphone image analysis,<sup>86, 138</sup> whilst maintaining the ability for highly accurate quantitation when required.



### 2.3.3 Comparison between LAMP and PCR

Next, we investigated whether the AgNPLs could interact with PCR products in a similar manner. Following an identical protocol, a similar colorimetric response was observed but with a limit of detection of  $10^2$  copies ( $10^3$  ag/ $\mu$ L, compared to 10 ag/ $\mu$ L (1 copy), for LAMP) and linearity up to  $10^7$  copies (**Figure 2.5c**). These results indicate that the AgNPLs interact with the PCR product DNA (**Figure 2.4b**), and that this can mediate etching by bromide, but that the structure of the LAMP product favours the protective effect of DNA against etching. For an identical *mecA* target concentration of  $10^3$  ag/ $\mu$ L, PCR yielded 2  $\mu$ g DNA product in 2 hours, whilst LAMP yielded 700 ng product in 30 minutes. Nevertheless, the assay response at  $10^3$  ag/ $\mu$ L is significantly stronger for LAMP than PCR (**Figure 2.5c**). The final assay then achieves a two-orders-of-magnitude better sensitivity with LAMP than with PCR, even with 90 minutes less incubation time (**Figure 2.5c**). We believe that the improved performance of LAMP versus PCR arises due to differences in amplicon structure. LAMP products are hundreds to thousands of bases in length, with a mixture of double-stranded stems and single-stranded loops. In contrast, PCR products are relatively short (685 bases) and double stranded. Accordingly, the lack of unpaired bases in PCR products reduces adsorption to AgNPLs and protection against incoming bromide ions. Conversely, the much larger LAMP products form globule-like structures (**Figures 2.1 and 2.4a**), in which the AgNPLs are embedded, increasing protection.

### 2.3.4 Sample testing and specificity study

Next, we tested the assay directly using lysate from bacterial colonies. Briefly, colonies were collected and lysed in TE buffer at  $95^\circ\text{C}$  for 5 minutes, then 1  $\mu$ L of the lysate was added to the assay working solutions before proceeding with the amplification reaction and readout. For both the LAMP and PCR test, red solutions were observed for MRSA, confirming a positive result for *mecA*. The selectivity for MRSA was assessed against other bacterial genera and human pathogens (*Escherichia coli*, *Enterococcus faecalis*, *Listeria monocytogenes*, and *Staphylococcus epidermidis*, and methicillin-sensitive *S. aureus* (MSSA)). Using PCR and LAMP with subsequent AgNPL incubation (**Figure 2.5d**), yellow solutions were observed for all interferent bacteria (indicating no amplification), confirming excellent selectivity for *mecA*.

Finally, detection accuracy was tested using a concentration series of *mecA* between  $10^3$  and  $10^5$  ag/ $\mu$ L. Three samples were assayed via LAMP and PCR, using the assay test plots (**Figure 2.5c**) as calibration curves. The LAMP reaction slightly overestimates *mecA* concentration (**Figure 2.55**), however the %RSD for  $10^3$ ,  $10^4$  and  $10^5$  ag/ $\mu$ L of target DNA were only 3.6, 4.2, and 5.5%, whilst the %recovery at each concentration was 109, 109, and 114%, respectively. Compared to PCR, a paired t-test indicates no significant difference between the results ( $t_{\text{calculated}}=0.003$  and  $t_{\text{critical}}=2.14$ ).

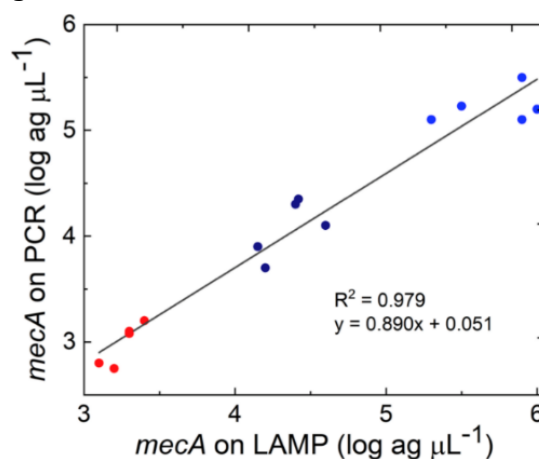


**Figure 2.6** Accuracy test comparing the LAMP and PCR assays using known concentration ( $10^3$ ,  $10^4$ , and  $10^5$  ag/ $\mu$ L) of *mecA* gene.

### 2.3.5 Paper-based device integration

Having established the utility of the combined LAMP and AgNPI assay for sensitive detection of MRSA in a tube assay, we next sought to transfer this mechanism onto a PAD to produce a PoC-viable diagnostic concept. The LAMP reaction herein uses six primers (Table 2.1). We immobilized one of the loop-forming primers, and therefore the resultant LAMP product, onto the paper surface. Immobilization of the primer was performed by binding streptavidin on cellulose *via* EDC/NHS coupling, followed by addition of the biotin-modified primer. To evaluate the effect of primer immobilization and confinement of the reaction, a direct comparison was made between the immobilized and non-immobilized cases (Figure 2.7a).

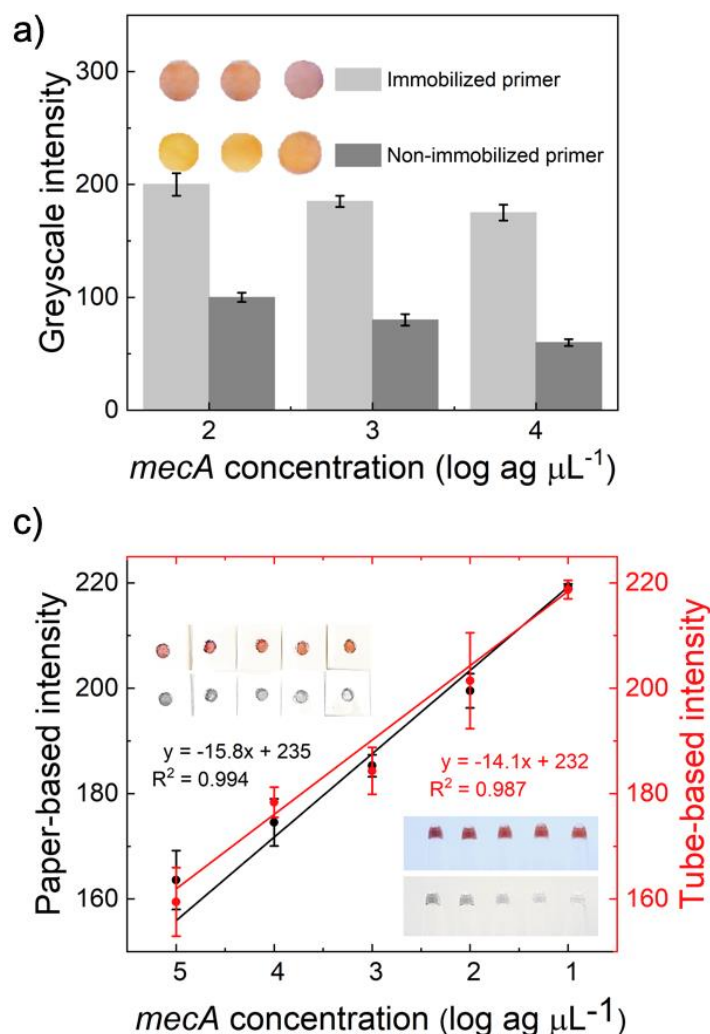


**Figure 2.7** a) Comparing the effect of immobilization versus non-immobilization of the LAMP primer on the cellulose surface, revealing an enhanced signal in the immobilized case. b) Direct comparison of the dose-response for the paper-based and tube-based formats, revealing no significant difference in performance.

It was found that by immobilizing the FIP primer (see varied immobilized primer study in the Supporting Information, and Figure 2.8), the AgNPIs were less etched (i.e. redder), compared to the free primers (orange-yellow in colour). The two-fold increase in acquired signal suggests that the concentration of LAMP product in the surface layer was higher in the immobilized case, leading to a greater sensitivity.

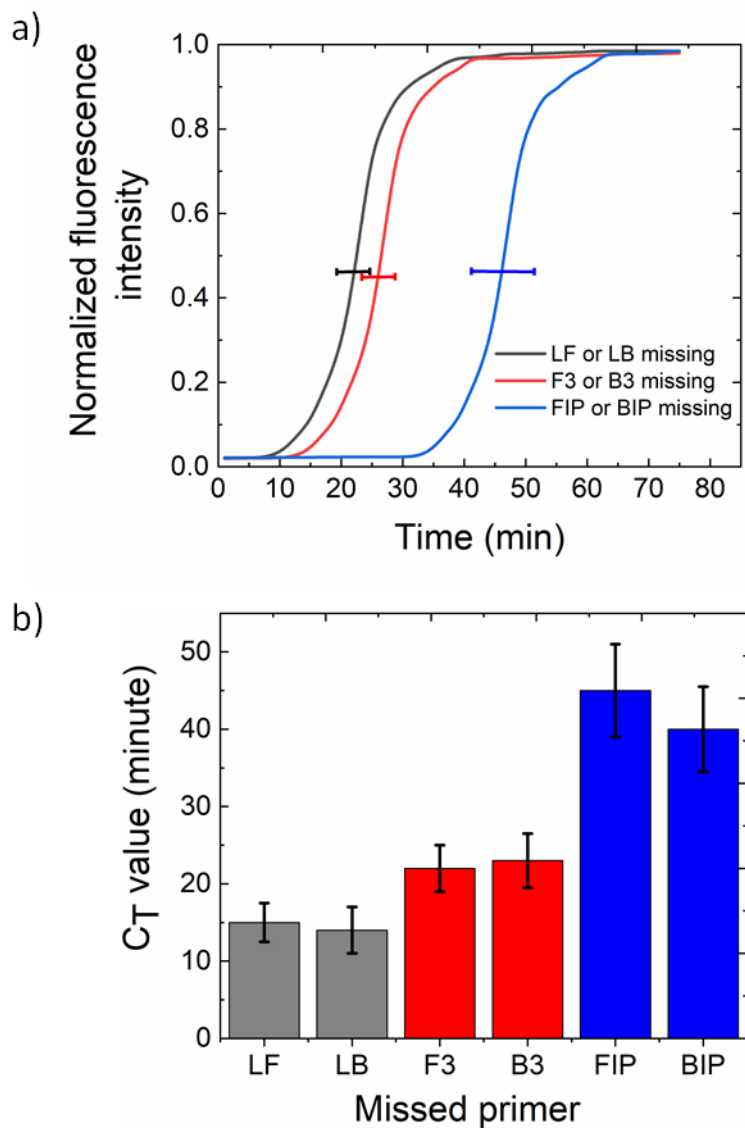


**Figure 2.8** a) Fluorescence response of DNA amplification of LAMP system by missing inner (FIP and BIP), outer (F3 and B3) and additional (LF and LB) primers b) CT value corresponding to the missing results in a).

Next, we developed a PAD to run the assay, as illustrated in **Figure 2.9**. It comprises five layers. Layers 1 and 5 are adhesive tape, used to prevent water evaporation, while layers 2 and 4 are punched-hole double-sided tape used to space the adhesive tape and the reaction solution. The layer 3 is a wax-patterned cellulose paper strip with FIP primers immobilized in each reaction well. This approach represents a simple and cost-effective solution to perform a sophisticated amplification reaction on paper.

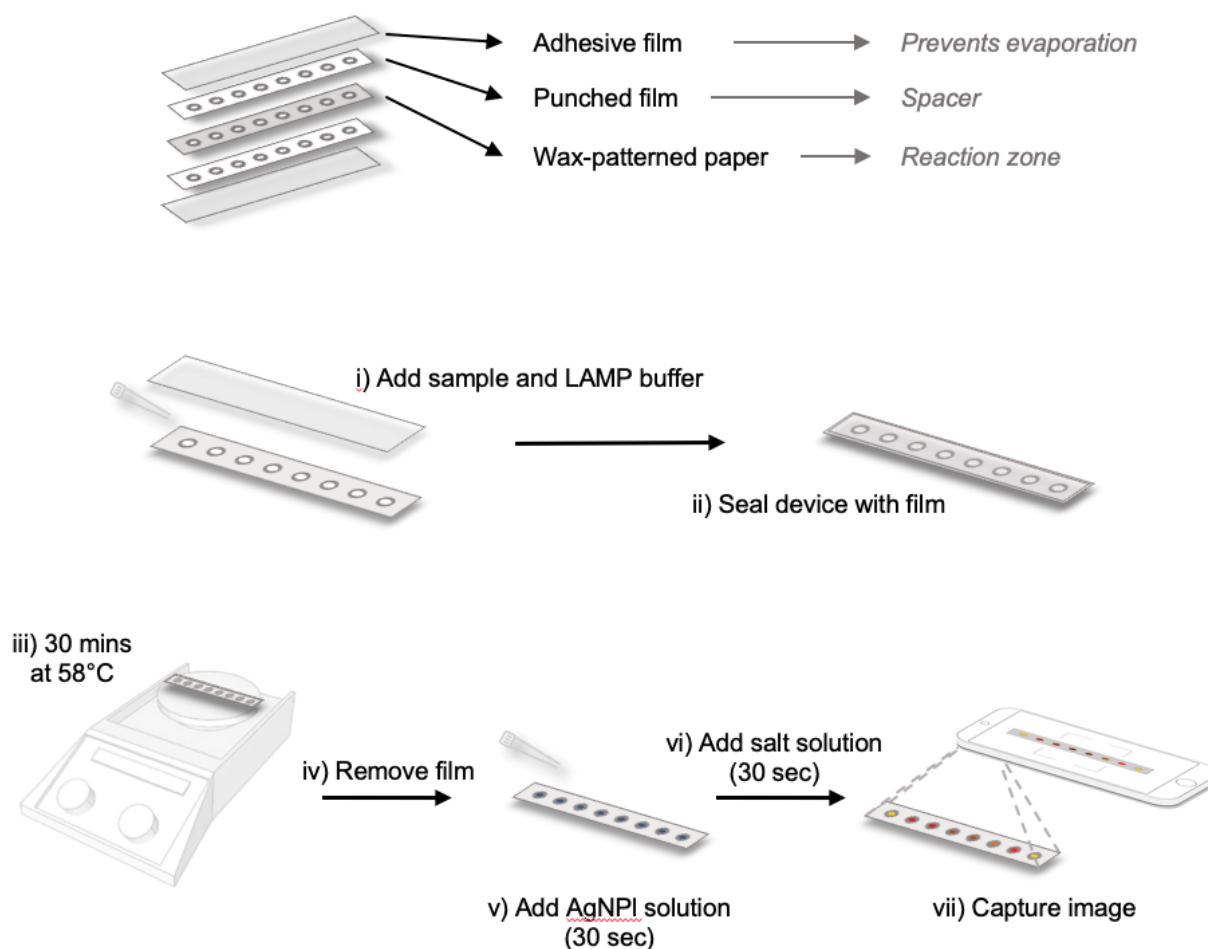


**Figure 2.9** The PAD device components and test process. After adding the sample and LAMP buffer to the device it is sealed and heated to 58°C for 30 minutes. A 30 second incubation with added AgNPIs, then NaBr, reveals the test result which can then be read by the naked eye (qualitative), or captured by a camera for image analysis (quantitative).

The paper-based test, illustrated in **Figure 2.9**, is conducted as follows: First, the LAMP primer solution (minus the FIP) is deposited on the paper, followed by a solution containing the target DNA, LAMP buffer and the polymerase. The whole device is heated to 58°C (on a hot plate, or in an oven) for 30 minutes, then the LAMP reaction proceeds *in situ* in the device. Next, AgNPIs are added (30 second incubation), followed by a NaBr solution to develop the colour (<30 seconds). For a positive result, the reaction chamber becomes red. For a negative result, it becomes yellow. Finally, the PAD is photographed (in our case, using a smartphone), the red channel isolated and converted to greyscale, and the greyscale intensity used to quantify the LAMP product.

Quantitative analysis of both tube- and paper-based tests was performed using a concentration series of *mecA* (10 to 10<sup>10</sup> ag/μL, 1 to 10<sup>9</sup> copies) to ascertain whether immobilization primer/product and the AgNPI reaction had any deleterious effect. **Figure 2.7b** shows a linear relationship from 10–10<sup>5</sup> ag/μL ( $R^2_{\text{tube}}=0.987$ ,  $R^2_{\text{PAD}}=0.994$ ). Due to the excellent sensitivity of the LAMP reaction and the concentration dependent etching of the AgNPIs, we could obtain

single-copy detection of the *mecA* gene with a colorimetric output. Further, given the comparable data for the tube- versus paper-based approach, there appears to be no detrimental effect of immobilizing the primer/product and AgNPI reaction on the paper.

As before, selectivity for MRSA was tested against other regularly found bacteria (Figure 2.10a) using sample lysates. Yellow (i.e. etched AgNPIs) was observed for all of the interferent bacteria, suggesting no amplification product. Red was observed for MRSA, demonstrating that the excellent selectivity the *mecA* gene was preserved in the paper-based test format. An accuracy test was performed by comparing LAMP for both tube- and paper-based systems directly with PCR, using the AgNPIs colorimetric readout. A concentration series of *mecA* ( $10^3$ ,  $10^4$ , and  $10^5$  ag/ $\mu$ L) was analysed using the tube- and paper-based LAMP, and tube-based PCR reactions (Figure 2.10b). The results exhibited excellent agreement, ( $R^2_{\text{tube}}=0.958$ ,  $R^2_{\text{PAD}}=0.956$ ) with no significant difference by a paired t-test ( $t_{\text{cal-tube}}=0.003$  and  $t_{\text{cal-PAD}}=0.028 < t_{\text{critical}}=2.14$ ).

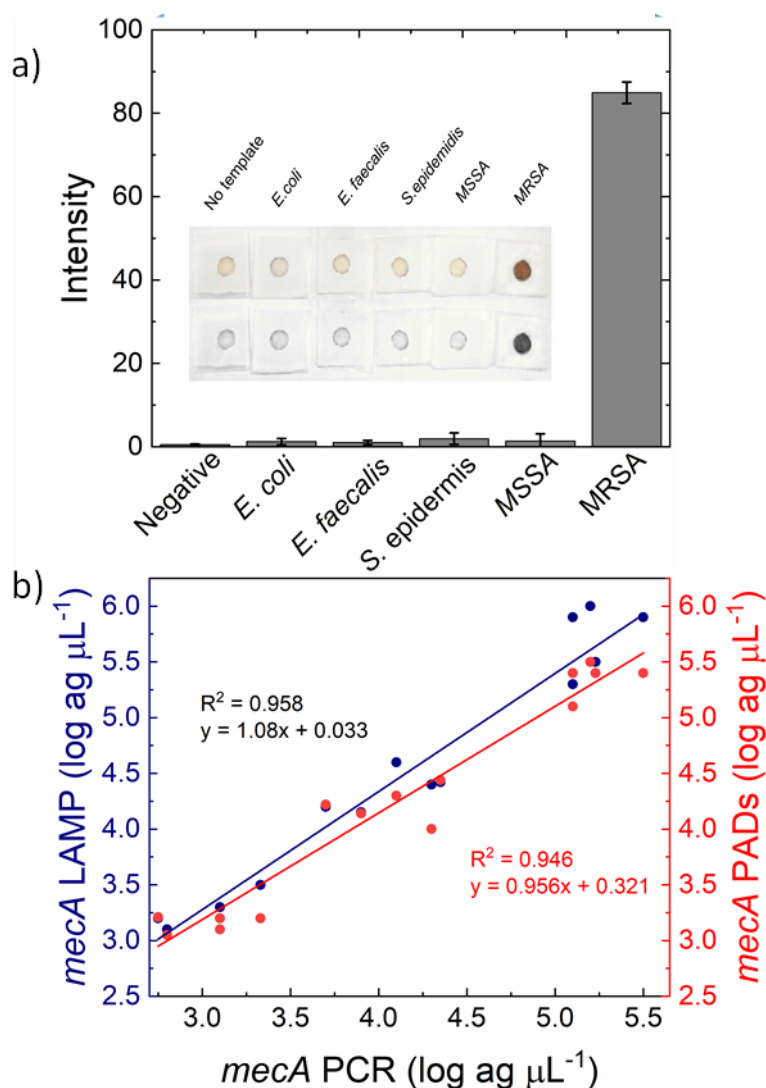


**Figure 2.10** a) Specificity test for MRSA versus other bacteria for the paper-based test, revealing excellent specificity. Inset: Raw (upper) and processed images (lower) of the devices. b) Accuracy test for the tube (left axis) and paper-based (right axis) assay formats, revealing excellent correlation with the PCR (bottom axis).

Finally, PAD stability over 28 days was studied using the same concentration series as the accuracy tests (Figure 2.11). A set of the PADs was stored (4 °C, N<sub>2</sub>), and fresh ones used each time. Setting the first tests at 100% efficiency, the final efficiency after 28 days was ca. 95%, based on the signal intensity, showing potential for longer term storage and use. We hypothesise that the slight degradation in performance was attributable to degradation of the DNA, which could be alleviated with better packaging in a dry environment.

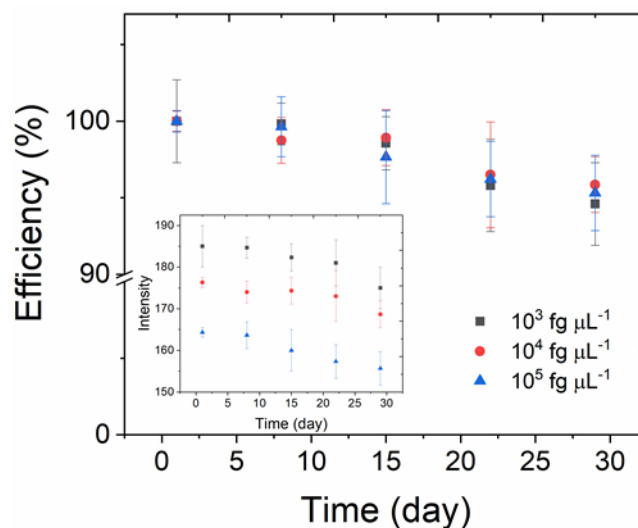


**Figure 2.11** Stability test of the paper-based device over one month using three concentrations of *mecA* (N=3).

## 2.4 Conclusions

We demonstrate an ultrasensitive and rapid assay and PAD using the interaction between AgNPLs and the globulus LAMP product, for the first time, allowing target-modulated particle etching. Using MRSA as a model target, we demonstrate detection via its *mecA* gene, achieving colorimetric detection even down to the single copy/μL level in just 30 minutes. The interaction of the cauliflower-like LAMP products with AgNPLs enhances signal three-fold versus PCR, which facilitates the extreme sensitivity of our approach. The developed sensing mechanism harnesses the unique nanoscale properties of AgNPLs, yielding qualitative analysis by visual inspection and quantitative analysis through the use of a smartphone camera. Specific advantages include high contrast, a wide colorimetric range, a direct proportionality between the degree of etching and the concentration of DNA and high sensitivity, as AgNPLs can be used at much lower concentrations than colorimetric dyes. This assay concept was used as the basis for the development of a paper-based test, where target amplification (by LAMP) and signal transduction (by AgNPLs) is performed *in situ* on paper, with a total reaction time of *ca.* 30 minutes. Immobilization of the FIP primer confines reaction products to the paper surface and yields a two-fold higher sensitivity when compared to the solution-based reaction. The PAD retained the excellent sensitivity and specificity of the tube-based assay, and high accuracy was observed by comparison with the tube-based LAMP and PCR methods.

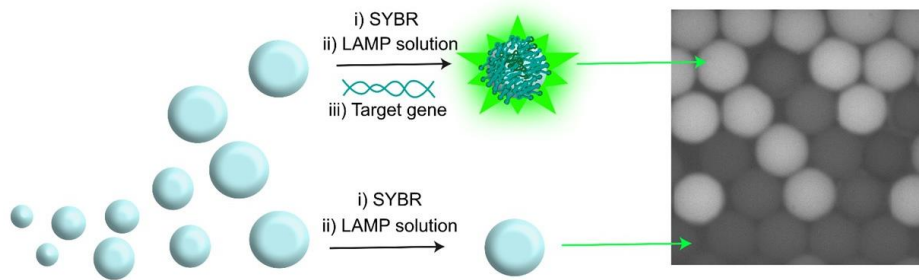
Regarding the use of the developed PAD in a PoC setting, there is a requirement for a degree of liquid handling (sample preparation, master mix and sample mixing, addition to PAD, addition of salt and AgNPIs solutions), and a heating step (to 58°C during incubation). Although these steps are relatively easy to execute, they would preclude use by a completely untrained user. Nevertheless, we feel that the platform as developed could be used in a low resource setting by a trained user, and with appropriate and realistic development (e.g. simplified sample preparation,<sup>125, 176</sup> or immobilization of further assay components on paper<sup>115</sup>), it could become and widely deployable PoC device. Further, having demonstrated that our simple but effective colorimetric sensing using AgNPI etching with PCR and LAMP, we feel that the same approach could be adapted to other nucleic acid amplification approaches, and could therefore achieve widespread uptake and impact in the field of paper-based nucleic acid diagnostics.

This novel device shows promise for the simple and rapid detection of infectious pathogens in a field setting. Rapid adaptation of our approach would allow targeting of a large range of infectious diseases (by redesigning the LAMP primers), and should facilitate sensitive colorimetric detection when used with other nucleic acid amplification methods.



# Chapter 3

## Hydrogel Digital LAMP Development for Highly Sensitive Drug-Resistance Bacteria Detection



The digital droplet method for nucleic acid quantification is one of the most impactful applications of microfluidics in the life sciences. However, the necessity for relatively complex microfluidic systems to handle these assays hinders translation towards simpler in vitro diagnostic based on this approach, for example for resource-limited settings or near point-of-care testing. Herein, we report a new digital droplet approach to diagnostics, combining hydrogel droplets with loop-mediated isothermal amplification (HD-LAMP) for the detection of Methicillin-resistant *Staphylococcus aureus* (MRSA), a common pathogen that poses a formidable risk with persistently high morbidity and mortality. Acrylamide-hydrogel beads were employed as templates for particle-templated emulsification, where LAMP reagents and primers diffused into the porous cross-linked polymer structure, before being encapsulated in an oil phase via simple shaking. Within 30 minutes, the HD-LAMP procedure is able to detect the target *mecA* gene, with a concentration limit of detection of 1 fg/ $\mu\text{L}$  (1000 copies/ $\mu\text{L}$ ), and a linear range from  $10^{-1}$  to  $10^2$  copies/ $\mu\text{L}$  ( $R^2 = 0.997$ ). The method displays excellent selectivity against common bacteria, with no significant difference versus the gold-standard approach, polymerase chain reaction (PCR) ( $t\text{-value} = 0.70$ ,  $< t\text{-critical} = 1.85$ ). Further, the hydrogel beads can be stored for months with no significant change of properties. Along with its excellent analytical performance, this HD-LAMP assay could benefit the field-deployability of droplet digital diagnostics.

This chapter is adapted from a manuscript entitled "*Hydrogel Digital LAMP Development for Highly Sensitive Drug-Resistance Bacteria Detection*", authored by Akkapol Suea-Ngam, Zahra A. Halvorsen, Vincent Revol, Stavros Stavrakis, Philip D. Howes and Andrew J. deMello. *In preparation*.

**Note:** This project was conducted by Akkapol Suea-Ngam (ASN) and Zahra Halvorsen (ZH), with an equal contribution from both. ASN designed and developed the LAMP part and provided all biological resources for the project, including gene analysis, LAMP primer design, LAMP system design, LAMP optimisation in bulk, LAMP data analysis, analytical method design and development, bacterial sample preparation, polymerase chain reaction design and data investigation, and original draft preparation. ZH designed and prepared the microfluidic device for hydrogel bead fabrication, including microfluidic device optimisation, micromixer optimisation, micromixer simulation, hydrogel optimisation and preparation, LAMP and hydrogel bead investigation in bulk and microfluidic platforms, LAMP solution to microfluidic device protocol optimisation, fluorometry setup, data analysis, and original draft preparation.



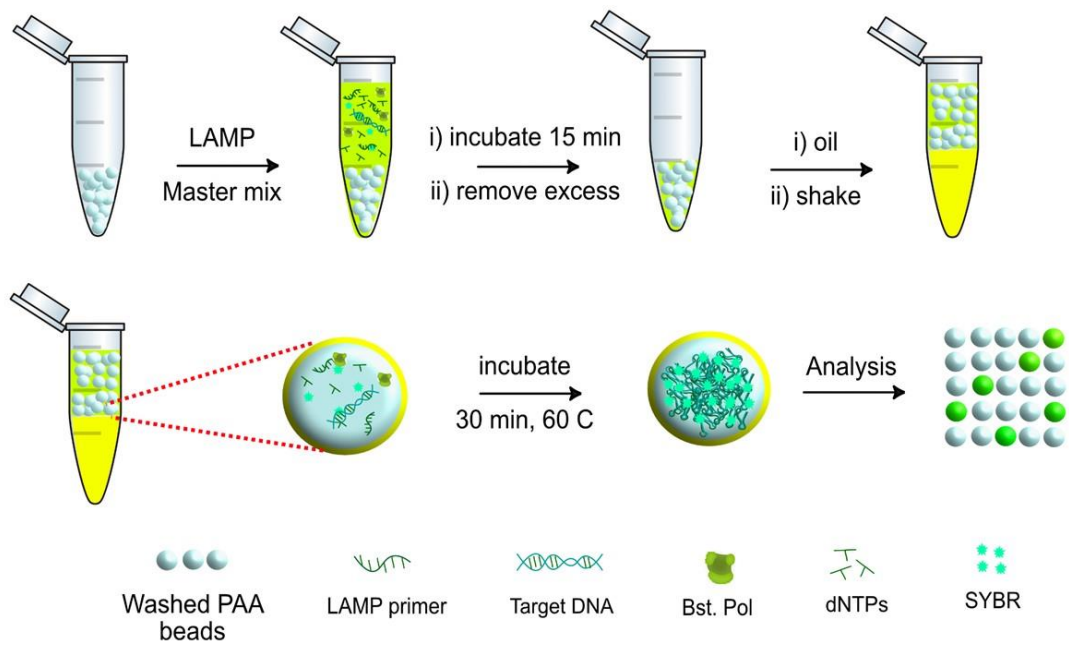
### 3.1 Introduction

The transfer of nucleic acid amplification tests (NAATs) away from specialized labs and towards the point-of-care or field settings is an ongoing challenge. To date, however there have been various promising examples of diagnostic devices that exhibit excellent analytical performance (i.e. sensitivity, accuracy, precision).<sup>177-179</sup> For NAATs, the digital quantification approach is highly attractive, as it allows for sensitive analysis without requiring a standard curve.<sup>180-182</sup> However, traditional digital droplet PCR (ddPCR) schemes possess some distinct disadvantages which limit suitability for integration into 'simpler' in vitro diagnostics devices and protocols. Notable amongst these are the fact that droplets cannot withstand shear forces and are unstable under changing temperatures. Moreover, it is difficult to generate and store droplets for later use, with complex microfluidic components often being needed.<sup>183-186</sup>

In recent years, hydrogel droplets have been applied in several biological applications, including cell culture, diagnostics and nucleic acid sequencing.<sup>187-189</sup> They have also been applied in NAATs as a ddPCR platform, where the microfluidically-generated hydrogels were used to increase robustness. However, this approach uses the same general method as standard ddPCR to generate droplet templates, which is complicated and involved. Recently, Abate and co-workers reported a microfluidic-free digital droplet platform using hydrogel droplets to perform ddPCR and cell culture.<sup>190</sup> By generating hydrogel beads and removing excess solution, DNA templates and cells can diffuse into the hydrogel structure, before being encapsulated within the an oil phase. For NAATs, the limit of template DNA detection achieved was  $10^2$  copies/ $\mu\text{L}$ . This formidable polymerase chain reaction approach required at least two hours to detect yeast and Lamda virus using TaqMan probe and thermocycler, which seemingly limits transition to field deployability.

Antimicrobial resistance (AMR) in bacterial infections kills more than seven hundred thousand people per year; a number predicted to rise to ten million by 2050.<sup>191</sup> Thus, rapid, simple, and effective detection, in particular in hospitals and health centers, is necessary.<sup>192</sup> The World Health Organization has emphasized the importance of controlling infections on the front line through the provision of appropriate in vitro diagnostics (IVD) for rapid AMR detection.<sup>193</sup> Motivated by this importance, we targeted the detection of methicillin-resistant *Staphylococcus aureus* (MRSA), the most prevalent AMR pathogen.<sup>194</sup> Cell culture is the gold-standard method to detect AMR.<sup>195-196</sup> However, this requires multiple days to obtain results, with cross-contamination of different bacteria frequently being observed.<sup>197</sup> In contrast, targeting the genetic material of pathogens in clinical samples using NAATs allows for quick and versatile IVDs that can be readily adapted to new targets.<sup>101, 198-200</sup>

In this paper, we report a template-type droplet hydrogel system for NAAT of MRSA using loop-mediated isothermal amplification (LAMP), an isothermal NAAT that is commonly used in point-of-care diagnostics, as shown in **Scheme 3.1**. Although LAMP has been developed in a number of a digital droplet platforms (ddLAMP), it has not yet been applied within hydrogel for digital droplet detection. The hydrogel droplets used in this work were generated via step-emulsification, resulting in millions of monodispersed hydrogels within ten minutes.<sup>201-203</sup> The *mecA* gene is amplified in a water-in-oil platform, down to 1000 copies/ $\mu\text{L}$  within 30 minutes. Further, the developed system was shown to be highly selective for MRSA against MSSA and other common bacteria. This ddLAMP platform proved to be sensitive and robust, without the need for complex microfluidic components and processing steps, enabling digital quantification in a field-deployable format.



**Scheme 3.1** Schematic illustrates HD-LAMP protocol using droplet hydrogel platform that absorbs LAMP master mix and target gene for MRSA analysis.

## 3.2 Materials and methods

### 3.2.1 Chemicals

All chemicals were analytical grade and used as received. Acrylamide, N,N'-methylenebis(acrylamide), ammonium persulfate, trichloro-(1H,1H,2H,2H-perfluorooctyl) silane, Triton-X100, perfluoro-1-octanol, NaCl, Ethylenediaminetetraacetic acid (EDTA), KCl, Tris-buffer (pH 8.0), tetramethylethylenediamine, Novel juice dye and SYBR Green I (10,000X) were purchased from Sigma Aldrich (Buchs, Switzerland). PFPE-PEG surfactant (008-Fluorosurfactant) was purchased from Ran Biotechnologies (Beverly, USA) and used with Novec HFE-7500 fluorinated oil (St. Paul, USA). All aqueous-based solutions except LAMP solution were prepared using ultrapure water from a Millipore Synergy water purification system 18  $\Omega$  (Darmstadt, Germany).

### 3.2.2 Biological samples and reagents

For LAMP, the *mecA* gene—located in the SCCmec region found in all MRSA strains—was chosen as the target. LAMP and PCR primers were designed based on a 685 bp *mecA* gene sequence, obtained from the NCBI database and analyzed using the program MEGA 7.0.26. The *mecA* sequence used in this work was amplified from the MRSA Newman strain using PCR primers, as shown in **Table 2.2**. The PCR products were quantified using a Nanodrop 2000 (Thermo Fisher Scientific, Reinach, Switzerland).

The LAMP reaction was performed following the standard methodology (**Table 2.2**), which required 0.8  $\mu$ M of the two outer primers (F3 and B3) for strand displacement during the non-cyclic step, and 1.6  $\mu$ M of the inner primers (FIB and BIP) for both the sense and the antisense sequence, which helps in loop formation. Further, two additional primers (LF and LB) were added (to 1.6  $\mu$ M) to accelerate the reaction, thus reducing the required incubation time. All LAMP solutions were prepared using DNase and RNase free water (Thermo Fisher Scientific, Reinach, Switzerland). Optimal concentrations of Bst polymerase, MgSO<sub>4</sub>, betaine, and dNTPs were found to be 100 U/mL (5 units per reaction), 10 mM, 1 M, and 1 mM, respectively. To obtain quantitative results from the tube-based LAMP reaction (at 58 °C), CT values (time at which the amplification curve reaches one-third of its maximum value), were plotted against the obtained signal to acquire the calibration curve, using a QuantStudio™ 5 Real-Time PCR System (Thermo Fisher Scientific, Reinach, Switzerland). The PCR reaction was carried out as follows: 12.5  $\mu$ L Go Taq® Hot Start Green Master Mix, 2.5  $\mu$ L of both the LF and LB primers, 1  $\mu$ L of MRSA lysate, and 6.5  $\mu$ L RNase/DNase free water. The amplification process was initiated by heating at 95 °C for 2 minutes, followed by 30 cycles of denaturation at 95 °C for 30 seconds, annealing at 55 °C for 30 seconds, and extension at 72 °C for 1 minute. The final extension was applied at 72 °C for 5 minutes before storing at 4 °C.

### 3.2.3 Microfluidic device design and fabrication

Conventional photolithography was used to create structures with micrometer-scale dimensions. Briefly, microchannel patterns were designed using AutoCAD 2017 (Autodesk, San Rafael, CA, USA) and printed onto a 177  $\mu$ m thick fine grain emulsion film (Micro Lithography Services Ltd., Chelmsford, UK) to form a photomask. This photomask was then used to pattern an SU-8 coated silicon wafer (Microchem Corporation, Westborough, MA, USA). The mold was developed in poly(ethylene glycol) methacrylate (Sigma, Buchs, Switzerland) for 15 minutes, then cleaned in isopropanol for a further 5 minutes. A degassed 10:1 mixture of polydimethylsiloxane (PDMS) monomer and curing agent (Sylgard 184, Dow Corning, Midland, MI, USA) was poured over the master mold and peeled off after polymerization at 70 °C for 4 hours. Inlet and outlet ports were created using a hole-puncher (Technical Innovations, West Palm Beach, FL, USA). Afterwards, the

structured PDMS substrate was bonded to a glass 1 mm thick substrate (Menzel-Glaser, Monheim am Rhein, Germany) after treating both surfaces in an oxygen plasma (EMITECH K1000X, Quorum Technologies, UK) for 60 seconds. The channels were treated with an HFE 7500-based solution containing 1% (v/v) trichloro-(1H,1H,2H,2H-perfluorooctyl) silane to generate hydrophobic walls, for 10 minutes, then rinsed with 100  $\mu$ L of the HFE 7500 oil.

### 3.2.4 Polyacrylamide microgel preparation

The acrylamide precursor solution was prepared according to a literature protocol.<sup>187</sup> Briefly, a solution containing 7% acrylamide, 0.2% N,N'-methylenebis(acrylamide) and 0.3% ammonium persulfate was prepared, then mixed via a static micromixer and used as an inner (aqueous) phase. The HFE-7500 oil containing 2% (w/w) PFPE-PEG surfactant and supplemented with 1% TEMED was used as an outer (oil) phase. Further, low-pressure dosing modules (neMESYS, Cetoni GmbH, Korbussen, Germany) were used to feed solutions from 1 mL gastight syringes (Hamilton Bonaduz AG, Bonaduz, Switzerland). Tygon tubing (dimensions 0.33 mm I.D., 0.6 mm O.D., Cole Palmer, Hanwell, UK) was used to connect syringes to the inlets of the microfluidic device. Droplets of ca. 50  $\mu$ m diameter were generated using the system to generate monodispersed polyacrylamide beads. During the entire production process, droplets were constantly monitored via bright-field microscopy, then collected in a glass reservoir and incubated on a heat block at 65 °C for 12 hours to polymerize. Excess oil from the bottom of the emulsion reservoir was extracted and replaced with an equal volume of perfluoro-1-octanol to dissolve the surfactant layer. Afterward, the monodispersed polyacrylamide (PAA) microgels were washed several times with washing buffer (as described in by Abete et al.), and finally redispersed in 0.5% Triton-X100 in DNase/RNase free water (Invitrogen, California, USA). PAA hydrogels were stored for at 4 °C until use.

### 3.2.5 MRSA assay procedure

A 30  $\mu$ L solution containing pelleted PAA particles was mixed with 30  $\mu$ L of LAMP master mix (making a total volume of 60  $\mu$ L), then incubated at room temperature for 15 minutes to allow the LAMP reagents to diffuse into the PAA beads. Then, excess solution was carefully removed. To compartmentalize the LAMP-primed PAA beads in oil, 100  $\mu$ L of HFE-7500 oil containing 5% (w/w) PFPE-PEG surfactant was added, and the whole mixture vortexed. The PAA hydrogels were then incubated at 60 °C for 30–60 min (and monitored in a real time-PCR machine when required), then 20  $\mu$ L of the solution was pipetted onto a glass slide in order to obtain a monolayer of well-ordered beads. An inverted Eclipse Ti-E microscope (Nikon, Zürich, Switzerland) equipped with an IDT high-speed camera (Motion Pro Y5.1, Niederoenz, Switzerland) and an ORCA-flash 4.0 CMOS camera (Hamamatsu, Solothurn, Switzerland) was used to image bead fluorescence, with images being analysed using ImageJ (U.S. National Institutes of Health, Bethesda, MD, USA) to quantify the *mecA* target. Bright-field imaging of the PAA hydrogels was performed using the high-speed camera, plasma light source illumination (HPLS200 series Thorlabs, Newton, NJ, USA), and a 20x 0.45 NA S Plan Fluor objective (Nikon, Switzerland). For the visualization of PAA particles, fluorescence imaging was performed using two different objective lenses, namely a 20x 0.45 NA, and Plano N 10x NA 0.25 objective (Olympus, Tokyo, Japan). Images were processed using ImageJ software.

### 3.2.6 Selectivity study

MRSA (*Staphylococcus aureus* USA300 JE2; source: Annelies Zinkernagel, Division of Infectious Diseases and Hospital Epidemiology, University Hospital Zurich, University of Zurich, Zurich, Switzerland; properties: methicillin-resistant *S. aureus*), *E. coli* (*Escherichia coli* JM109; source: Stratagene, San Diego, CA, USA; properties: *E. coli* lab strain, non-pathogenic), *E. faecalis* (*Enterococcus faecalis* ATCC 19433; source: ATCC 19433; properties: type strain), *L. monocytogenes* (*Listeria monocytogenes* Scott A; source: Weihenstephan *Listeria* Collection; properties: clinical isolate, serovar 4b), *S. epidermidis* (*Staphylococcus epidermidis* MP04; source: Max Paape, ARS, USDA, Beltsville, MD, USA; properties: bovine mastitis isolate) and methicillin-sensitive *S. aureus* (MSSA) (*Staphylococcus aureus* Newman; source: NCTC 8178, Annelies Zinkernagel, Division of Infectious Diseases and Hospital Epidemiology, University Hospital Zurich, University of Zurich, Zurich, Switzerland) were obtained from Institute of Food, Nutrition and Health, ETH Zurich, Switzerland. Bacterial colonies were collected and lysed in TE buffer (Fischer Scientific, Reinach, Switzerland) at 95 °C for 5 minutes. Then 1 µL of the lysate was added to the hydrogel with the LAMP master mix, before proceeding with the amplification reaction and readout.

## 3.3 Results and Discussion

### 3.3.1 PAA hydrogel characterization

To test the system, water-in-oil droplets (Milli-Q water in HFE-7500 with 5% surfactant) were generated via step emulsification. This technique is easy to handle compared to single nozzle droplet generators, such as T-junction and flow focusing systems.<sup>204-205</sup> This is because, during the initial stages of droplet formation, the onset of the Rayleigh-Plateau instability is purely controlled by the device geometry (nozzle height), allowing the Laplace pressure gradient to drive fluid flow into the growing drop. Accordingly, the droplet size does not depend on the flow rate, but on the Laplace pressure, which can be modulated by the nozzle height, resulting in exceptional monodispersity in the final droplet population. In the current studies, the height of the nozzle was 20 µm, with a channel height of 200 µm. To perform high-throughput droplet generation through a radial nozzle array (**Figure 3.1a**), oil was flowed into the main channel at a flow rate of 80 µL/min, with the aqueous solution at 60 µL/min. By injecting 600 µL of the aqueous solution, approximately  $3 \times 10^6$  droplets were generated in 10 minutes with an average diameter of  $75 \pm 5$  µm.

The obtained PAA beads are hydrogels, comprising >95% water. These are excellent hosts for compartmentalizing biochemical reactions.<sup>206</sup> PAA hydrogels demonstrate exceptional stability compared to standard droplets, which tend to rupture or coalesce under either mechanical shear or thermal instability. In our synthesis of PAA hydrogel beads, the monomers and initiators were prepared in separate glass syringes to avoid polymerization of the PAA and clogging of the syringes. After injection into the step emulsification device to generate pre-polymer droplets, the solution was incubated at 60 °C on a hot plate. Due to the low Reynolds number environment within the microfluidic channels, it is challenging to mix the monomer and initiator rapidly.<sup>207</sup> Therefore, use of a dedicated micromixer is highly beneficial, as it provides not only excellent mixing but also allows efficient heat transfer, preventing polymerization in the micromixer.

To prepare the PAA beads using our step-emulsification strategy, the aqueous phase containing the acrylamide monomer (7% w/v) and *N,N'*-methylenebis(acrylamide) (at 0.2% w/v) was injected into the first inlet. Ammonium persulfate (at 0.30% w/v) with Tris buffer (10 mM) was injected into the second inlet. A flow rate of 30 µL/min was applied to both inlets. The monomer and initiator solutions were mixed rapidly and efficiently using the specific geometries of the micromixers. The design of the micromixer was inspired by work by Wang and co-workers, where

the asymmetric shape accelerates mixing in low Capillary ( $Ca$ ) and Reynold ( $Re$ ) number environments.<sup>208-209</sup> The design is based on a “tesla” micromixer (Figure 3.1b), where the mixing interface is doubled in one mixing unit iteration, by a ‘splitting’ and ‘recombination’ process. After each mixing unit, the direction of flow is changed, and efficient mixing should be possible. To test this hypothesis, we performed both experiments and COMSOL simulations, as illustrated in Figure 3.1b. Briefly, a mixing index of 95% at a volumetric flow rate of 5–50  $\mu\text{L}/\text{min}$  was predicted. The performance of the fabricated micromixer was assessed by dilution of a fluorescein isothiocyanate (FITC) solution with water, which was monitored using fluorescence microscopy. The experimental results show that solution interfaces are increased exponentially, and a mixing of 90% was completed after the fifth mixing unit.

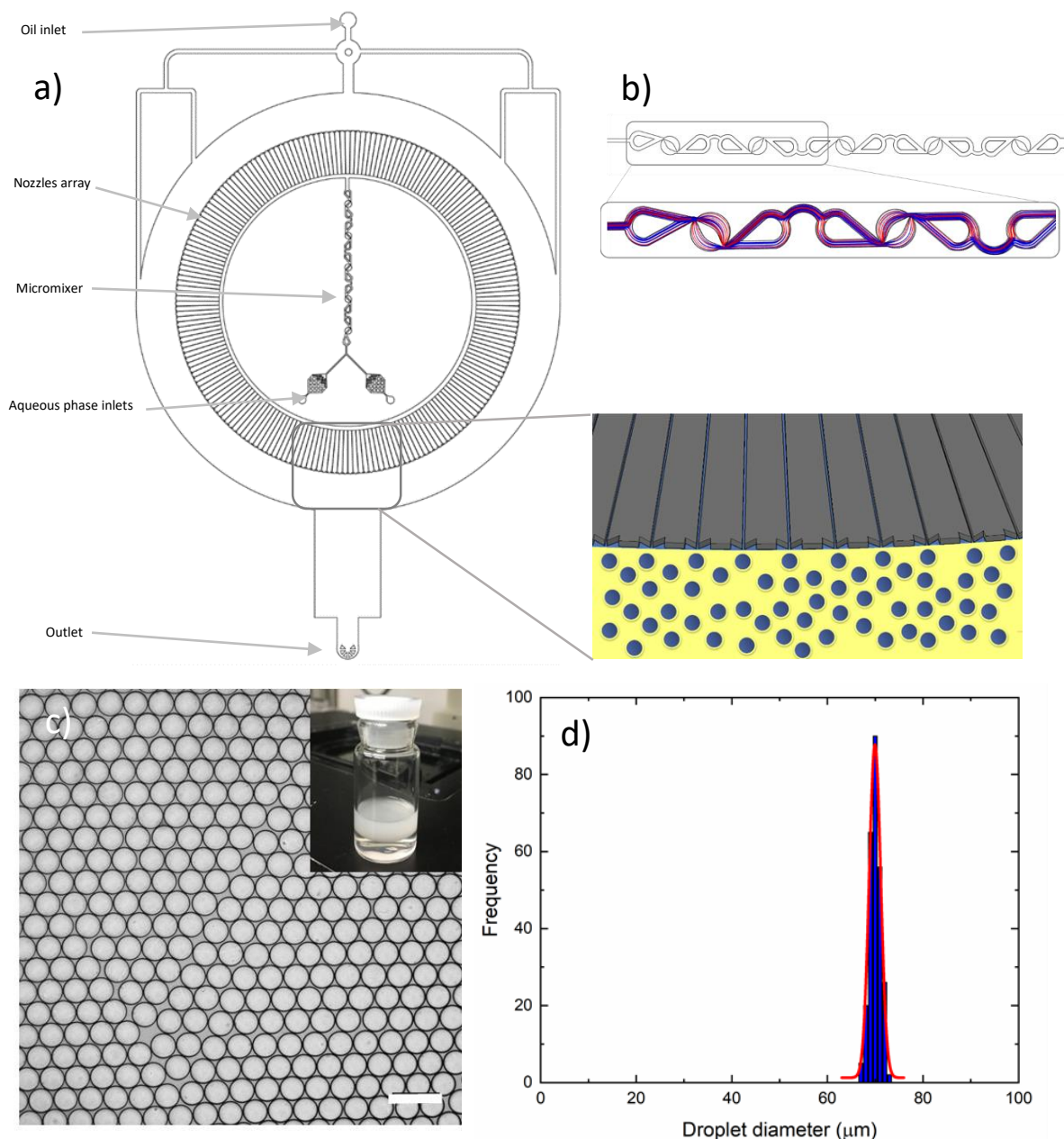


**Figure 3.1** a) The microfluidic step-emulsification device used for high-throughput generation of PAA microgel particles. b) overview of the static micromixer design and COMSOL simulation of mixing performance. c) The obtained PAA beads, imaged after 120 days at 4 °C. d) A histogram of the droplet size distribution.

Subsequently, the mixed monomer solution was flowed through the nozzle, generating droplets of pre-polymer solution, ready to be cured. Incubation of the pre-polymer droplets at 60 °C for 12 hours yielded the PAA beads. Next, excess monomer, precursor and oil was removed by washing with buffer after centrifugation. The obtained hydrogel beads were  $72 \pm 4.5 \mu\text{m}$  ( $n = 400$ ), as shown in **Figure 3.1c**. The size distribution of the generated beads is shown in **Figure 3.1d**, demonstrating their highly monodisperse nature.

### 3.3.2 HD-LAMP characterization

LAMP reagents and primers were used as detailed in our previous work in **Chapter 2**. The system was designed to work with any master mix, which commonly uses for bulk method, without complicated and reinvestigation of reagents and primers concentrations. Briefly, to test the system and provide a reference reaction for HD-LAMP development, we performed a tube-based LAMP reaction for the detection of the *mecA* target gene, with incubation at 60 °C for 30 minutes. Next, the amplified LAMP products were mixed with 'Novel Juice' dye (Sigma Aldrich, before loading into a 2% agarose gel with Diamond dye, to allow visual product monitoring. **Figure 3.2** shows an electropherogram of the LAMP reaction products, which confirmed successful and sensitive amplification of *mecA*. This result demonstrated that the designed LAMP protocol is feasible to detect *mecA* gene down to one fg/ $\mu\text{L}$  within 30 minutes, ensuring ultra-sensitive detection of LAMP assay in bulk method.

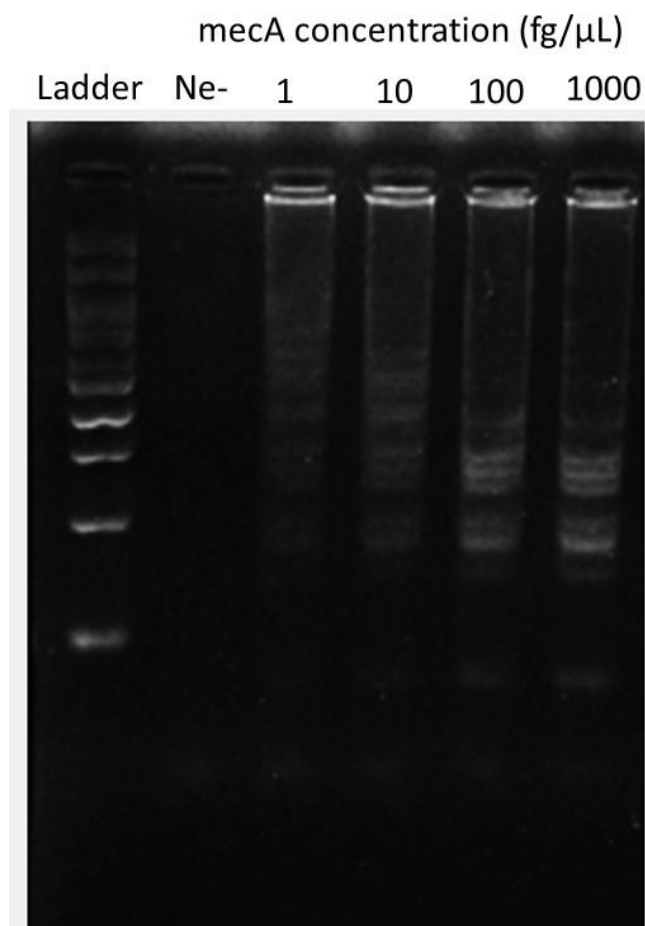


**Figure 3.2** Agarose gel electrophoresis of methicillin-resistance *mecA* gene with different concentration (1, 10,100,1000 fg/ $\mu\text{L}$ ) and negative control, ladder, negative control, 1, 10, 100, 1000 fg/ $\mu\text{L}$  of *mecA* gene.



Next, we tested the PAA beads to the LAMP reaction. Here, 30  $\mu\text{L}$  of washed PAA beads were added into 27  $\mu\text{L}$  of LAMP master mix, containing 1  $\mu\text{L}$  of DNA template, which was incubated for 15 minutes before adding 1  $\mu\text{L}$  of 1x SYBR green and 1  $\mu\text{L}$  of the polymerase. Next, the solution was compartmentalized by adding oil with 5% surfactant, and then vortexing for 30 seconds. For the negative control, the DNA template solution was replaced by DNase/RNase free water. After vortexing, the compartmentalized PAA beads were incubated in either a real-time PCR machine, or on a hot plate at 60  $^{\circ}\text{C}$  to allow the LAMP reaction to occur. As shown in **Figure 3.3a**, the positive results of 100  $\text{pg}/\mu\text{L}$  of the *mecA* gene showed bright green fluorescence under illumination, indicating that the dsDNA templates were amplified by LAMP reaction (as SYBR green fluoresces when bound to dsDNA). For the negative control (**Figure 3.3b**), the fluorescence signal was very low, indicating that amplification had not occurred. The corresponding real-time amplification curves are shown in **Figure 3.3c**.

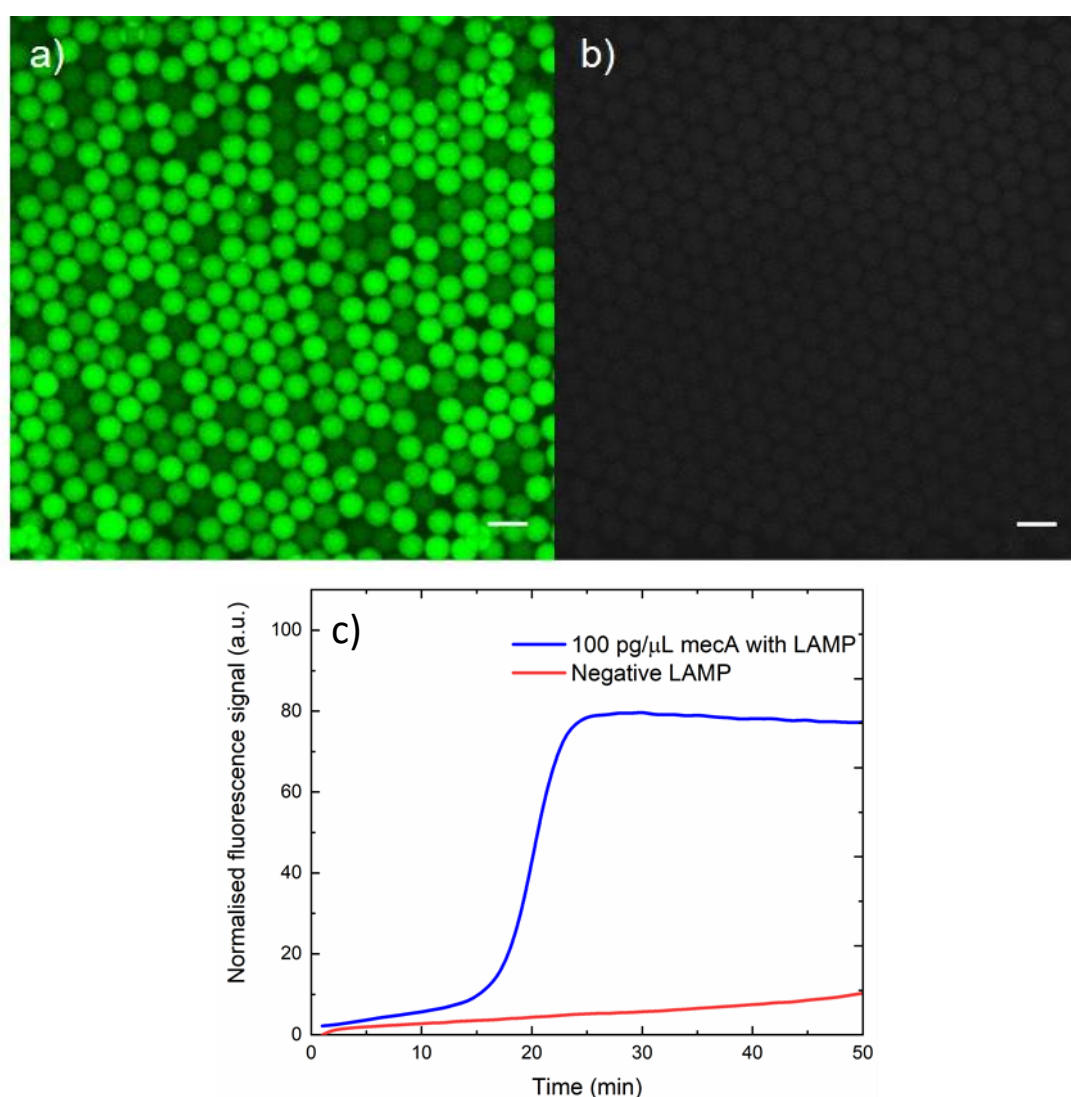


**Figure 3.3** Images of a) positive (100  $\text{pg}/\mu\text{L}$ ) and b) negative (0  $\text{pg}/\mu\text{L}$ ) LAMP reaction using hydrogel beads, incubated at 60  $^{\circ}\text{C}$  for 60 min. c) Variation of fluorescence as a function of time for both the positive and negative LAMP reactions in a) and b).



### 3.3.3 DNA quantitation with digital droplet LAMP

The primary aim of the current study was to enable rapid and simple digital LAMP by removing the necessity of using a microfluidic setup as part of the process, as required in other digital droplet approaches. Instead, the PAA hydrogel beads can be made in large batches and stored for long periods of time prior to use. To demonstrate this possibility, we encapsulated different concentrations of our target molecule (from 0.001 to 1000 pg/ $\mu$ L *mecA* gene) in droplet hydrogel and compartmentalised with oil. Just as in microfluidic ddLAMP, increasing the target concentration increases the relative number of fluorescent droplets, such that the ratio of 'on' to 'off' beads can be related to the concentration of target in the sample.

The encapsulated LAMP mastermix and *mecA* gene in hydrogel was tested with traditional real-time PCR method, observing the  $C_T$  value, the time required for the fluorescent signal to cross the one-third threshold, of the LAMP amplicon production. To determine whether this allows *mecA* concentration estimation, we follow conventional HD-LAMP analysis and quantify droplet fluorescence by plotting the fluorescence against  $C_T$  value obtained from real-time PCR instrument. As shown in **Figure 3.4a**, fluorescence signal of *mecA* (1 to 1000 pg/ $\mu$ L) amplification was observable in an hour, with the lowest concentrations require longer incubation time. To construct a calibration curve, the  $C_T$  values of the chosen concentrations were plotted against concentration, as illustrated in **Figure 3.4b**.

Analytical performance was assessed using a dilution series of PCR products of the *mecA* gene, from 1 to  $10^3$  pg/ $\mu$ L. Real-time fluorescence monitoring of the HD-LAMP reaction showed that higher concentrations of target led to faster amplification, indicating that the more target to amplify the lower  $C_T$  value can be observed. The calibration curve was constructed by plotting the  $C_T$  value against *mecA* concentration, as shown in **Figure 3.4b**. This exhibits a linear range between 1 and 1000 pg/ $\mu$ L ( $R^2 = 0.997$ ). By judging the  $C_T$  value against the *mecA* concentration, we observed that the LAMP amplicons detection is proportional to target copy number over a broad range, ensuring the HD-LAMP can be applied for quantitative analysis effectively.

For point-of-care diagnostics, a real-time fluorescence detector is not possible for a resource-limited setting. Although several LAMP-based point-of-care devices have developed for use in resource-limited settings, it should be noted that quantitative is challenging to be judged due to the uncontrollable amplification of LAMP reaction. DNA amplification in LAMP reaction is random after it forming the dumbbell shape, given a wide range of amplicon from few hundreds to thousands of base pairs in the isothermal environment. Therefore, considering the exact amount of the target gene is challenging since it is difficult to convert the amplicon amount to the initial target gene concentration. Having a digital platform which compartmentalises the target gene into a massive amount of small reactors could solve the quantitative analysis in LAMP to convert the 'on' signal into the initial amount of target gene precisely. Accordingly, imaging of hydrogel beads would be an ideal method to quantify target genes in PoC diagnostic platforms.

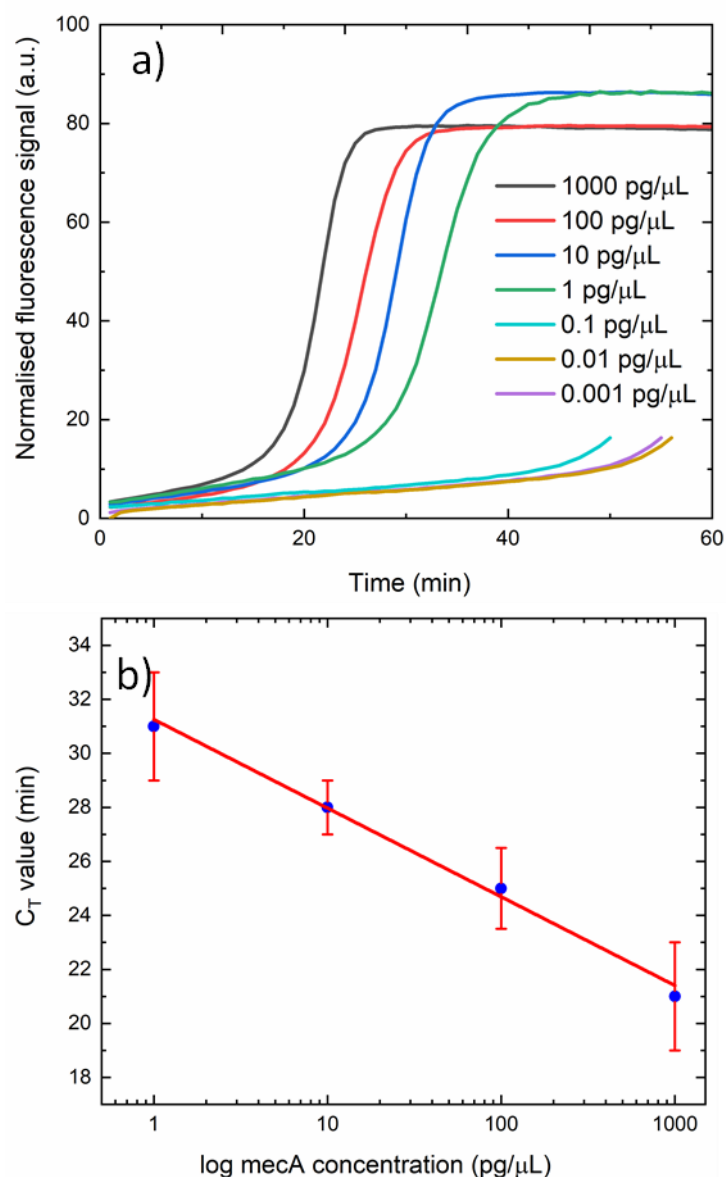


**Figure 3.4** a) Time-dependence fluorometric signal. b) Linear range of *mecA* gene using droplet hydrogel counting ratio.

Next, we tested our platform by taking images under fluorescence microscope and counting the droplet that given high fluorescent intensity (positive bead) compared to the negative control that give no fluorescence or dimmed signal (negative bead), indicating *mecA* gene was amplified. **Figure 3.5** shows images of droplet monolayers resulting from eight different concentrations of the *mecA* gene, after encapsulation in the PAA beads and amplification by LAMP. It can be observed that an increasing concentration of target leads to an increasing proportion of bright beads. To relate this proportion to the amplicon concentration, positive beads were counted and compared to the total number of beads in one frame, using

$$RB = NB/NT \times 100\% \quad (5.1)$$

where RB is the proportion of positive versus negative beads, NB is the number of positive beads per image (i.e. those containing LAMP product), and NT is the total number of beads per image. **Figure 3.6a** shows a calibration curve of BB% versus *mecA* concentration, using *mecA* concentrations between  $10^{-3}$  and  $10^3$  pg/ $\mu$ L, with linearity between  $10^{-1}$  to  $10^2$  pg/ $\mu$ L ( $R^2 = 0.983$ ). As shown in **Figure 3.5b**, the limit of detection was found to be 1 fg/ $\mu$ L ( $\sim 1000$  copies/ $\mu$ L) of *mecA* (at ca. 700 bp) per microliter, which exhibits RB value of 5%.

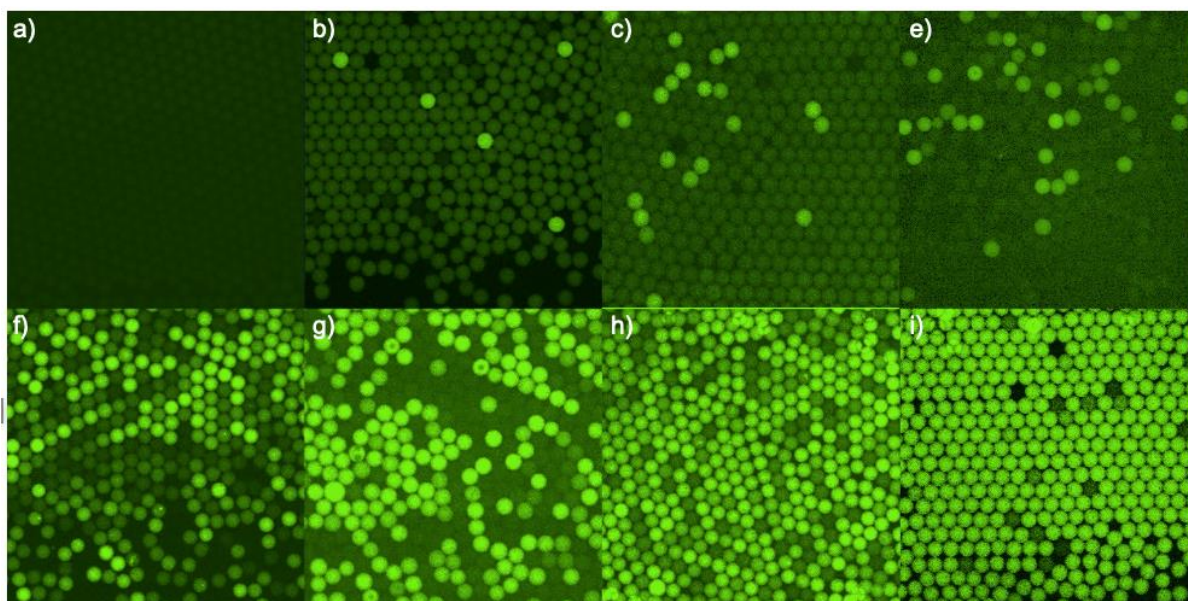


**Figure 3.5** Fluorescence images of the droplet monolayers in an observation channel for the tested concentrations (0.001, 0.01, 0.1, 1, 10, 100, 1000 pg/ $\mu$ L *mecA* gene) and the non-template control (NTC) for the HD-LAMP (representative image sections cropped). Bright green beads images represent positive droplets. negative control, 0.001, 0.01, 0.1, 1, 10, 100, and 1000 pg/ $\mu$ L, respectively.

### 3.3.4 Selectivity

To determine the selectivity of our approach, the LAMP master mix was used to detect MRSA (USA-300) bacteria against other common bacteria, including *E. coli*, *E. faecalis*, *L. monocytogenes*, *S. epidermidis* and *S. aureus*, which were isolated human sample, lab and clinical isolate strains, as described in **Section 5.2**. To obtain bacterial lysate, bacterial colonies were collected and lysed in TE buffer at 95 °C for 5 minutes. Then 1  $\mu$ L of the lysate was added to the LAMP-hydrogel working solution before proceeding with the amplification reaction and readout. The reagent was successfully encapsulated inside the PAA microgel and exhibited an excellent selectivity for the target gene. **Figure 3.6b** shows a positive result for MRSA, and a negative result for all other bacteria, indicating that the HD-LAMP can be applied in real bacteria lysate samples and has high specificity to detect only the target gene (*mecA*).

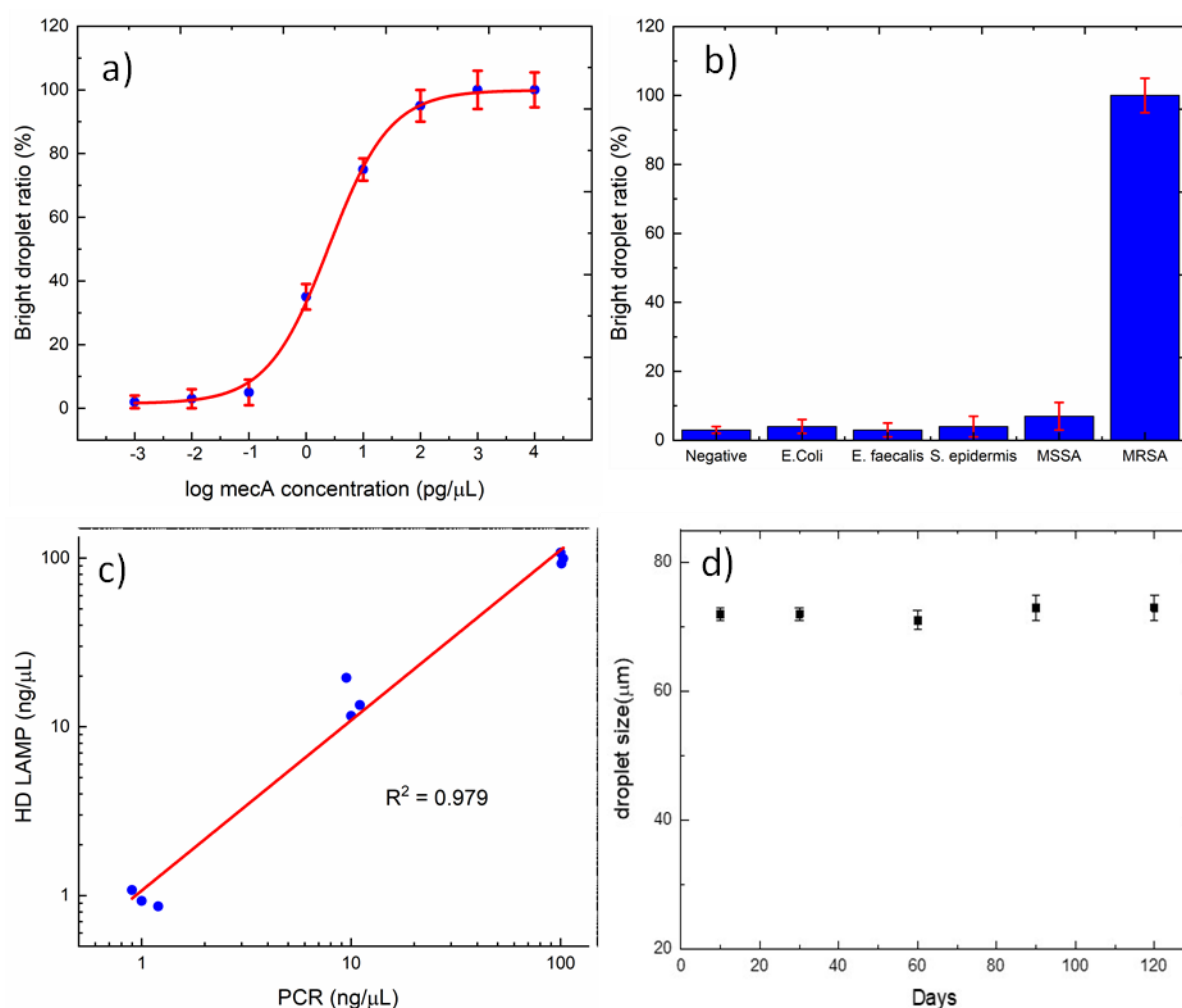


**Figure 3.6** a) Dynamic range of *mecA* gene using hydrogel counting ratio. b) Selectivity study of *E. coli*, *E. faecalis*, *S. epidermis*, MSSA, MRSA target DNA in HD-LAMP method. c) Accuracy test by comparing DNA amplification results (N=3) PCR tube and HD-LAMP system detecting *mecA* concentration (1 to 10<sup>2</sup> pg/μL) (*mecA* HDLAMP versus *mecA* PCR curve). d) Size stability test of hydrogel beads over 120 days.

### 3.3.5 Accuracy and precision

To validate the accuracy of the HD-LAMP method, the gold-standard method (PCR) was used as a comparison. A concentration series of the *mecA* target (1 to 10<sup>2</sup> pg/μL) was assessed using each method (N=3), yielding a coefficient of determination ( $R^2$ ) of 0.979 plotted against one-another (Figure 3.6c). There was no significant difference between the two methods (t-value = 0.70, <  $t$ -critical = 1.85,  $\alpha$  = 0.05, 95% confidence, N = 9), suggesting excellent agreement between HD-LAMP and PCR.

### 3.3.6 Stability of hydrogel beads

The size stability of our PAA hydrogel beads over extended periods is crucial in enabling further applications. To assess 'shelf lifetime', PAA microparticles were stored in a washing buffer for 4 months at 4°C. Figure 3.6d shows that there was no significant difference in droplet diameter over

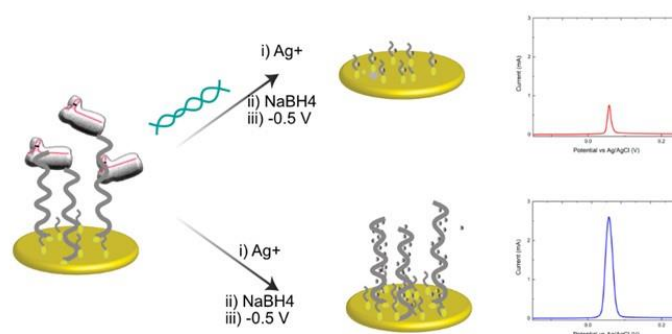
the 120 days testing period, suggesting high storage stability. In addition to the size consideration, hydrogel activity to the LAMP reaction was investigated, resulting in insignificant result for LAMP reaction which suggested that hydrogel composition unaltered. This observation is in agreement with Hatori et al.,<sup>190</sup> who showed that their hydrogel particles could be stored for up to a year without any change in particle integrity. We therefore note the promise of these hydrogel beads for deployment in real healthcare applications, for examples in field-deployable diagnostics.

### 3.4 Conclusions

Loop-mediated isothermal amplification was successfully conducted in a hydrogel-droplet system (HD-LAMP) to detect drug-resistant bacteria. A microfluidic device that included a tesla-inspired micromixer performed rapid mixing was used to form hydrogel droplets by step emulsification, achieving high-throughput generation of monodispersed droplets ( $10^9$  droplets in 600  $\mu\text{L}$  aqueous solution, within 10 minutes), and finally PAA beads after cross-linking. These beads were then used to compartmentalize a LAMP reaction by simple vortexing of the master mix with the beads in oil. Target quantification was achieved by simple counting of fluorescent versus non-fluorescent beads under fluorescence microscopy. The process yielded linearity between  $10^{-1}$  and  $10^2$   $\text{pg}/\mu\text{L}$  ( $R^2 = 0.997$ ), with a limit of detection down to 1  $\text{fg}/\mu\text{L}$  (1000 copies/ $\mu\text{L}$ ). Our HD-LAMP protocol showed excellent selectivity in the detection of MRSA versus other common bacteria, including *E. coli*, *E. faecalis*, *L. monocytogenes*, *S. epidermidis*, and *S. aureus*. Comparison with PCR showed no significant difference for quantification of the *mecA* gene. Overall, the developed HD-LAMP assay holds a great promise for rapid and cost-effective PoC devices with excellent analytical performance, enabling precision analysis in the field of digital biology. Although the analysis method has yet to be applied to resource-limited area, we expect that smartphone-based detection can be integrated in the short to medium term.

## Chapter 4

# An Amplification-Free Ultra-Sensitive Electrochemical CRISPR/Cas Biosensor for Drug-Resistant Bacteria Detection Using Silver Metallization



Antimicrobial resistance (AMR) in bacterial infections inflicts significant mortality and morbidity in the human population, in particular in hospital settings. Rapid and cost-effective tools are needed to determine if a patient has such an infection, so an appropriate course of treatment can be pursued. Here, we report an electrochemical CRISPR/Cas biosensor coupled with silver metallization (E-Si-CRISPR) to detect methicillin-resistant *Staphylococcus aureus* (MRSA), a prevalent drug-resistant bacterium causing hard-to-treat skin infections, and sometimes death. The enzyme Cas12a, with a custom-designed gRNA for the *mecA* gene (found in all MRSA strains), was employed, as its trans-cleavage activity effectively removed immobilized ssDNA from on a screen-printed gold electrode before silver metallization (chemically and electrochemically), and measuring electrochemically via square wave voltammetry (SWV). Excellent analytical performance was achieved, with detection and quantitation limits of 3.5 and 10 fM, respectively, and linearity from 10 fM to 0.1 nM (five orders,  $R^2 = 0.988$ ), with no significant difference between clean buffer and human serum. Further, the excellent selectivity of the Cas12a enzyme allowed specific detection of MRSA in human serum in the presence of other common bacteria. Overall, the E-Si-CRISPR technique has promise as an ultrasensitive field-deployable device for drug-resistance bacteria detection, without requiring nucleic acid amplification, allowing simple and effective gene-based analysis via modification of gRNA protospacer.

This chapter is adapted from a manuscript entitled "*An Amplification-Free Ultra-Sensitive Electrochemical CRISPR/Cas Biosensor for Drug-Resistant Bacteria Detection Using Silver Metallization*", authored by Akkapol Suea-Ngam, Philip D. Howes and Andrew J. deMello. *In preparation*.

## 4.1 Introduction

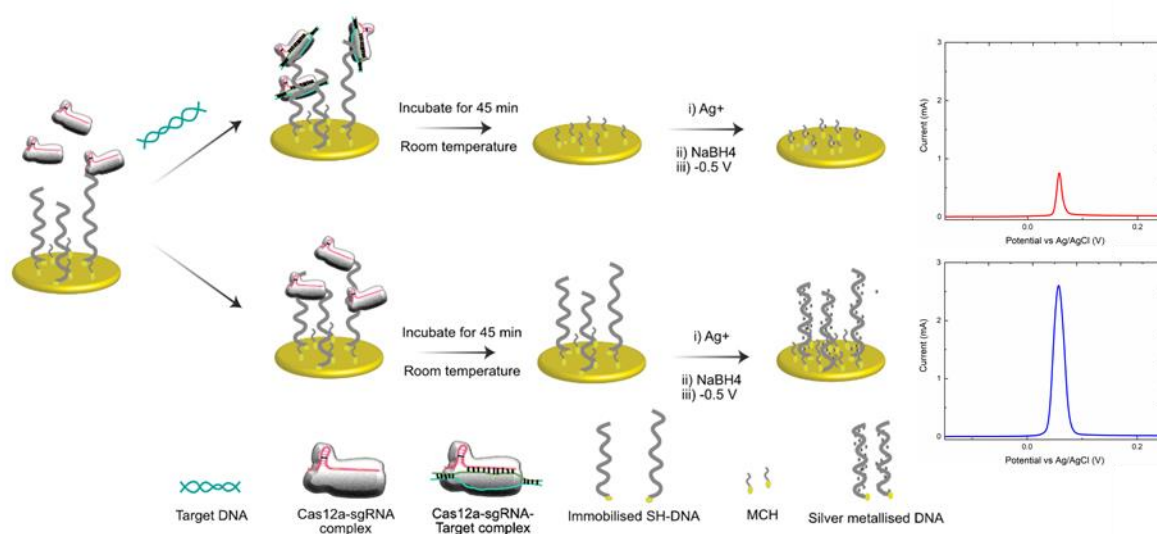
Antimicrobial-resistance (AMR) in bacterial infections has become one of the most urgent problems in global healthcare, with rapidly increasing numbers of bacterial strains that are resistant to antibiotics, coupled with a severe lack of new antibiotic discoveries.<sup>210</sup> It is predicted that, by 2050, AMR will up to 50 million death per year.<sup>211</sup> Methicillin-resistant *Staphylococcus aureus* (MRSA) is a prevalent AMR infection found in healthcare settings, and causes skin and bloodstream infections which lead to significant mortality and morbidity.<sup>212</sup> The drug-resistant character of MRSA was discovered in 1968 in the United States, which had developed resistance to penicillin-related antibiotics.<sup>213</sup> Motivated by these agendas, having rapid and cost-effective analytical devices for AMR detection, therefore, is urgent.

Since the early days of bacterial AMR detection, cell-culture based analysis is employed, requiring from days to weeks determine if AMR is present. Recently, nucleic acid amplification tests (NAATs) have been introduced for AMR detection, allowing rapid analysis from swabbing to results, typically within a day.<sup>214</sup> The polymerase chain reaction (PCR) is the gold-standard method for gene-based pathogen detection, which is applicable for AMR analysis.<sup>215</sup> However, PCR is a compromised technique for applying in the resource-limited areas due to the bulky instrumentation and the traditional approach to analyse the amplicon, electrophoresis. Although several isothermal NAATs (loop-mediated isothermal amplification, rolling circle amplification etc.) have been developed with great promise in field-deployable diagnostics,<sup>214</sup> the specificity of those methods, which is the most crucial parameter for gene analysis, is a typically insufficient. Accordingly, the requirement of a portable and straightforward platform for AMR detection with the required excellent specificity of gene recognition is prioritized.

Clustered regularly interspaced short palindromic repeats (CRISPR)-related technologies encompass a set of extremely versatile and effective enzyme-based tools in the biological sciences.<sup>216-218</sup> Recently, Gootenberg and Zhang group invented a CRISPR/Cas biosensor technology namely SHERLOCK, which has had a significant impact in the biosensing field.<sup>64-65, 125, 219-221</sup> Using the trans-cleavage activity of Cas13, probe-modified ssRNA is cleaved only after Cas13 has bound to a specific recombinase polymerase amplification (RPA) amplicon, which allowed highly sensitive detection of Zika and Dengue virus on a paper-based platform. Simultaneously, the Doudna group developed the DETECTR system using Cas12a to cleave the probe-modified ssDNA.<sup>59, 222-223</sup> Here, the trans-cleavage activity of Cas12a is activated by capturing loop-mediated isothermal amplification (LAMP) amplicons, allowing precise and ultrasensitive fluorometric detection of HPV16 or HPV18 fragments. These discoveries have led to the development of several other CRISPR/Cas biosensor platforms, including colorimetric, fluorometric, and electrochemical approaches with outstanding analytical performance, providing excellent selectivity down to single nucleotide level.<sup>50, 65, 224-225</sup> In particular, the electrochemical approach (E-CRISPR) has provided an alternative method for highly sensitive detection of pathogens and toxins without the assistance of DNA amplification, using either MB-ssDNA or enzyme-assisted signal amplification.<sup>226-227</sup> However, to date E-CRISPR has achieved a limit of detection for gene-based analysis only down to the picomolar level, leaving room for improvement for ultrasensitive analysis.



In this work, we report a sensing approach which combines E-CRISPR with DNA silver metallization (E-Si-CRISPR) on disposable screen-printed gold electrodes platform, achieving amplification-free gene-based detection down to the femtomolar level. As illustrated in **Scheme 4.1**, we targeted the detection of MRSA bacteria via the *mecA* gene, as it is common amongst the different strains and contains a protospacer adjacent motif (PAM) for the enzyme Cas12a. Cleavage activity was efficient in clean buffer and in human serum, allowing the developed E-Si-CRISPR platform to achieve an excellent analytical performance, with selectivity down to single nucleotide level in both PAM and protospacer-binding regimes, and detection of MRSA in human serum against common bacteria. This ultrasensitive gene-based detection platform shows great promise for applications as a field-deployable diagnostic, requiring only simple modification of protospacer regimes to target the genes of other pathogens.



**Scheme 4.1** Schematic of the E-Si-CRISPR technique. ssDNA immobilized on the electrode are removed by the triplex Cas, only in the presence of a target gene. Subsequent addition of the  $\text{Ag}^+$  and  $\text{NaBH}_4$  seeds the silver metallization, and an applied potential of  $-0.5\text{ V}$  allows the 'double metallization', providing a minimized SWV signal (target positive result). In the absence of target gene, the ssDNA cannot be removed, yielding a high electrochemical signal (target negative result).



## 4.2 Methodology

### 4.2.1 Materials and reagents

The DNA and RNA in **Table 4.1** were purchased from Microsynth (Balgach, Switzerland).<sup>228</sup> AgNO<sub>3</sub>, NaBH<sub>4</sub>, HEPES, EDTA, Trizma® base, NaNO<sub>3</sub>, CaCl<sub>2</sub>, 6-mercapto-1-hexanol (MCH), K<sub>3</sub>[Fe(CN)<sub>6</sub>], K<sub>4</sub>[Fe(CN)<sub>6</sub>], PBS tablets, NaOH, H<sub>2</sub>SO<sub>4</sub>, NaCl, and KCl (all analytical grade) were purchased from Sigma Aldrich (Buchs, Switzerland). All other reagents, TCEP (Alfa Aesar, Karlsruhe, Germany), HCl (Fluka, Buchs, Switzerland), MgCl<sub>2</sub> (Acros Organics, Geel, Belgium) were analytical reagent grade and used as received. Cas12a and its working buffer (50x) were purchased from New England Biolabs (Frankfurt am Main, Germany). All aqueous solutions were prepared with DNase and RNase free water (Invitrogen/Thermo Fisher, Reinach, Switzerland). Electrochemical measurements were performed with a PGSTAT204 AutoLab (Metrohm, Zofingen, Switzerland). Screen-printed gold electrodes (SPGE) were purchased from Dropsens (Metrohm, Zofingen, Switzerland). Cyclic voltammetry (CV) data for conductivity characterization were collected at 100 mV/s in 10 mM K<sub>3</sub>[Fe(CN)<sub>6</sub>], 1 M KCl, and 100 mM PBS (pH 7.42) unless otherwise indicated. Electrochemical impedance spectroscopy (EIS) was performed using an Impedance Analyzer SP-300 (Bio-Logic, Seyssinet-Pariset, France) in 0.1 M PBS containing 10 mM K<sub>3</sub>[Fe(CN)<sub>6</sub>]/K<sub>4</sub>[Fe(CN)<sub>6</sub>] (1:1) with 1 M KCl as the supporting electrolyte. Impedance spectra were recorded within the frequency range of 10<sup>-2</sup> to 10<sup>5</sup> Hz. The amplitude of the applied sine wave potential in each case was 5 mV. Further, a coulometric assay was performed after the silver metallization using 0.5 V applied potential for 60 seconds.

**Table 4.1** PCR primers for *mecA* amplification, and the oligonucleotides for E-Si-CRISPR

Name	Oligonucleotide Sequence
LF	5' AGATTGGGATCATAGCGTCAT 3'
LB	5' TTGAGGGTGGATAGCAGTACC 3'
up <i>mecA</i>	5'-TCT TCA TGT TGG AGC TTT TTA TCG TAA A-3'
down <i>mecA</i>	5'-TTT ACG ATA AAA AGC TCC AAC ATG AAG A-3'
mmPAM	5' TCTTCATGTTGGAGCTTTTTATCG TATA-3'
mmT1	5' TCTTCATGTTGGAGCTTTTTATCT TAAA-3'
mmA5	5' TCTTCATGTTGGAGCTTTTAATCG TAAA-3'
mmG10	5' TCTTCATGTTGGAGGTTTTTATCG TAAA-3'
10nt	5' AAAAAAAAAA-3'
20nt	5' AAAAAAAAAATTAAAAAAAAA-3'
30nt	5' AAAAAAAAAAAAAAAAAATTTAAAAAAAAAAAAA-3'
40nt	5' AAAAAAAAAAAAAAAAAAAAAAAAAATTTAAAAAAAAAAAAAAAAAAAAA-3'
FAM Probe	FAM-TTAATT-BHQ1
gRNA	5'-uaa uuuu cau cua agu gua gaucga uaa aaa gcu cca aca ug-3'

### 4.2.2 *mecA* gene preparation

A synthetic *mecA* gene fragment of length of 28 bp was used in a fluorometric assay to test the CRISPR/Cas approach for this gene. Next, the full *mecA* gene (685 bp) was amplified from a lysed MRSA solution using the PCR method, as described in our previous work in **Chapter 2**. Briefly, 1  $\mu$ L of lysed MRSA solution was added into the PCR master mix with the forward and backward primers. PCR was performed by preheating at 95 °C for 5 minutes, and then performing the thermocycles, using 55 °C (30 seconds), 72 °C (1 minute), and 95 °C (30 seconds) for 30 repeats. After this, the amplicon was allowed to complete the amplification at 72 °C for 10 minutes, yielding a 2  $\mu$ M *mecA* gene stock solution, which was stored at -20 °C before use. DNA reactions were analyzed using a Quanstudio Real-time PCR machine (Thermo Fisher Scientific, Reinach, Switzerland) and gel electrophoresis (85 V applied potential for 75 minutes in TBE buffer).

### 4.2.3 Electrochemical detection

#### 4.2.3.1 Electrode fabrication

The SPGE was electrochemically cleaned using a series of oxidation and reduction cycles in 0.5 M NaOH, 0.5 M H<sub>2</sub>SO<sub>4</sub>, 0.01 M KCl with 0.1 M H<sub>2</sub>SO<sub>4</sub>, and 0.05 M H<sub>2</sub>SO<sub>4</sub>, using cyclic voltammetry (100 mV/s, from -1 V to 1 V) before modification with a thiolated ssDNA probe (10 nt, 20 nt, 30 nt, 40 nt). For sample analysis, different concentrations of the thiolated ssDNA probe were pretreated with 10 mM TCEP in buffer (10 mM Tris-HCl, 1 mM EDTA, 0.1 M NaCl, pH 7.4) for 30 minutes to reduce the thiol-thiol bonds. Next, 10  $\mu$ L of the reduced aptamer solution was added on to the functionalized electrode surface and kept in a humid atmosphere in the dark at room temperature for 12 hours. Subsequently, the modified surface was rinsed with buffer solution and then passivated with MCH in Tris-HCl buffer (pH 8.3) for 30 minutes. After washing, the electrode was dried using nitrogen gas and stored in the dark under nitrogen.

#### 4.2.3.2 Electrochemical detection

For electrochemical detection, 25  $\mu$ L of Cas12a enzyme was incubated with 25  $\mu$ L gRNA at the same mole ratio (50 nM) for 30 min in the 1x Cas working buffer. Next, this solution was applied to the functionalized SPGE along with 1  $\mu$ L of the target gene, the solution was mixed well then left for 30 minutes. After washing, the electrode was immersed in 100  $\mu$ M AgNO<sub>3</sub> in 20 mM HEPES and 100 mM NaNO<sub>3</sub> (pH 7.4) for 30 minutes, then washed with water. Then the modified electrode was dipped into a freshly prepared 10 mM solution of NaBH<sub>4</sub> (in 20 mM HEPES buffer) (immersing for 10 minutes), washed with water, and then placed in an electrolyte (0.1 M NaCl and 0.1 M NaNO<sub>3</sub>) for the electrochemical measurement. Electrochemical deposition with -0.5 V applied potential was performed, before square wave voltammetry (SWV) from -0.3 V to 0.5 V versus Ag/AgCl.

### 4.2.4 Fluorescence detection

The fluorometric assay was carried out using the established protocol from Zhang and coworkers.<sup>65</sup> Briefly, Cas12a was incubated with the gRNA with at an equal molar ratio, followed by a ssDNA modified with FAM dye and BHQ1 quencher. When the *mecA* gene was introduced into the solution and mixed well, a room temperature incubation for 30 minutes allowed the evolution of a fluorescence signal, which was monitored using a real-time PCR machine.

### 4.2.5 Mismatch analysis

For mismatch analysis, the mismatch ssDNA of the *mecA* gene was inserted into the upper DNA strand. Mismatched nucleotide positions were assigned to the 2<sup>nd</sup> position of the protospacer adjacent motif, and the first, fifth and tenth position on the upper DNA target strand. Electrochemical detection was then performed to assess Cas selectivity.

#### 4.2.6 Human sample and bacterial sample analyses

All lysed bacteria solutions were prepared by dissolving bacterial colonies in TE buffer (Fischer Scientific, Reinach, Switzerland), with incubation at 95 °C for 5 minutes, and storage at -20 °C before use. All bacteria were obtained as a gift from Professor Mathias Schmelcher, University of Zurich, including, MRSA strain (*Staphylococcus aureus* USA300 JE2; source: Annelies Zinkernagel, Division of Infectious Diseases and Hospital Epidemiology, University Hospital Zurich, University of Zurich, Zurich, Switzerland; properties: methicillin-resistant *S. aureus*), *E. coli* (*Escherichia coli* JM109; source: Stratagene, San Diego, CA, USA; properties: *E. coli* lab strain, non-pathogenic), *E. faecalis* (*Enterococcus faecalis* ATCC 19433; source: ATCC 19433; properties: type strain), *L. monocytogenes* (*Listeria monocytogenes* Scott A; source: Weihenstephan Listeria Collection; properties: clinical isolate, serovar 4b), *S. epidermidis* (*Staphylococcus epidermidis* MP04; source: Max Paape, ARS, USDA, Beltsville, MD, USA; properties: bovine mastitis isolate) and methicillin-sensitive *S. aureus* (MSSA) (*Staphylococcus aureus* Newman; source: NCTC 8178, Annelies Zinkernagel, Division of Infectious Diseases and Hospital Epidemiology, University Hospital Zurich, University of Zurich, Zurich, Switzerland).

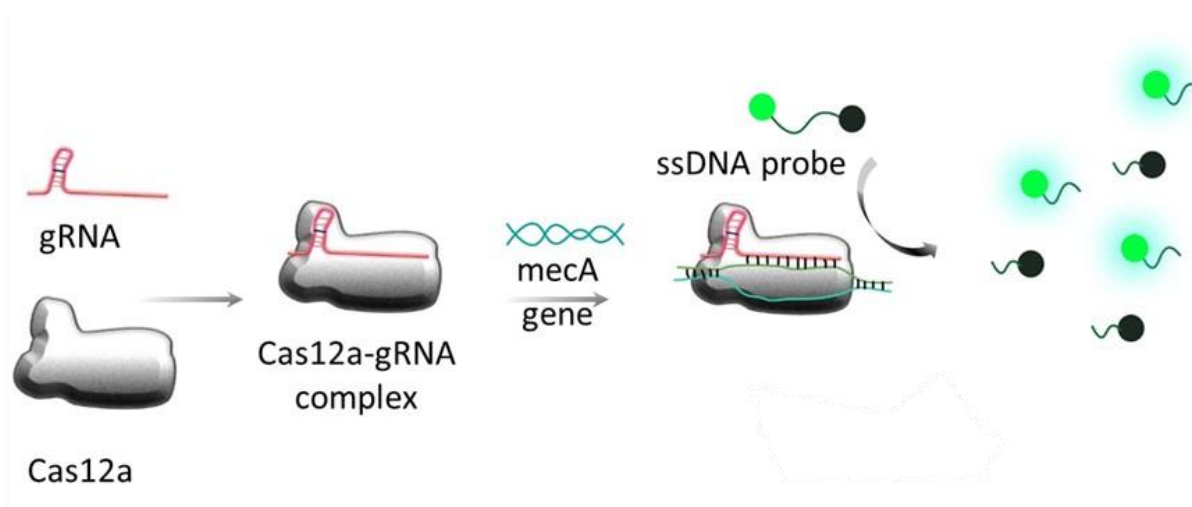
Human serum (Sigma Aldrich, Buchs, Switzerland) was employed to prepare a dilution series of the solution of the *mecA* gene from the stock amplicon solution. In addition, it was used to prepare the bacterial lysed solution by dilution at 1:1 with the human serum before use in the selectivity study. Here, 1 µL lysate was added into the Cas-gRNA complex solution on the electrode, incubated for 60 minutes, followed by electrochemical analysis.

## 4.3 Results and discussion

### 4.3.1 Electrode characterisation

Several reports have demonstrated that CRISPR/Cas biosensors show great promise for gene-based analysis. , once introducing gene to the system, it should be tested to ensure the ability of the Cas enzyme compared to the previous method. In this work, we chose the *mecA* gene as the gene to detect MRSA, since it is a shared gene in many MRSA strains. To detect *mecA* using a CRISPR/Cas biosensor, a protospacer adjacent motif (PAM) is required on the downstream side of the *mecA* gene.<sup>219</sup> Therefore, we used a synthetic DNA analog oligo (5'-TTT ACG ATA AAA AGC TCC AAC ATG AAG A-3'), which contained the "TTTA" on the downstream DNA, with the complementary to perform the initial test for CRISPR/Cas biosensor. In addition, the chosen protospacer binding sequence containing the PAM must be found only in the *mecA* gene, in order to achieve high selectivity. Thus, the chosen protospacer binding sequence was analyzed using the internet-based basic local alignment search tool (BLAST), available from the National Center for Biotechnology Information (NCBI). BLAST showed that the chosen PAM with protospacer binding sequence could be found only in the *mecA* gene. Thus, it was validated for MRSA analysis.

As demonstrated in **Scheme 4.2**, once the *mecA* gene forms the triplex with the Cas12a and gRNA, the cis-cleavage activity (where the Cas enzyme cleaves the target gene bound to the protospacer regime specifically), is activated. Consequently, the trans-cleavage (which is the random ssDNA cleavage of Cas12a after cis-cleavage activation) is activated to cleave the FAM-ssDNA-BQ1 oligo, resulting in evolution of a fluorometric signal (**Figure 4.1**). Next, the *mecA* gene amplicon (685 bp) from the PCR product was tested in a similar manner, and yielded similar results, showing that the designed CRISPR/Cas biosensor was capable of detecting the *mecA* gene.



**Scheme 4.2** Schematic of the fluorometric assay for the CRISPR/Cas biosensor.

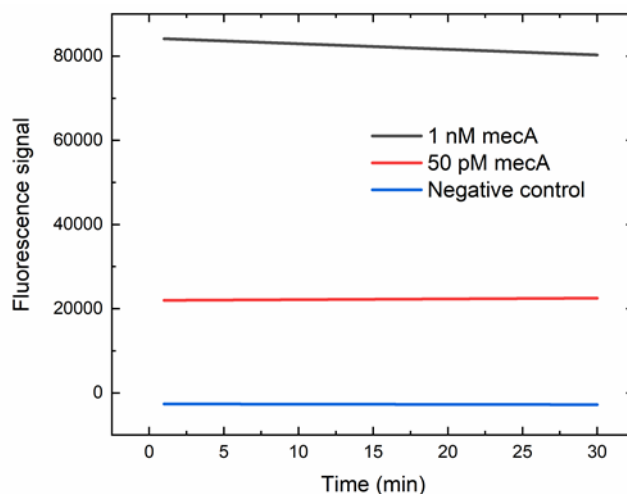


**Figure 4.1** Fluorometric signal of 1 nM and 50 pM *mecA* compared to the negative control (i.e. without the *mecA* gene target).

In a previous work in **Chapter 2**, we used silver metallization to enhance the sensitivity of an enzyme-assisted electrochemical approach to mycotoxin detection. Here, we employed electrochemical detection coupled with DNA silver metallization for a CRISPR/Cas biosensor (E-Si-CRISPR) to detect MRSA. **Scheme 4.1** illustrates the strategy of *mecA* gene detection. In the presence of the *mecA* gene, the Cas12a-gRNA complex activates cis-cleavage to cleave the target gene. This then initiates the trans-cleavage activity, where ssDNA is cleaved at random in the system. Thus, the immobilized ssDNA is cleaved by the triplex Cas enzyme, which removes ssDNA from the electrode surface. The remaining ssDNA is then silver metallized chemically *and* electrochemically, before the final electrochemical signal is read via square wave voltammetry (SWV).

The assay was characterized using cyclic voltammetry (CV), square wave voltammetry (SWV), electrochemical impedance spectroscopy (EIS), and coulometry. To observe the DNA metallization, CV was used to compare the redox signal of before and after DNA metallization on the electrode, as displayed in **Figure 4.2a**. The oxidation and reduction peaks of silver on ssDNA was observed at 0.16 V and -0.06 V, respectively. Subsequently, a signal reversibility of a 10 mM  $K_3[Fe(CN)_6]/K_4[Fe(CN)_6]$  solution was investigated for both the ssDNA-SPGE and silver-metallized ssDNA-SPGE, suggesting the increasing of the electroactive surface.<sup>229</sup> This CV indicated a larger surface, which was confirmed by the reversible system relationship of the cyclic voltammogram, inferred from the Randle-Sevcik equation:

$$i_p = 2.69 \times 10^5 ACn^{3/2}D^{1/2}v^{1/2} \quad (4.1)$$

where  $i_p$  is the peak current;  $A$  is the electrode surface area;  $C$  is the bulk concentration of analyte;  $D$  is the diffusion coefficient of the analyte;  $v$  is the scan rate).<sup>230</sup> Next, the cleaved and non-cleaved ssDNA signals on the electrode were measured by SWV. **Figure 4.2b** shows the high current of non-cleaved ssDNA on the SPGE (i.e. target negative case), while the cleaved ssDNA showed only 30% of the original signal (i.e. target positive case), providing greater sensitivity compare to previous methods.<sup>226</sup> These results were in good agreement with previous reports,<sup>226-227</sup> and are explained by the electrostatic attraction between the negatively-charged ssDNA and positively-charged  $Ag^+$ .<sup>231</sup>

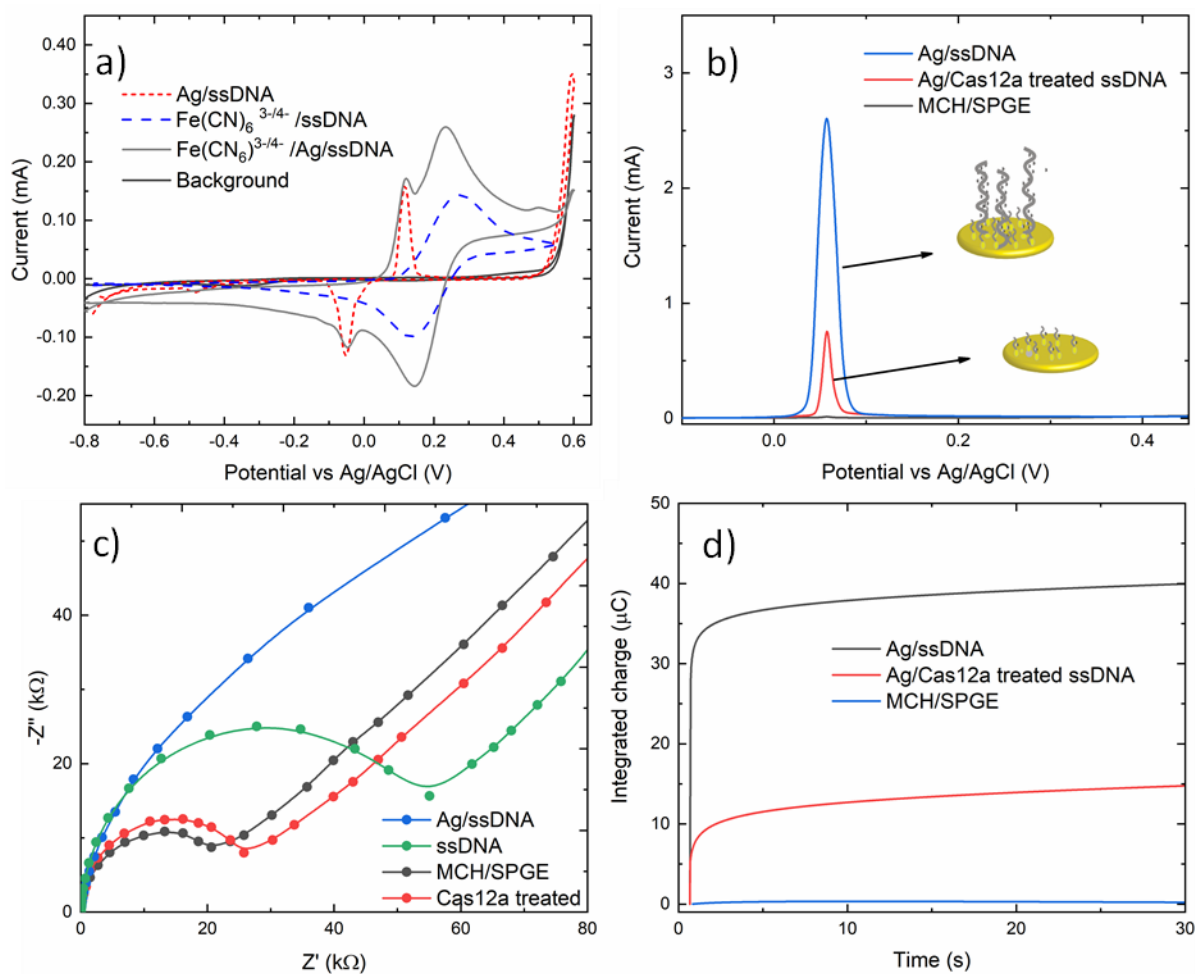


**Figure 4.2** MCH-modified, ssDNA-modified, and Cas-treated electrodes were compared using (a) square wave voltammetry (SWV), (b) cyclic voltammetry (CV), (c) electrochemical impedance spectroscopy (EIS), and (d) controlled potential coulometry. Square wave voltammograms of silver metallized electrodes were carried out using a potential step of 0.01 V, an amplitude of 0.06 V, and a frequency of 200 Hz. For cyclic voltammograms and Nyquist plots, 10 mM  $[\text{Fe}(\text{CN})_6]^{3-/4-}$  in 0.1 M PBS was used as the working solution and 0.1 M PBS was used as the background electrolyte. The reversible cyclic voltammograms were carried out using a scan rate of 100 mV/s, while Nyquist plots were obtained by applying a 5 mV sine wave potential within a frequency range of  $10^{-2}$  to  $10^5$  Hz. For coulometry, silver was deposited using a similar protocol as SWV, then applying 0.5 V potential for 30 seconds to collect silver metallized amount on electrode.

Further, DNA modification, Cas activity, and silver metallization on electrode surface were investigated using electrochemical impedance spectroscopy (EIS), an effective method for evaluating the interfacial electron transfer efficiency at different stages of biosensor preparation as each step can be readily evaluated by monitoring the change in electron transfer resistance (Rct), allowing electrode activities to be observed.<sup>232</sup> As illustrated in **Figure 4.2c**, the bare SPGE exhibited a slightly semicircular domain, indicating that the electroactive ions of  $[\text{Fe}(\text{CN})_6]^{3-/4-}$  are rapidly transported to the electrode interface. After the thiolated ssDNA was self-assembled onto the electrode surface, the Rct increased significantly as the oligonucleotides are non-electroactive, and yield a strong resistance to electron transfer. After digestion of the ssDNA by triplex Cas12a, the electrode showed an Rct value only slightly different from the MCH modified electrode, indicating trans-cleavage of the ssDNA, leaving MCH and cleaved ssDNA on the electrode surface. Importantly, we observed that the semicircular domain disappeared after silver metallization of the ssDNA-modified electrodes, suggesting full silver metallization of the ssDNA structure. These EIS results show that ssDNA modification, ssDNA silver metallization, and trans-cleavage of triplex Cas12a on the SPGE were successful.

Next, coulometry was employed to analyze the amount of  $\text{Ag}^0$  on the electrode surface. Silver metallization on the ssDNA and treated ssDNA with triplex Cas12a modified electrodes were investigated using controlled potential coulometry, and compared to the SPGE. The result, as shown in **Figure 4.2d**, shows the high integrated charge of the ssDNA ( $\sim 40$  ng of  $\text{Ag}^0$ ) and the lower integrated charge of the treated ssDNA with triplex Cas12a ( $\sim 10$  ng of  $\text{Ag}^0$ ), suggesting that the triplex Cas12a could remove  $\sim 70\%$  of the oligonucleotide on the electrode surface.

### 4.3.2 Optimization

SWV was chosen in this work due to the possibility of subtract the background, and the well-defined redox peaks that should yield excellent sensitivity.<sup>233</sup> To optimize the SWV system, we considered three parameters of the SWV peaks: peak full-width half maximum (FWHM), peak position (oxidative potential), and peak height (current). Accounting for the SWV theory, the ideal parameters for  $\text{Ag}^+/\text{Ag}^0$  (one electron involved electroactive species) are 90.5 mV of FWHM, 0 mV oxidative potential, maximum peak current.<sup>234</sup> Amplitude, frequency, and step potential are related parameters for SWV optimization; however, we observed that the step potential could be neglected due to the only very slight change that was observed during the studies. Thus, we optimized amplitude from 10 to 100 mV and frequency from 100 to 500 Hz. As displayed in **Figure 4.3 a-c**, the optimum regions for each parameter were made in mesh covered the heat maps. The optimum frequency and amplitude for FWHM, peak position, and peak currents are 200 Hz and 10 to 100 mV, 100 to 200 Hz and 50 to 100 mV, and 200-500 Hz and 60-100 mV, resulting in optimum values with 10 mV, 200 Hz, and 60 mV for step potential, frequency, and amplitude, respectively.

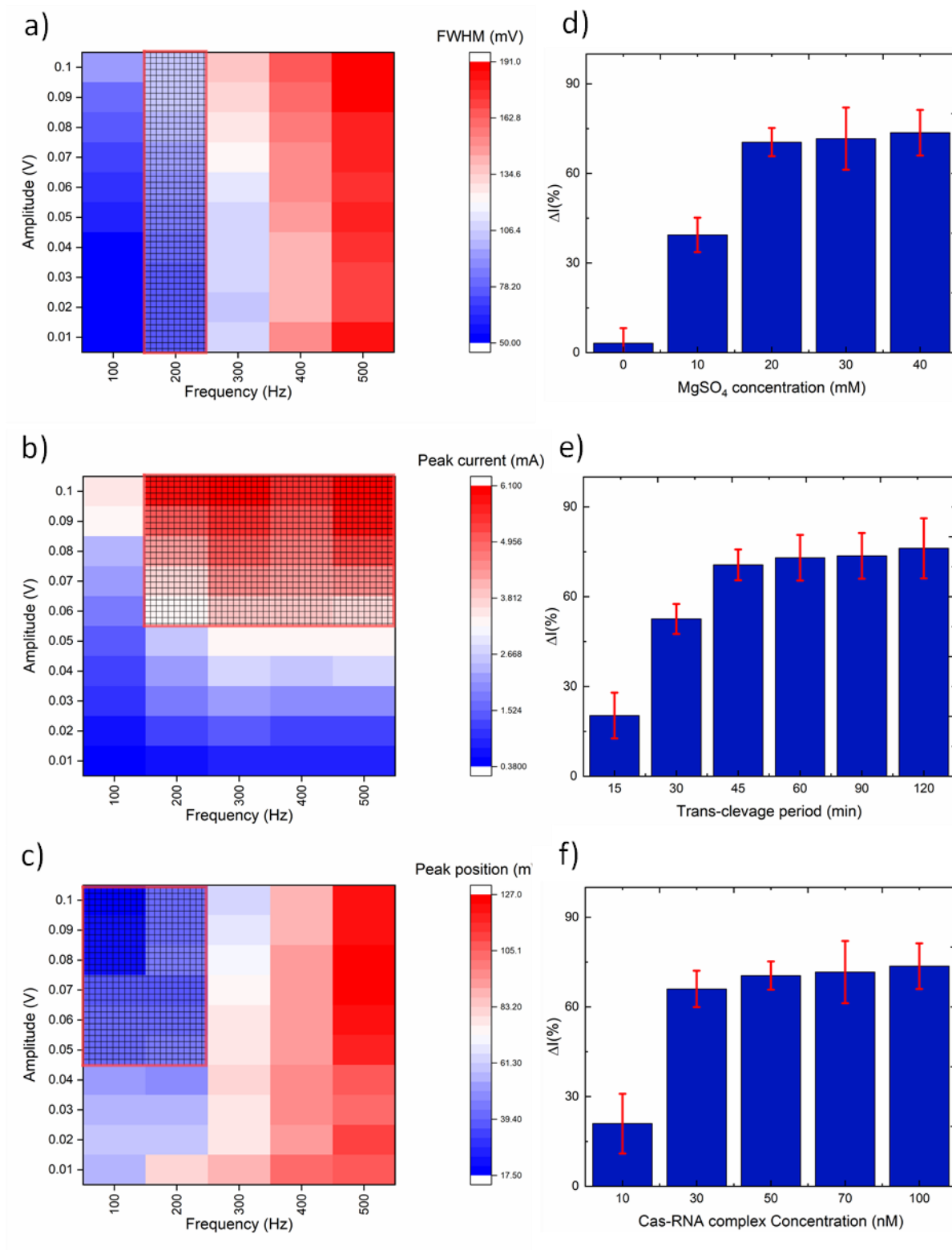


**Figure 4.3** Heat maps of square wave voltammetry optimization for (a) full width half maximum (FWHM), (b) peak current, and (c) peak position, where meshed areas show the desired value ranges. SWV optimization was carried out by varying frequency from 100 to 500 Hz and amplitude from 0.01 to 0.1 V. The CRISPR system was optimized for percentage difference between treated and untreated electrode current as a function of (d)  $\text{MgSO}_4$  concentration, (e) trans-cleavage period, and (f) Cas-gRNA complex concentration.



After electrochemical optimization, silver metallization was investigated. As we described in our previous work, combining electrochemical and chemical reduction of silver on ssDNA could provide a two-fold increase in oxidative signal.<sup>79</sup> Here, optimizing the reducing potential and time (Figure 4.4a and b), indicated maxima values of -0.5 V and 3 minutes to obtain the maximum oxidative peak current of silver on ssDNA.

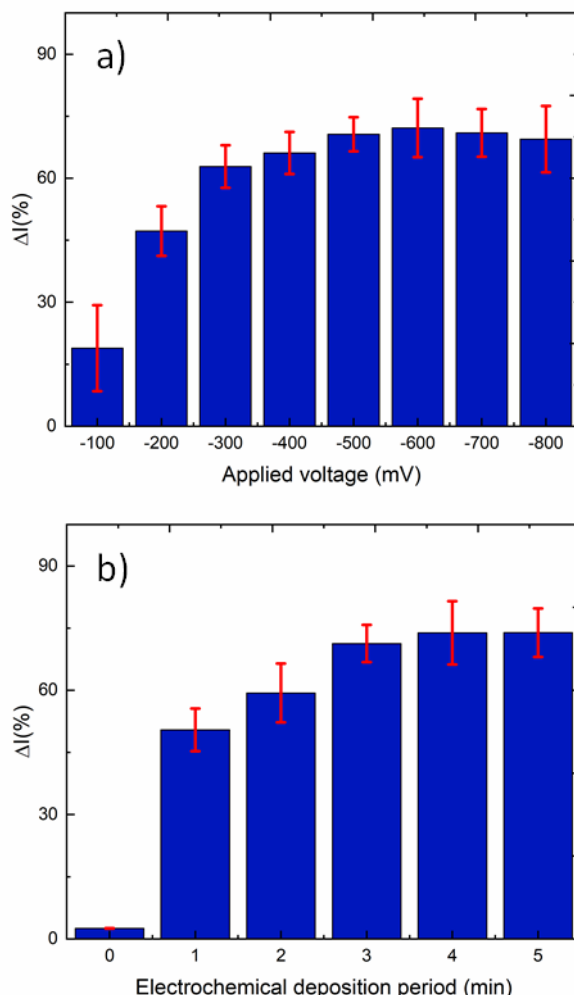


**Figure 4. 4** Electrochemical reduction optimization for E-Si-CRISPR as function of a) applied voltage (-100 to -800 mV), and b) electrodeposition time (0 to 5 minutes).

Next, the CRISPR/Cas system was optimized considering five parameters:  $\text{MgSO}_4$  concentration, triplex Cas12a concentration, trans-cleavage incubation time, ssDNA length, and ssDNA concentration. An important factor that can affect the Cas12a cleavage activity is the divalent cation  $\text{Mg}^{2+}$  concentration in the testing solution. The Cas12a RuvC domain is known to cleave ssDNA through the two metal ion mechanism, in which the  $\text{Mg}^{2+}$  ions induce conformational coordination of the RuvC domain and the ssDNA by shifting the spatial distribution of ssDNA around the RuvC active cutting center.<sup>235</sup> Therefore, we optimized the concentration of  $\text{MgSO}_4$  for the activity of trans-cleavage activity. As shown in Figure 4.3d, the Cas12a trans-cleavage is only activated in the presence of the  $\text{Mg}^{2+}$ , and we observed an optimal  $\text{MgSO}_4$  concentration of 20 mM. The triplex Cas12a was later optimized from 10 to 100 nM, with an optimum concentration observed at 50 nM (Figure 4.3f). Although the optimal trans-cleavage incubation time appears to be 45 minutes (Figure 4.3e), it should be noted that cis-cleavage is activated only for 30 min, whereas the trans-cleavage performs up to a few hours.<sup>226</sup>

We utilized the percentage difference in the electrochemical signal between the metallized ssDNA and triplex Cas12a-treated ssDNA using the following equation:

$$(\Delta I (\%)) = \frac{(\text{untreated ssDNA} - \text{treated ssDNA})}{(\text{untreated ssDNA signal})} \times 100 \quad (6.2)$$

for quantitative analysis, instead of direct electrochemical measurement, to obtain the best condition for E-Si-CRISPR. Having a trans-cleavage activity to cooperate with ssDNA silver metallization, ssDNA length is a necessary condition since it affects the obtained  $\Delta I$  value. In the general case, the longer the ssDNA, the greater the signal should be. However, the trans-cleavage is an uncontrollable activity, which should cleave the ssDNA at any position of the ssDNA on the electrode and give unpredictable results,<sup>65</sup> yet, we observed that it provided a reliable patterned results in rigid  $\Delta I$  value, as illustrated in **Figure 4.5a**. The  $\Delta I$  of 10 nt ssDNA provided the lowest value, while the optimum ssDNA length appeared to be 30 nt. Further, the ssDNA concentration was optimized not only to study the amount of that ssDNA that could be metallized, but also to study the accessibility of the Cas12a to cleave the ssDNA. **Figure 4.5b** shows that the optimal ssDNA condition is 1  $\mu\text{M}$ .

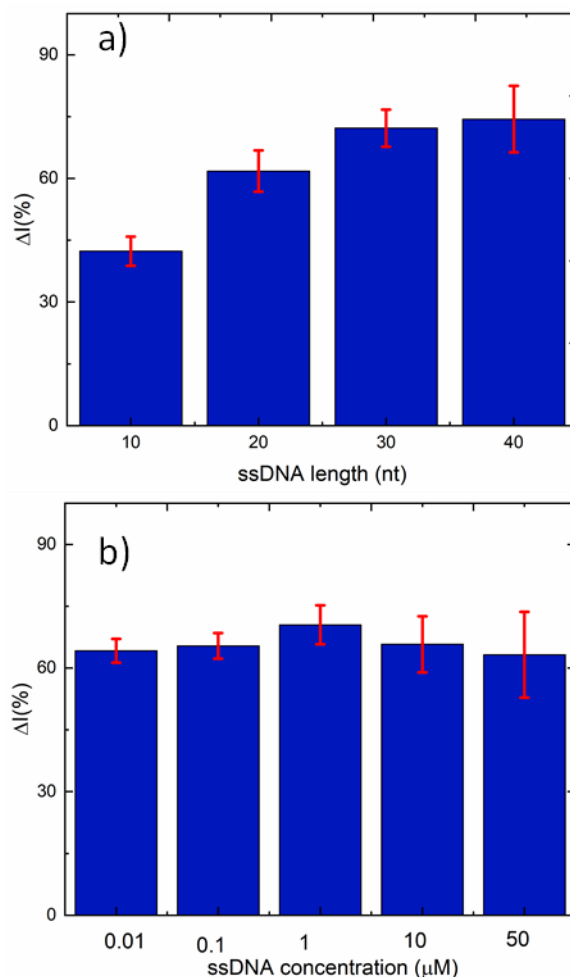


**Figure 4.5** a) Thiolated ssDNA length optimization on the electrode surface for E-Si-CRISPR, studied from 10 to 40 nt. b) Thiolated ssDNA concentration optimization on electrode surface for E-Si-CRISPR, studied from 0.01 to 50  $\mu\text{M}$ . The ssDNA was modified and the surface passivated by MCH later.

### 4.3.3 Analytical performance

#### 4.3.3.1 Linearity, LoD, and LoQ

Based on the optimized trans-cleavage conditions, we evaluated the E-Si-CRISPR platform for the detection of the *mecA* gene. A dilution series of the *mecA* amplicon was studied from  $10^{-6}$  to  $10^2$  nM, which yielded a calibration curve for *mecA* with a broad dynamic range (fM to nM). **Figure 4.6a** shows the square wave voltammograms of *mecA* analysis using E-Si-CRISPR. A decrease of the electrochemical signal was observed when the *mecA* concentration increased, and exhibited no significant change once the concentration was up to the nanomolar level (**Figure 4.6b**). Linearity was observed over five orders of magnitude (10 fM to 1 nM,  $R^2 = 0.988$ , inset of **Figure 4.6b**), resulting in a calculated limit of detection ( $LoD = 3SD/slope$ ) and quantification ( $LoQ = 10SD/slope$ ) of 3.5 fM and 10 fM, respectively. It is worth mentioning that this LoD surpasses the previously published LOD for non-enzymatically amplified nucleic-acid detections,<sup>226-227</sup> indicating that silver metallization indeed improves sensitivity for electrochemical-based CRISPR analysis.

#### 4.3.3.2 Accuracy and Precision

To ensure the accuracy of the E-Si-CRISPR technique, we chose three concentrations of the *mecA* gene (i.e. 0.1, 1, and 10 pM) and compared it directly with the PCR method. Results, as shown in **Figure 4.9a**, revealed no significant difference between the methods, judged by a paired t-test ( $t_{value} = 0.92 < t_{critical} = 1.86$ ;  $N = 9$ ; 95% confidence;  $\alpha=0.05$ ), indicating that the E-Si-CRISPR provides reliable accuracy for *mecA* gene analysis. Further, a multi-day study was performed to evaluate the precision of the E-Si-CRISPR technique. Running 10 repeats of 10 pM *mecA* amplicon concentration providing an acceptable %RSD ( $100 \times SD/average$ ) of 4.3% (less than 5%).<sup>82</sup> These accuracy and precision testes show the great promising of the E-Si-CRISPR for gene analysis with excellent analytical performance.

#### 4.3.3.3 Human serum

Since the MRSA is a bacterium that causes skin infection in wounds, and can ultimately infect the bloodstream, the ability to detect it in human serum is vital. Therefore, human serum was applied to prepare a concentration series of the *mecA* amplicon, then performed as described for the buffer-based analysis. The calibration curve is shown in **Figure 4.6c**, and exhibits only a slight difference was compared to the buffer-based calibration curve, with a slight decrease in the electrochemical signal in the serum case. However, it should be noted that the slope obtained from linearity could indicate the sensitivity of each system. Thus, we compared slope from the linear range for both media, observing that the slope of the human serum (15.5,  $R^2 = 0.946$ ) is only slightly decreased compared to the buffer (17.1,  $R^2 = 0.988$ ). However, it is not necessarily correct to assume that the excellent sensitivity of detection in buffer is exactly repeatable in serum. Therefore, we chose three *mecA* gene concentrations (1, 10, and 100 nM) from both media and compared the results. **Figure 4.6d** shows that both methods provided results that are not significantly different, judging by a paired t-test ( $t_{value} = 0.94 < t_{critical} = 1.86$ , 95% confidence level,  $\alpha=0.05$ ,  $N=9$ ). This could be due to the E-Si-CRISPR reaction only occurring on the electrode surface, which later will be washed before performing silver metallization. Therefore, there should low interference that could inhibit the detection. These results ensured that the E-Si-CRISPR is capable of being applied in human serum medium with excellent analytical performance.

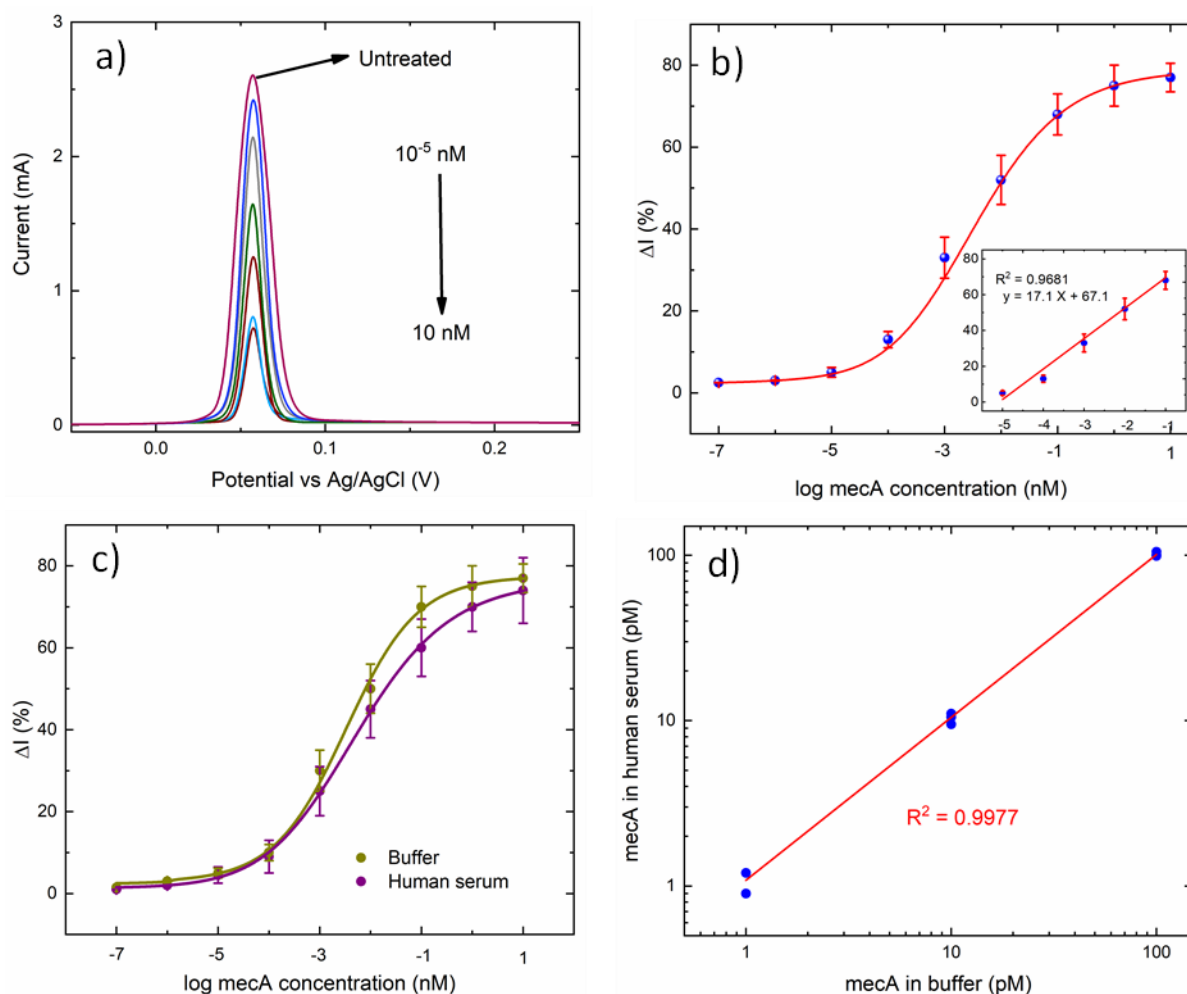


**Figure 4.6** (a) Square wave voltammograms of a series of *mecA* concentrations (10<sup>-6</sup> to 10<sup>2</sup> nM) using the previously optimized conditions: ssDNA concentration = 1  $\mu$ M, ssDNA length = 30 nt, applied potential = -0.5 V, electrochemical deposition time = 3 minutes, Cas-gRNA complex concentration = 50 nM, a trans-cleavage period = 45 min, MgSO<sub>4</sub> concentration = 20 mM, step potential = 0.01 V, amplitude = 0.06 V, and frequency = 200 Hz. (b) Calibration curve of anodic current ( $N = 3$ ) obtained from (a), versus *mecA* concentration (linear range 10 fM to 100 pM shown in inset). Comparison of (a) calibration curves between buffer- and human serum-based tests, using the concentration series of *mecA* as in figure b, and (d) detection of the *mecA* gene in both media, at 1, 10, and 100 pM.

#### 4.3.3.4 Cas selectivity

A distinct advantage of the CRISPR system compared to the other biosensor approaches is the excellent selectivity achieved in the detection of nucleic acids, tolerating mismatches even down to a single nucleotide level.<sup>219</sup> Therefore, we further studied the E-Si-CRISPR analytical performance by investigating Cas enzyme selectivity. Mismatched oligonucleotides at the upper strand target molecule were synthesized, as shown in red in **Figure 4.7a and b**, assigning to the second position of the PAM, and the first, fifth and tenth positions of the target molecule, denoted as mmTPAM, mmT1, mmA5, and mmG10, respectively. Although the PAM is not a complementary part of the protospacer, it is a crucial nucleotide sequence that activates Cas12a cleavage activity. Consequently, the lowest  $\Delta I$  was observed when a single mismatch was found in the PAM. In addition, when further mismatching on the protospacer binding nucleotide is tested, the greater the observed  $\Delta I$ . No significant difference was observed compared to the WT was observed when the mismatch was at the tenth position. These results indicated that the Cas12a works selectively once mismatching is found on PAM and on the target nucleotides that is close to the PAM, up to tenth position.

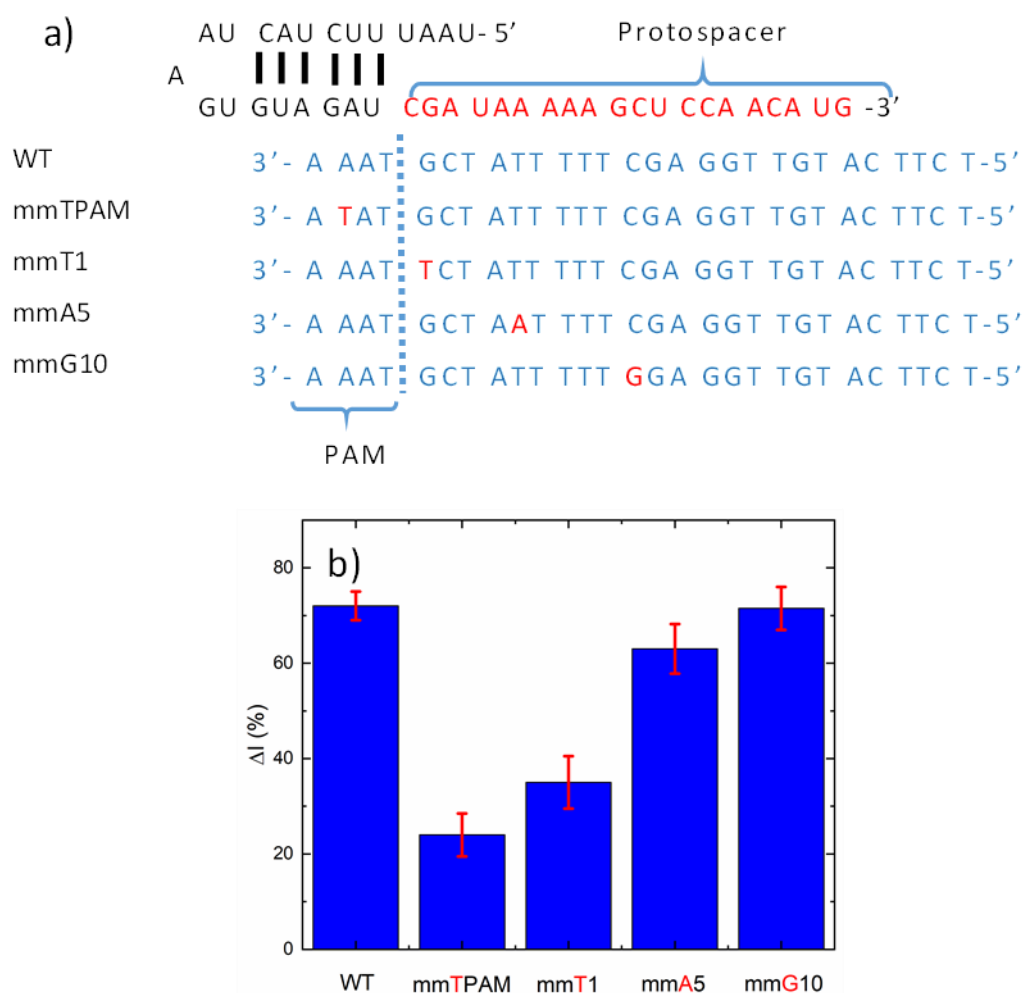


**Figure 4.7** (a) Target strands with mismatches at different positions, including in the PAM region and crRNA complement at different positions (1, 5, and 10). (b) Evaluation of the influence of mismatches at different positions on the E-CRISPR signal. A target concentration of 1 pM was applied for all the targets (wild type (WT) and mismatched targets).

#### 4.3.3.5 Bacterial selectivity

Since the site of MRSA infection is a wound/skin, the environment from which MRSA will be collected is blood serum, which can contain other common bacteria, including *E. coli*, *E. faecalis*, *L. monocytogenes*, *S. epidermidis*, and methicillin-sensitive *S. aureus* (MSSA). Therefore, to test the selectivity of the E-Si-CRISPR technique, we collected those bacteria colonies in TE buffer and incubated at 95 °C for 5 minutes, then prepared a human serum solution at 1:1 volume ratio, before application to the E-Si-CRISPR electrode.

The preliminary test showed that the sensitivity of detection was decreased when applying the real bacteria on the E-Si-CRISPR. However, it should be noted that our *mecA* gene amplicon that was used for the previous studies is 685 bp. We hypothesize that the drop in sensitivity is due to the fact that the size of MRSA genome is far longer than the *mecA* gene amplicon that we used in the previous studies, thus requiring a longer incubation time for the Cas enzyme to find the specific target. Jeon and coworkers reported that Cas enzymes use a ‘walking’ mechanism, which is randomly capturing the dsDNA and moving along to find the target gene; thus, the longer the target sequence, the longer incubation time is required.<sup>236</sup> Although the previous study of *mecA* gene detection in the human serum medium does not show a significantly different sensitivity compared to the buffer, a slight signal decrease was observed due to the complicated environment. Therefore, the lysed bacteria prepared in human serum could affect Cas activity, and thus incubation time for lysed bacteria in human serum should be further studied.

**Figure 4.8** presents the incubation time study for E-Si-CRISPR for lysed bacteria in human serum medium. The optimum incubation time was found to be 50 to 60 minutes, which is slightly different from the *mecA* amplicon in human serum, studied before. To ensure that the Cas works well in the complex matrix, we chose an incubation time of 60 minutes. As illustrated in **Figure 4.9b**, when E-Si-CRISPR was tested for MRSA against *E. coli*, *E. faecalis*, *L. monocytogenes*, *S. epidermidis*, and MSSA in human serum, the technique was clearly able to specifically identify MRSA. These results ensure that the chosen protospacer binding with the PAM sequence is highly selective, as well as the cleavage activity of the Cas even in the complex matrix.

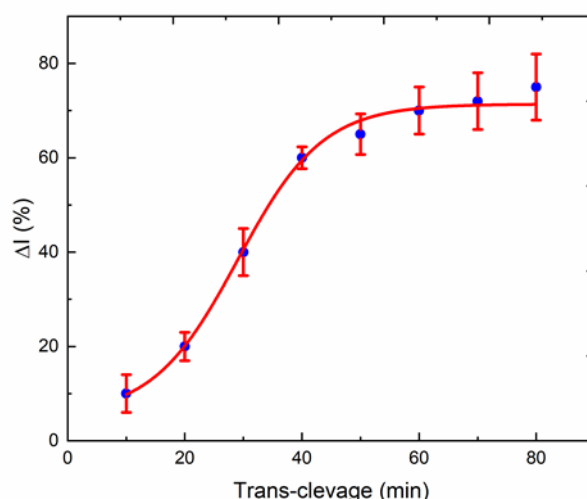


**Figure 4. 8** Trans-cleavage period optimization of the lysed MRSA for E-Si-CRISPR, studied from 10 to 80 minutes.

#### 4.3.3.6 Stability

In a real-world setting, a field-deployable device should be able to be stored for a reasonable time (i.e. at least month) without a significant decrease in inefficiency. To test the stability of the E-Si-CRISPR technique, we prepare the many ssDNA-modified electrodes and stored then in a dry box under nitrogen environment at 4 °C. As shown in **Figure 4.9c**, we collected E-Si-CRISPR data every five days for three concentrations (0.1 pM, 1 pM, and 10 pM) and compared the results gathered across thirty days. **Figure 4.9d** shows that the %efficiency is decreasing over the month, but by less than 10%. The decreasing signal could be due to the partial decomposition or deconjugation of the ssDNA from the electrode surface. Further, the electrochemical signals between the freshly and stored electrodes were compared, resulting in the insignificantly different judged by paired t-test study ( $t_{\text{value}} = 0.37 < t_{\text{critical}} = 1.86$ ;  $N = 9$ , 95% confidence,  $\alpha = 0.05$ ). This evidence confirmed that E-Si-CRISPR provides excellent stability and reproducibility for field-deployable diagnostics.

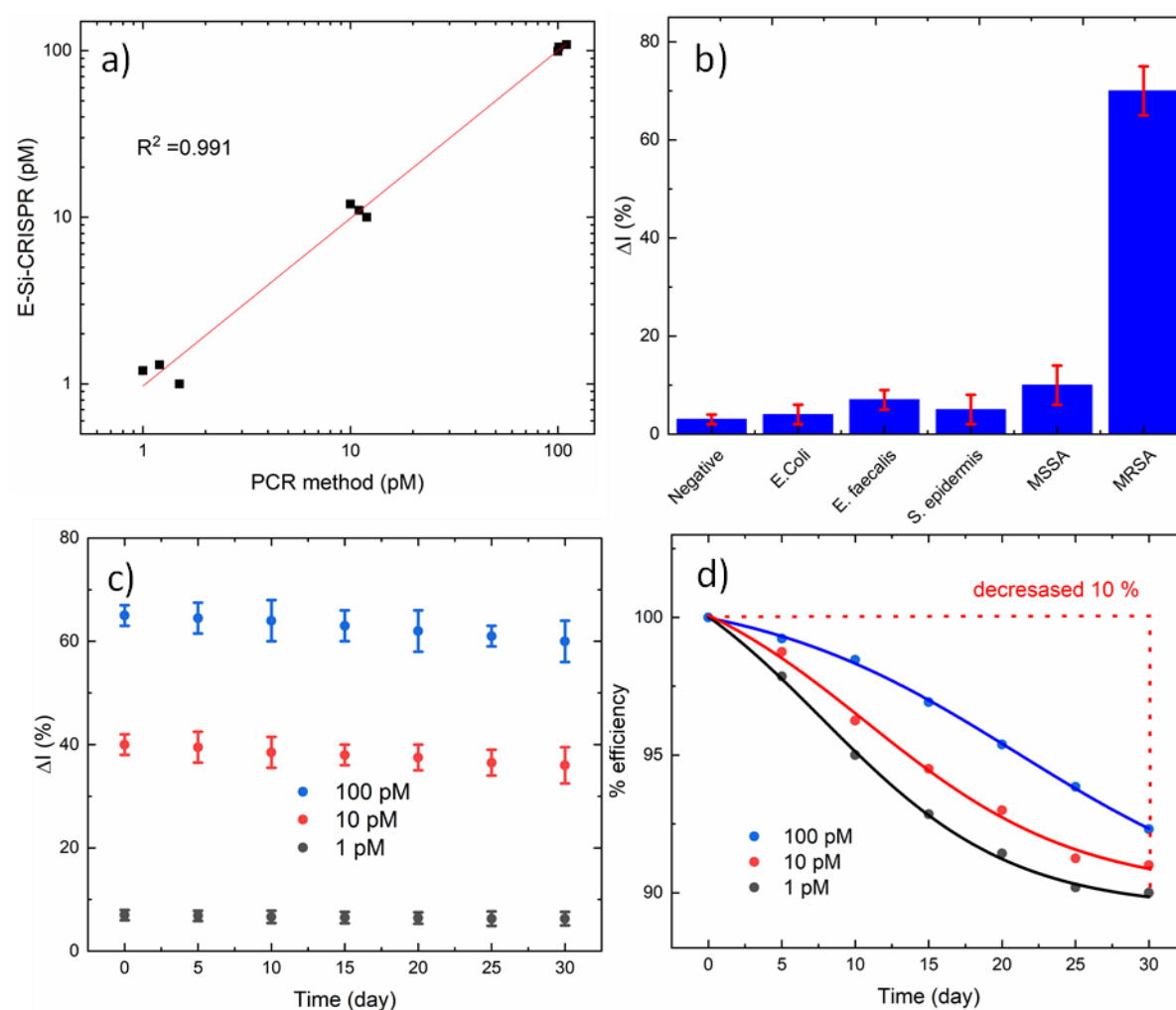


**Figure 4.9** (a) Comparison of *mecA* concentrations between the E-Si-CRISPR and PCR at 1, 10 and 100 pM. (b) Specificity test for MRSA versus other bacteria for the E-Si-CRISPR technique, revealing excellent specificity. (c, d) Stability of the ssDNA-immobilized electrode for detecting *mecA* (1, 10, and 100 pM) over 30 days ( $N = 3$ ).

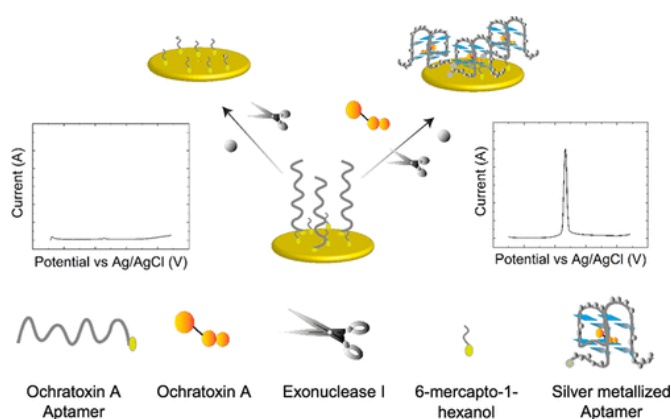
## 4.4 Conclusions

We have presented a novel ultra-sensitive electrochemical CRISPR/Cas biosensor using silver metallization to improve the sensitivity of the detection of drug-resistant bacteria, without requiring DNA amplification. The E-Si-CRISPR technique exhibited excellent specificity for the *mecA* gene, activating the cis- and trans-cleavage activities of Cas12a. Removal of immobilized ssDNA was performed on the electrode surface after trans-cleavage activation in the presence of the target gene. The addition of Ag<sup>+</sup> followed by a double reduction method metalized the remaining ssDNA, yielding a significant signal enhancement in square wave voltammetry-based measurements. CRISPR/Cas and square wave voltammetry were optimized carefully to achieve an excellent analytical performance for the E-Si-CRISPR technique, with an LoD of 3.5 fM, an LoQ of 10 fM, and linearity between 10 fM to 100 pM (five orders of magnitude) against the *mecA* amplicon (685 bp). E-Si-CRISPR was compared to the gold-standard PCR analysis, and showed excellent agreement for great accuracy. The E-Si-CRISPR analytical performance was maintained even in human serum. Further, mismatch analysis was performed to study the Cas12a selectivity, providing excellent selectivity down to the single nucleotide level. The selectivity of the E-Si-CRISPR technique was also employed to detect lysed MRSA solution against other common bacteria, yielding an excellent selectivity to detect specific genes. It should be noted that the use of an enzyme in such a sensor could pose potential complications for field-deployable applications, however we suggest that careful freeze-drying of enzymes could be used to extend the system shelf life.<sup>64</sup> Overall, the developed E-Si-CRISPR technique allows the detection of MRSA with high sensitivity, selectivity, accuracy, precision, and robustness even in lysed bacteria solution, and should be further developed for real samples in the near future.



## Chapter 5

# An Exonuclease I-Assisted Silver-Metallized Electrochemical Aptasensor for Ochratoxin A Detection



Ochratoxin A (OTA)—a mycotoxin produced by *Aspergillus* and *Penicillium* fungi—is a carcinogen and common trace contaminant in agricultural and processed food products. As consumption is detrimental to human and animal health, regular product monitoring is vital, and highly sensitive and portable OTA sensors are necessary in many circumstances. Herein, we report an ultrasensitive, electroanalytical aptasensor for precise determination of OTA at trace levels. The sensor leverages a DNA aptamer to capture OTA and silver metallization as a signal enhancer. Exonuclease I is used to digest unbound aptamers, engendering excellent background signal suppression and sensitivity enhancements. Efficient optimization of assay conditions is achieved using central composite design (CCD), allowing rapid evaluation of both the electrode and square wave voltammetry parameter space. The sensor exhibits excellent analytical performance, with a concentration limit of detection of 0.7 pg/mL, a limit of quantitation of 2.48 pg/mL, and a linear dynamic range ( $R^2 = 0.968$ ) of over 6 orders of magnitude (between 1 pg/mL and 0.1  $\mu\text{g/mL}$ ). Direct comparison with ultra-performance liquid chromatography (UPLC) indicates excellent analytical performance for standard solutions ( $R^2 = 0.995$ ) and spiked beer samples ( $R^2 = 0.993$ ), with almost quantitative recovery and less than 5% relative standard deviation (RSD).

This chapter is adapted from a paper entitled "*An Exonuclease I-Assisted Silver-Metallized Electrochemical Aptasensor for Ochratoxin A Detection*", authored by Akkapol Suea-Ngam, Philip D. Howes, Claire E. Stanley, and Andrew J. deMello. Published in *ACS Sensors* **2019**, *4*, 6, 1560–1568.

## 5.1 Introduction

Environmental toxins, and especially those contained in foods, present a major health burden, with particular severity in the developing world. This burden includes inducement of a number of diseases, including cancer, diabetes, neurotoxicology, and high blood pressure. Several toxins (e.g. cyanide and pesticides) can kill immediately by consumption in the milligram level. Other toxins, including OTA, aflatoxin, and heavy metals might not induce disease as fast as many pathogens, identifying the environmental cause of disease is non-trivial but absolutely vital. State-of-the-art technologies have been established and used as 'gold-standard' methods to detect toxins, in line with recommendations from international and national organisations.<sup>237</sup> Although these methods to detect toxins are commonly less complicated than those used for pathogens, they are typically cumbersome and costly system, preventing application in resource-limited areas; thus, point-of-use methods is needed.

An alternative point-of-need toxin analysis platform is the disposable microfluidic concept, i.e. PADs and screen-printed electrodes. These comprise ubiquitous materials, e.g. paper and hydrophobic materials, and require less reagent, making the approach increasingly popular. One crucial benefit of such platforms is the excellent sensitivity detection thanks to the large surface-to-volume character of microfluidic systems, which allows excellent and inexpensive analytical efficacy.<sup>214</sup> However, to detect organic compound-based toxins (e.g. OTA and aflatoxin), antibodies are typically required, which can massively increase manufacturing costs of devices, thus restricting their distribution in resource-limited settings.

Ochratoxin A (OTA) is a mycotoxin produced by various types of *Aspergillus* and *Penicillium* fungi. It is classified as a carcinogen to humans (Group 2B) by the International Agency for Research on Cancer.<sup>237</sup> It is commonly found in food products, including wheat, corn, coffee, wine, beer, and nuts because of the difficulty in controlling fungal growth, particularly in soil environments.<sup>238</sup> The current gold-standard for OTA detection uses HPLC coupled with fluorescence detection,<sup>239</sup> but this is operationally complex, costly, and limited for use in well-equipped laboratories. Accordingly, there is a need for efficient, cheap, and rapid analytical tools for application in non-laboratory and in-the-field environments.<sup>240</sup>

Electrochemical detection is commonly used in toxin analysis<sup>241</sup> and, due to its instrumental simplicity and high sensitivity, shows great promise for food and environmental control in non-laboratory or resource-limited settings.<sup>242-243</sup> Electrochemical detection is frequently facilitated through the use of biorecognition elements such as DNA, enzymes, and antibodies. Aptasensors, which use artificial oligonucleotides (aptamers) as recognition elements in biosensing, have recently been exploited as efficient and inexpensive biorecognition elements.<sup>244</sup> Indeed, such sensing platforms have found application in food control for detecting toxins from fungi, bacteria, algae, viruses, drugs, pesticide residues, and heavy metals.<sup>245</sup>

In a typical aptasensor, complementary DNA is used to facilitate binding of reporters, which in turn generate an electrochemical signal.<sup>111, 246-247</sup> However, such an approach increases both assay complexity and associated costs, and thus it is preferable to use only single-stranded DNA (ssDNA), without a complementary probe. Significantly, aptamers can be directly modified with redox active labels (such as methylene blue and ferrocene), to affect their use as ssDNA electrochemical probes.<sup>248-249</sup> However, with only one dye molecule per aptamer, at either the 3' or 5' end, signal generation capacity is severely limited. Furthermore, such dye-modified aptamers can only be efficiently conjugated to electrode surfaces at densities of below  $10^{13}$  molecules/cm<sup>2</sup>.<sup>250</sup> Since the extraction of well-defined electrochemical signals requires dye coverages of  $\sim 6 \times 10^{15}$  molecules cm<sup>-2</sup>, both sensitivity and limits of detection are severely compromised.<sup>251</sup> To address this issue, DNA metallization (where electrostatic attraction

between negatively charged DNA and positively charged metal ions is used to form metal nanowires subsequent to the application of a reducing agent or electric potential) can be used to realize sensitive biological sensing.<sup>252</sup> For example, Wang and co-workers have used silver metallization on DNA structures to obtain well-defined electrochemical signals,<sup>253</sup> with the basic method subsequently being used in a number of bioanalytical applications.<sup>254</sup> That said, although DNA metallization can provide for large enhancements in electrochemical signal, problems with excessive background currents have limited its application.<sup>255</sup> In an effort to address this problem, Wu et al. used exonuclease III, an enzyme that performs a unistrand 3' to 5' end digestion in double-stranded DNA (dsDNA), within a DNA-based electrochemical system to digest unoccupied DNA probes.<sup>231</sup> This approach successfully reduced background currents, and in turn enhanced both the sensitivity and selectivity of the detection process. Inspired by these advances, we herein report an electrochemical sensor for OTA detection using silver metallization of aptamers on disposable screen-printed gold electrodes (SPGEs), with sensitivity and selectivity enhancements effected by exonuclease I (Exo I). Exo I acts to digest ssDNA in the 3' to 5' direction, and thus removes unoccupied aptamers but cannot act on the G-quadruplex formed upon OTA binding. This significantly reduces nonspecific background metallization. Additionally, both chemical and electrochemical reduction are used to further enhance analytical sensitivity. For assay optimization we employ a central composite design (CCD) approach to explore assay parameter space in a rapid and efficient manner.<sup>230</sup> Finally, the resulting sensor platform is used to detect and quantify OTA in commercial beverage samples.

## 5.2 Material and methods

### 5.2.1 Materials and reagents

The OTA aptamer (5'-HS(CH<sub>2</sub>)<sub>6</sub> AAA AAA AAA AGAT CGG GTG TGG GTG GCG TAA AGG GAG CAT CGG ACA-3') was purchased from Microsynth (Balgach, Switzerland).<sup>228</sup> Ochratoxin A (OTA), Aflatoxin B1 (AFB1), Aflatoxin B2 (AFB2), AgNO<sub>3</sub>, NaBH<sub>4</sub>, HEPES, EDTA, Trizma base, NaNO<sub>3</sub>, CaCl<sub>2</sub>, 6-mercapto-1-hexanol (MCH), K<sub>3</sub>[Fe(CN)<sub>6</sub>], K<sub>4</sub>[Fe(CN)<sub>6</sub>], PBS tablets, NaOH, H<sub>2</sub>SO<sub>4</sub>, NaCl, and KCl were purchased from Sigma-Aldrich (Buchs, Switzerland) and used as received. All other reagents, including Ochratoxin B (OTB) (AdipoGen AG, Epalinges, Switzerland), TCEP (Alfa Aesar, Karlsruhe, Germany), HCl (Fluka, Buchs, Switzerland), and MgCl<sub>2</sub> (Acros Organics, Geel, Belgium), were analytical reagent grade and used as received. Exo I was purchased from New England Biolabs (Frankfurt am Main, Germany). All aqueous solutions were prepared with DNase and RNase free water (Thermo Fisher Scientific, Reinach, Switzerland). Electrochemical measurements were performed with a PGSTAT204 AutoLab (Metrohm, Zofingen, Switzerland). Screen-printed gold electrodes were purchased from Dropsens (Metrohm, Zofingen, Switzerland). Cyclic voltammetry (CV) data for conductivity characterization were collected at 100 mV s<sup>-1</sup> in 10 mM K<sub>3</sub>[Fe(CN)<sub>6</sub>], 1 M KCl, and 100 mM PBS (pH 7.42) unless otherwise indicated. Electrochemical impedance spectroscopy (EIS) was performed using an Impedance Analyzer SP-300 (Bio-Logic, Seyssinet-Pariset, France) in 0.1 M PBS containing 10 mM K<sub>3</sub>[Fe(CN)<sub>6</sub>]/K<sub>4</sub>[Fe(CN)<sub>6</sub>] (1:1), with 1 M KCl as the supporting electrolyte. Impedance spectra were recorded at frequencies between 10<sup>-2</sup> and 10<sup>5</sup> Hz. The applied potential was 0.2 V with a sinusoidal potential of 5 mV amplitude.

### 5.2.2 Electrochemical detection

SPGEs were electrochemically cleaned using a series of oxidation and reduction cycles in 0.5 M NaOH, 0.5 M H<sub>2</sub>SO<sub>4</sub>, 0.01 M KCl with 0.1 M H<sub>2</sub>SO<sub>4</sub>, and 0.05 M H<sub>2</sub>SO<sub>4</sub>, using cyclic voltammetry (100 mV s<sup>-1</sup>, from -1 to 1 V) prior to modification with the thiolated OTA aptamer. For sample

analysis, different concentrations of the thiolated OTA aptamer were pretreated with 10 mM TCEP in buffer (10 mM Tris-HCl, 1 mM EDTA, 0.1 M NaCl, pH 7.4) for 30 min to reduce thiol–thiol bonds. Next, 10  $\mu$ L of the reduced aptamer solution was dropped onto the electrochemically cleaned electrode surface, and kept under high humidity in the dark and at room temperature for 12 h. Subsequently, the modified surface was rinsed with buffer solution and then passivated with MCH in Tris-HCl buffer (pH 8.3) for 30 min. After washing, the electrode was dried using nitrogen gas, and again stored in the dark under nitrogen.

For electrochemical detection, modified electrodes were immersed for 10 min in the sample, as prepared in binding buffer (10 mM Tris, pH 8.5, 120 mM NaCl, 5 mM KCl, 10 mM MgCl<sub>2</sub>, and 20 mM CaCl<sub>2</sub>). Next, 50  $\mu$ L of Exo I enzyme solution (100–500 U/mL) was applied to the electrode, at room temperature, to digest excess aptamer. The washed electrode was then immersed in 100  $\mu$ M AgNO<sub>3</sub> in 20 mM HEPES and 100 mM NaNO<sub>3</sub> (pH 7.4) for 1 h and subsequently washed with water. Next, the modified electrode was dipped into a freshly prepared 10 mM of NaBH<sub>4</sub> (in 20 mM HEPES buffer) for 10 min, washed with water and placed in an electrolyte (0.1 M NaCl and 0.1 M NaNO<sub>3</sub>) for the electrochemical measurement. Electrochemical deposition was achieved with a  $-0.5$  V applied potential prior to square wave voltammetry from  $-0.3$  to  $0.5$  V versus Ag/AgCl.

### 5.2.3 System optimization

Central composite design (CCD) was used to optimize key experimental variables including aptamer concentration, enzyme concentration, and incubation time. All studied parameters were considered to be independent. The ranges and levels of the chosen variables are reported in **Table 5.1** and **Figure 5.1**.

**Table 5.1** Experimental Range and Level of the Respective Independent Variables for Electrode Optimization.

Variables (unit)	Actual			Coded Level		
	Low	Middle	High	Low	Middle	High
Aptamer concentration ( $\mu$ M)	0.5	1	1.5	-1	0	1
Enzyme concentration (U/mL)	200	300	400	-1	0	1
Incubation time (minutes)	30	60	90	-1	0	1

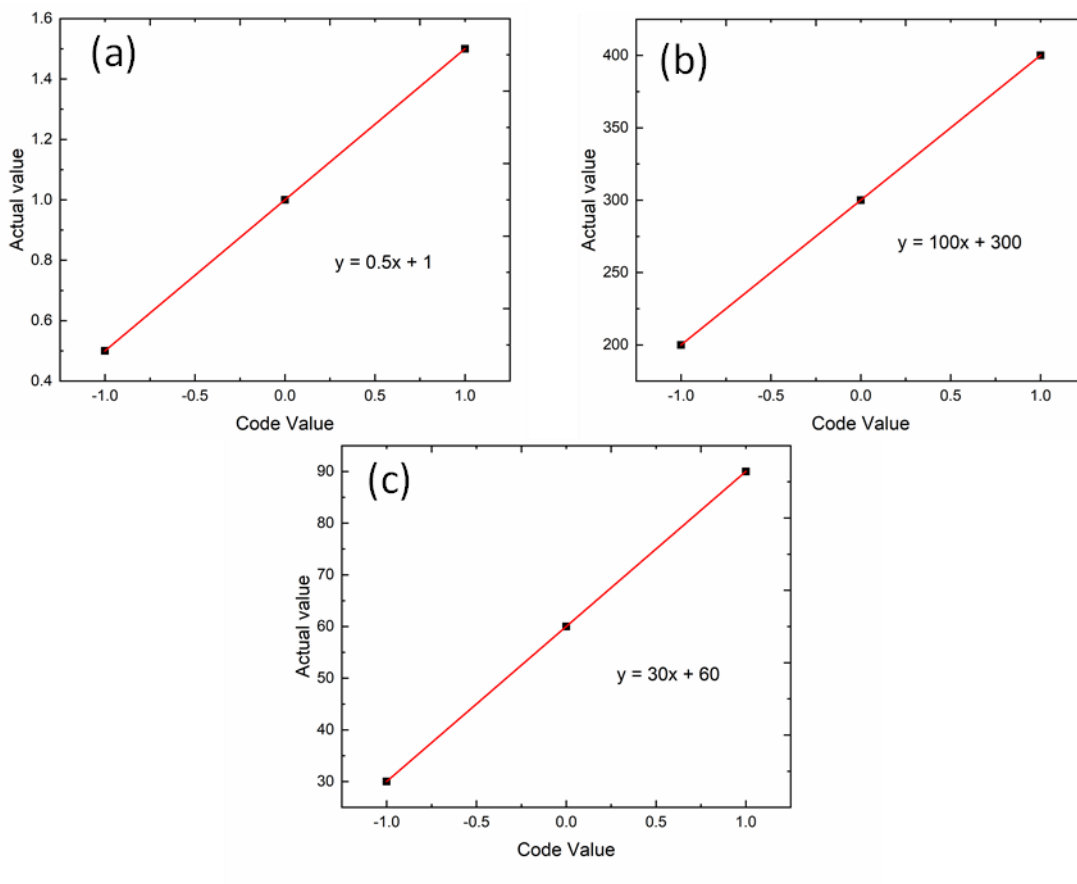


**Figure 5.1** Conversion of actual and coded values of (a) aptamer concentration, (b) enzyme concentration, and (c) incubation time for the central composite design.

Three factors with a total of 20 experimental runs were suggested by CCD, as displayed in **Table 5.4**.<sup>256</sup> Response surface modeling, statistical analysis, and optimization were conducted using the matrix shown in **Table 5.2** and **Equation 5.1** and **5.2**.

**Table 5.2** The central composite design model of the total 20 experimental runs and the polynomial factor for the equation calculation.

Run	Intercept	X <sub>1</sub>	X <sub>2</sub>	X <sub>3</sub>	X <sub>1</sub> <sup>2</sup>	X <sub>2</sub> <sup>2</sup>	X <sub>3</sub> <sup>2</sup>	X <sub>1</sub> X <sub>2</sub>	X <sub>1</sub> X <sub>3</sub>	X <sub>2</sub> X <sub>3</sub>	Response
1	1	1	1	1	1	1	1	1	1	1	Y
2	1	1	1	-1	1	1	1	1	-1	-1	Y
3	1	1	-1	1	1	1	1	-1	1	-1	Y
4	1	1	-1	-1	1	1	1	-1	-1	1	Y
5	1	-1	1	1	1	1	1	-1	-1	1	Y
6	1	-1	1	-1	1	1	1	-1	1	-1	Y
7	1	-1	-1	1	1	1	1	1	-1	-1	Y
8	1	-1	-1	-1	1	1	1	1	1	1	Y
9	1	1.68	0	0	2.8224	0	0	0	0	0	Y
10	1	-1.68	0	0	2.8224	0	0	0	0	0	Y
11	1	0	1.68	0	0	2.8224	0	0	0	0	Y
12	1	0	-1.68	0	0	2.8224	0	0	0	0	Y
13	1	0	0	1.68	0	0	2.8224	0	0	0	Y
14	1	0	0	-1.68	0	0	2.8224	0	0	0	Y
15	1	0	0	0	0	0	0	0	0	0	Y
16	1	0	0	0	0	0	0	0	0	0	Y
17	1	0	0	0	0	0	0	0	0	0	Y
18	1	0	0	0	0	0	0	0	0	0	Y
19	1	0	0	0	0	0	0	0	0	0	Y
20	1	0	0	0	0	0	0	0	0	0	Y

**Table 5.3** The square wave voltammetric signal obtained from conditions designed in the CCD.

RUN	Repeat						Average	Standard deviation		Δpeak	Normalized current (%)	
	1		2		3			Response	BG			
	Response	BG	Response	BG	Response	BG	Response	BG	Response	BG		
1	890	130	910	150	901	140	900.33	140.00	10.02	10.00	760.33	84.45
2	923	190	915	185	925	195	921.00	190.00	5.29	5.00	731.00	79.37
3	845	198	852	195	853	205	850.00	199.33	4.36	5.13	650.67	76.55
4	840	320	835	310	850	315	841.67	315.00	7.64	5.00	526.67	62.57
5	652	80	649	85	655	75	652.00	80.00	3.00	5.00	572.00	87.73
6	680	155	674	145	670	149	674.67	149.67	5.03	5.03	525.00	77.82
7	648	65	650	54	652	58	650.00	59.00	2.00	5.57	591.00	90.92
8	656	303	654	298	655	295	655.00	298.67	1.00	4.04	356.33	54.40
9	918	152	910	152	905	148	911.00	150.67	6.56	2.31	760.33	83.46
10	520	103	522	96	518	98	520.00	99.00	2.00	3.61	421.00	80.96
11	821	145	811	150	830	152	820.67	149.00	9.50	3.61	671.67	81.84
12	810	290	810	310	810	303	810.00	301.00	0.00	10.15	509.00	62.84
13	770	145	785	148	788	152	781.00	148.33	9.64	3.51	632.67	81.01
14	815	298	808	396	810	303	811.00	332.33	3.61	55.19	478.67	59.02
15	810	195	812	210	814	202	812.00	202.33	2.00	7.51	609.67	75.08
16	809	200	809	200	813	210	810.33	203.33	2.31	5.77	607.00	74.91
17	813	196	808	205	808	215	809.67	205.33	2.89	9.50	604.33	74.64
18	807	210	813	203	807	202	809.00	205.00	3.46	4.36	604.00	74.66
19	813	195	807	195	813	195	811.00	195.00	3.46	0.00	616.00	75.96
20	808	198	813	201	807	200	809.33	199.67	3.21	1.53	609.67	75.33

\*BG is background signal from the blank solution.

Using **Table 5.2** with the results from **Table 5.3**, it can be fitted with general regression **Equation 5.1**:

$$y = b \cdot D \quad (5.1)$$

where  $y$  is a matrix of response,  $b$  is a variable coefficient, and  $D$  is a matrix of variables. Here, matrix response and variables were known, as shown in **Table 5.2** and **5.3**, thus, the coefficient remains to be calculated. To obtain the coefficient, a pseudo inverse was applied to avoid bias of calculation due to the number of zeros in the variables matrix. Therefore, the coefficient can be calculated using **Equation 5.2**:

$$b = (D^T \cdot D)^{-1} \cdot D^T \cdot y \quad (5.2)$$

Where  $D^T$  is transposed variables matrix, and  $(D^T \cdot D)^{-1}$  is the inverse of the multiplied value of the transposed  $D$  and  $D$ . The calculated coefficients were rendered into a column where the first value was intercept and the others belonged to each of the variables, respectively.

Paired t tests and coefficients of determination ( $R^2$ ) were used in the analysis of output data. Currents were normalized using the percentage difference between the analyte peak and the background as shown in **Equation 5.3**:

$$\text{Normalized current (\%)} = \frac{|I_{\text{peak}} - I_{\text{background}}|}{I_{\text{peak}}} \times 100 \quad (5.3)$$

Here,  $I_{\text{peak}}$  is the current obtained in the presence of the analyte, and  $I_{\text{background}}$  is the current obtained in absence of the analyte. Response data from experiments were expressed by polynomial regression to generate the model shown in **Equation 5.4**:

$$y = \text{intercept} + \sum_{i=1}^n b_i X_i + \sum_{i=1}^n b_{ii} X_i^2 + \sum_{i=1}^{n-1} \sum_{j=i+1}^n b_{ij} X_i X_j + \epsilon \quad (5.4)$$

Here  $y$  represents the predicted responses,  $b_i$  is the linear coefficient,  $b_{ii}$  is the quadratic coefficient,  $b_{ij}$  is the interaction coefficient, while  $X_i$  and  $X_j$  represent variables. Optimum values of variables were predicted by response surface analysis of the combined variables. The constraints in this study were applied to predict the optimum variable conditions that would yield the highest normalized current by inserting the desired conditions into the design shown in **Table 5.4**. The efficiency of the model was evaluated by performing the suggested experiments and comparing the output with the predicted results. The coefficient of determination ( $R^2$ ) and t-test (paired) were used to determine model robustness. The numerical optimization of the response was predicted based on a second order polynomial model.

**Table 5.4** Central Composite Design for Electrode Optimization Using Aptamer Concentration, Enzyme Concentration, Incubation Time, and Normalized Peak Current Response Data

Run	Aptamer ( $\mu\text{M}$ )	Enzyme (U/mL)	Incubation Time (minutes)	%difference of Peak and Background	
				Experiment	Predicted
1	1.5 (1)	400 (1)	90 (1)	84.45	81.54
2	1.5 (1)	401 (1)	30 (-1)	79.37	82.25
3	1.5 (1)	200 (-1)	90 (1)	76.55	78.03
4	1.5 (1)	200 (-1)	30 (-1)	62.57	60.99
5	0.5 (-1)	400 (1)	90 (1)	87.73	87.81
6	0.5 (-1)	401 (1)	30 (-1)	77.82	74.83
7	0.5 (-1)	200 (-1)	90 (1)	90.92	86.54
8	0.5 (-1)	200 (-1)	30 (-1)	54.40	55.81
9	1.84 (1.68)	300 (0)	60 (0)	83.46	82.82
10	0.16 (-1.68)	300 (0)	60 (0)	80.96	83.73
11	1 (0)	468	60 (0)	81.84	82.87
12	1 (0)	132	60 (0)	62.84	63.94
13	1 (0)	300 (0)	110.4	81.01	83.69
14	1 (0)	300 (0)	9.6	59.02	58.47
15	1 (0)	300 (0)	60 (0)	75.08	75.03
16	1 (0)	300 (0)	60 (0)	74.91	75.03
17	1 (0)	300 (0)	60 (0)	74.64	75.03
18	1 (0)	300 (0)	60 (0)	74.66	75.03
19	1 (0)	300 (0)	60 (0)	75.96	75.03
20	1 (0)	300 (0)	60 (0)	75.33	75.03

For square wave voltammetry parameters, CCD was used to determine the step potential, amplitude, and frequency using a similar protocol as described for electrode optimizations, as shown in **Table 5.5**. In addition, peak potential and peak full-width-half-maximum (fwhm) were used to identify optimum values for square wave voltammetry.

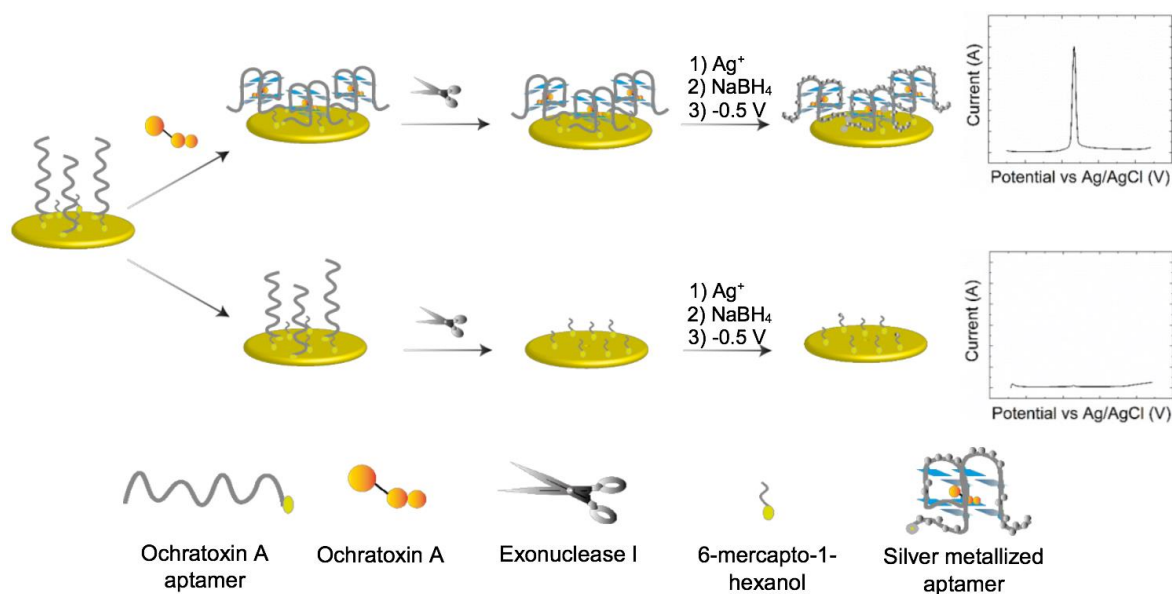
### 5.2.4 Real sample analysis

Ultrapformance liquid chromatography (UPLC) was used to compare both standard OTA solutions and spiked-beer samples, obtained from a local store, using conditions as reported by Wei et al.<sup>257</sup> Beer samples were degassed with argon gas before being directly applied to either the aptasensor electrode or UPLC analysis. Testing was performed by spiking OTA into beer at concentrations of 1, 10, and 100 ng/mL.



## 5.3 Results and discussion

The electrochemical aptasensor system described herein solves problems associated with both matrix interference in solution-based reactions and high background signals from DNA metallization. The assay procedure is illustrated in **Scheme 5.1**. OTA from the sample binds to the aptamer on the electrode surface, forming a G-quadruplex.<sup>23</sup> Exo I is introduced to digest unoccupied aptamers, leaving only G-quadruplexes that cannot be digested. Next, a  $\text{Ag}^+$  solution is applied (activation step), followed by a reducing agent ( $\text{NaBH}_4$ ) to form silver metallized aptamers (reduction step). Further reduction is achieved by applying a potential lower (more negative) than the reduction potential of  $\text{Ag}^+$ , to form additional  $\text{Ag}$ .<sup>252</sup> Finally, square wave voltammetry is used to detect the silver-metallized aptamer.



**Scheme 5.1** Schematic Illustration of the Silver Metallization Assay for OTA Detection Using Enzyme-Assisted Background Current Suppression.

### 5.3.1 Characterization of modified electrodes

Silver-metallized electrodes were investigated using a range of electrochemical methods. **Figure 5.2a** shows square wave voltammograms of the bare SPGE, MCH modified (MCH), aptamer and MCH modified (Apt/MCH) and OTA-aptamer and MCH modified (OTA-Apt/MCH) electrodes, illustrating well-defined peaks from the Apt/MCH and OTA-Apt/MCH electrodes. Data were in good agreement with previous reports,<sup>162, 258</sup> and can be explained by consideration of electrostatic attraction between the negatively charged aptamers and positively charged  $\text{Ag}^+$ . **Figure 5.2b** shows reversible cyclic voltammograms of the silver metallized aptamers, suggesting chemical reduction–oxidation. In the presence of  $10 \text{ mM } [\text{Fe}(\text{CN})_6]^{3-/4-}$ , the cathodic and anodic peaks of the metallized aptamer showed greater peak currents than the unmodified electrode. The increase in the voltammetric peaks obtained with metallized DNA on the working electrode surface could be indicative of an increased electroactive surface area due to solid silver deposition on the DNA.<sup>229</sup> Significantly, silver chloride redox peaks were observed in cyclic voltammograms of  $[\text{Fe}(\text{CN})_6]^{3-/4-}$  in the presence of the metallized aptamer, suggesting both an increased active electrode area and conductivity.

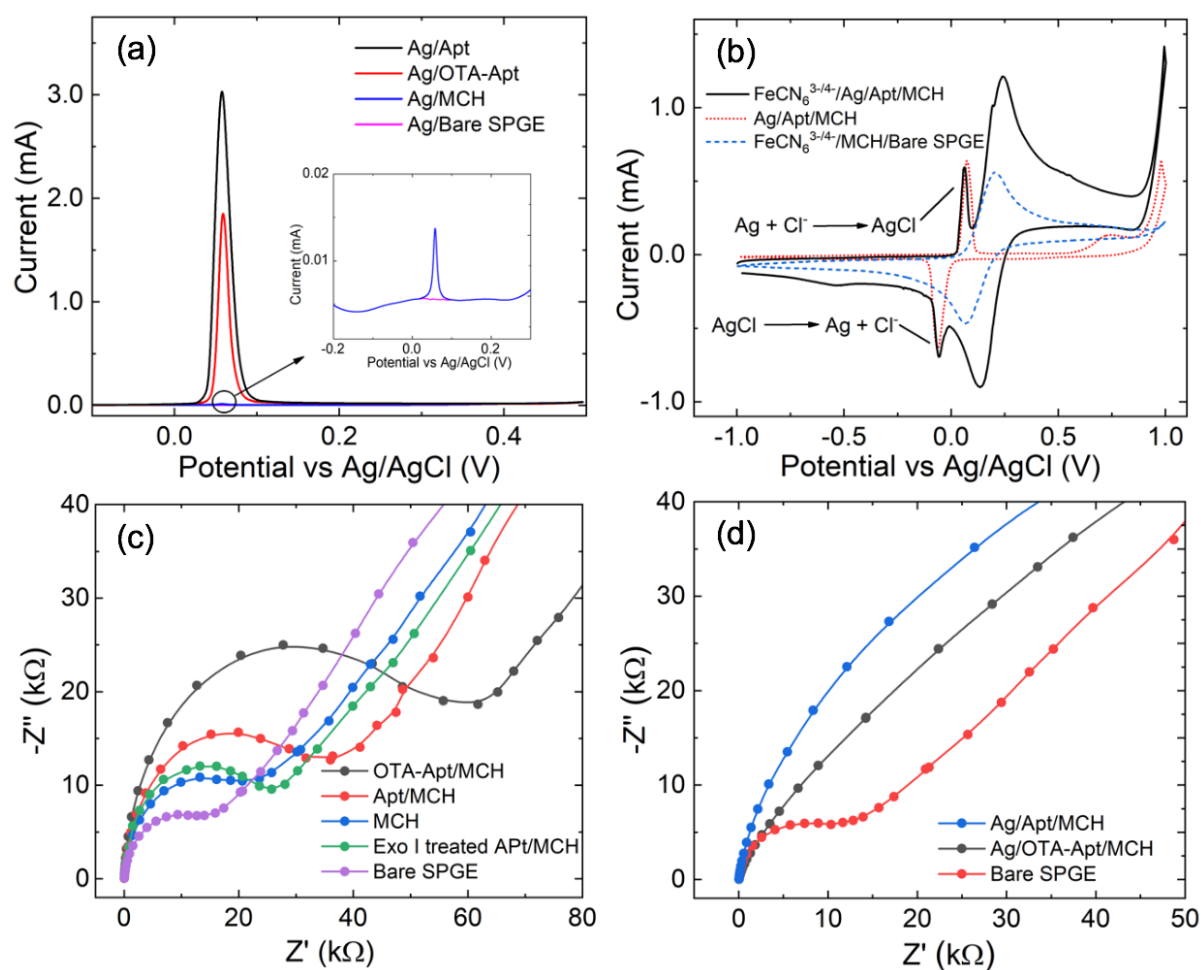


**Figure 5.2** MCH modified (MCH), aptamer modified (Apt), ochratoxin A-aptamer modified (OTA-Apt) and screen-printed gold electrodes (SPGE) were compared using (a) square wave voltammetry, (b) cyclic voltammetry, and (c,d) electrochemical impedance spectroscopy. Square wave voltammograms of silver-metallized electrodes were carried out using a potential step of 0.01 V, an amplitude of 0.06 V, and a frequency of 200 Hz. For cyclic voltammograms and Nyquist plots, 10 mM  $[\text{Fe}(\text{CN})_6]^{-3/-4}$  in 0.1 M PBS were used as the working solution and 0.1 M PBS was used as the background electrolyte. The reversible cyclic voltammograms were carried out using a scan rate of 100 mV/s, while Nyquist plots were obtained by applying a 5 mV sine wave potential within a frequency range of  $10^{-2}$  to  $10^5$  Hz.

Electrochemical impedance spectroscopy (EIS) was then used to evaluate the success of electrode modification with the aptamer. EIS is an effective method for evaluating the interfacial electron transfer efficiency at different stages of biosensor preparation, since each step can be evaluated by monitoring the change in electron transfer resistance ( $R_{ct}$ ), as read from the EIS plot.<sup>259</sup> As shown in **Figure 5.2c**, the  $R_{ct}$  of the bare SPGE was the lowest, which implies that the electroactive ions of  $[\text{Fe}(\text{CN})_6]^{3-/4-}$  are rapidly transported to the electrode interface. After MCH modification of the electrode the  $R_{ct}$  value increased, which is in line with an expected decrease in transport kinetics due to impairment by the MCH. Self-assembly of the thiolated aptamer onto the electrode surface led to a significant increase in  $R_{ct}$ , since oligonucleotides exhibit low electroactivity. The  $R_{ct}$  increased significantly upon further addition of OTA, due to the steric effect of the OTAaptamer G-quadruplex structure hindering electro-active species from reaching the electrode surface. When ExoI was used to digest the unoccupied aptamers from an aptamer-modified electrode (Apt/MCH, no OTA), the  $R_{ct}$  value was only marginally different from the MCH-modified electrode, indicating full DNA digestion, leaving only MCH on the electrode surface. The dome-shaped portions of the plots in **Figure 5.2c** indicate a kinetically controlled domain, and suggest impairment of electron transport to the electrode surface. This characteristic disappeared after silver metallization of Apt/ MCH and OTA-Apt/MCH electrodes, as shown in **Figure 5.2d**. Yet, silver metallization of the MCH electrode exhibited only a slight difference after metallization. In addition, coulometric analysis was carried out using a 0.2 V applied potential for a duration of 60 s, comparing the bare, aptamer-modified and silver-metallized aptamer-modified electrodes (**Figure 5.3**). Charge was calculated from the area under the  $i-t$  curve, and the amount of silver deposited was calculated to be 38.8 ng on the aptamer-modified electrode. This result confirmed that silver metallization of the DNA was successful. Together, these results indicate rapid kinetics in the silver-metallized electrodes, due to the deposition of solid silver on the DNA. In summary, the EIS data confirm that aptamer modification, aptamer binding, and aptamer metallization on the SPGE were successful.

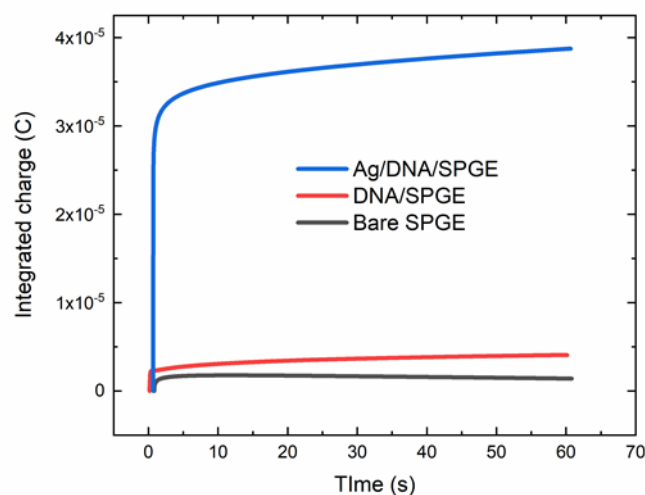


**Figure 5.3** Coulometric response of silver-metallized DNA, DNA modified, and bare SPGE electrodes, respectively, using applied potential at 0.2 V with the duration time of 60 s.

## 5.3.2 Optimization

### 5.3.2.1 Aptamer silver metallization

DNA metallization usually proceeds via three steps: activation, reduction and growth. For the reduction step, either chemical or electrochemical reduction is utilized. The combination of both reduction methods has not been reported previously. Herein, we observed that metallization using only a reducing agent provided a higher electrochemical signal compared to voltage-induced metallization, as illustrated in **Figure 5.4a**. Furthermore, we observed that combination of both methods increased the electrochemical signal by a factor of two. Specifically, an applied potential of  $-0.5$  V (vs. Ag/AgCl) was chosen. This is lower than the reduction potential of AgCl to Ag as indicated in the cyclic voltammogram (**Figure 5.2b**). An electrochemical reduction time of 3 minutes was observed to provide the highest electrochemical signal, allowing for full growth of silver on the aptamer (**Figure 5.4b**).

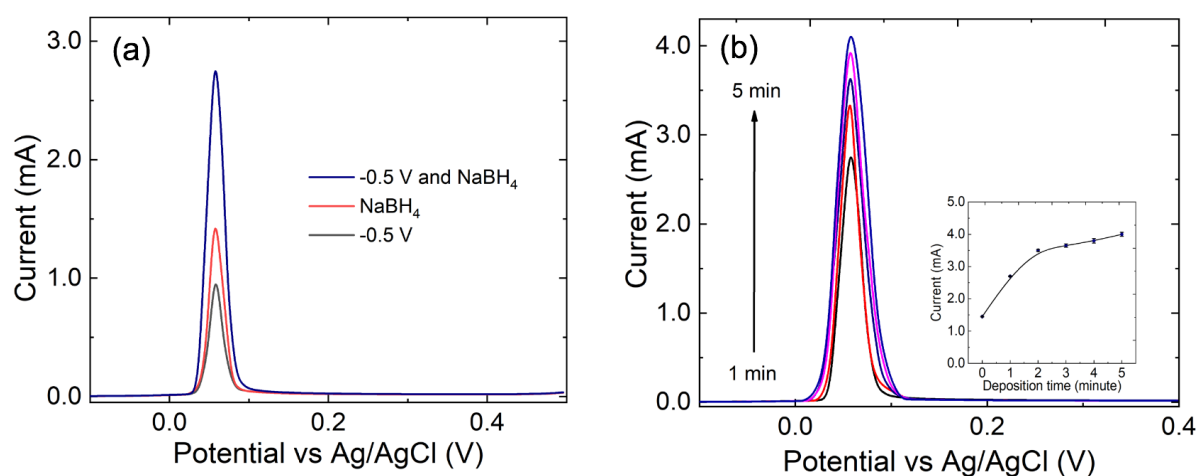


**Figure 5.4** (a) Square wave voltammograms of silver metallization comparing chemical, electrochemical and combined reductions. (b) Deposition time of Ag on the aptamer-modified SPGE. An applied potential of  $-0.5$  V, a potential step of  $0.01$  V, an amplitude of  $0.06$  V, and a frequency of  $200$  Hz, were used.

### 5.3.2.2 Central composite design

Having established the working principle of the OTA aptasensor electrode, we then set out to establish which experimental parameters yield optimal signal strength. We used central composite design as the analytical optimization model. CCD not only minimizes the number of experimental trials, but also provides linear, quadratic and interaction information, which is inaccessible through a one-factor-at-the-time approach. **Table 5.1** shows the independent variables tested, as well as their actual and associated coded values, the latter being used to avoid experimental bias. CCD analysis was performed as described in the Methods section above, using the model shown in **Table 5.4**. This resulted in the following polynomial regression,

$$\begin{aligned}
 y = & 75.03 - 0.27(\text{Aptamer}) + 5.63(\text{Enzyme}) + 7.51(\text{Time}) \\
 & + 2.92(\text{Aptamer})^2 - 0.58(\text{Enzyme})^2 - 1.40(\text{Time})^2 \\
 & + 0.56(\text{Aptamer} \times \text{Enzyme}) - 3.42(\text{Aptamer} \times \text{Time}) - 4.44(\text{Enzyme} \times \text{Time})
 \end{aligned}
 \tag{5.5}$$

which provides the percentage difference between the electrochemical signal and the background current. The predicted values obtained from **Equation 5.5** were compared with experimental data (shown in **Table 5.4**). Paired t-tests showed that the experimental and predicted data sets ( $n=20$ ) are not significantly different, as the t-value (0.002) is smaller than t-critical (2.09). Furthermore, both experimental and predicted data were compared and shown to exhibit excellent correspondence ( $R^2 = 0.956$ ) (**Figure 5.5d**).

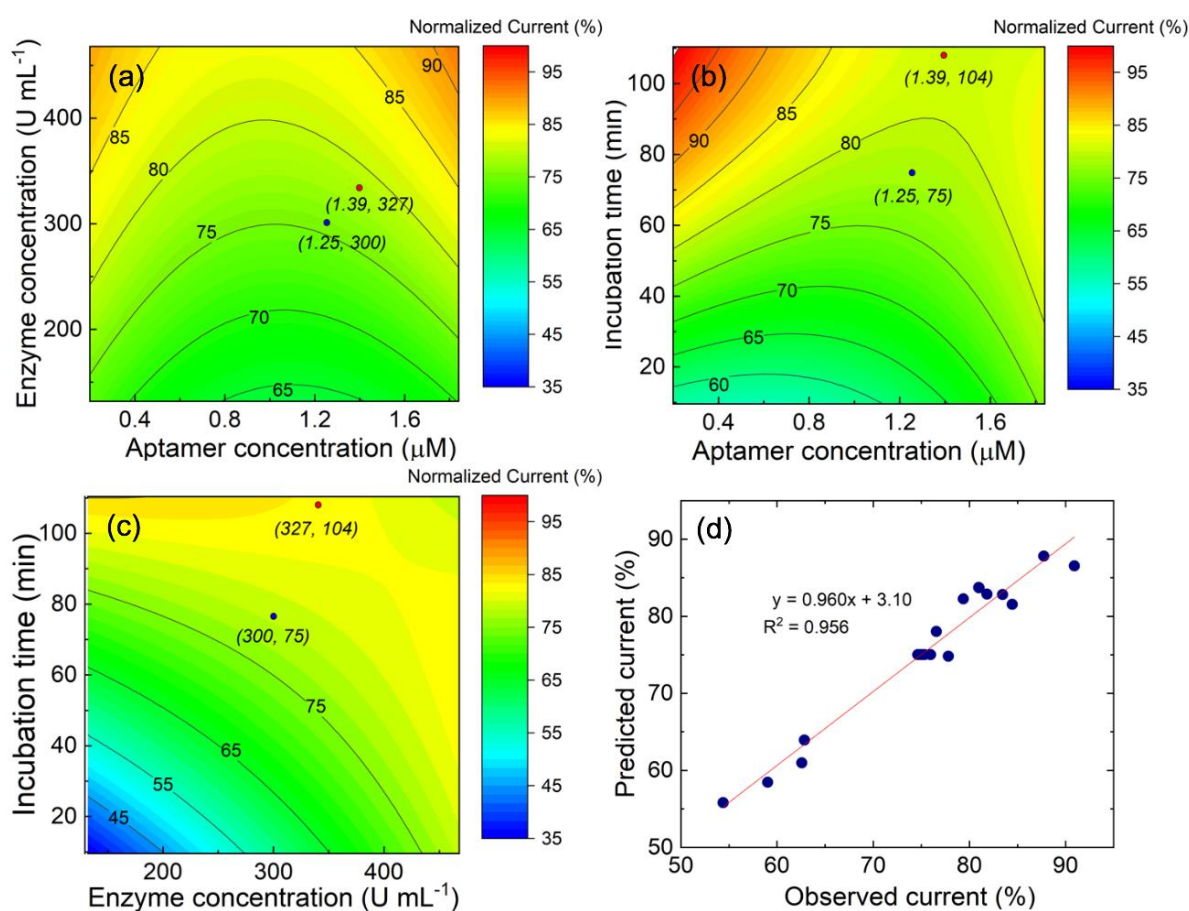


**Figure 5.5** Surface contour plots of the percentage difference between peak current and background as a function of (a) concentration of aptamer and enzyme, (b) concentration of aptamer and incubation time, and (c) enzyme concentration and incubation time. The red points indicate the theoretical optimum values, and the blue points indicate the practical optimum values. (d) A plot of the predicted values as obtained from regression (**Equation 5.3**) against experimental values.

**Equation 5.5** yields theoretical optimal values of 1.39  $\mu\text{M}$ , 327 U/mL, and 104 minutes for aptamer concentration, enzyme concentration, and incubation time, respectively. These values gave a predicted a response of 80% normalized current for 1 ng/mL of OTA. To optimize the practical value of the assay, we sought to further reduce the assay time and reagent consumption (enzyme and aptamer). This was done by consulting the CCD model data (**Figure 5.5a-c**) and deriving minimized parameter values that would still yield a sufficient normalized current. Setting a threshold of 78% predicted normalized current (i.e. a 2% reduction), practical optimal values of 1.25  $\mu\text{M}$ , 300 U/mL, and 75 minutes were obtained, for aptamer concentration, enzyme concentration, and incubation time, respectively. Thus, for a minor reduction in signal, significant reductions in assay time and reagent consumption were achieved.

Next, we attempted to optimize the square wave voltammetry variables of amplitude, voltage step and frequency. These control peak current, as shown in **Equation 5.6**.

$$i_p = \frac{nFAD^{1/2}C^*}{\pi^{1/2}t_p^{1/2}}\varphi_p(\Delta E_s, E_p) \quad (5.6)$$

Here  $i_p$  is the measured current during each pulse (A),  $n$  is the number of electrons transferred,  $F$  is the Faraday constant (C/mol),  $A$  is the area of the electrode ( $\text{cm}^2$ ),  $D$  is the reactant diffusion constant ( $\text{cm}^2/\text{s}$ ),  $C^*$  is the bulk concentration of the reactant (M),  $t_p$  is the pulse width (half of the staircase period) (s), and  $\varphi_p$  is the dimensionless current function which depends on step height ( $\Delta E_s$ ) and square wave amplitude ( $E_p$ ).<sup>233, 260</sup>

The SWV was optimized using the variables as provide in **Table 5.5** and **Figure 5.6**. After applying CCD for square wave voltammetry optimization, the model suggested using the maximum value for all variables (as shown in **Figure 5.7**).

**Table 5.5** The experimental range and level of the respective independent variables of square wave voltammetry

Variables (unit)	Actual			Coded Level		
	Low	Middle	High	Low	Middle	High
Voltage step (V)	0.01	0.015	0.02	-1	0	1
Amplitude (V)	0.03	0.05	0.07	-1	0	1
Frequency (Hz)	25	50	75	-1	0	1

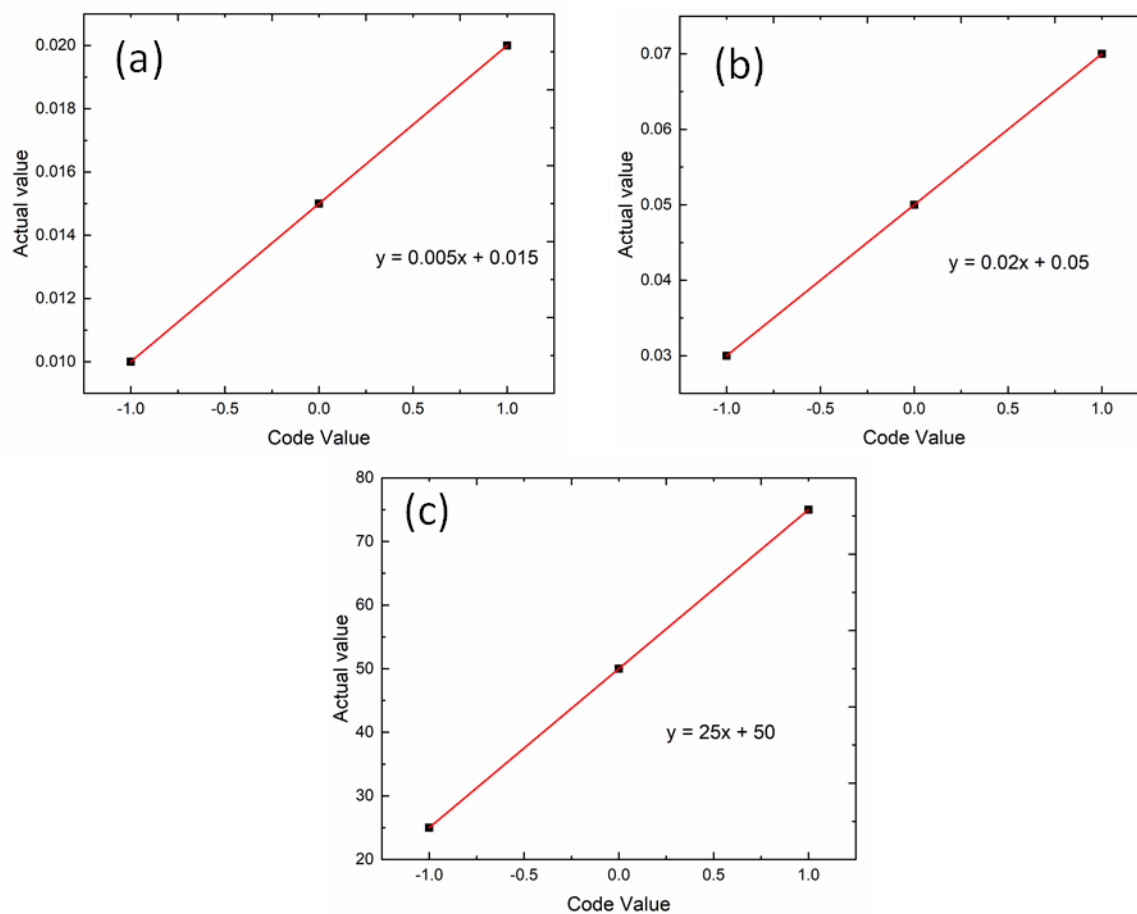


**Figure 5.6** Conversion of actual and coded values of (a) voltage step, (b) amplitude, and (c) frequency for central composite design.

By using the same square wave conditions as the electrode optimization, the calculated process rendered this **Equation 5.5**:

$$\begin{aligned}
 y = & 0.40 + 0.074(\text{Voltage step}) + 0.0150(\text{Amplitude}) + 0.0129(\text{Frequency}) \\
 & + 0.012(\text{Voltage Step})^2 + 0.021(\text{Amplitude})^2 + 0.021(\text{Frequency})^2 \\
 & + 0.09(\text{Voltage} \times \text{Amplitude}) + 0.07(\text{Voltage} \times \text{Frequency}) \\
 & + 0.085(\text{Amplitude} \times \text{Frequency})
 \end{aligned} \quad (5.7)$$

Next, the equation was illustrated as surface response in **Figure 5.7** using the same protocol as the electrode modification optimization



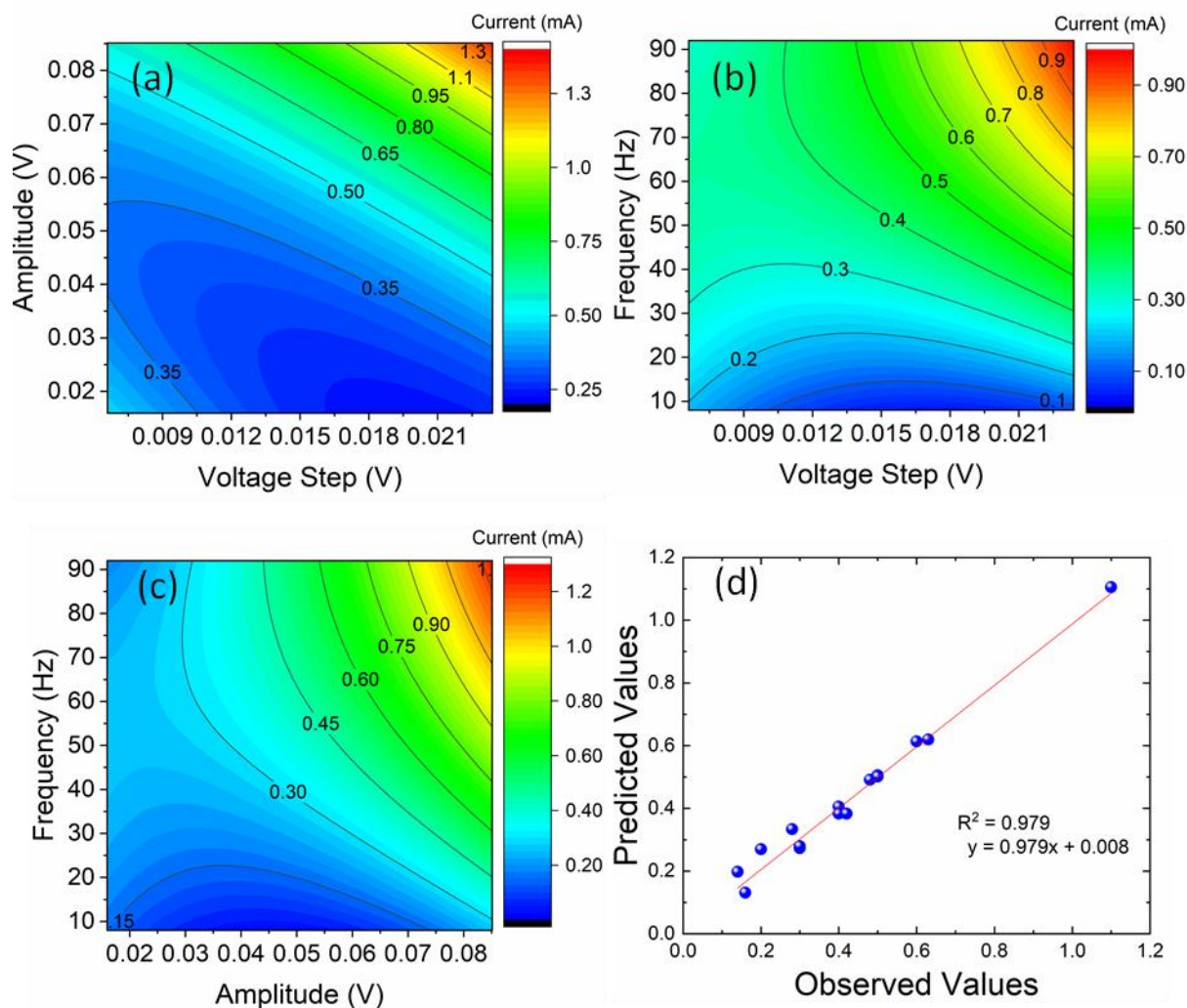


**Figure 5.7** Surface response and contour plots of the percentage difference between peak current and background as a function of (a) voltage step and amplitude, (b) voltage step and frequency, and (c) amplitude and frequency. (d) A plot of predicted values as obtained from the regression **Equation 5.7** against experimental values.

For further analysis, we took into consideration the peak height, peak position and peak full-width-half-maximum (FWHM) as indicators of the optimum variable combination, where the peak height should be as high as possible, peak position of silver oxidation versus Ag/AgCl should be at 0 V, and the FWHM should be 90.5 mV (corresponding to one electron involved in the redox reaction).<sup>234</sup> These conditions are indicated as bound regions in (**Figure 5.8**). From this, the practical optimum values obtained were an applied step potential of 0.01 V, an amplitude of 0.06 V, and a frequency of 200 Hz.



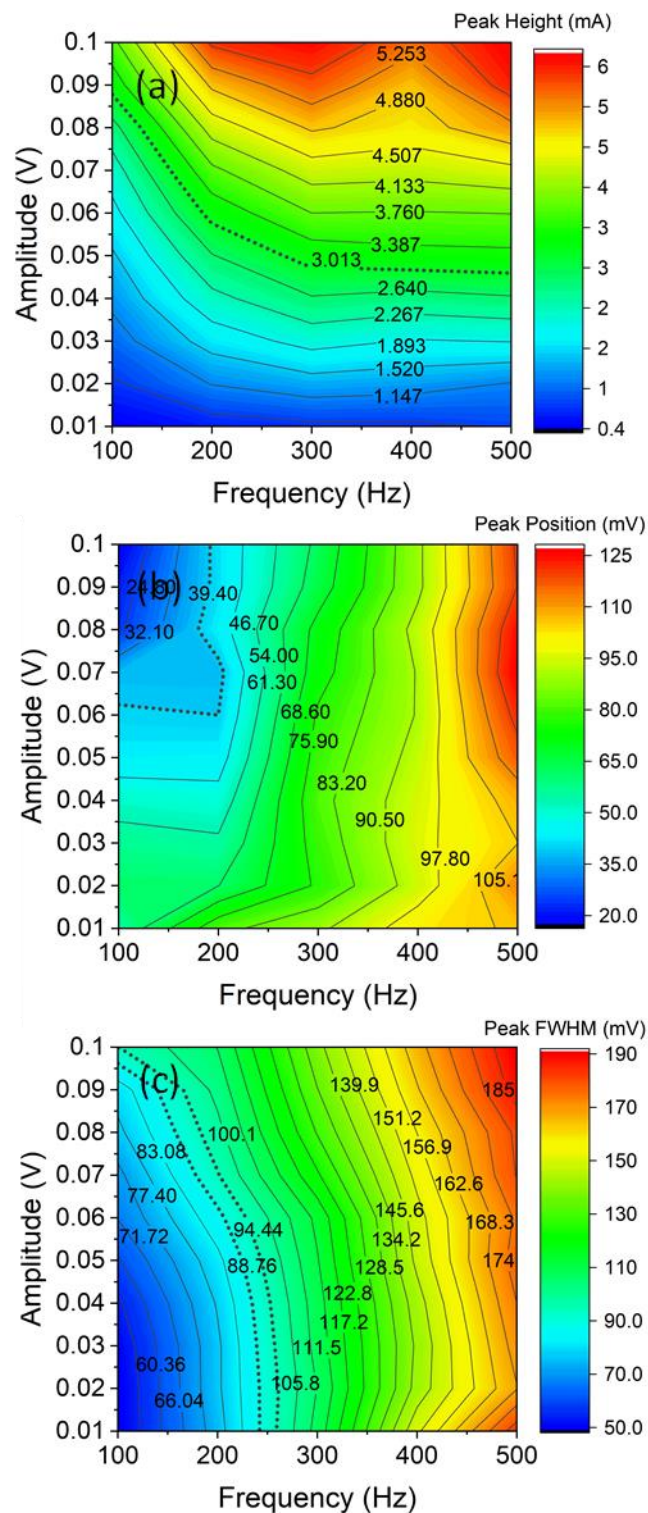


**Figure 5.8** Surface responses of the studied square wave voltammetry amplitude and frequency, obtaining current (a), peak position (b), and peak full-width half maximum (c). The preferred regions for the peak height peak position are indicated with a dotted line and an arrow in (a) and (b). The peak FWHM range lies between the two dotted lines in (c).

### 5.3.3 Analytical performance

#### 5.3.3.1 Dynamic range, limit of detection, and limit of quantitation

After obtaining optimum values for each variable, a calibration curve was constructed using an OTA concentration series between  $10^{-5}$  and  $10^4$  ng/mL. Using the optimized parameters, square wave voltammograms at each concentration were obtained, as shown in **Figure 5.9a**. The obtained electrochemical peak values ( $N=5$ ) were plotted against concentration, shown in the calibration curve in **Figure 5.9b**, yielding a linear range between  $10^{-3}$  and  $10^2$  ng/mL (**Figure 5.9b** inset). The limit of detection (LOD) and limit of quantitation (LOQ) were calculated using 3 and 10 times the background standard deviation, respectively, and determined from fits to the calibration curve. An LOD of 0.7 pg/mL and an LOQ of 2.48 pg/mL were obtained.

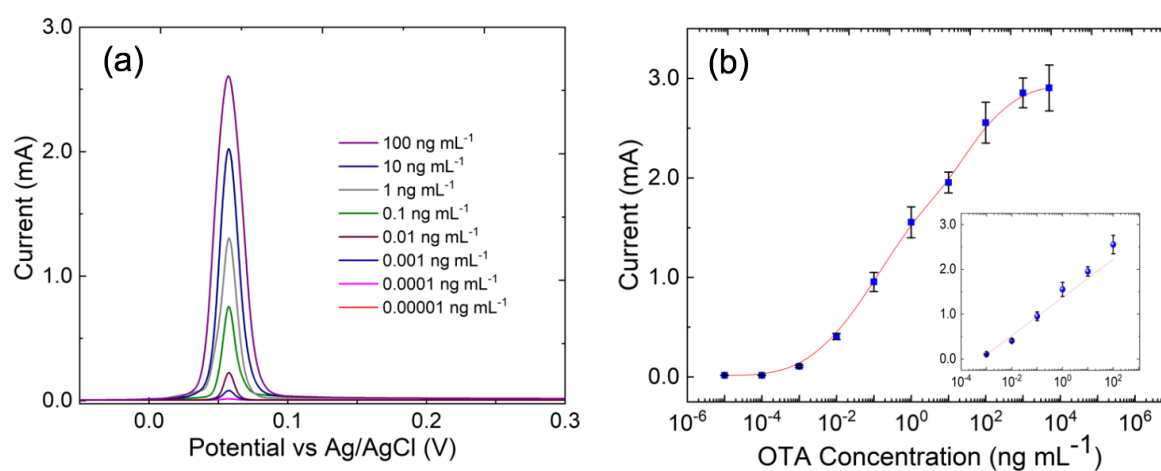


**Figure 5.9** (a) Square wave voltammograms of a series of OTA concentrations from  $10^{-5}$  to  $10^2$  using the CCD-optimized conditions: an aptamer concentration of  $1.25 \mu\text{M}$ , an enzyme concentration of  $375 \text{ U/mL}$ , an incubation time of 75 minutes, a step potential of  $0.01 \text{ V}$ , an amplitude of  $0.06 \text{ V}$  and a frequency of  $200 \text{ Hz}$ . (b) A calibration curve of anodic current ( $N=5$ ) obtained from (a), versus OTA concentration showing a linear range from  $10^{-3}$  to  $10^2$  ng/mL, as shown in the inset.

The analytical performance of the electrochemical aptasensor was compared with published studies on the electrochemical detection of OTA, as shown in **Table 5.6**. Significantly, the current approach provides a lower LOD and wider working range compared to other silver metallization assays.<sup>261-271</sup> The LOD of our system is marginally higher than the platforms presented in references<sup>272-273</sup>, however it is important to note that the linear range in the current system is much wider and the method far simpler to implement due to the use of disposable SPGEs.

**Table 5. 6** A comparison of reported electrochemical techniques for OTA determination.

Year	Electrochemical Methods	Bio-recognition elements	LOD	Linear Range	Reference
2015	DPV	Aptamer with Exo III	2 pg/mL	0.010-1 ng/mL	261
2016	Mott-Schottky	Antibody-conjugated magnetic nanoparticles	1.84 pg/mL	1-20 pg/mL	262
2016	DPV	Aptamer	0.04 ng/mL	0.15-5 ng/mL	263
2016	EIS	Antibody-conjugated BSA	2.5 ng/mL	2.5-100 ng/mL	264
2016	EIS	Aptasensor modified polypyrrole-dendrimers	2pg/mL	0.002-6 ng/mL	265
2017	DPV	Aptamer with Exo III	0.58 pg/mL	0.001-0.5 ng/mL	266
2017	DPV	Graphene-protected hinge-aptamer	5.6 pg/mL	0.01-50 ng/mL	267
2017	Amperometry	Aptamer and SWCNTs	0.021 ng/mL	0.07-12 ng/mL	268
2017	DPV	Aptamer and HCR	2 pg/mL	0.005-100 ng/mL	269
2018	DPV	2D layered black phosphorene	0.18 µg/mL	0.3-10 µg/mL	270
2018	DPV	Aptamer with carbon aerogel	0.1 pg/mL	0.1-10 ng/mL	271
2018	EIS	Polythiophene-3-carboxylic acid	0.125 ng/mL	0.125-2.5 ng/mL	272
2018	CV	Aptamer and carbon nitride nanosheet	0.030 ng/mL	0.080-2 ng/mL	273
	SWV	Silver metallization aptamer and Exo I	0.7 pg/mL	0.001-100ng/mL	This study

\*DPV = differential pulse voltammogram, EIS = electrochemical impedance spectroscopy, CV = cyclic voltammetry, and SWV = square wave voltammetry

### 5.3.3.2. Selectivity and stability

The selectivity of our electrochemical aptasensor was assessed by examining its response to potential (and common) interferences, including ochratoxin B (OTB), aflatoxin B1 (AFB1), aflatoxin B2 (AFB2). In the current experiments, the concentration of each interferent (1.0 ng/mL) was made one order of magnitude higher than that of OTA (0.1 ng/mL). The results of the selectivity assessment are shown in **Figure 5.10a**. In contrast to the significant square wave voltammetry signal of OTA and a mixed solution containing OTA, a negligible response was observed on addition of all interferences. This indicated excellent selectivity of the electrochemical aptasensor for OTA over the OTB, AFB1, and AFB2, which was attributable to the high selectivity of the aptamer probe sequence.

Stability over time and reproducibility are key factors in the practical application of sensing systems. To test storage stability, aptasensors were kept at 4 °C under nitrogen for up to 30 days, with square wave voltammetry then used to study the electrochemical response for 0.01, 0.1, and 1 ng/mL OTA using the optimum conditions (**Figure 5.10b**). It should be noted that electrodes were not reused, due to the silver reduction occurring directly on the aptamer structure. Data

indicate a minimal change in response to a series of OTA concentrations in comparison to a freshly prepared electrode. A t-test comparison showed no significant difference between the fresh and stored electrodes (t-values for the three concentrations were 0.09, 0.02, and 0.001 for 0.01, 0.1, and 1 ng/mL, respectively, where t-critical = 1.94). However, the average current of the stored electrode did exhibit a 10% reduction in electrochemical signal (shown in the inset of **Figure 5.10b**), which is likely a result of partial decomposition or deconjugation of the aptamer on the electrode surface.

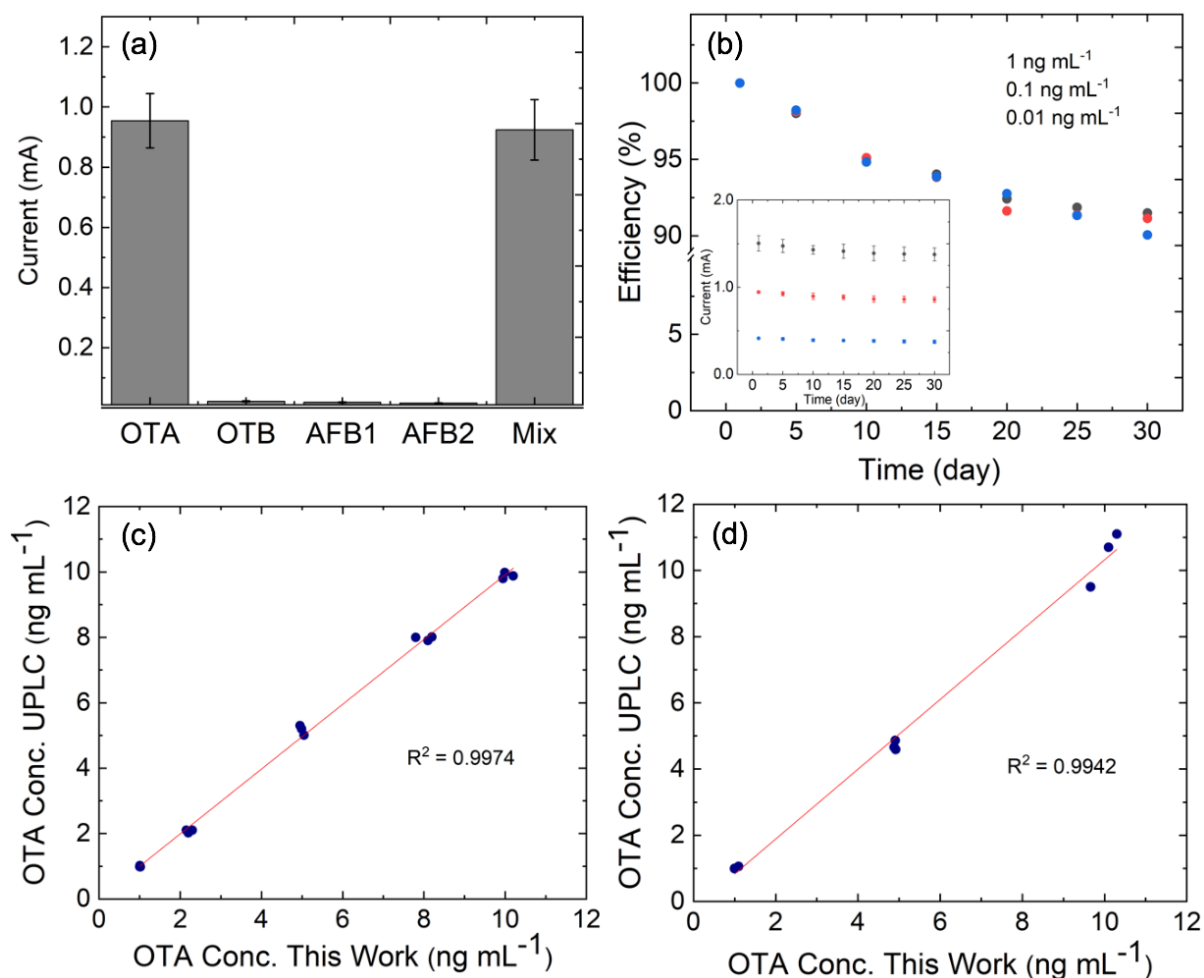


**Figure 5.10** (a) Electrochemical signal from the silver-metallized aptasensor in the presence of potential interferents, with OTB and AFB2 concentrations of 1.0 ng/mL, an OTA concentration of 0.1 ng/mL, and their mixture (N=3). (b) Stability of the electrochemical aptasensor for detecting OTA (0.01, 0.1, and 1 ng/mL) over 30 days (N=3). Comparison of OTA concentrations between the electrochemical aptasensor and UPLC carried out from the (c) standard solutions and (d) spiked beer samples.

### 5.3.3.3 Real sample analysis

The results using model samples indicate that the electrochemical aptasensor exhibits excellent biosensing performance, including high sensitivity, high selectivity, high stability and good reproducibility. To further validate the sensor, it was compared to the gold standard UPLC method, using OTA concentrations between 1 and 10 ng/mL. Data presented in **Figure 5.10c**, show excellent agreement between the detection methods ( $R^2 = 0.995$ ). Finally, to verify the practical applicability of the electrochemical aptasensor, sensing was performed using a real sample matrix, with beer chosen as an exemplar system. Different OTA concentrations (1, 5, and 10 ng/mL) were spiked into the degassed beer samples, and the presence of OTA detected and quantified using the aptasensor (**Figure 5.9**). As shown in **Table 5.7**, recovery ranged from 96.6 % to 109.7 %, with an RSD of less than 5%. The obtained results were compared to UPLC, confirming excellent correspondence ( $R^2 = 0.994$ , as shown in **Figure 5.10d**), and demonstrating the potential for use with real samples.

**Table 5.7** Determination of OTA concentration in spiked beer samples comparing the electrochemical aptasensor with UPLC.

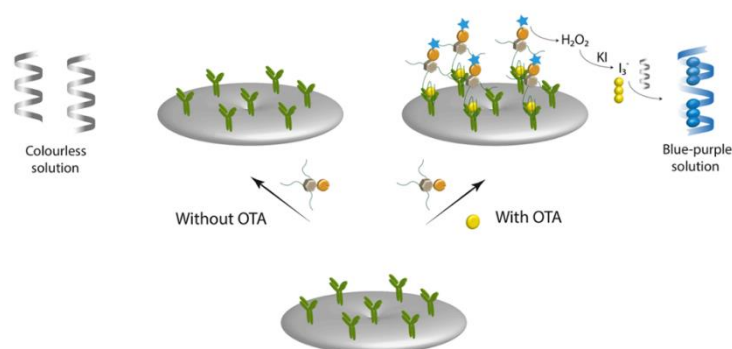
Sample	Spiked OTA (ng/mL)	Detected (ng/mL)		Recovery (%)		%RSD		t-value
		This study	UPLC	This study	UPLC	This study	UPLC	
Beer 1	1	1.00±0.01	1.00±0.02	100.4	99.69	1.04	2.63	0.28
	5	4.91±0.03	4.86±0.05	98.13	97.29	1.36	1.98	0.28
	10	9.66±0.18	9.50±0.32	96.57	94.97	1.45	1.01	0.08
Beer 2	1	1.00±0.02	0.99±0.04	100.4	99.17	0.49	0.46	0.06
	5	4.88±0.04	4.66±0.10	97.54	93.14	0.47	1.61	0.01
	10	10.3±0.21	11.1±0.31	103.4	110.7	1.58	0.55	0.01
Beer 3	1	1.10±0.01	1.06±0.05	109.7	105.8	0.55	1.41	0.04
	5	4.92±0.05	4.59±0.12	98.40	91.81	0.61	1.41	0.01
	10	10.1±0.25	10.7±0.35	100.9	107.5	1.97	0.70	0.01

## 5.4 Conclusions

We have presented a novel electroanalytical method to detect OTA using an enzyme-assisted silver-metallized aptasensor. The aptamers, which were readily conjugated to disposable SPGEs, exhibited excellent specificity for the target analyte. Degradation of unoccupied aptamers after addition of the test sample was performed by the enzyme Exo I, which significantly reduced the background signal and increased sensitivity. Addition of AgCl followed by a double reduction method metallized the target-bound aptamers, yielding a significant signal enhancement in square wave voltammetry-based measurements. Electrode preparation variables and square wave voltammetry parameters were optimized using central composite design, which allowed efficient and rapid assay optimization. The resultant electrochemical aptasensor exhibited an LOD of 0.7 pg/mL, an LOQ of 2.48 pg/mL and a linear range between 0.001 and 100 ng/mL (6 orders of magnitude) against standard OTA solutions. The electrochemical aptasensor was compared to gold-standard UPLC analysis, confirming excellent agreement when using both standard and beer-spiked OTA samples. It should be noted that use of an enzyme in such a sensor could pose potential complications for in-the-field application. However, recent advances in the preparation of freeze-dried enzymes on paper-based diagnostic strips,<sup>85, 125</sup> which are stable when stored and reactivated when sample is added, suggest that electrodes could be made using a similar approach. Overall, the developed aptasensor allows the detection of OTA with high sensitivity, selectivity, accuracy, precision and robustness in real samples.

## Chapter 6

# An Ultrasensitive Non-Noble Metal Colorimetric Assay Using Starch–Iodide Complexation for Ochratoxin A Detection



Colorimetric sandwich-type biosensors that can both provide sensitivity competitive with fluorescence-based approaches, and leverage reagents that are cost-effective, widely available and as safe as possible, are highly sought after. Herein, we demonstrate an alternative highly-sensitive colorimetric method for paper-based sandwich-type biosensing that uses starch-iodide complexation to simplify practical biosensing using ubiquitous reagents. Targeting the mycotoxin ochratoxin A (OTA), a covalently-immobilized OTA antibody on a cellulose surface captures OTA and forms a sandwich with OTA aptamer-conjugated glucose oxidase. Adding the chromogenic reagents at an optimized concentration, a distinct blue colour develops within 30 minutes, offering excellent contrast with the clear/white of the negative sample. With a sampling volume down to just 5  $\mu\text{L}$ , the assay exhibits concentration limits of detection and quantitation of 20 and 320  $\text{pg/mL}$ , respectively, and a linear range from  $10^{-1}$  to  $10^5$   $\text{ng/mL}$  ( $R^2 = 0.997$ ). The method displays excellent selectivity against related mycotoxins, excellent %recovery (95–117%) and robust operation in complex matrices (beer, urine and human serum), with no significant difference versus gold-standard liquid chromatography. Along with its excellent analytical performance, this assay benefits from non-toxic and extremely cheap reagents that can be safely disposed of in the field, and presents an attractive alternative to toxic dyes and nanoparticles.

This chapter is adapted from a paper entitled “*An ultrasensitive non-noble metal colorimetric assay using starch-iodide complexation for Ochratoxin A detection*”, authored by Akkapol Suea-Ngam, Leif-Thore Deck, Philip D. Howes and Andrew J. deMello. Published in *Analytica Chimica Acta* **2020**, *1135*, 29–37.

## 6.1 Introduction

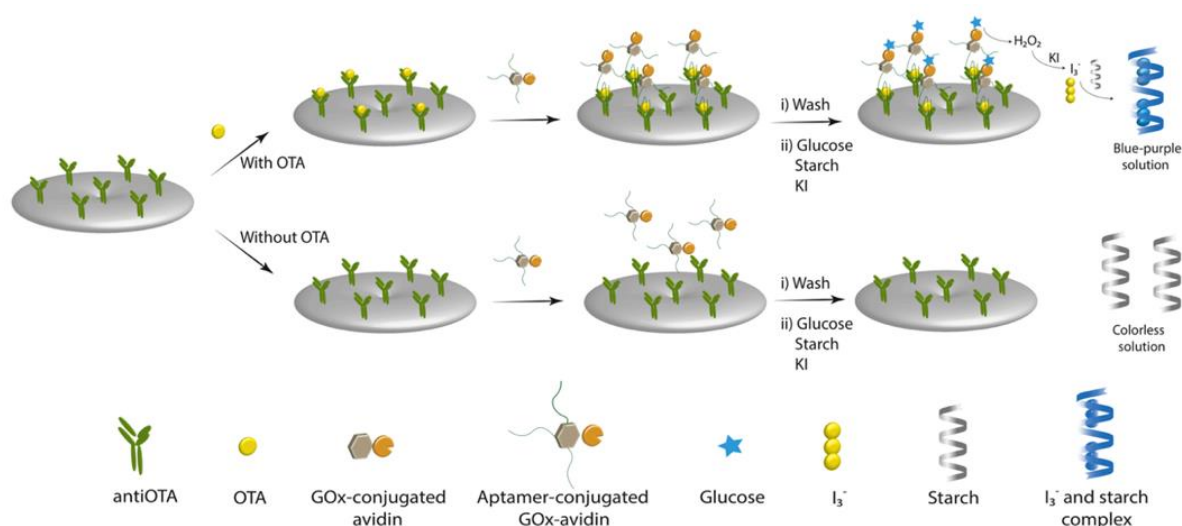
Simple and robust routes for colorimetric detection at low analyte concentrations have been sought after for centuries.<sup>274-276</sup> In more recent times, such approaches have been translated to paper-based analytical devices (PADs), providing simple solutions for point-of-need and point-of-use testing.<sup>277-279</sup> Although colorimetric detection schemes are typically less sensitive than electrochemical- or fluorescence-based methods,<sup>280</sup> they are ideally suited for application in PADs due to the simplicity of both readout and operation.<sup>144, 281</sup>

Colorimetric detection methods have traditionally used ligands that form complexes with a specific target ion or molecule (e.g. the complexation of Ni with dimethylglyoxime<sup>282</sup>), or covalent bond-forming reactions (e.g. creatinine with picrate<sup>275</sup>). However, such approaches are highly specific to their target analyte, and are thus inherently limited in their versatility and scope. More recently, noble metal nanoparticles have been extensively investigated and employed as reporters in colorimetric sensing<sup>283</sup>. Their intense localized surface plasmon resonance (LSPR) leads to phenomena that can readily be harnessed in biosensing<sup>284-285</sup>. However, there is an inherent cost associated with the use of gold, silver and platinum (even at low masses or concentrations) that limits how far device costs can be driven down<sup>286</sup>. In addition, the synthesis of noble metal nanoparticles remains a non-trivial and resource-intensive undertaking<sup>287</sup>. Finally, and critically, there are ongoing concerns related to the environmental effects of metal nanoparticles, with little understanding of how composition, size, shape and surface functionality effect their downstream toxicity<sup>288</sup>. Such disadvantages have inspired us to investigate viable alternatives that circumvent such issues, yet retain the required simplicity and sensitivity.

Various biosensor platforms have used the enzyme by-product  $H_2O_2$  to oxidise indicating dyes (e.g. 3,3',5,5'-Tetramethylbenzidine, TMB, and 2,2'-azino-di-(3-ethylbenzthiazoline sulfonic acid), ABTS™)<sup>69, 289</sup>, however such dyes are relatively expensive, offer low sensitivity, and are not environmentally friendly. Using the same oxidising strategy, but with the cheap and environmentally benign reagents iodine and potassium iodide (KI), an extremely effective colorimetric signal can be developed. Here, dissolution of elemental iodine in aqueous KI yields triiodide ( $I_3^-$ ), which can subsequently form intermolecular charge-transfer complexes and polyiodide homopolymers with starch molecules, yielding a dark blue/purple coloration<sup>290</sup>. Although this intense chromogenic response has commonly been used for direct starch testing in food<sup>291</sup>, few works have investigated the phenomenon as a novel concept in the medical diagnostics field, despite the obvious potential.<sup>292</sup> For example, an important work by Liu et al. demonstrated the use of starch-iodide complexation to generate a colorimetric response in a microwell plate-based assay for the detection of prostate specific antigen (PSA), showing detection down to 0.46 pg/mL.<sup>293</sup> However, although this approach would be suitable for clinical and laboratory settings, it is not deployable to the point-of-care or resource-limited settings. The idea has been recently extended to a PAD system to detect hydrogen peroxide and glucose (with LODs of 0.05 and 0.1 mM respectively)<sup>294</sup>, however the expansion and optimization of this approach into sandwich assays for field-deployable and point-of-care platforms for diagnostics has not been demonstrated previously. In summary, we feel there is much potential still to be unlocked in the application of this phenomenon for universal and point-of-care diagnostics, which inspired us to extend the technique into a PAD system incorporating a sandwich-type analyte capture mechanism, for a new class of molecular target.



Herein, we report a simple yet powerful antibody–aptamer-based PAD with colorimetric readout targeting ochratoxin A (OTA), a carcinogen (class 2B) generated by *Aspergillus* and *Penicillium* contaminated in food and drink and in bodily fluids, as a model toxin<sup>295</sup>. As illustrated in **Scheme 6.1**, covalent immobilization of anti-OTA antibodies (antiOTA) on a cellulose surface (**Scheme 6.2**) allows capture of OTA and further labelling by aptamer-conjugated glucose oxidase (AGOx) *via* a sandwich mechanism. Subsequent introduction of a starch, KI and glucose solution into the PAD chamber yields a distinct colour change to blue/purple for the positive test due to the H<sub>2</sub>O<sub>2</sub> produced by AGOx. Smartphone-captured images can be directly analyzed to extract colour intensity and quantify analyte levels. Due to high surface-to-volume ratio, this approach allows high sensitivity and precise quantitation of OTA in complex matrices, such as beer, urine, and human serum. Furthermore, through the use of experimental design, rapid and resource-efficient optimization of KI, starch and glucose concentrations was performed. The optimized PAD-based sensor demonstrates much promise for environmentally friendly, highly sensitive, cost-effective, simple and robust biosensing for deployment in a variety of low resource settings.



**Scheme 6.1** A schematic illustration of the colorimetric paper-based assay. Surface-immobilised antiOTA antibodies bind OTA from solution, with aptamer-GOx conjugates then binding to OTA and forming a sandwich complex. Subsequent addition of glucose, starch and potassium iodide sees the GOx produce H<sub>2</sub>O<sub>2</sub>, leading to the formation of triiodide that complexes with starch and produces the blue color. In the absence of OTA, the sandwich complex cannot form and the blue coloration does not occur.

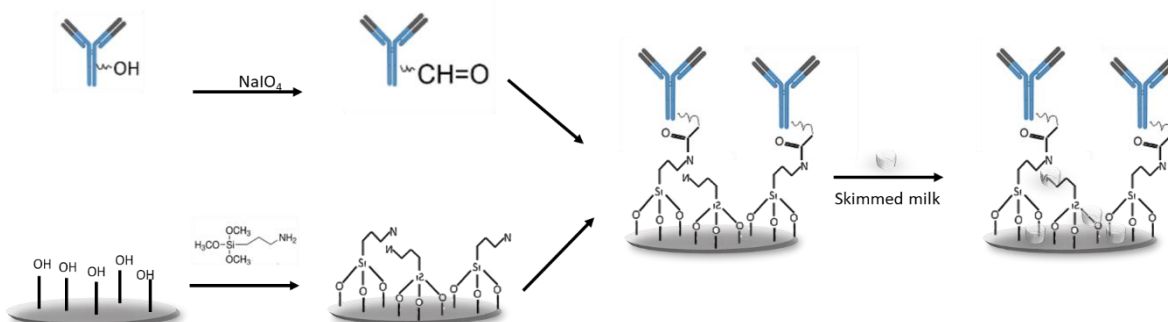
## 6.2 Materials and methods

### 6.2.1 Reagents and materials

Rabbit anti *Aspergillus ochraceus* ochratoxin A (antiOTA) was purchased from Bio-Rad (California, USA). The OTA aptamer (5'-biotin-AAA AAA AAA AGAT CGG GTG TGG GTG GCG TAA AGG GAG CAT CGG ACA-3') was purchased from Microsynth (Balgach, Switzerland). Ochratoxin A (OTA), Aflatoxin B1 (AFB1), Aflatoxin B2 (AFB2), citric acid, sodium citrate, glucose, KI, starch, HEPES, EDTA, Trizma base™, Tween 20, NaNO<sub>3</sub>, CaCl<sub>2</sub>, PBS tablets, NaCl, skimmed milk, NaIO<sub>4</sub> and KCl were purchased from Sigma-Aldrich (Buchs, Switzerland) and used as received. All other reagents, including Ochratoxin B (OTB) (AdipoGen AG, Epalinges, Switzerland), HCl (Fluka, Buchs, Switzerland), 3-aminopropyltrimethoxysilane (Tokyo Chemical Industry, Eschborn, Germany), glucose oxidase-conjugated avidin (Rockland, Hamburg, Germany) and MgCl<sub>2</sub> (Acros Organics, Geel, Belgium), were analytical reagent grade and used as received. All aqueous solutions were prepared with DNase and RNase free water (Thermo Fisher Scientific, Reinach, Switzerland). All images were taken using an unmodified Sony Xperia XZ Premium smartphone camera and analysed using ImageJ software (National Institutes of Health, Maryland, USA).

### 6.2.2. Device fabrication

Circular wax chambers of 8 mm diameter with 1 mm thickness were printed on Whatman No. 1 cellulose paper (Sigma-Aldrich, Buchs, Switzerland) prior to incubation at 170°C on a heating plate for 1 minute (to allow wax to penetrate into the paper). Yellow wax was chosen to define the sample reservoir, as it is the 'opposite' color—following the logic of typical color models—of our start-iodide complex, which develops as blue/purple. Using yellow has the added benefit of reducing the potential for interference by the color of the sample, which in the current study were also yellow (beer, human serum and urine). The antibody conjugation protocol reported by Peng et al., employing the amino-aldehyde reaction to form imine linkages, was used (Scheme 6.2).<sup>296</sup> Addition of amino groups onto the cellulose was achieved by applying a mixture of 3-aminopropyltrimethoxysilane (APS) and acetone (1:10) to the chambers, before drying at room temperature for 5 hours. Subsequently, the PAD was rinsed with acetone and baked in an oven at 110°C for 3 hours to complete silicon-oxygen condensation on the cellulose surface. Next, antiOTA antibodies were treated with NaIO<sub>4</sub> in acetate buffer (pH 5.5) to generate aldehyde groups at the end of the Fc-region, and then introduced into the amino functionalized chamber, forming imine linkages between the treated paper and antiOTA at room temperature, and over a period of 1 hour. Finally, devices were rinsed three times with buffer containing 10% (w/v) skimmed milk powder, 50 mM Tris, 0.15 M NaCl and 0.05% Tween 20 (pH 7.4), allowed to dry at room temperature and then stored in the dark at 4°C.



**Scheme 6.2** Schematic illustration of the covalent immobilization process of antibodies on the cellulose paper surface of the paper-based analytical device.

### 6.2.3 Aptasensor-GOx conjugation

Biotinylated aptamers (sequence previously reported<sup>79</sup>) were conjugated with avidin-conjugated glucose oxidase, via biotin-avidin binding at a 3:1 molar ratio (4°C overnight). Solutions were stored in the dark at 4°C, then diluted to 10 nM in binding buffer (10 mM Tris, pH 8.5, 120 mM NaCl, 5 mM KCl, 10 mM MgCl<sub>2</sub>, and 20 mM CaCl<sub>2</sub>) before use.

### 6.2.4 Assay procedures

For UV-vis spectroscopy experiment setup, 10 µL of 1000 U/L AGOx/GOx, 10 µL of 100 µM H<sub>2</sub>O<sub>2</sub>, 100 µL of 10% starch solution, 50 µL of 5200 µM KI, and 40 µL of 22500 µM of glucose were used and adjusted to 1 mL using PBS buffer 0.1 M pH 7.42, resulting in 10 U/L AGOx/GOx, 1 µM H<sub>2</sub>O<sub>2</sub>, 1% starch solution, 260 mM KI, and 900 µM of glucose.

### 6.2.5 GOx optimization

#### 6.2.5.1 Microwell plate assays:

Optimization of the GOx concentration for the solution phase test was carried out in a microwell plate. 25 µL of 3,600 µM glucose and 25 µL of AGOx/GOx into the wells, followed by 50 µL of 520 mM KI and 2% starch solution, and incubated for 30 min before taking images via smart phone and analyse data via imageJ.

#### 6.2.5.2 PAD assay:

For the GOx concentration study, we apply 1 µL of GOx and 1 µL of glucose into the reservoir and then added 3 µL of optimised iodine and starch solution on the reservoir to generate colour for 30 min in highly humid environment before taking images via a smartphone and analyse data via imageJ.

To perform analytical performance, 5 µL of standard solution was applied on the antibody-immobilised reservoir for 10 minute and the samples were removed by micropipette, following with 20 µL milliQ water to wash the residues for three times. Then, 5 µL aptamer/GOx was allowed applied to form sandwich before washing with milliQ water 3 times, and followed with 5 µL of the optimised chromogenic reagents for 30 minutes in high humid chamber before taking images for analysis.

### 6.2.6 System optimization

Central composite design (CCD), an experimental design method, was used to optimize concentrations of KI, glucose and starch. The levels and ranges of these (independent) variables are provided in **Table 6.1** and **Figure 6.1**.

**Table 6.1** Experimental ranges and levels of the three independent variables used in the central composite design for signal optimisation

Variables (unit)	Actual Level			Coded Level		
	Low	Middle	High	Low	Middle	High
Starch (% w/v)	0.5	1	1.5	-1	0	1
KI (mM)	100	200	300	-1	0	1
Glucose (µM)	300	600	900	-1	0	1

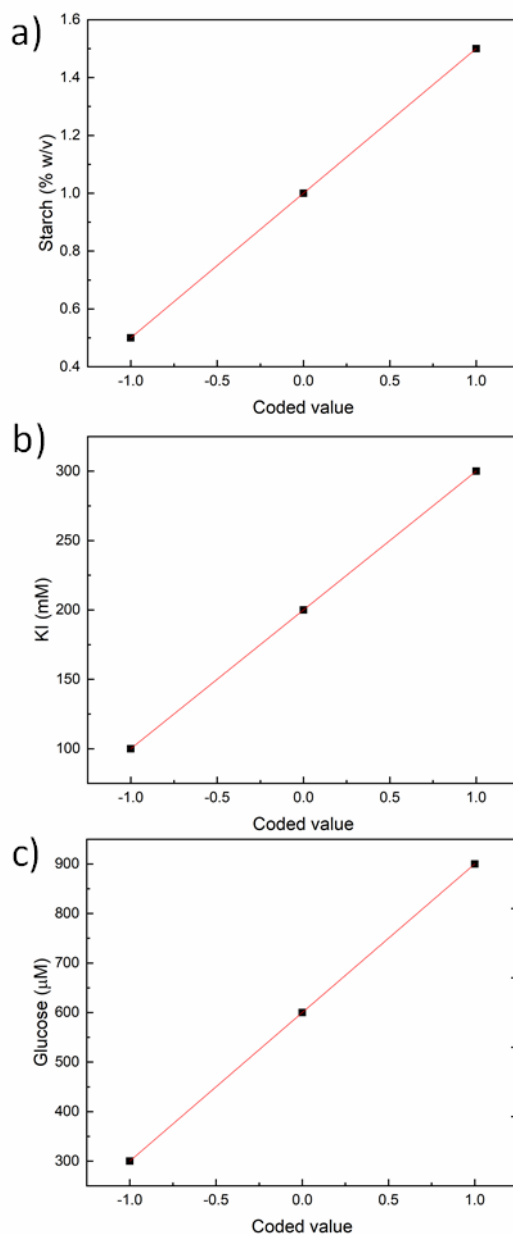


**Figure 6.1** Conversion of actual and coded values of (a) aptamer concentration, (b) enzyme concentration and (c) incubation time for the central composite design.

The three variables/factors were studied at three levels; therefore, the CCD model required 20 separate experiments, inclusive of 5 centre point repeats (**Table 6.2 and 6.3**). To allow application of PADs in a field, remote or point-of-care setting, negative (i.e. no analyte or  $\text{H}_2\text{O}_2$ ) controls were used for background subtraction.

**Table 6. 2** Experiments conducted for the central composite design for signal optimisation using KI concentration, starch concentration, glucose concentration. The normalised intensity response data for the experiments and the back-calculated response from the resultant model are shown.

Run	Coded value			%normalised intensity	
	KI	Starch	Glucose	Experiment	Predicted
1	1	1	1	63.32±0.76	63.77
2	1	1	-1	29.78±0.19	33.61
3	1	-1	1	60.38±0.47	62.12
4	1	-1	-1	31.86±0.05	29.31
5	-1	1	1	60.41±0.12	59.24
6	-1	1	-1	31.62±0.15	26.16
7	-1	-1	1	72.20±0.31	64.65
8	-1	-1	-1	33.10±0.35	28.93
9	1.68	0	0	50.05±0.48	46.18
10	-1.68	0	0	32.92±0.08	42.05
11	0	1.68	0	51.64±0.33	51.25
12	0	-1.68	0	46.53±0.21	52.19
13	0	0	1.68	68.56±0.10	70.65
14	0	0	-1.68	12.14±0.34	15.31
15	0	0	0	50.95±0.17	51.00
16	0	0	0	51.37±0.15	51.00
17	0	0	0	51.20±0.20	51.00
18	0	0	0	51.59±0.15	51.00
19	0	0	0	51.03±0.17	51.00
20	0	0	0	50.80±0.17	51.00

**Table 6.3** Central composite design model for a total of 20 experimental runs and the polynomial factor for equation calculation.

Run	Intercept	X <sub>1</sub>	X <sub>2</sub>	X <sub>3</sub>	X <sub>1</sub> <sup>2</sup>	X <sub>2</sub> <sup>2</sup>	X <sub>3</sub> <sup>2</sup>	X <sub>1</sub> X <sub>2</sub>	X <sub>1</sub> X <sub>3</sub>	X <sub>2</sub> X <sub>3</sub>	Response
1	1	1	1	1	1	1	1	1	1	1	Y
2	1	1	1	-1	1	1	1	1	-1	-1	Y
3	1	1	-1	1	1	1	1	-1	1	-1	Y
4	1	1	-1	-1	1	1	1	-1	-1	1	Y
5	1	-1	1	1	1	1	1	-1	-1	1	Y
6	1	-1	1	-1	1	1	1	-1	1	-1	Y
7	1	-1	-1	1	1	1	1	1	-1	-1	Y
8	1	-1	-1	-1	1	1	1	1	1	1	Y
9	1	1.68	0	0	2.8224	0	0	0	0	0	Y
10	1	-1.68	0	0	2.8224	0	0	0	0	0	Y
11	1	0	1.68	0	0	2.8224	0	0	0	0	Y
12	1	0	-1.68	0	0	2.8224	0	0	0	0	Y
13	1	0	0	1.68	0	0	2.8224	0	0	0	Y
14	1	0	0	-1.68	0	0	2.8224	0	0	0	Y
15	1	0	0	0	0	0	0	0	0	0	Y
16	1	0	0	0	0	0	0	0	0	0	Y
17	1	0	0	0	0	0	0	0	0	0	Y
18	1	0	0	0	0	0	0	0	0	0	Y
19	1	0	0	0	0	0	0	0	0	0	Y
20	1	0	0	0	0	0	0	0	0	0	Y

**Table 6. 4** The colorimetric signal obtained from conditions designed in the CCD.

Run	Normalized value (%)			Normalized average value (%)
	1	2	3	
1	63.32	63.775	62.29	63.32±0.76
2	29.779	29.78	29.45	29.78±0.19
3	60.376	59.45	59.77	60.38±0.47
4	31.86	31.77	31.77	31.86±0.05
5	60.409	60.65	60.56	60.41±0.12
6	31.618	31.776	31.47	31.62±0.15
7	72.204	72.795	72.68	72.20±0.31
8	33.102	33.8	33.33	33.10±0.35
9	50.046	50.89	50.08	50.05±0.48
10	32.916	32.77	32.77	32.92±0.08
11	51.643	51.77	51.13	51.64±0.33
12	46.525	46.27	46.69	46.53±0.21
13	68.561	68.66	68.46	68.56±0.10
14	12.139	12.77	12.24	12.14±0.34
15	50.945	50.67	50.99	50.95±0.17
16	51.366	51.11	51.11	51.37±0.15
17	51.204	51.17	51.13	51.20±0.20
18	51.591	51.25	51.24	51.59±0.15
19	51.026	51.24	51.31	51.03±0.17
20	50.795	51.14	51.01	50.80±0.17

Using **Table 6.3** with the results from **Table 6.4**, data can be fitted with the general regression **Equation 6.1**, i.e.

$$y = b \cdot D \quad (6.1)$$

where  $y$  is a matrix of response,  $b$  is a variable coefficient, and  $D$  is a matrix of variables. Here, matrix response and variables were known, as shown in **Table 6.3** and **6.4**. Thus, the coefficient remained to be calculated. To obtain the coefficient, a pseudo inversion was applied to avoid calculation bias due to the number of zeros in the variables matrix. Accordingly, the coefficient could be calculated using **Equation 6.2**, i.e.

$$b = (D^T \cdot D)^{-1} \cdot D^T \cdot y \quad (6.2)$$

Where  $D^T$  is transposed variables matrix, and  $(D^T \cdot D)^{-1}$  is the inverse of the multiplied value of the  $D^T$  and  $D$ . The calculated coefficients were rendered into a column where the first value was the intercept and the others belonged to each of the variables, respectively.

Captured images were imported into the ImageJ software, where simple RGB analysis was performed. The signal color intensity was determined by subtracting the negative control as a background for each image. Thus, the response signals were normalised using **Equation 6.3**

$$\text{Normalized intensity} = \frac{\text{Background intensity} - \text{Sample intensity}}{\text{Background intensity}} \times 100 \quad (6.3)$$

before optimization. Response surface modelling, statistical analysis and optimisation were performed using the matrix and equations described in previous studies.<sup>79, 230</sup> Paired t-tests and coefficients of determination ( $R^2$ ) were used to assess output data. Intensities were normalised using the percentage difference between the analyte and the background signal. Data operation was investigated using **Equation 6.2** and **6.3**. Response data from the experiments were expressed by polynomial regression, generating the following model,

$$y = \text{intercept} + \sum_{i=1}^n b_i X_i + \sum_{i=1}^n b_{ii} X_i^2 + \sum_{i=1}^{n-1} \sum_{j=i+1}^n b_{ij} X_i X_j + \epsilon \quad (6.4)$$

where  $y$  is the predicted response,  $b_i$  is the linear coefficient,  $b_{ii}$  is the quadratic coefficient,  $b_{ij}$  is the interaction coefficient, with  $X_i$  and  $X_j$  representing the variables. Optimum variable values were predicted via response surface analysis of the combined variables. Constraints in this regard were applied to predict the optimum variable conditions that would yield the highest normalised signal intensity (**Table 6.2**). Model efficiency was assessed by performing the suggested experiments and comparing real and predicted results. Coefficients of determination and paired t-tests were then used to assess model robustness. The numerical optimisation of the response was predicted according to a second order polynomial model.



### 6.2.7 Operation of PAD and real sample analysis

The PAD assay was performed by adding 5  $\mu\text{L}$  of sample into the paper well (with pre-immobilized antibodies), left for 10 minutes, then the excess sample solution was removed by micropipette. The wells were washed three times with 20  $\mu\text{L}$  milliQ water to remove unbound sample. Next, 5  $\mu\text{L}$  aptamer/GOx was applied to form the sandwich complex for 10 min, before washing with milliQ water three times. Finally, 5  $\mu\text{L}$  of chromogenic reagents were added and incubated for 30 minutes in humid chamber before taking images for analysis. Ultrahigh performance liquid chromatography (UPLC) was used to compare both standard OTA solutions and spiked-beer samples (following procedures reported by Wei et al.<sup>257</sup>) Beer samples were degassed with argon and then applied directly to either the PADs or UPLC for analysis. Testing was performed by spiking OTA into beer at 1, 5 and 10 ng/mL. For complex sample analysis, artificial urine and human serum (Sigma-Aldrich, Buchs, Switzerland) were assayed, comparing blank and OTA-spiked samples at the same concentration used for the beer samples.

### 6.2.8 Characterization

Limits of detection (LOD) and limits of quantification (LOQ) were calculated as 3 and 10 times the standard deviation of the blank measurement, respectively. Then, the results were calculated by dividing with the slope of the linear range, resulting in “log concentration” which later solved to obtain real concentration by  $10(\log \text{ concentration})$

## 6.3 Results and discussion

### 6.3.1 Colorimetric method validation

To confirm that starch-iodide complex formation is initiated by  $\text{H}_2\text{O}_2$ , a series of solutions containing permutations of 0.1 mM  $\text{H}_2\text{O}_2$ , 0.2 M KI and/or 1% (w/v) starch in PBS were probed using absorption spectroscopy. Starch solutions containing either KI or  $\text{H}_2\text{O}_2$  exhibited minimal absorbance between 300 and 800 nm (**Figure 6.2**). In contrast, the  $\text{H}_2\text{O}_2$  and KI solution was pale-yellow in colour, with a distinct absorption peak between 290 and 360 nm, indicative of residual  $\text{I}_3^-$  formation<sup>297</sup>. With all three components present, the solution turned a distinct blue, with a broad absorption peak centered at 560 nm, and lower intensity  $\text{I}_3^-$  peaks still visible below 400 nm. The reduction and shift of the  $\text{I}_3^-$  peaks, and the emergence of the 560 nm peak, confirmed starch-iodide complexation<sup>293</sup>, which only occurs when the  $\text{I}^-$  is oxidised by  $\text{H}_2\text{O}_2$  into  $\text{I}_2$  and recombined with  $\text{I}^-$  to form  $\text{I}_3^-$ .

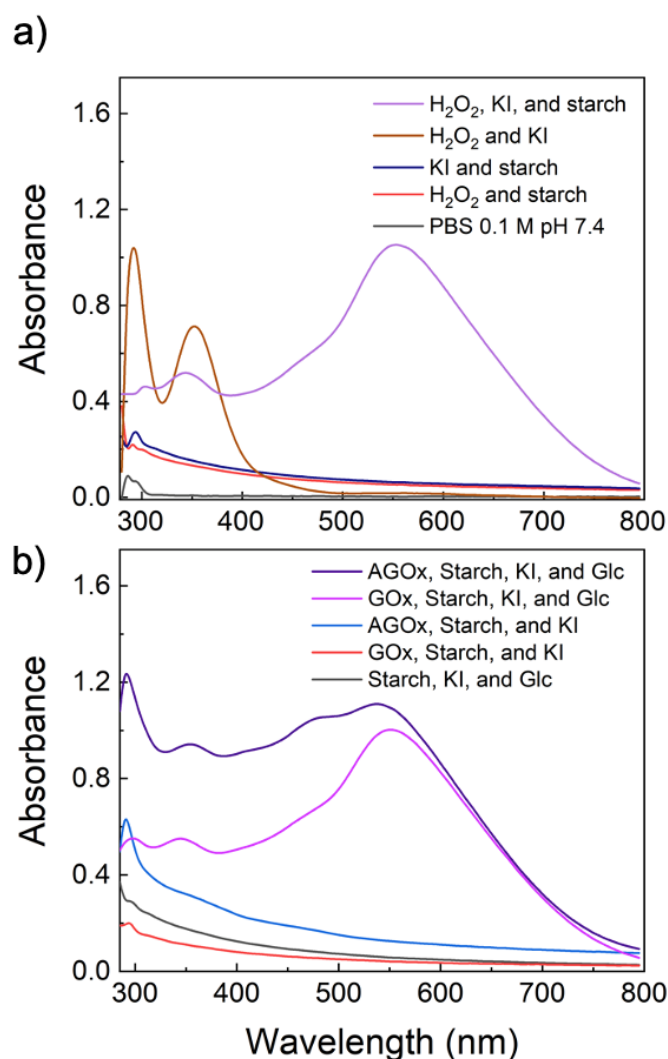


**Figure 6.2** Different permutations of the assay components were studied in solution by UV-vis absorption spectroscopy to characterise the starch-iodide complexation process. The plots present absorption spectra of (a) H<sub>2</sub>O<sub>2</sub>, starch and KI combinations, and (b) starch, KI tested with and without glucose (Glc), aptamer-conjugated GOx (AGOx) and unconjugated GOx. All solutions were prepared in 0.1 M PBS buffer at pH 7.4.

Next, we investigated whether H<sub>2</sub>O<sub>2</sub> generated by GOx would also initiate starch-iodide complexation, and whether AGOx, which requires to allow biotinylated aptamer and GOx conjugation *via* biotin-avidin interaction, showed the same efficacy as unconjugated GOx. Specifically, enzyme was introduced into a KI/starch solution, with subsequent addition of glucose initiating the production of H<sub>2</sub>O<sub>2</sub>. **Figure 6.2b** shows the development of absorption features indicative of starch-iodide complexation for both GOx and AGOx, with solutions turning blue/purple. Interestingly, in the presence of AGOx, an increasing of absorption band between 300–560 nm was observed, which indicates formation of amylopectin (an insoluble hyper-branched glucose polymer)<sup>298</sup>, and suggests that avidin could form an amylopectin-like amylose complex. This observation is consistent with the results of Lui *et al.*, who suggested that peptides or proteins enhance colour intensity in starch-iodide complexes *via* the formation of films or particles<sup>294</sup>. Here, we believe that avidin, present in the AGOx conjugate, plays a similar roll. Overall, the data confirm that the proposed AGOx-based H<sub>2</sub>O<sub>2</sub>-induced colorimetric signal transduction strategy is viable and of potential utility in a surface-based analyte sandwich format.

### 6.3.2 Assay optimization

Having established the basic working principle, we then determined which reagent concentrations (glucose, starch and potassium iodide) would yield optimal signal strength. In previous studies, assay optimisation was performed *via* a one-factor-at-a-time (OFAT) approach to determine appropriate iodine, starch and H<sub>2</sub>O<sub>2</sub> levels. In this respect, it is likely that application of a design of experiments (DoE) approach—such as central composite design (CCD), which utilises simple matrix-based regression to predict optimal values<sup>299</sup>—would be useful in extending and optimising the performance of the starch-iodide system towards a range of biosensing applications. Here, we used CCD to guide this process, as this model contains linear, quadratic, and interaction coefficients that allow capture of non-linear relationships between variables that are overlooked in the typical OFAT approach<sup>299</sup>. **Table 6.1** and **Figure 6.1** presents the independent variables used in the optimisation. The ranges were refined from literature results by performing a small number of initial test experiments, and then converted to coded values (which are used to normalise the values/ranges between variables such that resultant coefficients can be directly compared). CCD analysis was performed using a microwell plate-based assay as described in the Methods section (see **Figure 6.1**), using the design model shown in **Table 6.2** and **6.4**. This yielded the polynomial equation

$$y = 51.0 + 1.23[KI] - 0.28[Starch] + 16.5[Glucose] - 2.43[KI]^2 + 0.25[Starch]^2 - 2.84[Glucose]^2 + 1.77[KI][Starch] - 0.73[KI][Glucose] - 0.66[Starch][Glucose] \quad (6.5)$$

which models the percentage difference between the analyte signal and the background intensity, given the coded values of the reaction variable concentrations. **Figure 6.3a–c** shows three contour plots of normalised signal intensities as a function of two variables at a time. **Figure 6.3a** and **6.3b** indicate an optimal range for starch and KI concentrations between 0.5–1.5% (w/v) and 200–300 mM, respectively, with **Figure 6.3b** and **6.3c** indicating an increasing signal intensity with increasing glucose concentration. Optimal values for each variable were determined by partial differentiation of **Equation 6.5**, and yielded values of 258.8 mM for KI, 1.01% (w/v) for starch, and 902 μM for glucose. These estimates were rounded to 260 mM for KI, 1% (w/v) for starch, and 900 μM for glucose in subsequent experiments. Red circles in **Figure 6.3a–c** indicate the as-calculated values, with optimised parameters providing 72% of the normalised intensity for the blue/purple starch–iodide complex in the presence of 0.1 U/L GOx, for 30 minutes. The predicted response values extracted from the model were then compared to experimental data (**Table 6.4**), with paired t-tests ( $t\text{-value} = 0.027 < t\text{-critical} = 2.09$ ,  $\alpha = 0.05$ , 95% confidence) indicating no significant difference between the experimental and predicted data sets ( $N = 20$ ). Additionally, both experimental and predicted data exhibited excellent correspondence ( $R^2 = 0.934$ ), as shown in **Figure 6.3d**.

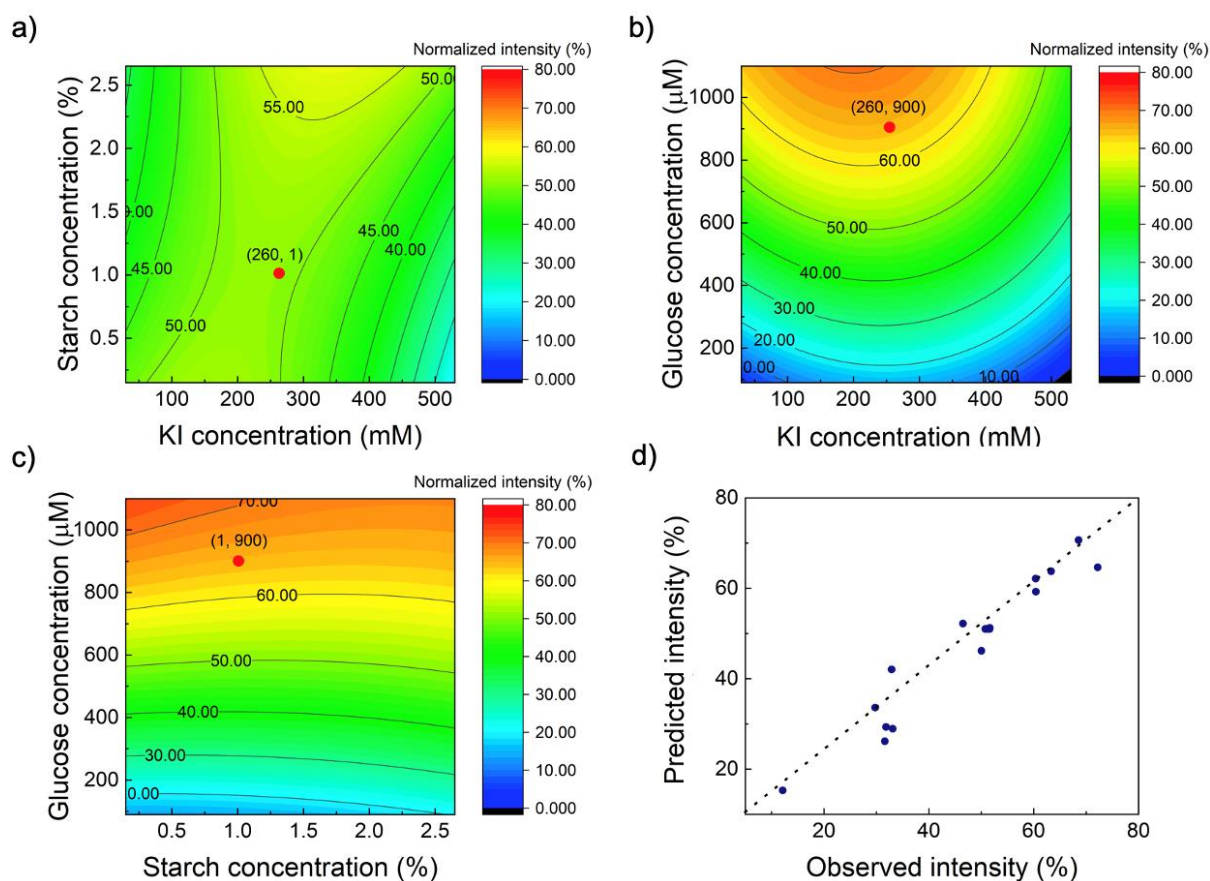


**Figure 6.3** Central composite design was used to ascertain the concentrations of three assay variables, starch concentration (%), glucose concentration ( $\mu\text{M}$ ) and KI concentration ( $\mu\text{M}$ ), that yielded optimal assay response. (a, b, c) Surface contour plots report how normalised signal intensities (assay response) vary across parameter space; plotted against two variables at a time. (d) The variation of predicted values (obtained from regression of **Equation 6.5**) as a function of experimental values reveals close correspondence between the model and experimental data (dashed line indicates  $y=x$ ).

### 3.3.3 Enzymatic activity

After optimising reagent concentrations, we next assessed the GOx activity. In our system,  $\text{H}_2\text{O}_2$  is first produced by oxidation of glucose to glucono-1,5-lactone, and free  $\text{I}^-$  is then oxidised to  $\text{I}_3^-$ , which subsequently initiates starch-iodide complexation. A GOx concentration series between 0.1 to 10 U/L was prepared in solutions containing the optimised reagent concentrations in a microwell plate format. **Figure 6.4a** shows the dose-dependent relationship between GOx and signal intensity, measured 30 minutes after GOx addition.

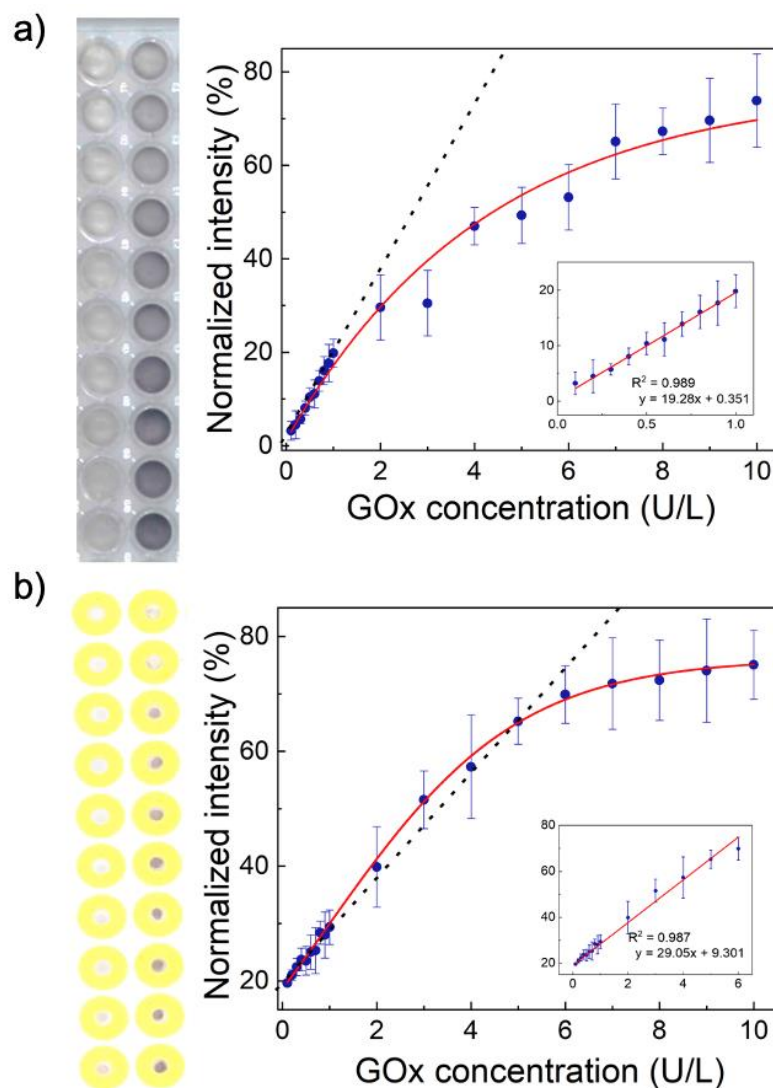


**Figure 6.4** A study of the colorimetric response due starch–iodide complexation in the presence of GOx and glucose under optimised conditions ( $N=3$ ). (a) Variation of intensity as a function of GOx concentration for experiments performed in microwell plate format. The photo (left) shows the assay solutions in the microwells, with GOx concentration increasing down the columns. (b) Variation of intensity as a function of GOx concentration for experiments performed in the PAD device. The photo (left) shows the paper device, with GOx concentration increasing down the columns. Insets show the linear response regions for both microwell- and paper-based assays, and the black dashed lines indicate the position of the linear range in the context of the whole data set.

This time was chosen based on a study of signal intensity over time, which showed the response to plateau after 30 minutes (**Figure 6.5**). These data are extracted by image analysis of the microwell plate, showing a linear range between 0.1 and 1.0 U/L ( $R^2 = 0.989$ , **Figure 6.4a** inset). The use of optimised reagent concentrations ensured high analytical sensitivity with respect to GOx detection, yielding an LOD of 0.03 U/L and a limit of quantitation (LOQ) of 0.10 U/L, based on 3 and 10 times the standard deviation of background, respectively.

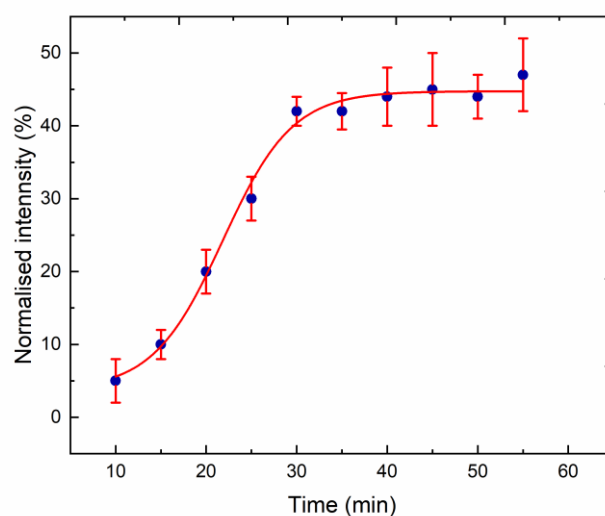


**Figure 6.5** Time course study of assay response using the optimized values from the CCD study. Based on this, a time of 30 minutes was chosen for GOx incubation.

Having determined the efficacy of the approach in free solution, we next sought to translate the sensing and signal transduction mechanisms to a PAD format. Antibody was modified on PAD covalently using process as illustrated in **Scheme 6.2**. **Figure 6.4b** presents data measured using the same conditions as in **Figure 6.4a**, but with reactions proceeding in paper wells instead of microwells. The paper wells require a sample volume of just 5  $\mu\text{L}$ , compared to 100  $\mu\text{L}$  for the well plate. but still achieve an equivalent LOD (0.03 U/L) and LOQ (0.09 U/L), and wider linear range (0.1 to 6.0 U/L,  $R^2 = 0.987$ ), compared to the well-based assay (**Figure 6.4b** inset). The main factor in this excellent performance of the PAD-based measurements is the large surface-to-volume ratio—a key advantage in microfluidic systems<sup>185,300</sup>—resulting in a much larger effective sensing area versus the microwell surface assay. These preliminary data indicate that the proposed strategy is highly suitable for use within a PAD-based sensing format.

### 6.3.4 Analytical performance

*Dynamic Range, Limit of Detection and Limit of Quantitation:* To test the developed sensing system (illustrated in **Scheme 6.1**), a calibration curve was constructed using an OTA concentration series between  $10^{-2}$  and  $10^6$  ng/mL. Using the optimised reagent concentrations, signals were extracted and quantified by image analysis, as shown in **Figure 6.6a**. Variation of extracted intensity values ( $N=5$ ) as a function of OTA concentration was linear between  $10^{-1}$  and  $10^5$  ng/mL (**Figure 6.6a** dashed line), with an LOD and LOQ for OTA of 20 pg/mL and 320 pg/mL, respectively. Moreover, comparison of the LOD and linear range of the paper-based sensor with literature OTA colorimetric sensors (**Table 6.5**), confirms significant enhancements in sensor performance over the state-of-the-art.

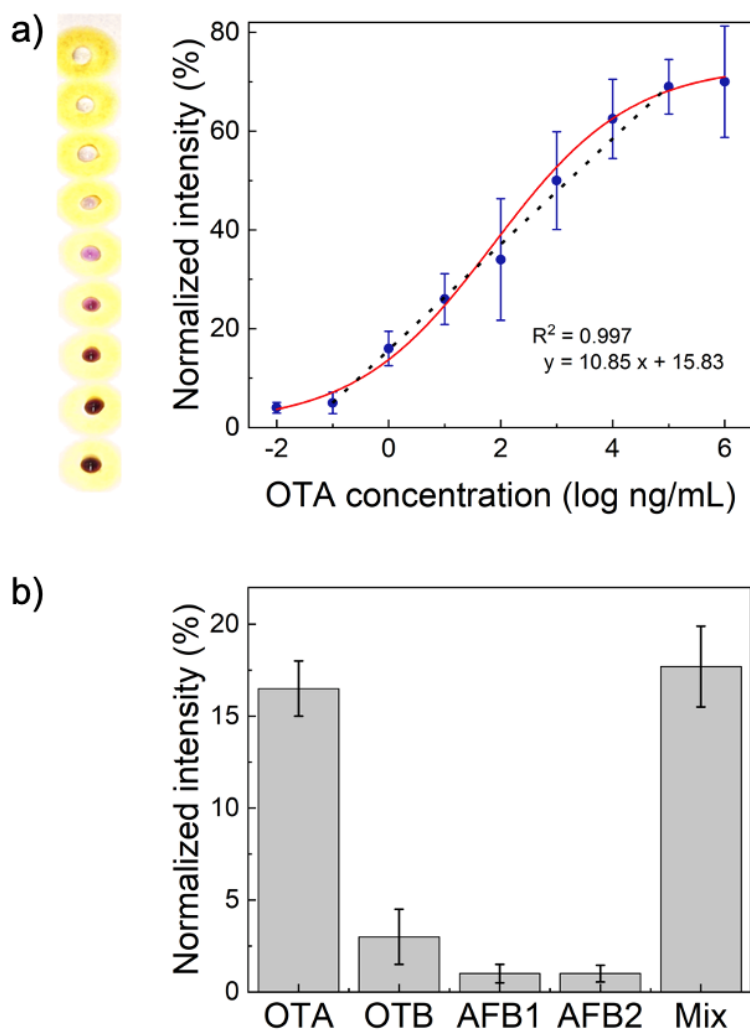


**Figure 6.6** Characterisation of the paper-based assay. (a) A calibration curve presenting normalised signal intensity obtained from the corresponding PAD image as a function of OTA concentration, with the inset showing the linear range from  $10^0$  to  $10^4$  ng/mL ( $N=5$ ). (b) Normalised signal intensity from PADs in the presence of potential interferents (OTB, AFB1, and AFB2 at 10 ng/mL) and OTA at 1 ng/mL, and their mixture ( $N=3$ ).

**Table 6.5** A comparison of reported colorimetric detection techniques for OTA determination

Bio-recognition elements	LOD (ng/mL)	Linearity (ng/mL)	Sample	References
Aptasensor and DNAzyme	0.4	N/A	Buffer	301
CMOS sensor	2	2–10	Beer and Wine	302
Aptasensor and Au@Fe <sub>3</sub> O <sub>4</sub>	0.03	0.5–100	Cereal	303
Aptasensor and AuNPs	20	32–1024	White Wine	304
ELISA with acid-base indicator	0.05	0.125–3.0	Corn	305
ELISA/urease-induced AuNP	0.04	0.05–0.64	Corn, Rice, Wheat, White Wine	306
Aptasensor/enzyme in liposome	0.023	0.05–2.0	Corn	307
Aptasensor with nanozyme	0.35	0.5–120	Grape Juice	308
Antibody/Aptasensor-GOx	0.025	0.1–10 <sup>5</sup>	Beer, Urine, and Human Serum	This work

**6.3.4.1 Assay Selectivity:**

The selectivity of the biosensor was assessed by examination of its response to potential (and common) interferents, including ochratoxin B (OTB), aflatoxin B1 (AFB1), and aflatoxin B2 (AFB2). In all experiments, the concentration of each interferent was set to 10 ng/mL; a value that is an order of magnitude higher than OTA (1 ng/mL). **Figure 6.6b** shows that a high intensity signal for OTA, but a negligible response from all studied interferents, with signals originating from the pure OTA sample and mixed sample being identical. It should be noted that a marginally higher signal from OTB (versus AFB1 and AFB2) is expected since antiOTA exhibits trace binding with OTB (<1% in comparison with OTA, as indicated by the manufacturer) <sup>309-310</sup>. However, when compared to the pure OTA sample, such a signal is insignificant ( $t$ -value = 0.11,  $t$ -critical = 2.90,  $N=3$ ). Accordingly, the biosensor achieves excellent selectivity for OTA over OTB, AFB1, and AFB2, which is a direct result of the high selectivity inherent in the antibody-aptamer system.

**6.3.4.2 Assay Accuracy:**

To validate the accuracy of the developed PAD system, we compared it to the gold standard method ultrahigh performance liquid chromatography (UPLC), and a previously developed electrochemical aptasensor <sup>311</sup>. Testing an OTA concentration series (1–10 ng/mL) with each method ( $N=3$ ), the PAD gave a coefficient of determination ( $R^2$ ) of 0.985 against UPLC and 0.987 against the electrochemical aptasensor (**Figure 6.7a**). A  $t$ -test comparison indicated no significant difference between each method, with excellent agreement at the 95% confidence level ( $\alpha = 0.05$ ;  $t$ -values = 1.20 and 0.57 versus UPLC and electrochemical aptasensor, respectively;  $t$ -critical = 2.30).



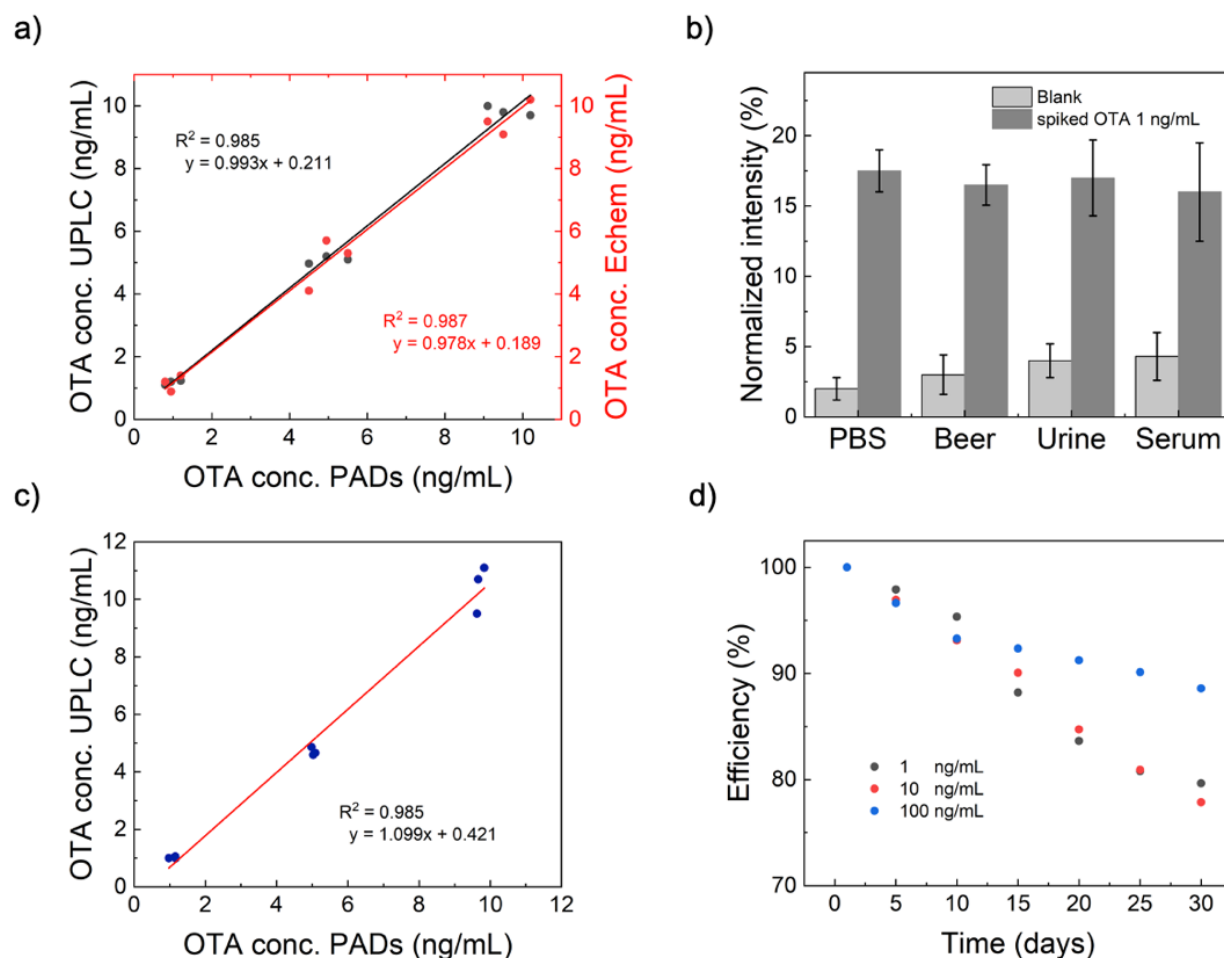


**Figure 6.7** Further characterization of the paper-based assay. (a) A comparison of OTA concentrations obtained when using the PAD, UPLC and an electrochemical aptasensor, to analyse standard solutions. (b) Normalized signal intensity obtained from the different sample matrices: PBS, beer, artificial urine and human serum, both blank and spiked with OTA to 1 ng/mL. (c) Comparison of OTA concentrations between the PADs and UPLC in beer samples spiked with OTA to 1, 5 and 10 ng/mL. (d) Variation of efficiency as a function of storage time for PADs detecting OTA (1, 10, and 100 ng/mL) over a period of 30 days ( $N=3$ ).

### 6.3.5 Complex sample analysis

Complex matrix validation was performed through the analysis of beer, artificial urine and human serum, all spiked to 1 ng/mL OTA. The results demonstrated excellent performance of the aptasensor in all matrices (**Figure 6.7b**). The larger variance in serum was likely due to the large amount of protein, predominantly serum albumin, interfering with sandwich complex formation<sup>312</sup>. Similarly, the artificial urine sample used in the current study contains 0.5% peptone, a soluble protein formed in the early stage of protein breakdown during digestion<sup>313</sup>. Thus, samples containing high concentrations of protein can slightly compromise detection efficiency through interference of the binding of AGOx and antiOTA with analyte. Next, we spiked beer, artificial urine, and human serum with OTA at concentrations between 1 and 10 ng/mL, and calculated the detectable amount of OTA as a %recovery (**Table 6.6**). Significantly, all recoveries were measured to be between 95 and 117%, comparing well with corresponding recoveries from UPLC analyses. Further, we used the spiked beer samples as a direct comparison with UPLC (**Figure 6.7c**), confirming excellent agreement between detection methods ( $R^2 = 0.985$ ) with RSD less than 5%.

### 6.3.6 Assay stability

Reagents and device stability over extended periods of time are vital factors for the practical application of sensing systems. To assess shelf lifetimes, a set of PADs (totalling 500 detection chambers) was stored under nitrogen at 4°C for up to 30 days. Colour intensity (extracted using ImageJ) was then used to quantify the response for 1, 10, and 100 ng/mL OTA solutions in PBS (**Figure 6.7d**). Collected data indicate a deterioration in response for all OTA concentrations when compared to data originating from freshly prepared PADs, however these were determined to not be statistically significant ( $t$ -values for the three concentrations were 2.76, 3.26, and 4.18 for 1, 10, and 100 ng/mL ( $N=3$ ), respectively, with  $t$ -critical = 4.30). However, the average intensities originating from stored PADs did exhibit a 20% reduction in intensity signal (**Figure 6.7d**), which is likely a result of partial denaturization of the antibodies on the paper surface. Such effects could be further minimized by freeze-drying the PADs prior to storage.

**Table 6. 6** Determination of OTA concentration in spiked beer samples comparing the PADs with UPLC, and comparing OTA concentration in blank and spiked artificial urine and human serum.

Sample	Spiked OTA (ng/mL)	Detected (ng/mL)		Recovery (%)		%RSD		t-value
		PADs	UPLC	PADs	UPLC	PADs	UPLC	
Beer 1	1	0.98±0.05	1.00±0.02	98.00	99.69	4.99	2.63	0.07
	5	4.98±0.20	4.86±0.05	99.60	97.29	4.01	1.98	0.36
	10	9.63±0.41	9.50±0.32	96.30	94.97	4.32	1.01	0.3
Beer 2	1	1.17±0.04	0.99±0.04	117.0	99.17	3.39	0.46	0.15
	5	5.09±0.12	4.66±0.10	101.8	93.14	2.26	1.61	0.45
	10	9.83±0.15	11.1±0.31	98.30	110.71	1.49	0.55	0.33
Beer 3	1	1.16±0.03	1.06±0.05	116.0	105.8	2.58	1.41	0.46
	5	5.03±0.25	4.59±0.12	100.6	91.81	4.97	1.41	0.45
	10	9.66±0.47	10.7±0.35	96.60	107.5	4.93	0.7	0.41
Urine	1	0.96±0.03	-	96.00	-	3.75	-	-
	5	5.08±0.12	-	101.6	-	2.49	-	-
	10	10.0±0.08	-	100.1	-	0.84	-	-
Human Serum	1	1.00±0.03	-	100.0	-	3.76	-	-
	5	5.01±0.07	-	100.2	-	1.55	-	-
	10	9.53±0.25	-	95.30	-	2.69	-	-

## 6.4 Conclusions

We show for the first time the application of starch-iodide complexation as a colorimetric reagent in a PAD device for biomolecular detection using a sandwich-based assay format. Targeting OTA as a model analyte using an antibody-aptamer capture mechanism, we optimised reagent concentrations (iodine, starch, and glucose) using central composite design, and achieved an LOD of 20 pg/mL, an LOQ of 320 pg/mL and a linear range between  $10^{-1}$  and  $10^5$  ng/mL (over six orders of magnitude) against standard OTA solutions. The system exhibits excellent performance in complex matrices (human serum, artificial urine, and beer), comparing well with gold-standard UPLC. Overall, the sensing approach described herein exhibits great potential as a universal, environmentally friendly and cost-effective PAD biosensing platform to detect a wide range of analytes based on antibody and/or aptamer-based affinity reactions. We have demonstrated excellent sensitivity, selectivity, accuracy, precision and robustness in real-world samples, and excellent promise for universal point-of-use analyses. For example, this approach could be developed as an *in vitro* diagnostic device for widespread medical testing, and for deployment in resource-limited settings.

# Chapter 7

## Outlook for Field-Deployable Diagnostics

This chapter is adapted from a paper entitled "*Enzyme-Assisted Nucleic Acid Detection for Infectious Disease Diagnostics: Moving toward the Point-of-Care*", authored by Akkapol Suea-Engam, Leonard Bezing, Bogdan Mateescu, Philip D. Howes, Andrew J. deMello and Daniel A. Richards. Published in *ACS Sensors* **2020**, 5, 2701–2723

### 7.1 Current state and future prospects

The initial stages of the COVID-19 pandemic highlighted the critical role of IVDs in infectious disease control.<sup>314</sup> A key issue in this respect was the need for gene-based (i.e., nucleic acid) or antigen-based (i.e., protein) testing as opposed to serology; antibody testing was ineffective at revealing early stage infections when people were at their most infectious.<sup>315</sup> Unfortunately, the unavailability of widespread and rapid diagnostics led to a severe data deficit in the initial phase of the disease, data that were urgently needed to inform critical time-sensitive interventions (i.e., test, trace, and isolate). Notably, regions that managed to perform extensive testing, e.g., South Korea, Germany, Singapore, Taiwan, and Hong Kong, had the greatest success in containing early outbreaks, highlighting the vital role of epidemiology alongside healthcare.<sup>316</sup> As researchers in the field of IVDs, our community was uniquely positioned to analyze diagnostic efforts and draw conclusions to aid in future outbreaks. Importantly, we observed a deep gulf between the “state-of-the-art” technologies and the “ready now” technologies. For COVID-19, the “ready now” turned out to be the decades-old but reliable PCR, run in centralized laboratories by highly skilled professionals. This restricted the global capacity for testing, and often resulted in significant delays between sampling and result. A more agile technology, capable of providing faster diagnoses to a larger proportion of the population, would have substantially changed the course of the pandemic. As highlighted in the thesis introduction, at a fundamental research level, many technologies to facilitate this already exist; the problems arise primarily from our ability to translate these technologies from the research lab to the end user in a timely fashion. In the spirit of the REASSURED criteria, despite past experience and knowledge of the challenges,<sup>317-318</sup> we failed on the “D”—delivery. Delivery refers to the organizational structures and relationships established with the purpose of coordinating and steering the logistics of selecting, procuring, shipping, storing, distributing and delivering a new health technology to ensure it reaches the end users.<sup>5</sup>

In the future, widespread availability of cheap and accurate IVDs will play an increasing and integral role in global management of infectious disease and healthcare monitoring. It will also play a key part in moving our general healthcare model from pure “crisis intervention” toward “preventative maintenance”, a transition that is vital for improving global health. Further, research and discoveries in enzymology and synthetic biology undoubtedly hold immense potential for impact in enzyme-assisted nucleic acid IVDs. Regarding natural enzymes, even considering humanity’s expansive investigations and knowledge in enzymology, we have likely only scratched the surface of nature’s pool of useful biocatalysts.<sup>319</sup> Thus, further fundamental studies in biology will continue to reveal new and important enzymes for advanced applications. For example, further study of bacteria and viruses, in particular, the mechanisms by which

bacteria defend themselves,<sup>320</sup> could give rise to new opportunities in nucleic acid assays; this is precisely what happened after the discovery of CRISPR-Cas enzymes.<sup>321</sup> Another exciting area of exploration is the field of enzyme engineering. We believe that advances in de novo enzyme design, for example, using protein structure modeling, computational enzyme design, and molecular dynamics simulations, will give rise to ever more advanced enzymes for manipulating and detecting of nucleic acids.<sup>322</sup> These techniques are already having a huge impact in other fields of research;<sup>323</sup> therefore, we have good reason to be optimistic about the impact they will have in enzyme-assisted nucleic acid IVDs.

The ultimate goal for point-of-care testing, in the context of infectious disease and healthcare monitoring, is to create a simple sample-in, answer-out platform that requires minimal user input and infrastructure to operate effectively. Despite the multitude of advances described in this field, it is clear that we have not yet achieved this goal—at least not in a format that has been practical enough for widespread adoption during recent pandemics. Considering the complexity, the drive toward making these tests simpler (i.e., smaller, easy to operate) is a challenge, particularly while maintaining affordability. After all, these challenges are what necessitate the current reliance on complex machinery and centralized laboratories. Accordingly, we have to be smart in identifying whether our new ideas in the lab have any chance of finding real-world application, with a particular focus on practicality and affordability.

## 7.2 Future areas of focus

The versatility and adaptability of IVDs are vital considerations in their marketability. We suggest that a key opportunity exists in looking for synergies between IVDs for chronic and infectious diseases. Chronic diseases such as cancer, diabetes, and obesity are increasing in wealthier populations, which is establishing an attractive market for companies looking to maximize their profits in the area of IVDs. However, the burden of infectious diseases is predominant in less wealthy nations, and the market for IVDs can be unstable given the transient or inconsistent demand for particular tests. One way to reconcile this conflict is to look for synergies in IVD requirements between chronic and infectious disease, such that IVDs that are developed to serve the chronic market could be rapidly reengineered and deployed against an infectious disease threat. In the context of epidemics, this would yield platform technologies that are “epidemic sensitive” rather than “epidemic specific”.

Although the power of combining nucleic acid IVDs and mHealth solutions is obvious, there are still many challenges in practical implementation. For example, the policy and regulation governing mHealth concepts, software, and devices provide a headache for regulatory bodies that have evolved to work within the traditional centralized medicine model, though there are advanced global efforts to make vital reforms here.<sup>324</sup> There must be caution with regard to how mHealth solutions are marketed and implemented, taking great care not to impose upon people’s privacy, and balancing this against potential stifling of innovation and impact. Another consideration is that the deployment and operation of diagnostics should not become completely reliant on digital connectivity, given that 33% of the global population are not connected to mobile Internet.<sup>325</sup>

The seemingly simple transition from “does the patient have disease X?” to “which disease does the patient have?” encompasses a huge technological challenge. It requires tests to be multiplexed to cover a range of infectious diseases, which increases the complexity of the molecular biology and the device design, with inevitable ramifications for end-point price. However, the power of this approach is well worth the technological investment required in engineering new solutions.

Beyond multiplexing, conceptually the most powerful gene-based diagnosis of an infectious disease is to perform genome-sequencing and compare the results to extensive libraries of known sequences. Therefore, instead of performing many tests in parallel, one is performing a single test that can output the data necessary to diagnose multiple diseases. However, current methods for sequencing are still technologically demanding, and it is an open question as to how far toward the point-of-care this technology can penetrate. Nevertheless, there are some extremely exciting examples of how sequencing can be used in infectious disease diagnostics,<sup>326-327</sup> and enzyme-assisted amplification and/or detection could play a key role here.

It is important to highlight the severe and increasing threat to human health and wellness posed by antimicrobial resistance (AMR). Currently, it is estimated that AMR leads to at least 700,000 global deaths each year, a figure that could rise to 10 million per year by 2050 if no action is taken.<sup>328</sup> While this number represents a worst case scenario, it is clear that we must do something to combat AMR. Part of our battle against the evolution of AMR is being able to quickly discern whether an infection is viral or bacterial in nature, and preferably what the pathogen is.<sup>329</sup> With this knowledge, deciding which treatment is required is far simpler, thus circumventing the current approach of using broad spectrum antibiotics as a first port of call for undiagnosed infections. Future nucleic acid IVDs will likely play a key role here.

In the past century, scientists have developed a number of tools to detect toxins in food using fluorometry, electrochemistry, and colorimetry, coupled with separation techniques, for example chromatography.<sup>239</sup> The state-of-the-art technologies have been established and used as 'gold-standard' methods to detect toxins, in line with recommendations from international and national organisations.<sup>237</sup> Although these methods to detect toxins are commonly less complicated than those used for pathogens, they typically require bulky instrumentation, large amounts of reagents, and a continuous and large supply of power. Such cumbersome and costly system prevent application in resource-limited areas, as discussed previously for the pathogen detection, and thus point-of-use methods need to be developed.

Using nucleic acid-based affinity binding units, known as aptamers, is a cost-effective way to ensure our safe food.<sup>244</sup> Aptamers have been discovered that can bind with high specificity to analytes by adopting particular forms (e.g. G-quadruplex, i-motif, and hairpin) and provide altered resistance against nucleic acid-related enzymes (e.g. polymerases and nucleases). Aptamers should be considered as an ultimate biorecognition material for toxin analysis, as they can be produced on a massive scale relatively cheaply, whilst maintaining excellent analytical performance versus antibodies. Further development of aptamer-enzyme biosensors could improve point-of-use devices and play key role for food and health safety. Thus, such platforms could form the basis of the next generation of toxin analysis kits for commercial and home use, addressing current insufficiencies in toxin analysis instrumentation in developing world.

Infectious diseases strike indiscriminately, leaving us all at risk regardless of national boundaries and economic status. Further, with the heaviest burden of infectious disease being felt in resource-limited areas, the world's poorest people are, by no fault of their own, the most susceptible to life-threatening infections. Diagnosis is an absolutely key, but often overlooked, part of disease treatment. The shift toward the point-of-care requires a concerted, multidisciplinary effort; advances in enzyme engineering, molecular biology, chemistry, and engineering all contribute to the development of fully integrated RDTs. While a substantial amount of work remains to realize truly effective PoC nucleic acid diagnostics, each step forward has brought the technology closer to the end user. Likewise, exposure to environmental toxins inflicts substantial mortality and morbidity to the human population, and new tools for detection and toxicology will help us to protect ourselves from detrimental exposure.

# Chapter 8

## Conclusions

Although many technologies have been developed over the last century to detect toxins and diseases, the typically required instrumentation is complicated, bulky and expensive. In my work, I aim to develop cost-effective analytical platforms that will allow anyone to detect anything they want, anywhere. Accordingly, this thesis presents the development of enzyme-enabled field-deployable diagnostic platforms for toxin and pathogen detection. Utilizing enzyme-enabled nucleic acid concepts, ultrasensitive point-of-care diagnostic devices were developed. Enzymes were deployed to digest, trigger, amplify, and cleave DNA within the developed microfluidic platforms, with the aim of using less reagent to reduce cost per detection, whilst retaining excellent analytical performance. These projects have successfully demonstrated a guideline for further development of field-deployable diagnostic devices, facilitating future improvement for effective real-world, field-deployable diagnostics.

The first part of the thesis covers work aimed at infectious pathogen detection. Drug-resistant bacteria, which are typically contagious, kill almost a million people yearly, which is predicted to kill up to 10 million yearly by 2050. Thus, MRSA was chosen as a representative drug-resistant bacterium in this work. Loop-mediated isothermal amplification (LAMP) was employed to amplify the *mecA* gene of MRSA, since it can amplify a massive amount of the target gene while using a constant temperature, unlike PCR which requires complicated thermocycling. The first project developed a colorimetric assay to detect LAMP amplicons using silver nanoplates (AgNPLs), giving outstanding analytical performance. Moreover, this colorimetric assay was applied on PADs, allowing single-molecule detection of drug-resistant bacteria by the naked eye for the first time. LAMP was also performed in microdroplets in the fourth project, where the fabrication of microdroplet hydrogels allowed development of a digital droplet platform for LAMP, which is feasible without a microfluidic device in a real-field setting. The developed HD-LAMP platform allows MRSA detection down to 1000 copies/ $\mu\text{L}$ . Both methods provide excellent analytical performance that is comparable to the polymerase chain reaction (PCR).

The next project was on the development of an electrochemical detection method coupled with silver metallization for a CRISPR/Cas biosensor (E-Si-CRISPR), which was employed to detect the MRSA *mecA* gene. The E-Si-CRISPR technique showed excellent sensitivity, down to the fM level without the assistance of DNA amplification. The approach showed excellent selectivity down to single nucleotide level, which allowed highly specific detection of MRSA against other common bacteria. The developed method is comparable to the gold-standard PCR method, and could facilitate simple detection of various pathogens by only changing the protospacer sequence.

Further, food toxins taken in through our daily consumption can lead to a myriad of harmful diseases. I chose ochratoxin A (OTA) as a representative food toxin since it can often be found in our daily life, and in many foodstuffs, including grains, beverages, and meats. OTA aptamer immobilized on an electrode surface was chosen, allowing OTA to bind and form a G-quadruplex, which prevented digestion by the exonuclease I enzyme. The unbound aptamer was digested and removed from the electrode, while the remaining OTA-bound aptamer was silver metallized electrochemically and chemically, eventually yielding ultrasensitive electrochemical detection

down to sub-pg/mL levels. The next project saw the development of a paper-based analytical device (PAD), where surface modification with an anti-OTA antibody allowed OTA to form a sandwich complex after applying aptamer-conjugated GOx. By applying glucose, starch, and iodine solution, the GOx generated H<sub>2</sub>O<sub>2</sub> that oxidized the iodine into I<sub>3</sub><sup>-</sup>, which gave a blue/purple solution in the presence of starch. This colorimetric assay was applied to detect OTA on PADs, allowing the ultrasensitive OTA detection down to the pg/mL level. Both methods provided excellent analytical performance comparable to the gold-standard method (UPLC), facilitating the further development of field-deployable food toxin detection devices.

Although the projects presented herein have demonstrated great promise for toxin and disease detection, with excellent analytical performance, they are not yet ready for in field use. Further studies (e.g. clinical sample and complex matrix analysis) are required to ensure that they can be used with no false-positive or false-negative results. Further, even though the presented platforms were quite simple to fabricate in our lab setting, such approaches might not be scalable to mass production, for various reasons. Therefore, future work would have to focus on using scalable fabrication methodologies whilst incorporating the advances presented in this thesis.

Although many seemingly excellent PoC devices have been developed over recent decades, very few of them have reached commercialization, and many of the commercialized systems have failed to reach significant market penetration. Notably, during the emergence of the Covid-19 pandemic, we observed a remarkably slow roll out of urgently required PoC tests, which had a dramatically detrimental impact on the evolution of the crisis. This issue has raised many questions about the multitudes of novel PoC methods that are continually published in academic journals. I feel we, scientists and engineers, are not going in the wrong direction—having more choices of detection is always better for moving towards commercialization and real impact, allowing the marketing mechanisms to deliver best solutions for everyone. A big remaining issue is that governments and national organisations appear to pay less attention to the PoC test development than they ought to. I hope this pandemic scenario will make the relevant health organizations realize how important PoC testing really is. If the required backing is given, then such delays in the development and deployment of PoC devices will cease to be such an issue, and we should be able to fight future outbreaks, epidemics and pandemics much more effectively than we have managed in the pandemic year of 2020.

Inspired by my mother, who passed away due to the delay of realizing that she had liver cancer, I am motivated to develop devices that could allow us to detect diseases easily, anytime, anywhere, and by anyone. I feel developing such devices is not only assisting people who live in resource-limited areas like the countryside of Thailand, my home country, or people who live in the mountains, but it is also helping everyone to access a healthier life. Being able to detect suspicious diseases that we have potential to get at home would help us to seek treatment before it is too late to cure them. Besides, having cost-effective PoC devices will increase equality for all citizens in our world. Having a healthy life should be a human right that everyone can access. It should not be a privilege for the rich, or for people living in developed areas, but everyone. I hope these devices could help us bring humanity to our society with greater equality, at least giving the choice to enjoy health and wellbeing.



# References

1. World Health Organisation Coronavirus Diseases (COVID-19) Dashboard; covid10.who.int. (access August 20th, 2020).
2. Top Ten Causes of Death, Global Health Observatory (GHO) Data; [www.who.int/gho/mortality\\_burden\\_disease/causes\\_death/top\\_10/en](http://www.who.int/gho/mortality_burden_disease/causes_death/top_10/en). (accessed August 20th, 2020).
3. World Health Organization List of Prequalified in Vitro Diagnostic Products; [www.who.int/diagnostics\\_laboratory/evaluations/PQ\\_list/en/](http://www.who.int/diagnostics_laboratory/evaluations/PQ_list/en/). (accessed August 20th, 2020).
4. Slutkin, G.; Okware, S.; Naamara, W.; Sutherland, D.; Flanagan, D.; Carael, M.; Blas, E.; Delay, P.; Tarantola, D., How Uganda reversed its HIV epidemic. *AIDS and Behavior* **2006**, *10* (4), 351-360.
5. Land, K. J.; Boeras, D. I.; Chen, X.-S.; Ramsay, A. R.; Peeling, R. W., REASSURED diagnostics to inform disease control strategies, strengthen health systems and improve patient outcomes. *Nature microbiology* **2019**, *4* (1), 46-54.
6. Yuan, M.; Wu, N. C.; Zhu, X.; Lee, C.-C. D.; So, R. T.; Lv, H.; Mok, C. K.; Wilson, I. A., A highly conserved cryptic epitope in the receptor binding domains of SARS-CoV-2 and SARS-CoV. *Science* **2020**, *368* (6491), 630-633.
7. Gussow, A. B.; Auslander, N.; Faure, G.; Wolf, Y. I.; Zhang, F.; Koonin, E. V., Genomic determinants of pathogenicity in SARS-CoV-2 and other human coronaviruses. *Proceedings of the National Academy of Sciences* **2020**.
8. Zhu, N.; Zhang, D.; Wang, W.; Li, X.; Yang, B.; Song, J.; Zhao, X.; Huang, B.; Shi, W.; Lu, R., A novel coronavirus from patients with pneumonia in China, 2019. *New England Journal of Medicine* **2020**.
9. Institut Pasteur Sequences the Whole Genome of the Coronavirus, 2019-NCoV. [www.pasteur.fr/en/press-area/press-documents/institutpasteur-sequences-whole-genome-coronavirus-2019-ncov](http://www.pasteur.fr/en/press-area/press-documents/institutpasteur-sequences-whole-genome-coronavirus-2019-ncov) (accessed August 20th, 2020).
10. Kelley, B., Developing therapeutic monoclonal antibodies at pandemic pace. *Nature biotechnology* **2020**, *38* (5), 540-545.
11. Broughton, J. P.; Deng, X.; Yu, G.; Fasching, C. L.; Servellita, V.; Singh, J.; Miao, X.; Streithorst, J. A.; Granados, A.; Sotomayor-Gonzalez, A., CRISPR-Cas12-based detection of SARS-CoV-2. *Nature Biotechnology* **2020**, 1-5.
12. Toh, S. Y.; Citartan, M.; Gopinath, S. C.; Tang, T.-H., Aptamers as a replacement for antibodies in enzyme-linked immunosorbent assay. *Biosensors and bioelectronics* **2015**, *64*, 392-403.
13. Saiki, R. K.; Scharf, S.; Faloona, F.; Mullis, K. B.; Horn, G. T.; Erlich, H. A.; Arnheim, N., Enzymatic amplification of beta-globin genomic sequences and restriction site analysis for diagnosis of sickle cell anemia. *Science* **1985**, *230* (4732), 1350-1354.
14. Mullis, K.; Faloona, F.; Scharf, S.; Saiki, R.; Horn, G.; Erlich, H. In *Specific enzymatic amplification of DNA in vitro: the polymerase chain reaction*, Cold Spring Harbor symposia on quantitative biology, Cold Spring Harbor Laboratory Press: 1986; pp 263-273.
15. Higuchi, R.; Fockler, C.; Dollinger, G.; Watson, R., Kinetic PCR analysis: real-time monitoring of DNA amplification reactions. *Bio/technology* **1993**, *11* (9), 1026-1030.
16. Cobas(R) 6000 Analyzer Series; [diagnostics.roche.com/global/en/products/systems/cobas\\_-6000-analyzer-series.html](http://diagnostics.roche.com/global/en/products/systems/cobas_-6000-analyzer-series.html) (accessed August 20th, 2020).

17. Holland, P. M.; Abramson, R. D.; Watson, R.; Gelfand, D. H., Detection of specific polymerase chain reaction product by utilizing the 5'----3'exonuclease activity of *Thermus aquaticus* DNA polymerase. *Proceedings of the National Academy of Sciences* **1991**, *88* (16), 7276-7280.
18. Notomi, T.; Okayama, H.; Masubuchi, H.; Yonekawa, T.; Watanabe, K.; Amino, N.; Hase, T., Loop-mediated isothermal amplification of DNA. *Nucleic acids research* **2000**, *28* (12), e63-e63.
19. Goto, M.; Honda, E.; Ogura, A.; Nomoto, A.; Hanaki, K.-I., Colorimetric detection of loop-mediated isothermal amplification reaction by using hydroxy naphthol blue. *Biotechniques* **2009**, *46* (3), 167-172.
20. Goto, M.; Shimada, K.; Sato, A.; Takahashi, E.; Fukasawa, T.; Takahashi, T.; Ohka, S.; Taniguchi, T.; Honda, E.; Nomoto, A., Rapid detection of *Pseudomonas aeruginosa* in mouse feces by colorimetric loop-mediated isothermal amplification. *Journal of microbiological methods* **2010**, *81* (3), 247-252.
21. Soli, K. W.; Kas, M.; Maure, T.; Umezaki, M.; Morita, A.; Siba, P. M.; Greenhill, A. R.; Horwood, P. F., Evaluation of colorimetric detection methods for *Shigella*, *Salmonella*, and *Vibrio cholerae* by loop-mediated isothermal amplification. *Diagnostic Microbiology and Infectious Disease* **2013**, *77* (4), 321-323.
22. Connelly, J. T.; Rolland, J. P.; Whitesides, G. M., "Paper machine" for molecular diagnostics. *Analytical chemistry* **2015**, *87* (15), 7595-7601.
23. Zhang, H.; Xu, Y.; Fohlerova, Z.; Chang, H.; Iliescu, C.; Neuzil, P., LAMP-on-a-chip: Revising microfluidic platforms for loop-mediated DNA amplification. *TrAC Trends in Analytical Chemistry* **2019**, *113*, 44-53.
24. Piepenburg, O.; Williams, C. H.; Stemple, D. L.; Armes, N. A., DNA detection using recombination proteins. *PLoS Biol* **2006**, *4* (7), e204.
25. Li, J.; Macdonald, J.; von Stetten, F., a comprehensive summary of a decade development of the recombinase polymerase amplification. *Analyst* **2018**, *144* (1), 31-67.
26. Yehia, N.; Arafa, A.-S.; Abd El Wahed, A.; El-Sanousi, A. A.; Weidmann, M.; Shalaby, M. A., Development of reverse transcription recombinase polymerase amplification assay for avian influenza H5N1 HA gene detection. *Journal of virological methods* **2015**, *223*, 45-49.
27. Abd El Wahed, A.; Patel, P.; Faye, O.; Thaloengsok, S.; Heidenreich, D.; Matangkasombut, P.; Manopwisedjaroen, K.; Sakuntabhai, A.; Sall, A. A.; Hufert, F. T., Recombinase polymerase amplification assay for rapid diagnostics of dengue infection. *PloS one* **2015**, *10* (6), e0129682.
28. Faye, O.; Faye, O.; Soropogui, B.; Patel, P.; Abd El Wahed, A.; Loucoubar, C.; Fall, G.; Kiory, D.; Magassouba, N. F.; Keita, S., Development and deployment of a rapid recombinase polymerase amplification Ebola virus detection assay in Guinea in 2015. *Eurosurveillance* **2015**, *20* (44), 30053.
29. Fire, A.; Xu, S.-Q., Rolling replication of short DNA circles. *Proceedings of the National Academy of Sciences* **1995**, *92* (10), 4641-4645.
30. Kool, E. T., Rolling circle synthesis of oligonucleotides and amplification of select randomized circular oligonucleotides. Google Patents: 1998.
31. Mohsen, M. G.; Kool, E. T., The discovery of rolling circle amplification and rolling circle transcription. *Accounts of chemical research* **2016**, *49* (11), 2540-2550.
32. Zhuang, J.; Lai, W.; Chen, G.; Tang, D., A rolling circle amplification-based DNA machine for miRNA screening coupling catalytic hairpin assembly with DNAzyme formation. *Chemical communications* **2014**, *50* (22), 2935-2938.
33. Nayak, S.; Blumenfeld, N. R.; Laksanasopin, T.; Sia, S. K., Point-of-care diagnostics: recent developments in a connected age. *Analytical chemistry* **2017**, *89* (1), 102-123.
34. Lizardi, P. M.; Huang, X.; Zhu, Z.; Bray-Ward, P.; Thomas, D. C.; Ward, D. C., Mutation detection and single-molecule counting using isothermal rolling-circle amplification. *Nature genetics* **1998**, *19* (3), 225-232.

35. Walker, G. T.; Little, M. C.; Nadeau, J. G.; Shank, D. D., Isothermal in vitro amplification of DNA by a restriction enzyme/DNA polymerase system. *Proceedings of the National Academy of Sciences* **1992**, *89*(1), 392-396.
36. Walker, G. T.; Fraiser, M. S.; Schram, J. L.; Little, M. C.; Nadeau, J. G.; Malinowski, D. P., Strand displacement amplification—an isothermal, in vitro DNA amplification technique. *Nucleic acids research* **1992**, *20*(7), 1691-1696.
37. Toley, B. J.; Covelli, I.; Belousov, Y.; Ramachandran, S.; Kline, E.; Scarr, N.; Vermeulen, N.; Mahoney, W.; Lutz, B. R.; Yager, P., Isothermal strand displacement amplification (iSDA): a rapid and sensitive method of nucleic acid amplification for point-of-care diagnosis. *Analyst* **2015**, *140*(22), 7540-7549.
38. Lafleur, L. K.; Bishop, J. D.; Heiniger, E. K.; Gallagher, R. P.; Wheeler, M. D.; Kauffman, P.; Zhang, X.; Kline, E. C.; Buser, J. R.; Kumar, S., A rapid, instrument-free, sample-to-result nucleic acid amplification test. *Lab on a Chip* **2016**, *16*(19), 3777-3787.
39. Vincent, M.; Xu, Y.; Kong, H., Helicase-dependent isothermal DNA amplification. *EMBO reports* **2004**, *5*(8), 795-800.
40. An, L.; Tang, W.; Ranalli, T. A.; Kim, H.-J.; Wytiaz, J.; Kong, H., Characterization of a thermostable UvrD helicase and its participation in helicase-dependent amplification. *Journal of Biological Chemistry* **2005**, *280*(32), 28952-28958.
41. Yang, Z.; McLendon, C.; Hutter, D.; Bradley, K. M.; Hoshika, S.; Frye, C.; Benner, S. A., Helicase dependent isothermal amplification of DNA and RNA using self-avoiding molecular recognition systems. *Chembiochem: a European journal of chemical biology* **2015**, *16*(9), 1365.
42. Tong, Y.; Tang, W.; Kim, H.-J.; Pan, X.; Ranalli, T. A.; Kong, H., Development of isothermal TaqMan assays for detection of biothreat organisms. *Biotechniques* **2008**, *45*(5), 543-557.
43. Barreda-García, S.; Miranda-Castro, R.; de-los-Santos-Álvarez, N.; Miranda-Ordieres, A. J.; Lobo-Castañón, M. J., Helicase-dependent isothermal amplification: a novel tool in the development of molecular-based analytical systems for rapid pathogen detection. *Analytical and bioanalytical chemistry* **2018**, *410*(3), 679-693.
44. Jordan, J. A.; Ibe, C. O.; Moore, M. S.; Host, C.; Simon, G. L., Evaluation of a manual DNA extraction protocol and an isothermal amplification assay for detecting HIV-1 DNA from dried blood spots for use in resource-limited settings. *Journal of clinical virology* **2012**, *54*(1), 11-14.
45. Frech, G. C.; Munns, D.; Jenison, R. D.; Hicke, B. J., Direct detection of nasal *Staphylococcus aureus* carriage via helicase-dependent isothermal amplification and chip hybridization. *BMC Research Notes* **2012**, *5*(1), 430.
46. Miller, N. S.; Yen-Lieberman, B.; Poulter, M. D.; Tang, Y.-W.; Granato, P. A., Comparative clinical evaluation of the IsoAmp® HSV Assay with ELVIS® HSV culture/ID/typing test system for the detection of herpes simplex virus in genital and oral lesions. *Journal of Clinical Virology* **2012**, *54*(4), 355-358.
47. Compton, J., NUCLEIC-ACID SEQUENCE-BASED AMPLIFICATION. *Nature* **1991**, *350*(6313), 91-92.
48. Fakruddin, M.; Mazumdar, R. M.; Chowdhury, A.; Bin Mannan, K. S., NUCLEIC ACID SEQUENCE BASED AMPLIFICATION (NASBA)-PROSPECTS AND APPLICATIONS. *Int. J. Life Sci. Pharma Res.* **2012**, *2*(1), L106-L121.
49. Gulliksen, A.; Keegan, H.; Martin, C.; O'Leary, J.; Solli, L. A.; Falang, I. M.; Grønn, P.; Karlgård, A.; Mielnik, M. M.; Johansen, I.-R.; Tofteberg, T. R.; Baier, T.; Gransee, R.; Drese, K.; Hansen-Hagge, T.; Riegger, L.; Koltay, P.; Zengerle, R.; Karlsen, F.; Ausen, D.; Furuberg, L., Towards a "Sample-In, Answer-Out" Point-of-Care Platform for Nucleic Acid Extraction and Amplification: Using an HPV E6/E7 mRNA Model System. *Journal of Oncology* **2012**, *2012*, 905024.
50. Pardee, K.; Green, A. A.; Takahashi, M. K.; Braff, D.; Lambert, G.; Lee, J. W.; Ferrante, T.; Ma, D.; Donghia, N.; Fan, M., Rapid, low-cost detection of Zika virus using programmable biomolecular components. *Cell* **2016**, *165*(5), 1255-1266.

51. Makarova, K. S.; Wolf, Y. I.; Iranzo, J.; Shmakov, S. A.; Alkhnbashi, O. S.; Brouns, S. J. J.; Charpentier, E.; Cheng, D.; Haft, D. H.; Horvath, P.; Moineau, S.; Mojica, F. J. M.; Scott, D.; Shah, S. A.; Siksnys, V.; Terns, M. P.; Venclovas, Č.; White, M. F.; Yakunin, A. F.; Yan, W.; Zhang, F.; Garrett, R. A.; Backofen, R.; van der Oost, J.; Barrangou, R.; Koonin, E. V., Evolutionary classification of CRISPR–Cas systems: a burst of class 2 and derived variants. *Nature Reviews Microbiology* **2020**, *18* (2), 67-83.
52. Jinek, M.; Chylinski, K.; Fonfara, I.; Hauer, M.; Doudna, J. A.; Charpentier, E., A Programmable Dual-RNA–Guided DNA Endonuclease in Adaptive Bacterial Immunity. *Science* **2012**, *337* (6096), 816-821.
53. Ma, E.; Harrington, Lucas B.; O’Connell, Mitchell R.; Zhou, K.; Doudna, Jennifer A., Single-Stranded DNA Cleavage by Divergent CRISPR–Cas9 Enzymes. *Molecular Cell* **2015**, *60* (3), 398-407.
54. Strutt, S. C.; Torrez, R. M.; Kaya, E.; Negrete, O. A.; Doudna, J. A., RNA-dependent RNA targeting by CRISPR–Cas9. *eLife* **2018**, *7*, 17.
55. Xiang, X.; Qian, K.; Zhang, Z.; Lin, F.; Xie, Y.; Liu, Y.; Yang, Z., CRISPR-cas systems based molecular diagnostic tool for infectious diseases and emerging 2019 novel coronavirus (COVID-19) pneumonia. *Journal of Drug Targeting* **2020**, *28* (7-8), 727-731.
56. Huang, M.; Zhou, X.; Wang, H.; Xing, D., Clustered Regularly Interspaced Short Palindromic Repeats/Cas9 Triggered Isothermal Amplification for Site-Specific Nucleic Acid Detection. *Analytical Chemistry* **2018**, *90* (3), 2193-2200.
57. Müller, V.; Rajer, F.; Frykholm, K.; Nyberg, L. K.; Quaderi, S.; Fritzsche, J.; Kristiansson, E.; Ambjörnsson, T.; Sandegren, L.; Westerlund, F., Direct identification of antibiotic resistance genes on single plasmid molecules using CRISPR/Cas9 in combination with optical DNA mapping. *Scientific Reports* **2016**, *6* (1), 37938.
58. Quan, J.; Langelier, C.; Kuchta, A.; Batson, J.; Teyssier, N.; Lyden, A.; Caldera, S.; McGeever, A.; Dimitrov, B.; King, R.; Wilhelm, J.; Murphy, M.; Ares, L. P.; Travisano, K. A.; Sit, R.; Amato, R.; Mumbengegwi, D. R.; Smith, J. L.; Bennett, A.; Gosling, R.; Mourani, P. M.; Calfee, C. S.; Neff, N. F.; Chow, E. D.; Kim, P. S.; Greenhouse, B.; DeRisi, J. L.; Crawford, E. D., FLASH: a next-generation CRISPR diagnostic for multiplexed detection of antimicrobial resistance sequences. *Nucleic Acids Research* **2019**, *47* (14), e83-e83.
59. Chen, J. S.; Ma, E.; Harrington, L. B.; Da Costa, M.; Tian, X.; Palefsky, J. M.; Doudna, J. A., CRISPR–Cas12a target binding unleashes indiscriminate single-stranded DNase activity. *Science* **2018**, *360* (6387), 436-439.
60. Li, S. Y.; Cheng, Q. X.; Wang, J. M.; Li, X. Y.; Zhang, Z. L.; Gao, S.; Cao, R. B.; Zhao, G. P.; Wang, J., CRISPR–Cas12a-assisted nucleic acid detection. *Cell Discov.* **2018**, *4*, 4.
61. Li, L.; Li, S.; Wu, N.; Wu, J.; Wang, G.; Zhao, G.; Wang, J., HOLMESv2: A CRISPR–Cas12b-Assisted Platform for Nucleic Acid Detection and DNA Methylation Quantitation. *ACS Synthetic Biology* **2019**, *8* (10), 2228-2237.
62. Yan, W. X.; Hunnewell, P.; Alfonse, L. E.; Carte, J. M.; Keston-Smith, E.; Sothiselvam, S.; Garrity, A. J.; Chong, S.; Makarova, K. S.; Koonin, E. V.; Cheng, D. R.; Scott, D. A., Functionally diverse type V CRISPR–Cas systems. *Science* **2019**, *363* (6422), 88-91.
63. Harrington, L. B.; Burstein, D.; Chen, J. S.; Paez-Espino, D.; Ma, E.; Witte, I. P.; Cofsky, J. C.; Kyrpides, N. C.; Banfield, J. F.; Doudna, J. A., Programmed DNA destruction by miniature CRISPR–Cas14 enzymes. *Science* **2018**, *362* (6416), 839-842.
64. Gootenberg, J. S.; Abudayyeh, O. O.; Lee, J. W.; Essletzbichler, P.; Dy, A. J.; Joung, J.; Verdine, V.; Donghia, N.; Daringer, N. M.; Freije, C. A., Nucleic acid detection with CRISPR–Cas13a/C2c2. *Science* **2017**, *356* (6336), 438-442.
65. Kellner, M. J.; Koob, J. G.; Gootenberg, J. S.; Abudayyeh, O. O.; Zhang, F., SHERLOCK: nucleic acid detection with CRISPR nucleases. *Nature protocols* **2019**, *14* (10), 2986-3012.
66. Gootenberg, J. S.; Abudayyeh, O. O.; Kellner, M. J.; Joung, J.; Collins, J. J.; Zhang, F., Multiplexed and portable nucleic acid detection platform with Cas13, Cas12a, and Csm6. *Science* **2018**, *360* (6387), 439-444.
67. Ackerman, C. M.; Myhrvold, C.; Thakku, S. G.; Freije, C. A.; Metsky, H. C.; Yang, D. K.; Ye, S. H.; Boehm, C. K.; Kosoko-Thoroddsen, T.-S. F.; Kehe, J.; Nguyen, T. G.; Carter, A.; Kulesa, A.;

- Barnes, J. R.; Dugan, V. G.; Hung, D. T.; Blainey, P. C.; Sabeti, P. C., Massively multiplexed nucleic acid detection with Cas13. *Nature* **2020**, *582* (7811), 277-282.
68. Sherlock CRISPR SARS-CoV-2 Kit; [www.fda.gov/media/137747/download](http://www.fda.gov/media/137747/download) (accessed August 20th, 2020).
69. Bezinge, L.; Suea-Ngam, A.; deMello, A. J.; Shih, C.-J., Nanomaterials for molecular signal amplification in electrochemical nucleic acid biosensing: recent advances and future prospects for point-of-care diagnostics. *Molecular Systems Design & Engineering* **2020**.
70. Zhang, L.; Li, D.; Meng, W.; Huang, Q.; Su, Y.; Wang, L.; Song, S.; Fan, C., Sequence-specific DNA detection by using biocatalyzed electrochemiluminescence and non-fouling surfaces. *Biosensors and Bioelectronics* **2009**, *25* (2), 368-372.
71. Bodulev, O. L.; Gribas, A. V.; Sakharov, I. Y., Microplate chemiluminescent assay for HBV DNA detection using 3-(10'-phenothiazinyl)propionic acid/N-morpholinopyridine pair as enhancer of HRP-catalyzed chemiluminescence. *Analytical Biochemistry* **2018**, *543*, 33-36.
72. Zhang, J.; Lao, R.; Song, S.; Yan, Z.; Fan, C., Design of an Oligonucleotide-Incorporated Nonfouling Surface and Its Application in Electrochemical DNA Sensors for Highly Sensitive and Sequence-Specific Detection of Target DNA. *Analytical Chemistry* **2008**, *80* (23), 9029-9033.
73. Azek, F.; Grossiord, C.; Joannes, M.; Limoges, B.; Brossier, P., Hybridization Assay at a Disposable Electrochemical Biosensor for the Attomole Detection of Amplified Human Cytomegalovirus DNA. *Analytical Biochemistry* **2000**, *284* (1), 107-113.
74. Wu, S.-H.; Huang, X.-B.; Tang, Y.; Ma, L.-M.; Liu, Y.; Sun, J.-J., Temperature controllable electrochemical sensors based on horseradish peroxidase as electrocatalyst at heated Au disk electrode and its preliminary application for H<sub>2</sub>O<sub>2</sub> detection. *Analytica Chimica Acta* **2020**, *1096*, 44-52.
75. Mao, X.; Jiang, J.; Xu, X.; Chu, X.; Luo, Y.; Shen, G.; Yu, R., Enzymatic amplification detection of DNA based on "molecular beacon" biosensors. *Biosensors and Bioelectronics* **2008**, *23* (10), 1555-1561.
76. Farzin, L.; Shamsipur, M.; Sheibani, S., A review: Aptamer-based analytical strategies using the nanomaterials for environmental and human monitoring of toxic heavy metals. *Talanta* **2017**, *174*, 619-627.
77. Shevelev, I. V.; Hübscher, U., The 3'-5' exonucleases. *Nature reviews Molecular cell biology* **2002**, *3* (5), 364-376.
78. Yong-Xi, Z.; Lin, Q.; Wei-Jun, Y.; Shuai, W.; Ya-Ling, W., Amplified Fluorescence Detection of Pb<sup>2+</sup> Using Pb<sup>2+</sup>-dependent DNzyme Combined with Nicking Enzyme-Mediated Enzymatic Recycling Amplification. *Chinese Journal of Analytical Chemistry* **2012**, *40* (8), 1236-1240.
79. Suea-Ngam, A.; Howes, P. D.; Stanley, C. E.; deMello, A. J., An Exonuclease I-Assisted Silver-Metallized Electrochemical Aptasensor for Ochratoxin A Detection. *ACS sensors* **2019**, *4* (6), 1560-1568.
80. Liu, R.; Wu, H.; Lv, L.; Kang, X.; Cui, C.; Feng, J.; Guo, Z., Fluorometric aptamer based assay for ochratoxin A based on the use of exonuclease III. *Microchimica Acta* **2018**, *185* (5), 254.
81. Huang, J.-Y.; Lin, H.-T.; Chen, T.-H.; Chen, C.-A.; Chang, H.-T.; Chen, C.-F., Signal amplified gold nanoparticles for cancer diagnosis on paper-based analytical devices. *ACS sensors* **2018**, *3* (1), 174-182.
82. Suea-Ngam, A.; Deck, L.-T.; Howes, P. D.; deMello, A. J., An ultrasensitive non-noble metal colorimetric assay using starch-iodide complexation for Ochratoxin A detection. *Analytica Chimica Acta* **2020**.
83. Hu, R.; Wen, W.; Wang, Q.; Xiong, H.; Zhang, X.; Gu, H.; Wang, S., Novel electrochemical aptamer biosensor based on an enzyme-gold nanoparticle dual label for the ultrasensitive detection of epithelial tumour marker MUC1. *Biosensors and Bioelectronics* **2014**, *53*, 384-389.

84. Ryu, G.; Huang, J.; Hofmann, O.; Walshe, C. A.; Sze, J. Y. Y.; McClean, G. D.; Mosley, A.; Rattle, S. J.; deMello, J. C.; deMello, A. J.; Bradley, D. D. C., Highly sensitive fluorescence detection system for microfluidic lab-on-a-chip. *Lab on a Chip* **2011**, *11* (9), 1664-1670.
85. Pardee, K.; Green, Alexander A.; Ferrante, T.; Cameron, D. E.; DaleyKeyser, A.; Yin, P.; Collins, James J., Paper-Based Synthetic Gene Networks. *Cell* **2014**, *159* (4), 940-954.
86. Wood, C. S.; Thomas, M. R.; Budd, J.; Mashamba-Thompson, T. P.; Herbst, K.; Pillay, D.; Peeling, R. W.; Johnson, A. M.; McKendry, R. A.; Stevens, M. M., Taking connected mobile-health diagnostics of infectious diseases to the field. *Nature* **2019**, *566* (7745), 467-474.
87. International Telecommunication Union; [www.itu.int/en/ITU-D/Statistics/Pages/stat](http://www.itu.int/en/ITU-D/Statistics/Pages/stat) (accessed August 20th, 2020).
88. Loeffelholz, M. J.; Tang, Y.-W., Laboratory diagnosis of emerging human coronavirus infections – the state of the art. *Emerging Microbes & Infections* **2020**, *9* (1), 747-756.
89. Yang, S.; Rothman, R. E., PCR-based diagnostics for infectious diseases: uses, limitations, and future applications in acute-care settings. *The Lancet Infectious Diseases* **2004**, *4* (6), 337-348.
90. Qiagen; [www.qiagen.com/](http://www.qiagen.com/) (accessed August 20th, 2020).
91. Crannell, Z. A.; Rohrman, B.; Richards-Kortum, R., Equipment-Free Incubation of Recombinase Polymerase Amplification Reactions Using Body Heat. *PLOS ONE* **2014**, *9* (11), e112146.
92. Hopkins, H.; González, I. J.; Polley, S. D.; Angutoko, P.; Ategeka, J.; Asimwe, C.; Agaba, B.; Kyabayinze, D. J.; Sutherland, C. J.; Perkins, M. D.; Bell, D., Highly Sensitive Detection of Malaria Parasitemia in a Malaria-Endemic Setting: Performance of a New Loop-Mediated Isothermal Amplification Kit in a Remote Clinic in Uganda. *The Journal of Infectious Diseases* **2013**, *208* (4), 645-652.
93. Martin, A.; Grant, K. B.; Stressmann, F.; Ghigo, J.-M.; Marchal, D.; Limoges, B., Ultimate Single-Copy DNA Detection Using Real-Time Electrochemical LAMP. *ACS Sensors* **2016**, *1* (7), 904-912.
94. Lucchi, N. W.; Gaye, M.; Diallo, M. A.; Goldman, I. F.; Ljolje, D.; Deme, A. B.; Badiane, A.; Ndiaye, Y. D.; Barnwell, J. W.; Udhayakumar, V.; Ndiaye, D., Evaluation of the Illumigene Malaria LAMP: A Robust Molecular Diagnostic Tool for Malaria Parasites. *Scientific Reports* **2016**, *6* (1), 36808.
95. Alere; [www.alere.com/en/home/product-details/id-now.html](http://www.alere.com/en/home/product-details/id-now.html). (accessed August 20th, 2020).
96. Chiu, D. T.; deMello, A. J.; Di Carlo, D.; Doyle, P. S.; Hansen, C.; Maceiczky, R. M.; Wootton, R. C. R., Small but Perfectly Formed? Successes, Challenges, and Opportunities for Microfluidics in the Chemical and Biological Sciences. *Chem* **2017**, *2* (2), 201-223.
97. Yager, P.; Edwards, T.; Fu, E.; Helton, K.; Nelson, K.; Tam, M. R.; Weigl, B. H., Microfluidic diagnostic technologies for global public health. *Nature* **2006**, *442* (7101), 412-418.
98. Kopp, M. U.; Mello, A. J. d.; Manz, A., Chemical Amplification: Continuous-Flow PCR on a Chip. *Science* **1998**, *280* (5366), 1046-1048.
99. demello, A. J., Focus DNA amplification: does 'small' really mean 'efficient'? *Lab on a Chip* **2001**, *1* (2), 24N-29N.
100. Woolley, A. T.; Hadley, D.; Landre, P.; deMello, A. J.; Mathies, R. A.; Northrup, M. A., Functional Integration of PCR Amplification and Capillary Electrophoresis in a Microfabricated DNA Analysis Device. *Analytical Chemistry* **1996**, *68* (23), 4081-4086.
101. Schaerli, Y.; Wootton, R. C.; Robinson, T.; Stein, V.; Dunsby, C.; Neil, M. A.; French, P. M.; DeMello, A. J.; Abell, C.; Hollfelder, F., Continuous-flow polymerase chain reaction of single-copy DNA in microfluidic microdroplets. *Analytical chemistry* **2009**, *81* (1), 302-306.
102. Opollo, V. S.; Nikuze, A.; Ben-Farhat, J.; Anyango, E.; Humwa, F.; Oyaro, B.; Wanjala, S.; Omwoyo, W.; Majiwa, M.; Akelo, V.; Zeh, C.; Maman, D., Field evaluation of near point of care Cepheid GeneXpert HIV-1 Qual for early infant diagnosis. *PLOS ONE* **2018**, *13* (12), e0209778.



103. Andrews, D.; Chetty, Y.; Cooper, B. S.; Virk, M.; Glass, S. K.; Letters, A.; Kelly, P. A.; Sudhanva, M.; Jeyaratnam, D., Multiplex PCR point of care testing versus routine, laboratory-based testing in the treatment of adults with respiratory tract infections: a quasi-randomised study assessing impact on length of stay and antimicrobial use. *BMC Infectious Diseases* **2017**, *17*(1), 671.
104. Ahrberg, C. D.; Ilic, B. R.; Manz, A.; Neuzil, P., Handheld real-time PCR device. *Lab on a Chip* **2016**, *16*(3), 586-592.
105. Li, T.-J.; Chang, C.-M.; Chang, P.-Y.; Chuang, Y.-C.; Huang, C.-C.; Su, W.-C.; Shieh, D.-B., Handheld energy-efficient magneto-optical real-time quantitative PCR device for target DNA enrichment and quantification. *NPG Asia Materials* **2016**, *8*(6), e277-e277.
106. Yeh, E.-C.; Fu, C.-C.; Hu, L.; Thakur, R.; Feng, J.; Lee, L. P., Self-powered integrated microfluidic point-of-care low-cost enabling (SIMPLE) chip. *Science Advances* **2017**, *3*(3), e1501645.
107. Gökçe, O.; Castonguay, S.; Temiz, Y.; Gervais, T.; Delamarche, E., Self-coalescing flows in microfluidics for pulse-shaped delivery of reagents. *Nature* **2019**, *574*(7777), 228-232.
108. McLeod, E.; Nguyen, C.; Huang, P.; Luo, W.; Veli, M.; Ozcan, A., Tunable Vapor-Condensed Nanolenses. *ACS Nano* **2014**, *8*(7), 7340-7349.
109. Bueno, D.; Muñoz, R.; Marty, J. L., Fluorescence analyzer based on smartphone camera and wireless for detection of Ochratoxin A. *Sensors and Actuators B: Chemical* **2016**, *232*, 462-468.
110. Vietz, C.; Schütte, M. L.; Wei, Q.; Richter, L.; Lalkens, B.; Ozcan, A.; Tinnefeld, P.; Acuna, G. P., Benchmarking Smartphone Fluorescence-Based Microscopy with DNA Origami Nanobeads: Reducing the Gap toward Single-Molecule Sensitivity. *ACS Omega* **2019**, *4*(1), 637-642.
111. Hsieh, K.; Patterson, A. S.; Ferguson, B. S.; Plaxco, K. W.; Soh, H. T., Rapid, Sensitive, and Quantitative Detection of Pathogenic DNA at the Point of Care through Microfluidic Electrochemical Quantitative Loop-Mediated Isothermal Amplification. *Angewandte Chemie International Edition* **2012**, *51*(20), 4896-4900.
112. Marshall, L. A.; Wu, L. L.; Babikian, S.; Bachman, M.; Santiago, J. G., Integrated Printed Circuit Board Device for Cell Lysis and Nucleic Acid Extraction. *Analytical Chemistry* **2012**, *84*(21), 9640-9645.
113. Toumazou, C.; Shepherd, L. M.; Reed, S. C.; Chen, G. I.; Patel, A.; Garner, D. M.; Wang, C.-J. A.; Ou, C.-P.; Amin-Desai, K.; Athanasiou, P.; Bai, H.; Brizido, I. M. Q.; Caldwell, B.; Coomber-Alford, D.; Georgiou, P.; Jordan, K. S.; Joyce, J. C.; La Mura, M.; Morley, D.; Sathyavrudhan, S.; Temelso, S.; Thomas, R. E.; Zhang, L., Simultaneous DNA amplification and detection using a pH-sensing semiconductor system. *Nature Methods* **2013**, *10*(7), 641-646.
114. Martinez, A. W.; Phillips, S. T.; Whitesides, G. M.; Carrilho, E., Diagnostics for the Developing World: Microfluidic Paper-Based Analytical Devices. *Analytical Chemistry* **2010**, *82*(1), 3-10.
115. Yamada, K.; Shibata, H.; Suzuki, K.; Citterio, D., Toward practical application of paper-based microfluidics for medical diagnostics: state-of-the-art and challenges. *Lab on a Chip* **2017**, *17*(7), 1206-1249.
116. World Health Organization List of Prequalified in Vitro Diagnostic Products, 2020; [www.who.int/diagnostics\\_laboratory/evaluations/PQ\\_list/en/](http://www.who.int/diagnostics_laboratory/evaluations/PQ_list/en/) (accessed August 20th, 2020).
117. Choi, J. R.; Yong, K. W.; Tang, R.; Gong, Y.; Wen, T.; Li, F.; Pingguan-Murphy, B.; Bai, D.; Xu, F., Advances and challenges of fully integrated paper-based point-of-care nucleic acid testing. *TrAC Trends in Analytical Chemistry* **2017**, *93*, 37-50.
118. Magro, L.; Escadafal, C.; Garneret, P.; Jacquelin, B.; Kwasiborski, A.; Manuguerra, J.-C.; Monti, F.; Sakuntabhai, A.; Vanhomwegen, J.; Lafaye, P.; Tabeling, P., Paper microfluidics for nucleic acid amplification testing (NAAT) of infectious diseases. *Lab on a Chip* **2017**, *17*(14), 2347-2371.

119. Aveyard, J.; Mehrabi, M.; Cossins, A.; Braven, H.; Wilson, R., One step visual detection of PCR products with gold nanoparticles and a nucleic acid lateral flow (NALF) device. *Chemical Communications* **2007**, (41), 4251-4253.
120. Nathavitharana, R. R.; Cudahy, P. G. T.; Schumacher, S. G.; Steingart, K. R.; Pai, M.; Denkinger, C. M., Accuracy of line probe assays for the diagnosis of pulmonary and multidrug-resistant tuberculosis: a systematic review and meta-analysis. *European Respiratory Journal* **2017**, *49* (1), 1601075.
121. Line Probe Assays for Drug-Resistant Tuberculosis Detection. Interpretation and Reporting Guide for Laboratory Staff and Clinicians; [www.stoptb.org/wg/gli/assets/documents/LPA\\_test\\_web\\_ready.pdf](http://www.stoptb.org/wg/gli/assets/documents/LPA_test_web_ready.pdf) (accessed August 20th, 2020).
122. TwistDx, TwistAmp Nfo; [www.twistdx.co.uk/en/products/product/twistamp-nfo](http://www.twistdx.co.uk/en/products/product/twistamp-nfo) (accessed August 20th, 2020).
123. Chander, Y.; Koelbl, J.; Puckett, J.; Moser, M. J.; Klingele, A. J.; Liles, M. R.; Carrias, A.; Mead, D. A.; Schoenfeld, T. W., A novel thermostable polymerase for RNA and DNA loop-mediated isothermal amplification (LAMP). *Frontiers in Microbiology* **2014**, *5* (395).
124. Du, Y.; Pothukuchy, A.; Gollihar, J. D.; Nourani, A.; Li, B.; Ellington, A. D., Coupling Sensitive Nucleic Acid Amplification with Commercial Pregnancy Test Strips. *Angewandte Chemie International Edition* **2017**, *56* (4), 992-996.
125. Myhrvold, C.; Freije, C. A.; Gootenberg, J. S.; Abudayyeh, O. O.; Metsky, H. C.; Durbin, A. F.; Kellner, M. J.; Tan, A. L.; Paul, L. M.; Parham, L. A., Field-deployable viral diagnostics using CRISPR-Cas13. *Science* **2018**, *360* (6387), 444-448.
126. Point-of-Care Testing for COVID-19 Using SHERLOCK Diagnostics, 2020, v.20200505; [www.stopcovid.science/docs/STOPCovid%20Whitepaper.pdf](http://www.stopcovid.science/docs/STOPCovid%20Whitepaper.pdf) (accessed August 20th, 2020).
127. Linnes, J. C.; Rodriguez, N. M.; Liu, L.; Klapperich, C. M., Polyethersulfone improves isothermal nucleic acid amplification compared to current paper-based diagnostics. *Biomedical Microdevices* **2016**, *18* (2), 30.
128. Byrnes, S. A.; Bishop, J. D.; Yager, P., Enabling lateral transport of genomic DNA through porous membranes for point-of-care applications. *Analytical Methods* **2017**, *9* (23), 3450-3463.
129. Byrnes, S. A.; Bishop, J. D.; Lafleur, L.; Buser, J. R.; Lutz, B.; Yager, P., One-step purification and concentration of DNA in porous membranes for point-of-care applications. *Lab on a Chip* **2015**, *15* (12), 2647-2659.
130. Su, X.; Comeau, A. M., Cellulose as a Matrix for Nucleic Acid Purification. *Analytical Biochemistry* **1999**, *267* (2), 415-418.
131. Zou, Y.; Mason, M. G.; Wang, Y.; Wee, E.; Turni, C.; Blackall, P. J.; Trau, M.; Botella, J. R., Nucleic acid purification from plants, animals and microbes in under 30 seconds. *PLoS Biology* **2017**, *15* (11), e2003916.
132. Xu, G.; Nolder, D.; Reboud, J.; Oguike, M. C.; van Schalkwyk, D. A.; Sutherland, C. J.; Cooper, J. M., Paper-Origami-Based Multiplexed Malaria Diagnostics from Whole Blood. *Angewandte Chemie International Edition* **2016**, *55* (49), 15250-15253.
133. Reboud, J.; Xu, G.; Garrett, A.; Adriko, M.; Yang, Z.; Tukahebwa, E. M.; Rowell, C.; Cooper, J. M., Paper-based microfluidics for DNA diagnostics of malaria in low resource underserved rural communities. *Proceedings of the National Academy of Sciences* **2019**, *116* (11), 4834-4842.
134. Yang, Z.; Xu, G.; Reboud, J.; Ali, S. A.; Kaur, G.; McGiven, J.; Boby, N.; Gupta, P. K.; Chaudhuri, P.; Cooper, J. M., Rapid Veterinary Diagnosis of Bovine Reproductive Infectious Diseases from Semen Using Paper-Origami DNA Microfluidics. *ACS Sensors* **2018**, *3* (2), 403-409.
135. Magro, L.; Jacquelin, B.; Escadafal, C.; Garneret, P.; Kwasiborski, A.; Manuguerra, J.-C.; Monti, F.; Sakuntabhai, A.; Vanhomwegen, J.; Lafaye, P.; Tabeling, P., Paper-based RNA detection and multiplexed analysis for Ebola virus diagnostics. *Scientific Reports* **2017**, *7* (1), 1347.



136. Kelly-Cirino, C. D.; Nkengasong, J.; Kettler, H.; Tongio, I.; Gay-Andrieu, F.; Escadafal, C.; Piot, P.; Peeling, R. W.; Gadde, R.; Boehme, C., Importance of diagnostics in epidemic and pandemic preparedness. *BMJ Global Health* **2019**, *4* (Suppl 2), e001179.
137. Kaur, N.; Toley, B. J., Paper-based nucleic acid amplification tests for point-of-care diagnostics. *Analyst* **2018**, *143* (10), 2213-2234.
138. Soda, Y.; Bakker, E., Quantification of Colorimetric Data for Paper-Based Analytical Devices. *ACS Sensors* **2019**, *4* (12), 3093-3101.
139. van Belkum, A.; Rochas, O., Laboratory-Based and Point-of-Care Testing for MSSA/MRSA Detection in the Age of Whole Genome Sequencing. *Frontiers in Microbiology* **2018**, *9* (1437).
140. Zhao, Y.; Chen, F.; Li, Q.; Wang, L.; Fan, C., Isothermal amplification of nucleic acids. *Chemical reviews* **2015**, *115* (22), 12491-12545.
141. Becherer, L.; Borst, N.; Bakheit, M.; Frischmann, S.; Zengerle, R.; von Stetten, F., Loop-mediated isothermal amplification (LAMP) – review and classification of methods for sequence-specific detection. *Analytical Methods* **2020**, *12* (6), 717-746.
142. Rivero, R.; Bisio, M.; Velázquez, E. B.; Esteva, M. I.; Scollo, K.; González, N. L.; Altcheh, J.; Ruiz, A. M., Rapid detection of *Trypanosoma cruzi* by colorimetric loop-mediated isothermal amplification (LAMP): A potential novel tool for the detection of congenital Chagas infection. *Diagnostic Microbiology and Infectious Disease* **2017**, *89* (1), 26-28.
143. Cate, D. M.; Adkins, J. A.; Mettakoonpitak, J.; Henry, C. S., Recent Developments in Paper-Based Microfluidic Devices. *Analytical Chemistry* **2015**, *87* (1), 19-41.
144. Gong, M. M.; Sinton, D., Turning the page: advancing paper-based microfluidics for broad diagnostic application. *Chem. Rev.* **2017**, *117* (12), 8447-8480.
145. Boehle, K. E.; Gilliland, J.; Wheeldon, C. R.; Holder, A.; Adkins, J. A.; Geiss, B. J.; Ryan, E. P.; Henry, C. S., Utilizing Paper-Based Devices for Antimicrobial-Resistant Bacteria Detection. *Angewandte Chemie International Edition* **2017**, *56* (24), 6886-6890.
146. Kollef, M. H., Inadequate Antimicrobial Treatment: An Important Determinant of Outcome for Hospitalized Patients. *Clinical Infectious Diseases* **2000**, *31* (Supplement\_4), S131-S138.
147. Seok, Y.; Joung, H.-A.; Byun, J.-Y.; Jeon, H.-S.; Shin, S. J.; Kim, S.; Shin, Y.-B.; Han, H. S.; Kim, M.-G., A Paper-Based Device for Performing Loop-Mediated Isothermal Amplification with Real-Time Simultaneous Detection of Multiple DNA Targets. *Theranostics* **2017**, *7* (8), 2220-2230.
148. Li, B.; Zhou, X.; Liu, H.; Deng, H.; Huang, R.; Xing, D., Simultaneous Detection of Antibiotic Resistance Genes on Paper-Based Chip Using [Ru(phen)<sub>2</sub>dppz]<sup>2+</sup> Turn-on Fluorescence Probe. *ACS Applied Materials & Interfaces* **2018**, *10* (5), 4494-4501.
149. Roy, S.; Mohd-Naim, N. F.; Safavieh, M.; Ahmed, M. U., Colorimetric Nucleic Acid Detection on Paper Microchip Using Loop Mediated Isothermal Amplification and Crystal Violet Dye. *ACS Sensors* **2017**, *2* (11), 1713-1720.
150. Hongwarittorn, I.; Chaichanawongsaroj, N.; Laiwattanapaisal, W., Semi-quantitative visual detection of loop mediated isothermal amplification (LAMP)-generated DNA by distance-based measurement on a paper device. *Talanta* **2017**, *175*, 135-142.
151. D. Howes, P.; Rana, S.; M. Stevens, M., Plasmonic nanomaterials for biodiagnostics. *Chemical Society Reviews* **2014**, *43* (11), 3835-3853.
152. Ma, X.; He, S.; Qiu, B.; Luo, F.; Guo, L.; Lin, Z., Noble Metal Nanoparticle-Based Multicolor Immunoassays: An Approach toward Visual Quantification of the Analytes with the Naked Eye. *ACS Sensors* **2019**, *4* (4), 782-791.
153. Parolo, C.; Merkoçi, A., Paper-based nanobiosensors for diagnostics. *Chemical Society Reviews* **2013**, *42* (2), 450-457.
154. Marquez, S.; Morales-Narváez, E., Nanoplasmonics in Paper-Based Analytical Devices. *Frontiers in Bioengineering and Biotechnology* **2019**, *7* (69).
155. Zhan, L.; Guo, S.-z.; Song, F.; Gong, Y.; Xu, F.; Boulware, D. R.; McAlpine, M. C.; Chan, W. C. W.; Bischof, J. C., The Role of Nanoparticle Design in Determining Analytical Performance of Lateral Flow Immunoassays. *Nano Letters* **2017**, *17* (12), 7207-7212.

156. Chen, P.; Liu, X.; Goyal, G.; Tran, N. T.; Shing Ho, J. C.; Wang, Y.; Aili, D.; Liedberg, B., Nanoplasmonic Sensing from the Human Vision Perspective. *Analytical Chemistry* **2018**, *90* (7), 4916-4924.
157. Ravindran, A.; Chandran, P.; Khan, S. S., Biofunctionalized silver nanoparticles: Advances and prospects. *Colloids and Surfaces B: Biointerfaces* **2013**, *105*, 342-352.
158. Sabela, M.; Balme, S.; Bechelany, M.; Janot, J.-M.; Bisetty, K., A Review of Gold and Silver Nanoparticle-Based Colorimetric Sensing Assays. *Advanced Engineering Materials* **2017**, *19* (12), 1700270.
159. Sun, Y.; Xia, Y., Shape-Controlled Synthesis of Gold and Silver Nanoparticles. *Science* **2002**, *298* (5601), 2176-2179.
160. Ahamed, M.; Karns, M.; Goodson, M.; Rowe, J.; Hussain, S. M.; Schlager, J. J.; Hong, Y., DNA damage response to different surface chemistry of silver nanoparticles in mammalian cells. *Toxicology and Applied Pharmacology* **2008**, *233* (3), 404-410.
161. Chen, Y.; Phipps, M. L.; Werner, J. H.; Chakraborty, S.; Martinez, J. S., DNA Templated Metal Nanoclusters: From Emergent Properties to Unique Applications. *Accounts of Chemical Research* **2018**, *51* (11), 2756-2763.
162. Kondo, J.; Tada, Y.; Dairaku, T.; Hattori, Y.; Saneyoshi, H.; Ono, A.; Tanaka, Y., A metallo-DNA nanowire with uninterrupted one-dimensional silver array. *Nature chemistry* **2017**, *9* (10), 956-960.
163. O'Neil, J., Review on Antimicrobial Resistance. Antimicrobial Resistance: Tackling a Crisis for the Health and Wealth of Nations 2014.
164. WHO Competency Framework for Health Workers' Education and Training on Antimicrobial Resistance; 2018.
165. Turner, N. A.; Sharma-Kuinkel, B. K.; Maskarinec, S. A.; Eichenberger, E. M.; Shah, P. P.; Carugati, M.; Holland, T. L.; Fowler, V. G., Methicillin-resistant *Staphylococcus aureus*: an overview of basic and clinical research. *Nature Reviews Microbiology* **2019**, *17* (4), 203-218.
166. Miragaia, M., Factors Contributing to the Evolution of *mecA*-Mediated  $\beta$ -lactam Resistance in *Staphylococci*: Update and New Insights From Whole Genome Sequencing (WGS). *Frontiers in Microbiology* **2018**, *9* (2723).
167. Xia, J.; Dong, Z.; Cai, Y.; Guan, G.; Zhang, S.; Kovács, A.; Boothroyd, C.; Phang, I. Y.; Liu, S.; Wu, M.; Zhang, Y. W.; Hu, X.; Han, M.-Y., Morphological Growth and Theoretical Understanding of Gold and Other Noble Metal Nanoplates. *Chemistry – A European Journal* **2018**, *24* (58), 15589-15595.
168. Rycenga, M.; Cobley, C. M.; Zeng, J.; Li, W.; Moran, C. H.; Zhang, Q.; Qin, D.; Xia, Y., Controlling the synthesis and assembly of silver nanostructures for plasmonic applications. *Chemical reviews* **2011**, *111* (6), 3669-3712.
169. Zheng, Y.; Zeng, J.; Ruditskiy, A.; Liu, M.; Xia, Y., Oxidative Etching and Its Role in Manipulating the Nucleation and Growth of Noble-Metal Nanocrystals. *Chemistry of Materials* **2014**, *26* (1), 22-33.
170. Li, J.; Zhu, Z.; Liu, F.; Zhu, B.; Ma, Y.; Yan, J.; Lin, B.; Ke, G.; Liu, R.; Zhou, L.; Tu, S.; Yang, C., DNA-Mediated Morphological Control of Silver Nanoparticles. *Small* **2016**, *12* (39), 5449-5487.
171. Parnklang, T.; Lertvachirapaiboon, C.; Pienpinijtham, P.; Wongravee, K.; Thammacharoen, C.; Ekgasit, S., H<sub>2</sub>O<sub>2</sub>-triggered shape transformation of silver nanospheres to nanoprisms with controllable longitudinal LSPR wavelengths. *RSC Advances* **2013**, *3* (31), 12886-12894.
172. Lee, K. E.; Hesketh, A. V.; Kelly, T. L., Chemical stability and degradation mechanisms of triangular Ag, Ag@Au, and Au nanoprisms. *Physical Chemistry Chemical Physics* **2014**, *16* (24), 12407-12414.
173. Tang, B.; Xu, S.; An, J.; Zhao, B.; Xu, W.; Lombardi, J. R., Kinetic effects of halide ions on the morphological evolution of silver nanoplates. *Physical Chemistry Chemical Physics* **2009**, *11* (44), 10286-10292.

174. Hu, S.; Yi, T.; Huang, Z.; Liu, B.; Wang, J.; Yi, X.; Liu, J., Etching silver nanoparticles using DNA. *Materials Horizons* **2019**, *6* (1), 155-159.
175. Kitaev, V.; Subedi, T., Synthesis of well-defined pentagonally prismatic silver nanoparticles: role of bromide in (100) stabilization and facet preservation. *Chemical Communications* **2017**, *53* (48), 6444-6447.
176. Noviana, E.; Jain, S.; Hofstetter, J.; Geiss, B. J.; Dandy, D. S.; Henry, C. S., Paper-based nuclease protection assay with on-chip sample pretreatment for point-of-need nucleic acid detection. *Analytical and Bioanalytical Chemistry* **2020**, *412* (13), 3051-3061.
177. Gorgannezhad, L.; Stratton, H.; Nguyen, N.-T., Microfluidic-Based Nucleic Acid Amplification Systems in Microbiology. *Micromachines* **2019**, *10* (6), 408.
178. Li, H.-W.; Mao, J.-Y.; Lien, C.-W.; Wang, C.-K.; Lai, J.-Y.; Mandal, R. P.; Chang, H.-T.; Chang, L.; Ma, D. H.-K.; Huang, C.-C., Platinum ions mediate the interactions between DNA and carbon quantum dots: diagnosis of MRSA infections. *Journal of Materials Chemistry B* **2020**, *8* (16), 3506-3512.
179. Naik, P.; Manna, R.; Paul, D., Nucleic Acid Amplification on Paper Substrates. In *Paper Microfluidics*, Springer: 2019; pp 115-146.
180. Schulz, M.; Calabrese, S.; Hausladen, F.; Wurm, H.; Drossart, D.; Stock, K.; Sobieraj, A. M.; Eichenseher, F.; Loessner, M. J.; Schmelcher, M., Point-of-care testing system for digital single cell detection of MRSA directly from nasal swabs. *Lab on a Chip* **2020**, *20* (14), 2549-2561.
181. Coelho, B.; Veigas, B.; Fortunato, E.; Martins, R.; Águas, H.; Igreja, R.; Baptista, P. V., Digital microfluidics for nucleic acid amplification. *Sensors* **2017**, *17* (7), 1495.
182. Xiong, D.; Ying, M., Research and application progress of digital nucleic acid amplification detection techniques. *Chinese Journal of Analytical Chemistry* **2016**, *44* (4), 512-521.
183. Lindner, L.; Cayrou, P.; Jacquot, S.; Birling, M.-C.; Herault, Y.; Pavlovic, G., Reliable and robust droplet digital PCR (ddPCR) and RT-ddPCR protocols for mouse studies. *Methods* **2020**.
184. Rice, L.; Robb, L.; Hartman, D.; Anderson, J.; Kading, R., Application of the Droplet Digital Polymerase Chain Reaction (ddPCR) Platform for Detection and Quantification of Vertebrate Host DNA in Engorged Mosquitoes. *Journal of medical entomology* **2019**, *56* (4), 1150-1153.
185. Suea-Ngam, A.; Howes, P. D.; Srisa-Art, M.; DeMello, A. J., Droplet microfluidics: from proof-of-concept to real-world utility? *Chemical Communications* **2019**, *55* (67), 9895-9903.
186. i Solvas, X. C.; DeMello, A., Droplet microfluidics: recent developments and future applications. *Chemical Communications* **2011**, *47* (7), 1936-1942.
187. Demaree, B.; Weisgerber, D.; Dolatmoradi, A.; Hatori, M.; Abate, A. R., Direct quantification of EGFR variant allele frequency in cell-free DNA using a microfluidic-free digital droplet PCR assay. In *Methods in cell biology*, Elsevier: 2018; Vol. 148, pp 119-131.
188. Demaree, Z.; Yang, C. J., Hydrogel droplet microfluidics for high-throughput single molecule/cell analysis. *Accounts of chemical research* **2017**, *50* (1), 22-31.
189. Li, M.; van Zee, M.; Goda, K.; Di Carlo, D., Size-based sorting of hydrogel droplets using inertial microfluidics. *Lab on a Chip* **2018**, *18* (17), 2575-2582.
190. Hatori, M. N.; Kim, S. C.; Abate, A. R., Particle-templated emulsification for microfluidics-free digital biology. *Analytical chemistry* **2018**, *90* (16), 9813-9820.
191. World Health Organization, Global action plan for the prevention and control of noncommunicable diseases 2013-2020. World Health Organization: 2013.
192. Steward, C. D.; Wallace, D.; Hubert, S. K.; Lawton, R.; Fridkin, S. K.; Gaynes, R. P.; McGowan Jr, J. E.; Tenover, F. C., Ability of laboratories to detect emerging antimicrobial resistance in nosocomial pathogens: a survey of project ICARE laboratories. *Diagnostic microbiology and infectious disease* **2000**, *38* (1), 59-67.
193. Centers for Disease Control, Morbidity and mortality weekly report, Laboratory capacity to detect antimicrobial resistance, 1998.

194. World Health Organization, Technical consultation on in vitro diagnostics for AMR, 27–28 March 2019, WHO Headquarters, Geneva: meeting report; World Health Organization: 2019.
195. Trotter, A. J.; Aydin, A.; Strinden, M. J.; O'grady, J., Recent and emerging technologies for the rapid diagnosis of infection and antimicrobial resistance. *Current opinion in microbiology* **2019**, *51*, 39-45.
196. Azizi, M.; Zaferani, M.; Cheong, S. H.; Abbaspourrad, A., Pathogenic bacteria detection using RNA-based loop-mediated isothermal-amplification-assisted nucleic acid amplification via droplet microfluidics. *ACS sensors* **2019**, *4* (4), 841-848.
197. Pilecky, M.; Schildberger, A.; Orth-Höller, D.; Weber, V., Pathogen enrichment from human whole blood for the diagnosis of bloodstream infection: prospects and limitations. *Diagnostic Microbiology and Infectious Disease* **2019**, *94* (1), 7-14.
198. Cantera, J. L.; White, H.; Diaz, M. H.; Beall, S. G.; Winchell, J. M.; Lillis, L.; Kalnoky, M.; Gallarda, J.; Boyle, D. S., Assessment of eight nucleic acid amplification technologies for potential use to detect infectious agents in low-resource settings. *PloS one* **2019**, *14* (4), e0215756.
199. Baylis, S.; Wallace, P.; McCulloch, E.; Niesters, H.; Nübling, C., Standardization of nucleic acid tests: the approach of the World Health Organization. *Journal of clinical microbiology* **2019**, *57*(1).
200. Kumar, I. S. C.; Babu, B. S.; Babu, K. S., Nucleic acid amplification testing–A paradigm shift. *Journal of Clinical and Scientific Research* **2020**, *9*(1), 50.
201. Chung, C. H. Y.; Cui, B.; Song, R.; Liu, X.; Xu, X.; Yao, S., Scalable Production of Monodisperse Functional Microspheres by Multilayer Parallelization of High Aspect Ratio Microfluidic Channels. *Micromachines* **2019**, *10* (9), 592.
202. Vladisavljević, G. T.; Ekanem, E. E.; Zhang, Z.; Khalid, N.; Kobayashi, I.; Nakajima, M., Long-term stability of droplet production by microchannel (step) emulsification in microfluidic silicon chips with large number of terraced microchannels. *Chemical Engineering Journal* **2018**, *333*, 380-391.
203. Kobayashi, I.; Lou, X.; Mukataka, S.; Nakajima, M., Preparation of monodisperse water-in-oil-in-water emulsions using microfluidization and straight-through microchannel emulsification. *Journal of the American Oil Chemists' Society* **2005**, *82* (1), 65-71.
204. Srisa-Art, M.; DeMello, A. J.; Edel, J. B., High-throughput DNA droplet assays using picoliter reactor volumes. *Analytical chemistry* **2007**, *79* (17), 6682-6689.
205. Dressler, O. J.; Maceiczuk, R. M.; Chang, S.-I.; deMello, A. J., Droplet-based microfluidics: enabling impact on drug discovery. *Journal of biomolecular screening* **2014**, *19* (4), 483-496.
206. Nozdriukhin, D.; Filatov, N.; Evstrapov, A.; Bukatin, A., Formation of Polyacrylamide and PEGDA Hydrogel Particles in a Microfluidic Flow Focusing Droplet Generator. *Technical Physics* **2018**, *63* (9), 1328-1333.
207. Lee, C.-Y.; Chang, C.-L.; Wang, Y.-N.; Fu, L.-M., Microfluidic mixing: a review. *International journal of molecular sciences* **2011**, *12* (5), 3263-3287.
208. Wang, C.-T.; Chen, Y.-M.; Hong, P.-A.; Wang, Y.-T., Tesla valves in micromixers. *International Journal of Chemical Reactor Engineering* **2014**, *1* (open-issue).
209. Yang, A.-S.; Chuang, F.-C.; Su, C.-L.; Chen, C.-K.; Lee, M.-H. In *Development of a 3D-tesla micromixer for bio-applications*, 2013 IEEE International Conference on Mechatronics and Automation, IEEE: 2013; pp 152-157.
210. Organization, W. H. *Technical consultation on in vitro diagnostics for AMR, 27–28 March 2019, WHO Headquarters, Geneva: meeting report*; World Health Organization: 2019.
211. O'Neill, J., AMR Review Paper-Tackling a crisis for the health and wealth of nations. *AMR Review Paper* **2014**.
212. Bartels, M. D.; Worning, P.; Andersen, L. P.; Bès, M.; Enger, H.; Ås, C. G.; Hansen, T. A.; Holzknecht, B. J.; Larssen, K. W.; Laurent, F., Repeated introduction and spread of the MRSA clone t304/ST6 in Northern Europe. *Clinical Microbiology and Infection* **2020**.

213. Rocha, L. E.; Singh, V.; Esch, M.; Lenaerts, T.; Liljeros, F.; Thorson, A., Dynamic contact networks of patients and MRSA spread in hospitals. *Scientific Reports* **2020**, *10* (1), 1-10.
214. Suea-Ngam, A.; Bezinge, L.; Mateescu, B.; Howes, P. D.; deMello, A. J.; Richards, D., Enzyme-assisted nucleic acid detection for infectious disease diagnostics: moving towards the point-of-care. *ACS sensors* **2020**.
215. Cunningham, R.; Jenks, P.; Northwood, J.; Wallis, M.; Ferguson, S.; Hunt, S., Effect on MRSA transmission of rapid PCR testing of patients admitted to critical care. *Journal of Hospital Infection* **2007**, *65* (1), 24-28.
216. Cong, L.; Ran, F. A.; Cox, D.; Lin, S.; Barretto, R.; Habib, N.; Hsu, P. D.; Wu, X.; Jiang, W.; Marraffini, L. A., Multiplex genome engineering using CRISPR/Cas systems. *Science* **2013**, *339* (6121), 819-823.
217. Li, Y.; Li, S.; Wang, J.; Liu, G., CRISPR/Cas systems towards next-generation biosensing. *Trends in biotechnology* **2019**, *37* (7), 730-743.
218. Amitai, G.; Sorek, R., CRISPR-Cas adaptation: insights into the mechanism of action. *Nature Reviews Microbiology* **2016**, *14* (2), 67.
219. Zetsche, B.; Gootenberg, J. S.; Abudayyeh, O. O.; Slaymaker, I. M.; Makarova, K. S.; Essletzbichler, P.; Volz, S. E.; Joung, J.; Van Der Oost, J.; Regev, A., Cpf1 is a single RNA-guided endonuclease of a class 2 CRISPR-Cas system. *Cell* **2015**, *163* (3), 759-771.
220. Cox, D. B.; Gootenberg, J. S.; Abudayyeh, O. O.; Franklin, B.; Kellner, M. J.; Joung, J.; Zhang, F., RNA editing with CRISPR-Cas13. *Science* **2017**, *358* (6366), 1019-1027.
221. Engreitz, J.; Abudayyeh, O.; Gootenberg, J.; Zhang, F., CRISPR tools for systematic studies of RNA regulation. *Cold Spring Harbor perspectives in biology* **2019**, *11* (8), a035386.
222. Knott, G. J.; Doudna, J. A., CRISPR-Cas guides the future of genetic engineering. *Science* **2018**, *361* (6405), 866-869.
223. Huang, C.-H.; Lee, K.-C.; Doudna, J. A., Applications of CRISPR-Cas enzymes in cancer therapeutics and detection. *Trends in cancer* **2018**, *4* (7), 499-512.
224. Qin, P.; Park, M.; Alfson, K. J.; Tamhankar, M.; Carrion, R.; Patterson, J. L.; Griffiths, A.; He, Q.; Yildiz, A.; Mathies, R., Rapid and fully microfluidic Ebola virus detection with CRISPR-Cas13a. *ACS sensors* **2019**, *4* (4), 1048-1054.
225. Dai, Y.; Wu, Y.; Liu, G.; Gooding, J. J., CRISPR Mediated Biosensing Toward Understanding Cellular Biology and Point-of-Care Diagnosis. *Angewandte Chemie* **2020**.
226. Dai, Y.; Somoza, R. A.; Wang, L.; Welter, J. F.; Li, Y.; Caplan, A. I.; Liu, C. C., Exploring the Trans-Cleavage Activity of CRISPR-Cas12a (cpf1) for the Development of a Universal Electrochemical Biosensor. *Angewandte Chemie International Edition* **2019**, *58* (48), 17399-17405.
227. Bruch, R.; Baaske, J.; Chatelle, C.; Meirich, M.; Madlener, S.; Weber, W.; Dincer, C.; Urban, G. A., CRISPR/Cas13a-powered electrochemical microfluidic biosensor for nucleic acid amplification-free miRNA diagnostics. *Advanced Materials* **2019**, *31* (51), 1905311.
228. Lv, L.; Li, D.; Liu, R.; Cui, C.; Guo, Z., Label-free aptasensor for ochratoxin A detection using SYBR Gold as a probe. *Sensors and Actuators B: Chemical* **2017**, *246*, 647-652.
229. Suea-Ngam, A.; Rattanarat, P.; Chailapakul, O.; Srisa-Art, M., Electrochemical droplet-based microfluidics using chip-based carbon paste electrodes for high-throughput analysis in pharmaceutical applications. *Analytica Chimica Acta* **2015**, *883*, 45-54.
230. Suea-Ngam, A.; Rattanarat, P.; Wongravee, K.; Chailapakul, O.; Srisa-Art, M., Droplet-based glucosamine sensor using gold nanoparticles and polyaniline-modified electrode. *Talanta* **2016**, *158*, 134-141.
231. Wu, L.; Wang, J.; Ren, J.; Qu, X., Ultrasensitive telomerase activity detection in circulating tumor cells based on DNA metallization and sharp solid-state electrochemical techniques. *Advanced Functional Materials* **2014**, *24* (18), 2727-2733.
232. Orazem, M. E.; Tribollet, B., Electrochemical impedance spectroscopy. *New Jersey* **2008**.
233. Osteryoung, J. G.; Osteryoung, R. A., Square wave voltammetry. *Analytical Chemistry* **1985**, *57* (1), 101-110.
234. Ramaley, L.; Krause, M. S., Theory of square wave voltammetry. *Analytical Chemistry* **1969**, *41* (11), 1362-1365.

235. Sundaresan, R.; Parameshwaran, H. P.; Yogesha, S.; Keilbarth, M. W.; Rajan, R., RNA-independent DNA cleavage activities of Cas9 and Cas12a. *Cell reports* **2017**, *21* (13), 3728-3739.
236. Jeon, Y.; Choi, Y. H.; Jang, Y.; Yu, J.; Goo, J.; Lee, G.; Jeong, Y. K.; Lee, S. H.; Kim, I.-S.; Kim, J.-S., Direct observation of DNA target searching and cleavage by CRISPR-Cas12a. *Nature communications* **2018**, *9* (1), 1-11.
237. International Agency for Research on Cancer, Some naturally occurring substances: food items and constituents, heterocyclic aromatic amines and mycotoxins; IARC Monographs on the Evaluation of Carcinogenic Risks to Humans; 1993, Vol 56.
238. Authority, E. F. S., Opinion of the Scientific Panel on contaminants in the food chain [CONTAM] related to ochratoxin A in food. *EFSA journal* **2006**, *4* (6), 365.
239. Cantafora, A.; Grossi, M.; Miraglia, M.; Benelli, L., Determination of ochratoxin A in coffee beans using reversed-phase high performance liquid chromatography. *Riv. Soc. Ital. Sci. Aliment* **1983**, *12*, 103-108.
240. Meulenberg, E. P., Immunochemical methods for ochratoxin A detection: a review. *Toxins* **2012**, *4* (4), 244-266.
241. Reverté, L.; Prieto-Simón, B.; Campàs, M., New advances in electrochemical biosensors for the detection of toxins: Nanomaterials, magnetic beads and microfluidics systems. A review. *Analytica Chimica Acta* **2016**, *908*, 8-21.
242. Rackus, D. G.; Shamsi, M. H.; Wheeler, A. R., Electrochemistry, biosensors and microfluidics: a convergence of fields. *Chemical Society Reviews* **2015**, *44* (15), 5320-5340.
243. Nemiroski, A.; Christodouleas, D. C.; Hennek, J. W.; Kumar, A. A.; Maxwell, E. J.; Fernández-Abedul, M. T.; Whitesides, G. M., Universal mobile electrochemical detector designed for use in resource-limited applications. *Proceedings of the National Academy of Sciences* **2014**, *111* (33), 11984-11989.
244. Song, S.; Wang, L.; Li, J.; Fan, C.; Zhao, J., Aptamer-based biosensors. *TrAC Trends in Analytical Chemistry* **2008**, *27* (2), 108-117.
245. Duan, N.; Wu, S.; Dai, S.; Gu, H.; Hao, L.; Ye, H.; Wang, Z., Advances in aptasensors for the detection of food contaminants. *Analyst* **2016**, *141* (13), 3942-3961.
246. Miao, P.; Han, K.; Wang, B.; Luo, G.; Wang, P.; Chen, M.; Tang, Y., Electrochemical detection of aqueous Ag<sup>+</sup> based on Ag<sup>+</sup>-assisted ligation reaction. *Scientific reports* **2015**, *5* (1), 1-5.
247. Si, Y.; Sun, Z.; Zhang, N.; Qi, W.; Li, S.; Chen, L.; Wang, H., Ultrasensitive electroanalysis of low-level free microRNAs in blood by maximum signal amplification of catalytic silver deposition using alkaline phosphatase-incorporated gold nanoclusters. *Analytical chemistry* **2014**, *86* (20), 10406-10414.
248. White, R. J.; Plaxco, K. W., Exploiting binding-induced changes in probe flexibility for the optimization of electrochemical biosensors. *Analytical chemistry* **2010**, *82* (1), 73-76.
249. Li, H.; Dauphin-Ducharme, P.; Ortega, G.; Plaxco, K. W., Calibration-free electrochemical biosensors supporting accurate molecular measurements directly in undiluted whole blood. *Journal of the American Chemical Society* **2017**, *139* (32), 11207-11213.
250. Steel, A. B.; Herne, T. M.; Tarlov, M. J., Electrochemical quantitation of DNA immobilized on gold. *Analytical chemistry* **1998**, *70* (22), 4670-4677.
251. Wang, J.; Wang, F.; Dong, S., Methylene blue as an indicator for sensitive electrochemical detection of adenosine based on aptamer switch. *Journal of Electroanalytical Chemistry* **2009**, *626* (1-2), 1-5.
252. Chen, Z.; Liu, C.; Cao, F.; Ren, J.; Qu, X., DNA metallization: principles, methods, structures, and applications. *Chemical Society Reviews* **2018**, *47* (11), 4017-4072.
253. Wang, J.; Xu, D.; Polsky, R., Magnetically-induced solid-state electrochemical detection of DNA hybridization. *Journal of the American Chemical Society* **2002**, *124* (16), 4208-4209.
254. Hwang, S.; Kim, E.; Kwak, J., Electrochemical detection of DNA hybridization using biometallization. *Analytical chemistry* **2005**, *77* (2), 579-584.

255. Wang, J.; Rincón, O.; Polsky, R.; Dominguez, E., Electrochemical detection of DNA hybridization based on DNA-templated assembly of silver cluster. *Electrochemistry communications* **2003**, *5*(1), 83-86.
256. Talib, N. A. A.; Salam, F.; Yusof, N. A.; Ahmad, S. A. A.; Sulaiman, Y., Optimization of peak current of poly (3, 4-ethylenedioxythiophene)/multi-walled carbon nanotube using response surface methodology/central composite design. *RSC advances* **2017**, *7* (18), 11101-11110.
257. Wei, D.; Wu, X.; Xu, J.; Dong, F.; Liu, X.; Zheng, Y.; Ji, M., Determination of Ochratoxin A contamination in grapes, processed grape products and animal-derived products using ultra-performance liquid chromatography-tandem mass spectroscopy system. *Scientific reports* **2018**, *8*(1), 1-8.
258. Chen, X.; Karpenko, A.; Lopez-Acevedo, O., Silver-mediated double helix: structural parameters for a robust DNA building block. *ACS omega* **2017**, *2* (10), 7343-7348.
259. Retter, U.; Lohse, H., Electrochemical impedance spectroscopy. In *Electroanalytical Methods*, Springer: 2010; pp 159-177.
260. Bard, A. J.; Salzman, H., Electroanalytical chemistry. *Journal of The Electrochemical Society* **1969**, *116* (11), 378C.
261. Tan, Y.; Wei, X.; Zhang, Y.; Wang, P.; Qiu, B.; Guo, L.; Lin, Z.; Yang, H.-H., Exonuclease-catalyzed target recycling amplification and immobilization-free electrochemical aptasensor. *Analytical chemistry* **2015**, *87* (23), 11826-11831.
262. Bougrini, M.; Baraket, A.; Jamshaid, T.; El Aissari, A.; Bausells, J.; Zabala, M.; El Bari, N.; Bouchikhi, B.; Jaffrezic-Renault, N.; Abdelhamid, E., Development of a novel capacitance electrochemical biosensor based on silicon nitride for ochratoxin A detection. *Sensors and Actuators B: Chemical* **2016**, *234*, 446-452.
263. Mishra, R. K.; Hayat, A.; Catanante, G.; Istamboulie, G.; Marty, J.-L., Sensitive quantitation of Ochratoxin A in cocoa beans using differential pulse voltammetry based aptasensor. *Food Chemistry* **2016**, *192*, 799-804.
264. Badea, M.; Floroian, L.; Restani, P.; Cobzac, S. C. A.; Moga, M., Ochratoxin A detection on antibody-immobilized on BSA-functionalized gold electrodes. *PLoS One* **2016**, *11* (7), e0160021.
265. Mejri-Omrani, N.; Miodek, A.; Zribi, B.; Marrakchi, M.; Hamdi, M.; Marty, J.-L.; Korri-Youssoufi, H., Direct detection of OTA by impedimetric aptasensor based on modified polypyrrole-dendrimers. *Analytica Chimica Acta* **2016**, *920*, 37-46.
266. Sun, A.-L.; Zhang, Y.-F.; Sun, G.-P.; Wang, X.-N.; Tang, D., Homogeneous electrochemical detection of ochratoxin A in foodstuff using aptamer-graphene oxide nanosheets and DNase I-based target recycling reaction. *Biosensors and Bioelectronics* **2017**, *89*, 659-665.
267. Abnous, K.; Danesh, N. M.; Alibolandi, M.; Ramezani, M.; Taghdisi, S. M., Amperometric aptasensor for ochratoxin A based on the use of a gold electrode modified with aptamer, complementary DNA, SWCNTs and the redox marker Methylene Blue. *Microchimica Acta* **2017**, *184* (4), 1151-1159.
268. Qing, Y.; Li, X.; Chen, S.; Zhou, X.; Luo, M.; Xu, X.; Li, C.; Qiu, J., Differential pulse voltammetric ochratoxin A assay based on the use of an aptamer and hybridization chain reaction. *Microchimica Acta* **2017**, *184* (3), 863-870.
269. Xiang, Y.; Camarada, M. B.; Wen, Y.; Wu, H.; Chen, J.; Li, M.; Liao, X., Simple voltammetric analyses of ochratoxin A in food samples using highly-stable and anti-fouling black phosphorene nanosensor. *Electrochimica Acta* **2018**, *282*, 490-498.
270. Zejli, H.; Goud, K. Y.; Marty, J. L., Label free aptasensor for ochratoxin A detection using polythiophene-3-carboxylic acid. *Talanta* **2018**, *185*, 513-519.
271. Zhu, X.; Kou, F.; Xu, H.; Han, Y.; Yang, G.; Huang, X.; Chen, W.; Chi, Y.; Lin, Z., Label-free ochratoxin A electrochemical aptasensor based on target-induced noncovalent assembly of peroxidase-like graphitic carbon nitride nanosheet. *Sensors and Actuators B: Chemical* **2018**, *270*, 263-269.
272. Liu, C.; Guo, Y.; Luo, F.; Rao, P.; Fu, C.; Wang, S., Homogeneous Electrochemical Method for Ochratoxin A Determination Based on Target Triggered Aptamer Hairpin Switch and

- Exonuclease III-Assisted Recycling Amplification. *Food Analytical Methods* **2017**, *10* (6), 1982-1990.
273. Wei, M.; Zhang, W., The determination of Ochratoxin A based on the electrochemical aptasensor by carbon aerogels and methylene blue assisted signal amplification. *Chemistry Central Journal* **2018**, *12* (1), 45.
274. Harvey, S., On the detection of lead in potable waters by means of potassium bichromate. *Analyst* **1881**, *6* (August), 146-148.
275. Jaffé, M., Ueber den Niederschlag, welchen Pikrinsäure in normalem Harn erzeugt und über eine neue Reaction des Kreatinins. *Zeitschrift für physiologische Chemie* **1886**, *10* (5), 391-400.
276. Budden, E. R.; Hardy, H., Preliminary notes on the colorimetric estimation of minute quantities of lead, copper, tin, and iron. *Analyst* **1894**, *19* (August), 169-178.
277. Martinez, A. W.; Phillips, S. T.; Butte, M. J.; Whitesides, G. M., Patterned paper as a platform for inexpensive, low-volume, portable bioassays. *Angew. Chem. Int. Ed.* **2007**, *46* (8), 1318-1320.
278. Martinez, A. W.; Phillips, S. T.; Whitesides, G. M., Three-dimensional microfluidic devices fabricated in layered paper and tape. *Proc. Natl. Acad. Sci. U.S.A.* **2008**, *105* (50), 19606-19611.
279. Yang, Y.; Noviana, E.; Nguyen, M. P.; Geiss, B. J.; Dandy, D. S.; Henry, C. S., based microfluidic devices: emerging themes and applications. *Anal. Chem.* **2016**, *89* (1), 71-91.
280. Dungchai, W.; Chailapakul, O.; Henry, C. S., Electrochemical detection for paper-based microfluidics. *Anal. Chem.* **2009**, *81* (14), 5821-5826.
281. Almeida, M. I. G.; Jayawardane, B. M.; Kolev, S. D.; McKelvie, I. D., Developments of microfluidic paper-based analytical devices ( $\mu$ PADs) for water analysis: A review. *Talanta* **2018**, *177*, 176-190.
282. Mitchell, A.; Mellon, M., Colorimetric determination of nickel with dimethylglyoxime. *Industrial & Engineering Chemistry Analytical Edition* **1945**, *17* (6), 380-382.
283. Quesada-González, D.; Merkoçi, A., Nanomaterial-based devices for point-of-care diagnostic applications. *Chem. Soc. Rev.* **2018**, *47* (13), 4697-4709.
284. Zeng, S.; Yong, K.-T.; Roy, I.; Dinh, X.-Q.; Yu, X.; Luan, F., A review on functionalized gold nanoparticles for biosensing applications. *Plasmonics* **2011**, *6* (3), 491.
285. Howes, P. D.; Rana, S.; Stevens, M. M., Plasmonic nanomaterials for biodiagnostics. *Chem. Soc. Rev.* **2014**, *43* (11), 3835-3853.
286. Luechinger, N. A.; Athanassiou, E. K.; Stark, W. J., Graphene-stabilized copper nanoparticles as an air-stable substitute for silver and gold in low-cost ink-jet printable electronics. *Nanotechnology* **2008**, *19* (44), 445201.
287. Ellingsen, L. A.-W.; Hung, C. R.; Majeau-Bettez, G.; Singh, B.; Chen, Z.; Whittingham, M. S.; Strømman, A. H., Nanotechnology for environmentally sustainable electromobility. *Nat. Nanotechnol.* **2016**, *11* (12), 1039.
288. Khlebtsov, N.; Dykman, L., Biodistribution and toxicity of engineered gold nanoparticles: a review of in vitro and in vivo studies. *Chem. Soc. Rev.* **2011**, *40* (3), 1647-1671.
289. Weng, X.; Gaur, G.; Neethirajan, S., Rapid detection of food allergens by microfluidics ELISA-based optical sensor. *Biosensors* **2016**, *6* (2), 24.
290. Madhu, S.; Evans, H. A.; Doan-Nguyen, V. V.; Labram, J. G.; Wu, G.; Chabiny, M. L.; Seshadri, R.; Wudl, F., Infinite Polyiodide Chains in the Pyrroloperylene-Iodine Complex: Insights into the Starch-Iodine and Perylene-Iodine Complexes. *Angew. Chem. Int. Ed.* **2016**, *55* (28), 8032-8035.
291. McCready, R.; Guggolz, J.; Silveira, V.; Owens, H., Determination of starch and amylose in vegetables. *Anal. Chem.* **1950**, *22* (9), 1156-1158.
292. Nie, J.; Brown, T.; Zhang, Y., New two dimensional liquid-phase colorimetric assay based on old iodine-starch complexation for the naked-eye quantitative detection of analytes. *Chemical Communications* **2016**, *52* (47), 7454-7457.



293. Liu, Y.; Lei, L.; Zhang, Z., An ultrasensitive colorimetric immunoassay based on glucose oxidase catalyzed cascade formation of blue–black iodine–starch complex. *Sensors and Actuators B: Chemical* **2017**, *248*, 195-200.
294. Liu, M.-M.; Lian, X.; Liu, H.; Guo, Z.-Z.; Huang, H.-H.; Lei, Y.; Peng, H.-P.; Chen, W.; Lin, X.-H.; Liu, A.-L., A colorimetric assay for sensitive detection of hydrogen peroxide and glucose in microfluidic paper-based analytical devices integrated with starch-iodide-gelatin system. *Talanta* **2019**, *200*, 511-517.
295. Malir, F.; Ostry, V.; Pfohl-Leszkowicz, A.; Malir, J.; Toman, J., Ochratoxin A: 50 years of research. *Toxins* **2016**, *8*(7), 191.
296. Peng, Y.; Gelder, V. V.; Amaladoss, A.; Patel, K. H., Covalent Binding of Antibodies to Cellulose Paper Discs and Their Applications in Naked-eye Colorimetric Immunoassays. *JoVE* **2016**, (116), e54111.
297. Gardner, J. M.; Abrahamsson, M.; Farnum, B. H.; Meyer, G. J., Visible light generation of iodine atoms and I– I bonds: sensitized I– oxidation and I3– photodissociation. *J. Am. Chem. Soc.* **2009**, *131*(44), 16206-16214.
298. Wang, Z.; Chen, B.; Zhang, X.; Li, Y.; Fang, W.; Yu, X.; Dang, L., Fractionation of kudzu amylose and amylopectin and their microstructure and physicochemical properties. *Starch-Stärke* **2017**, *69*(3-4), 1500305.
299. Bezerra, M. A.; Santelli, R. E.; Oliveira, E. P.; Villar, L. S.; Escaleira, L. A., Response surface methodology (RSM) as a tool for optimization in analytical chemistry. *Talanta* **2008**, *76*(5), 965-977.
300. Suea-Ngam, A.; Srisa-Art, M.; Furutani, Y., PDMS-Based Microfluidic Device for Infrared-Transmission Spectro-Electrochemistry. *Bulletin of the Chemical Society of Japan* **2018**, *91*(5), 728-734.
301. Lee, J.; Jeon, C. H.; Ahn, S. J.; Ha, T. H., Highly stable colorimetric aptamer sensors for detection of ochratoxin A through optimizing the sequence with the covalent conjugation of hemin. *Analytist* **2014**, *139*(7), 1622-1627.
302. Bueno, D.; Valdez, L.; Gutiérrez Salgado, J.; Marty, J.; Muñoz, R., Colorimetric analysis of ochratoxin a in beverage samples. *Sensors* **2016**, *16*(11), 1888.
303. Wang, C.; Qian, J.; Wang, K.; Yang, X.; Liu, Q.; Hao, N.; Wang, C.; Dong, X.; Huang, X., Colorimetric aptasensing of ochratoxin A using Au@ Fe<sub>3</sub>O<sub>4</sub> nanoparticles as signal indicator and magnetic separator. *Biosensors and Bioelectronics* **2016**, *77*, 1183-1191.
304. Yin, X.; Wang, S.; Liu, X.; He, C.; Tang, Y.; Li, Q.; Liu, J.; Su, H.; Tan, T.; Dong, Y., Aptamer-based colorimetric biosensing of ochratoxin A in fortified white grape wine sample using unmodified gold nanoparticles. *Analytical Sciences* **2017**, *33*(6), 659-664.
305. Pei, K.; Xiong, Y.; Li, X.; Jiang, H.; Xiong, Y., Colorimetric ELISA with an acid–base indicator for sensitive detection of ochratoxin A in corn samples. *Analytical methods* **2018**, *10*(1), 30-36.
306. Pei, K.; Xiong, Y.; Xu, B.; Wu, K.; Li, X.; Jiang, H.; Xiong, Y., Colorimetric ELISA for ochratoxin A detection based on the urease-induced metallization of gold nanoflowers. *Sensors and Actuators B: Chemical* **2018**, *262*, 102-109.
307. Lin, C.; Zheng, H.; Sun, M.; Guo, Y.; Luo, F.; Guo, L.; Qiu, B.; Lin, Z.; Chen, G., Highly sensitive colorimetric aptasensor for ochratoxin A detection based on enzyme-encapsulated liposome. *Analytica chimica acta* **2018**, *1002*, 90-96.
308. Tian, F.; Zhou, J.; Jiao, B.; He, Y., A nanozyme-based cascade colorimetric aptasensor for amplified detection of ochratoxin A. *Nanoscale* **2019**.
309. Bonel, L.; Vidal, J. C.; Duato, P.; Castillo, J. R., Ochratoxin A nanostructured electrochemical immunosensors based on polyclonal antibodies and gold nanoparticles coupled to the antigen. *Analytical Methods* **2010**, *2*(4), 335-341.
310. Bio-Rad Datasheet. Rabbit Anti Aspergillus Ochraceus Ochratoxin A. **2020**, 6999-2130.
311. Suea-Ngam, A.; Howes, P. D.; Stanley, C.; deMello, A. J., An Exonuclease I-Assisted Silver-Metallized Electrochemical Aptasensor for Ochratoxin A Detection. *ACS sens.* **2019**.
312. Fanali, G.; Di Masi, A.; Trezza, V.; Marino, M.; Fasano, M.; Ascenzi, P., Human serum albumin: from bench to bedside. *Molecular aspects of medicine* **2012**, *33*(3), 209-290.

313. Brooks, T.; Keevil, C., A simple artificial urine for the growth of urinary pathogens. *Letters in applied microbiology* **1997**, *24* (3), 203-206.
314. Udugama, B.; Kadhiresan, P.; Kozlowski, H. N.; Malekjahani, A.; Osborne, M.; Li, V. Y. C.; Chen, H.; Mubareka, S.; Gubbay, J. B.; Chan, W. C. W., Diagnosing COVID-19: The Disease and Tools for Detection. *ACS Nano* **2020**, *14* (4), 3822-3835.
315. Zhou, F.; Yu, T.; Du, R.; Fan, G.; Liu, Y.; Liu, Z.; Xiang, J.; Wang, Y.; Song, B.; Gu, X.; Guan, L.; Wei, Y.; Li, H.; Wu, X.; Xu, J.; Tu, S.; Zhang, Y.; Chen, H.; Cao, B., Clinical course and risk factors for mortality of adult inpatients with COVID-19 in Wuhan, China: a retrospective cohort study. *The Lancet* **2020**, *395* (10229), 1054-1062.
316. Sheridan, C., Fast, portable tests come online to curb coronavirus pandemic. *Nat Biotechnol* **2020**, *38* (5), 515-518.
317. Soper, G. A., THE LESSONS OF THE PANDEMIC. *Science* **1919**, *49* (1274), 501-506.
318. Wellcome Trust. Advancing Epidemics R&D to Keep up with a Changing World: Progress, Challenges and Opportunities; [wellcome.ac.uk/sites/default/files/advancing-epidemics-rd-2019.pdf](http://wellcome.ac.uk/sites/default/files/advancing-epidemics-rd-2019.pdf) (accessed August 20th, 2020).
319. Sheldon, R. A.; Pereira, P. C., Biocatalysis engineering: the big picture. *Chemical Society Reviews* **2017**, *46* (10), 2678-2691.
320. Seed, K. D., Battling Phages: How Bacteria Defend against Viral Attack. *PLOS Pathogens* **2015**, *11* (6), e1004847.
321. Lander, Eric S., The Heroes of CRISPR. *Cell* **2016**, *164* (1), 18-28.
322. Sheldon, R. A.; Brady, D., The limits to biocatalysis: pushing the envelope. *Chemical Communications* **2018**, *54* (48), 6088-6104.
323. Chen, K.; Arnold, F. H., Engineering new catalytic activities in enzymes. *Nature Catalysis* **2020**, *3* (3), 203-213.
324. Russell, S. M.; de la Rica, R., Policy Considerations for Mobile Biosensors. *ACS Sensors* **2018**, *3* (6), 1059-1068.
325. Global Systems for Mobile Communications Association. The Mobile Economy, 2019; [www.gsma.com/mobileeconomy](http://www.gsma.com/mobileeconomy) (GMSA,2019) (accessed August 20th, 2020).
326. Schlager, R.; Chiu, C. Y.; Miller, S.; Procop, G. W.; Weinstock, G.; Committee, t. P. P.; Microbiology, C. o. L. P. o. t. A. S. f.; Pathologists, t. M. R. C. o. t. C. o. A., Validation of Metagenomic Next-Generation Sequencing Tests for Universal Pathogen Detection. *Archives of Pathology & Laboratory Medicine* **2017**, *141* (6), 776-786.
327. Deng, X.; Achari, A.; Federman, S.; Yu, G.; Somasekar, S.; Bartolo, I.; Yagi, S.; Mbala-Kingebeni, P.; Kapetshi, J.; Ahuka-Mundeke, S.; Muyembe-Tamfum, J.-J.; Ahmed, A. A.; Ganesh, V.; Tamhankar, M.; Patterson, J. L.; Ndembi, N.; Mbanya, D.; Kaptue, L.; McArthur, C.; Muñoz-Medina, J. E.; Gonzalez-Bonilla, C. R.; López, S.; Arias, C. F.; Arevalo, S.; Miller, S.; Stone, M.; Busch, M.; Hsieh, K.; Messenger, S.; Wadford, D. A.; Rodgers, M.; Cloherty, G.; Faria, N. R.; Thézé, J.; Pybus, O. G.; Neto, Z.; Morais, J.; Taveira, N.; R. Hackett, J.; Chiu, C. Y., Metagenomic sequencing with spiked primer enrichment for viral diagnostics and genomic surveillance. *Nature Microbiology* **2020**, *5* (3), 443-454.
328. World Health Organization. No Time to Wait: Securing the Future from Drug-Resistant Infections; [www.who.int/antimicrobialresistance/interagency-coordination-group/final-report/en/](http://www.who.int/antimicrobialresistance/interagency-coordination-group/final-report/en/) (accessed August 20th, 2020).
329. Leonard, H.; Colodner, R.; Halachmi, S.; Segal, E., Recent Advances in the Race to Design a Rapid Diagnostic Test for Antimicrobial Resistance. *ACS Sensors* **2018**, *3* (11), 2202-2217.

# Curriculum Vitae

**Akkapol** comes from Bangkok, Thailand. He completed his undergraduate degree in chemistry at Chulalongkorn University, receiving the best Bachelor thesis and the Hitachi Trophy 2014 awards. His research supervisor was Dr. Monpichar Srisa-Art who received her Ph.D. from deMello group at Imperial College London in 2010. He received his Master's degree in Analytical Chemistry from same department, having also spent a five-month period in the Furutani group at the Institute of Molecular Science in Okazaki, Japan, and was the recipient of the best Master Research Award from his department. Thereafter, he also received Ratchdapiseksompotch as the best Master Thesis Award from Chulalongkorn University. Akkapol joined the deMello group in 2016 as the recipient of a Swiss Government Excellence Scholarship. Akkapol has been awarded an Early Postdoc.Mobility grant to pursue his postdoctoral research in point-of-care diagnostics at Imperial College London in the Stevens group from 2021–2023. He has experience in developing electrochemical detectors for droplet-based and paper-based microfluidic systems, colorimetric assay, nanomaterials, electrochemical biosensors for single cell analysis, and spectroelectrochemical analysis.

**EMAIL:** [Palmarine@live.com](mailto:Palmarine@live.com)

**ORCID:** <https://orcid.org/0000-0002-2463-4548>

**Google Scholar:** Akkapol Suea-Ngam

**Publons:** Akkapol Suea-Ngam



## Education

- |                                 |   |
|---------------------------------|---|
| <b>2016 (Sept) – 2020 (Oct)</b> | <b>Dr.Sc. in Chemsitry</b> ETH Zürich, Zürich, SWITZERLAND (Prof. Dr. Andrew J. deMello as the thesis supervisor)   |
| <b>2014 (Sept) - 2016 (Aug)</b> | <b>M.Sc. in Chemistry</b> , (GPA: 3.79/4.00) Chulalongkorn University, Bangkok, THAILAND (Prof. Dr. Orawon Chilapakul and Assoc. Prof. Dr. Kanet Wongravee as co-advisors and Assist. Prof. Dr. Monpichar Srisa-Art as the thesis supervisor) |
| <b>2010 (Jun) - 2014 (Mar)</b>  | <b>B.Sc. in Chemistry</b> (GPA: 3.11/4.00), Chulalongkorn University, Bangkok, THAILAND (Assist. Prof. Dr. Monpichar Srisa-Art as the thesis supervisor)  |
| <b>2004 (May) - 2010 (Feb)</b>  | <b>High School</b> (GPA: 3.79/4.00), Suankularb Wittayalai School, Bangkok, THAILAND  |

## Employment History

- 2017 (Feb)- 2021 (Jan)**      **Scientific Assistant** (Ph.D. Student under the supervision of Prof. Dr. Andrew deMello)  
deMello Group, Institute for Chemical and Bioengineering (ICB), Department of Chemistry and Applied Bioscience (D-CHAB), ETH Zürich, SWITZERLAND
- 2015 (Sept) - 2016 (Aug)**      **Research Assistant** (as a Master Student for Assist. Prof. Dr. Monpichar Srisa-Art)  
90th Anniversary of Chulalongkorn University, Rachadapisek Sompote Fund, Department of Chemistry, Faculty of Science, Chulalongkorn University, THAILAND
- 2015 (Nov) - 2016 (Apr)**      **Research Fellow** (for Assoc. Prof. Dr. Yuji Furutani)  
Institute of Molecular Science, SOKENDAI, Okazaki, JAPAN
- 2014 (Sept) - 2016 (Aug)**      **Research Assistant** (as a Master Student for Prof. Dr. Orawon Chailapakul) Electrochemistry and Optical Spectroscopy Center of Excellence, Department of Chemistry, Faculty of Science, Chulalongkorn University, THAILAND
- 2014 (Sept) - 2015 (Aug)**      **Research Assistant** (as a Bachelor Student for Assist. Prof. Dr. Monpichar Srisa-Art) National Research University Project, Office of Higher Education Commission, Department of Chemistry, Faculty of Science, Chulalongkorn University, THAILAND
- 2013 (March-May)**              **R&D Intern Researcher** (as a Bachelor Student)  
INOAC (THAILAND) CO., LTD., IWCT, Bangkok, THAILAND

## Individual scientific reviewing activities

- 2020 (Sept-Present)**              Review Confirmation Certification (at least 1 manuscript)  
The Editors of **Processes**, MDPI Publisher, Basel, SWITZERLAND
- (Aug-Present)**                      Review Confirmation Certification (at least 1 manuscript)  
The Editors of **Coating**, MDPI Publisher, Basel, SWITZERLAND
- (Jun-present)**                      Referee (at least 2 Manuscripts) The editorial board of  
**RSC Advances**, The Royal Society of Chemistry, UNITED KINGDOM.
- (Apr-present)**                      Review Confirmation Certification (at least 2 manuscripts)  
The Editors of **Sensors**, MDPI Publisher, Basel, SWITZERLAND
- (Mar-present)**                      Review Confirmation Certification (at least 3 manuscripts)  
The Editors of **Materials**, MDPI Publisher, Basel, SWITZERLAND
- (Feb-present)**                      Review Confirmation Certification (at least 3 Manuscripts)  
The Editors of **Applied Science**, MDPI Publisher, SWITZERLAND
- (Jan-Present)**                      Review Confirmation Certification (at least 6 manuscripts)  
The Editors of **Micromachines**, MDPI Publisher, SWITZERLAND
- 2019 (Jun-present)**              Recognized reviewer achievement (at least 52 manuscripts)  
The Editors of **Analytical Chimica Acta** and the Reviewer Recognition Team, Elsevier Publisher, Amsterdam, The NETHERLANDS

---

## Grants and Awards

- 2021 (Mar) - 2023 (Feb)**      **Early Postdoc.Mobility**  
The Swiss national Science Foundation, SWITZERLAND
- 2016 (Sep) -2019 (Sep)**      **Swiss Government Excellent Scholarship for Foreign Scholars**  
The Federal Commission for Scholarships for Foreign Students (FCS), Swiss Confederation, SWITZERLAND
- 2018 (Aug)**      **BASF International Summer Course 2018 Grant**  
BASF SE, Ludwigshafen, GERMANY
- (Jan)**      **Kondeesrikaemee 2018 (Man of the year)**  
Department of Chemistry, Faculty of Science, Chulalongkorn University, THAILAND
- 2017 (Apr)**      **Ratchadapisek Sompoch Award** (the Best Master Thesis in Chulalongkorn University)  
Chulalongkorn University, THAILAND
- 2016 (Aug)**      **Excellent Thesis for Master Student**  
Department of Chemistry, Faculty of Science, Chulalongkorn University, THAILAND
- 2015 (Nov-Apr)**      **Institute of Molecular Science International Internship Program Grant**  
Institute of molecular science (IMS), Okazaki, JAPAN
- (Aug)**      **Excellence Thesis for Bachelor Student**  
Department of Chemistry, Faculty of Science, Chulalongkorn University, THAILAND
- (Jan)**      **Outstanding Oral Presentation**  
Pure and Applied Chemistry International Conference 2015 (PACCON 2015), THAILAND
- 2014 (Oct)**      **CBMS Student/Young Researcher Grant**  
18th International Conference on Miniaturized System for Chemistry and Life Science (microTAS 2014), San Antonio, TX, UNITED STATE of AMERICA
- (Mar)**      **1st prize for oral presentation in Physical Sciences, Mathematics and Computer Sciences**  
The Hitachi Trophy 2014, The Science Forum, Faculty of Science, Chulalongkorn University, THAILAND

## Publications in peer-reviewed scientific journals

Choopara; I., **Suea-Ngam; A.**, Teethaisong; Y., Howes; P.D., Schmelcher; M., Leelahavanichkul; A., Thunyaharn; S., Wongsawaeng; D., deMello; A.J., Dean; D., Somboonna; N. Fluorometric Paper-Based, Loop-Mediated Isothermal Amplification Devices for Quantitative Point-of-Care Detection of Methicillin Resistant Staphylococcus aureus (MRSA). *ACS Sens.*, **2021**, *In press*. <https://doi.org/10.1021/acssensors.0c01405>

**Suea-Ngam; A.**, Coopara; I., Somboonna; N., Schemelcher; M., Howes; P. D., deMello; A. J. Paper-based analytical devices for the naked eye detection of single copy drug-resistance bacteria using silver nanoplates. *Adv. Health. Mat.*, **2021**, *In press*. <https://doi.org/10.1002/adhm.202001755>

**Suea-Ngam; A.**, Bezing; L., Mateescu; B., Howes; P.H., deMello A.J., Richards; D. Enzyme-assisted nucleic acid detection for infectious disease diagnostics: moving towards the point-of-care. *ACS Sens.*, **2020**, *5*, 2701–2723. DOI: <https://doi.org/10.1021/acssensors.0c01488>

**Suea-Ngam; A.**, Deck; L.-T., Howes; P., deMello; A.J. An ultrasensitive non-noble metal colorimetric assay using starch-iodide complexation for Ochratoxin A detection. *Anal. Chim. Acta* **2020**, *1135*, 29-37. DOI: <https://doi.org/10.1016/j.aca.2020.08.028>

Bezing; L., **Suea-Ngam; A.**, deMello; A.J., Shih; C.J. Nanomaterials for molecular signal amplification in electrochemical nucleic acid biosensing: recent advances and future prospects for point-of-care diagnostics. *Mol. Syst. Des. Eng.* **2020**, *5*, 49-66. DOI: <https://doi.org/10.1039/C9ME00135B>

**Suea-Ngam; A.**, Howes; P., Srisa-Art; M., deMello; A.J. Droplet microfluidics: from proof-of-concept to real-world utility?. *Chem. Comm.* **2019**, *55*, 9895-9903. (Highlight) DOI: <https://doi.org/10.1039/C9CC04750F>

**Suea-Ngam; A.**, Stanley; C. E., Howes; P. D., deMello; A. D. An Exonuclease I-Assisted Silver-Metallized Electrochemical Aptasensor for Ochratoxin A Detection. *ACS sens.*, **2019**, *461*, 560-1568. (Cover) DOI: <https://doi.org/10.1021/acssensors.9b00237>

**Suea-Ngam; A.**, Srisa-Art; M., Furutani; Y. PDMS-Based Microfluidic Device for Infrared-Transmission Spectroelectrochemistry. *Bull. Chem. Soc. Jpn.*, **2018**, *91*, 728-734. (Selected Paper) DOI: <https://doi.org/10.1246/bcsj.20170430>

Jirasirichote; A., Punrat; E., **Suea-Ngam; A.**, Chailapakul; O., Chuanuwatanakul; S. Voltammetric detection of carbofuran determination using screen-printed carbon electrodes modified with gold nanoparticles and graphene oxide. *Talanta*, **2017**, *175*, 331-337. DOI: <https://doi.org/10.1016/j.talanta.2017.07.050>

**Suea-Ngam; A.**, Rattanarat; P., Wongravee; K., Chailapakul; O. and Srisa-Art; M. Droplet-based glucosamine sensor using gold nanoparticles and polyaniline-modified electrode. *Talanta*, **2016**, *158*, 134-141. DOI: <https://doi.org/10.1016/j.talanta.2016.05.052>

Rattanarat; P., **Suea-Ngam; A.**, Siangproh; W., Srisa-Art; M., and Chailapakul; O. Graphene-Polyaniline Modified Electrochemical Droplet-Based Microfluidic Sensor for High-throughput Determination of 4-Aminophenol. *Anal. Chem. Acta*, **2016**, *925*, 51-60. DOI: <https://doi.org/10.1016/j.aca.2016.03.010>

**Suea-Ngam; A.**, Rattanarat; P., Chailapakul; O. and Srisa-Art; M. Electrochemical droplet-based microfluidics using chip-based carbon paste electrodes for high-throughput analysis in pharmaceutical applications. *Anal. Chem. Acta*, **2015**, *883*, 45-54. DOI: <https://doi.org/10.1016/j.aca.2015.03.008>

## Peer-reviewed conference proceedings

**Suea-Ngam;** A., Rattanarat; P., Siangproh; W., Wongravee, K., Chailapakul; O. and Srisa-Art; M. (2015). On-line Single Cell Monitoring Using Electrochemical Sensor Coupled with Droplet-based Microfluidics. Proceeding of the 19th International Conference on Miniaturized System for Chemistry and Life Science (MicroTAS); **2015** October 25-29; Gyeongju, Korea.

**Suea-Ngam;** A., Rattanarat; P., Wongravee; K., Chailapakul; O. and Srisa-Art; M. (2015). Chip-based Polyaniline and Gold-nanoparticles Modified Electrode for Determination of D-Glucosamine. Proceeding of the Pure and Applied Chemistry International Conference (PACCON); **2015** January 31-23; Bangkok, Thailand.

**Suea-Ngam;** A., Rattanarat; P., Chailapakul; O. and Srisa-Art; M. (2014). Chip-based Carbon Paste Electrode for Electrochemical Detection of Droplet-based Microfluidics. Proceeding of the 18th International Conference on Miniaturized System for Chemistry and Life Science (MicroTAS); **2014** October 26-30; San Antonio, TX, USA.

## Contributions to international conferences

**2020** Suea-Ngam; A., **Halvorsen; Z.A.**, Revol; V., Stavrakis; S., Howes; P.D., and deMello; A.J., Hydrogel Digital LAMP Development for Highly Sensitive Drug-Resistance Bacteria Detection. **Poster presentation:** Swiss Symposium in Point-of-care Diagnostics, Visp, Switzerland, October 2020.

**2019** **Suea-Ngam;** A., Coopara; I., Schmelcher; M., Howes; P. D., and deMello; A. J. Paper-Based Analytical Devices (PADs) for Rapid and Cost Effective Single Copy Detection of Methicillin-Resistant Staphylococcus aureus (MRSA). **Oral Presentation:** 5th Meeting of Swiss Analytical Scientists, CHanalysis 2019, Dorint Hotel Beatenberg, Switzerland, April 2019.

**Suea-Ngam;** A., Coopara; I., Howes; P. D., and deMello; A. J. Paper-based analytical devices for single copy detection of Methicillin-Resistant Staphylococcus aureus (MRSA). **Oral Presentation:** Single-Molecule Sensors and NanoSystems International Conference (S3IC) 2019, Konferenzzentrum München, Munich, Germany, April 2019.

**Suea-Ngam;** A., Howes; P. D., and deMello; A. J. Ultra-Sensitive Aptamer-Based Electrochemical Detection of Ochratoxin A Using Silver Metallization and Exonuclease I. **Oral Presentation:** The Pittsburgh Conference & Exposition (PITTCON) 2019, Pennsylvania Convention Centre, Philadelphia, Pennsylvania, USA, March 2019.

- 2018**      **Suea-Ngam**; A. The Development and Optimization in Green Electrochemistry. Poster Presentation: BASF International Summer Course, BASF SE, Ludwigshafen, Germany, August 2018.
- 2016**      Furutani; Y., **Suea-Ngam**; A. Development of PDMA Microfluidic Devices Feasible for On-Chip Electrochemistry with Visible and IR Spectroscopy. Poster presentation: 10th Annual Meeting of Japan Society of Molecular Science, Kobe, Japan, September 2016.
- 2015**      **Suea-Ngam**; A., Rattanarat; P., Siangproh; W., Wongravee, K., Chilapakul; O. and Srisa-Art; M. On-line Single Cell Monitoring Using Electrochemical Sensor Coupled with Droplet-based Microfluidics. Poster presentation: The 19<sup>th</sup> International Conference on Miniaturized System for Chemistry and Life Science (MicroTAS 2015), Gyeongju, Korea, October, 2015.
- Suea-Ngam**; A., Rattanarat; P., Wongravee; K., Chailapakul; O. and Srisa-Art; M. Chip-based Polyaniline and Gold-nanoparticles Modified Electrode for Determination of D-Glucosamine. Oral presentation: The Pure and Applied Chemistry International Conference (PACCON 2015), Bangkok, Thailand, January, 2015.
- 2014**      Rattanarat; P., **Suea-Ngam**; A., Siangproh; W., Srisa-Art; M., and Chilapakul; O. An Electrochemical Droplet-Based Microfluidic Device for Selective Determination of 4-Aminophenol in Paracetamol Liquid Drug. Poster presentation: The 19<sup>th</sup> International Conference of Flow Injection Analysis and Related Technique, Fukuoka, Japan, December, 2014.
- Suea-Ngam**; A., Rattanarat; P., Chailapakul; O. and Srisa-Art; M. Chip-based Carbon Paste Electrode for Electrochemical Detection of Droplet-based Microfluidics. Poster presentation: The 18<sup>th</sup> International Conference on Miniaturized System for Chemistry and Life Science (MicroTAS2014), San Antonio, TX, USA, October, 2014.
- Suea-Ngam**; A., Rattanarat; P., Chailapakul; O. and Srisa-Art; M. An Application of Electrochemical Detection for Droplet-Based Microfluidics. Oral presentation: The Hitachi Trophy 2014, Science Senior Project, Thailand, April, 2014.



## Submitted publications

### Patents

Somboona; N., Choopara; I., **Suea-Ngam**; A., Srisa-Art; M., Chailapakul; O. Paper-based DNA amplification using Loop-mediated isothermal amplification. Thailand Patent, *Submitted since July 2019*.

Somboona; N., Choopara; I., **Suea-Ngam**; A., Srisa-Art; M., Wongravee; K. Quantitative detection methods for Staphylococcus aureus methicillin resistance (*MecA*) using loop mediated isothermal amplification combined with purple silver nanoparticles. Thailand Patent, *Submitted since July 2019*.

## Unpublished works

**Suea-Ngam**; A., Rattanarat; P., Wongravee, K., Chailapakul; O. and Srisa-Art; M. Fragmented flow Electrochemical detection for Single-cells Analysis Application. *In preparation*.

**Suea-Ngam**; A., Rattanarat; P., Wongravee; K., Chailapakul; O. and Srisa-Art; M. Ultra-High-Sensitivity Hg<sup>2+</sup> Detection Using Alkyl-thiol Modified Silver Nanoparticles on Electrochemical Paper-based Analytical Device (ePAD). *In preparation*.

**Suea-Ngam**; A., Halvorsen; Z.A., Revol; V., Stavrakis; S., Howes; P.D., and deMello; A.J., Hydrogel Digital LAMP Development for Highly Sensitive Drug-Resistance Bacteria Detection. *In preparation*.

**Suea-Ngam**; A., Howes; P.D., and deMello; A.J., An Amplification-Free Ultra-Sensitive Electrochemical CRISPR/Cas Biosensor for Drug-Resistant Bacteria Detection Using Silver Metallization. *In preparation*.